



## **Optical Experiments on Shared Quantum Correlations**

### **Author**

Bennet, Adam Joseph

### **Published**

2015

### **Thesis Type**

Thesis (PhD Doctorate)

### **School**

School of Biomolecular and Physical Sciences

### **DOI**

[10.25904/1912/1206](https://doi.org/10.25904/1912/1206)

### **Downloaded from**

<http://hdl.handle.net/10072/365930>

### **Griffith Research Online**

<https://research-repository.griffith.edu.au>

# **Optical experiments on shared quantum correlations**

Adam Joseph Bennet  
BPhotNanSc (Hons)

School of Biomolecular and Physical Sciences  
Science, Environment, Engineering and Technology  
Griffith University

Submitted in partial fulfilment of the requirements of the degree of  
Doctor of Philosophy

May 7, 2015



# Abstract

Shared quantum correlations find application in a wide range of modern quantum information protocols. This thesis presents several optical experiments towards the improved certification of shared quantum correlations, using photonic qubits.

The first experiment demonstrates the Einstein–Podolsky–Rosen (EPR) steering effect with no detection loophole. Polarisation–entangled photon pairs generated in a Sagnac interferometer were used to test new loss–tolerant EPR steering inequalities. To test the robustness of the loss–tolerant EPR steering inequalities, a transmission loss of  $-4.3\text{dB}$  was introduced using a 1km optical fibre loop, finding inequality violations for  $n = 10$  and  $n = 16$  measurement settings with no detection loophole (equating to a total loss of 87%). The findings demonstrate how the new loss–tolerant protocols can be used to certify the EPR steering effect for arbitrarily high losses, and may find application in one–sided device–independent quantum key distribution protocols.

The second experiment introduces EPR steering in the context of an EPR steering game. The rules of the game allow for certification of shared quantum correlations via EPR steering inequalities without requiring trust in devices or parties external to a quantum referee. In particular, the experiment successfully demonstrates EPR steering in a measurement–device independent framework; a framework which has typically been accessible only through Bell inequality violations. The findings suggest the possibility for quantum–refereed one–sided device–independent quantum key distribution protocols.

The third experiment presents an extension of Bell’s inequality, introducing a local model applicable to shared quantum correlations generated in an entanglement swapping experiment. The new model employs a pair of

local hidden variables (one for each particle source), eliciting the description ‘bilocal model’. By assuming the pair of particle sources are independent and uncorrelated with one another, nonlinear Bell-like bilocal inequalities are introduced. The experiment violates two different bilocal inequalities, depending on the type of measurement used to enact the entanglement swapping. The bilocal inequalities rectify a disconnect between Bell’s theorem and the experimental architecture of entanglement swapping.

Entangled measurements can generate entangled quantum states and find widespread use in quantum information protocols. The fourth experiment introduces a witness for the certification of entangled measurements. The witnesses introduced are semi-device-independent, making their implementation easier than alternative measurement characterisation protocols like quantum detector or quantum process tomography. The witnesses are tested experimentally using uncharacterised (in principle) quantum probe states of restricted Hilbert space dimension, and demonstrate how measurements can be certified as entangled without reference to their physical implementation.

The experiments presented herein may find applications in quantum key distribution protocols, and directly contribute to the the certification of distributed entanglement, both in entanglement swapping architectures and over long transmission channels, and offers new strategies for the characterisation of measurement devices regularly employed in quantum information processing scenarios. In all cases, the resource potential of quantum correlations is demonstrated, and the technological and foundational importance of their unequivocal verification is established.

This work has not previously been submitted for a degree or diploma in any university. To the best of my knowledge and belief, the dissertation contains no material previously published or written by another person except where due reference is made in the dissertation itself.

Adam Bennet

# List of Publications

## Chapter 3

A. J. Bennet, D. A. Evans, D. J. Saunders, C. Branciard, E. G. Cavalanti, H. M. Wiseman, and G. J. Pryde. Arbitrarily loss-tolerant Einstein-Podolsky-Rosen-steering allowing a demonstration over 1 km of optical fibre with no detection loophole. *Phys. Rev. X.* 2:031003, 2012.

## Chapter 4

S. Kocsis, M.J.W. Hall, A. J. Bennet, D. J. Saunders, and G. J. Pryde. Experimental measurement-device-independent verification of quantum steering. *Nat. Comms.* 6:5886, 2015.

## Chapter 5

D. J. Saunders, A. J. Bennet, C. Branciard, and G. J. Pryde. Experimental demonstration of bilocal inequality violations. *Manuscript in preparation.*

## Chapter 6

A. Bennet, T. Vértesi, D. J. Saunders, G. J. Pryde, and N. Brunner. Experimental semi-device-independent certification of entangled measurements. *Phys. Rev. Lett.* 113:080405, 2014.

## Other

M. S. Palsson, J.J. Wallman, A. J. Bennet, and G. J. Pryde. Experimentally demonstrating reference-frame-independent violations of Bell inequalities. *Phys. Rev. A.* 86:032322, 2012.

# Contents

<b>Abstract</b>	iii
<b>List of Publications</b>	vi
<b>Contents</b>	ix
<b>List of Figures</b>	xi
<b>List of Tables</b>	xii
<b>1 Introduction</b>	1
<b>2 Quantum Optics and Quantum Information</b>	10
2.1 Introduction . . . . .	10
2.2 Qubits . . . . .	10
2.2.1 Describing Qubits . . . . .	12
2.2.2 Entangled Qubits . . . . .	14
2.3 Quantum Optics . . . . .	15
2.3.1 Quantisation of the Electromagnetic Field . . . . .	17
2.3.2 Number States . . . . .	19
2.3.3 Coherent states . . . . .	20
2.4 Nonlinear Optics . . . . .	21
2.4.1 Three-Wave Mixing Effects . . . . .	24
2.4.2 Phase Matching . . . . .	25
2.4.3 Second Harmonic Generation . . . . .	27
2.4.4 Spontaneous Parametric Down Conversion . . . . .	29
2.5 Techniques for Optical Quantum Information Science . . . . .	32
2.5.1 Polarisation . . . . .	33
2.5.2 Wave plates . . . . .	33
2.5.3 Beam splitters . . . . .	36
2.5.4 Hong-Ou-Mandel interference . . . . .	36

2.5.5	Photon Detection . . . . .	41
2.5.6	Projective Measurements . . . . .	41
2.5.7	Quantum State Tomography . . . . .	44
2.6	Nonclassical Correlations . . . . .	46
2.6.1	Bell's theorem . . . . .	47
2.6.2	Bell's Inequality . . . . .	48
2.6.3	CHSH Inequality . . . . .	50
2.6.4	Local Models for EPR Steering . . . . .	52
2.6.5	Entanglement Swapping . . . . .	58
2.7	Summary . . . . .	60
<b>3</b>	<b>Loss-Tolerant Einstein-Podolsky-Rosen Steering</b>	<b>61</b>
3.1	Introduction . . . . .	61
3.2	A Loss-Tolerant EPR Steering Protocol . . . . .	64
3.2.1	Loss-Tolerant EPR-Steering Inequality . . . . .	65
3.3	Demonstration of Loss-Tolerant EPR Steering . . . . .	70
3.3.1	Photon Source . . . . .	71
3.3.2	Results and Analysis . . . . .	74
3.4	Discussion . . . . .	80
<b>4</b>	<b>Quantum Refereed EPR Steering</b>	<b>82</b>
4.1	Introduction . . . . .	82
4.2	Formulating the Quantum Refereed EPR Steering game . . . . .	84
4.3	Experiment . . . . .	87
4.3.1	Photon Sources . . . . .	89
4.3.2	Partial Bell State Measurement Device . . . . .	91
4.3.3	Results and Analysis . . . . .	92
4.4	Discussion . . . . .	96
<b>5</b>	<b>Locality and Bi-locality</b>	<b>98</b>
5.1	Introduction . . . . .	98
5.2	The Bilocal model . . . . .	102
5.3	Bilocal Inequalites . . . . .	103
5.3.1	Bilocal Inequality for Ideal Bell-State Measurement . . . . .	104
5.3.2	Bilocal Inequality for Partial BSM . . . . .	106
5.4	Experiment . . . . .	108
5.4.1	Photon Sources . . . . .	109
5.4.2	Strengthening Source Independence . . . . .	110
5.4.3	Bell State Measurement Device . . . . .	111
5.4.4	Results and Analysis . . . . .	114

5.5 Discussion . . . . .	115
<b>6 Verifying Entangled Measurements</b>	<b>118</b>
6.1 Introduction . . . . .	118
6.2 Witness for Entangled Measurements . . . . .	122
6.2.1 Witness for Quantum Unentangled Measurements . .	126
6.3 Experiment . . . . .	127
6.3.1 Photon Sources . . . . .	129
6.3.2 Partial Bell State Measurement Device . . . . .	129
6.3.3 Results and Analysis . . . . .	131
6.4 Discussion . . . . .	135
<b>7 Conclusion</b>	<b>137</b>

# List of Figures

2.1	A qubit described on the Bloch Sphere. . . . .	12
2.2	The optical axis and index ellipsoid of a uniaxial dielectric material . . . . .	26
2.3	Type-I collinear second Harmonic Generation in a $\chi^{(2)}$ non-linear crystal. . . . .	28
2.4	Type-I and Type-II noncollinear spontaneous parametric down conversion configurations. . . . .	31
2.5	Polarisation encoded qubit states on the Poincaré sphere and in real space. . . . .	34
2.6	Common beam splitter types. . . . .	37
2.7	Coincidence pattern indicative of Hong-Ou-Mandel interference. .	40
2.8	Illustration of the axes corresponding to the Pauli spin matrices on the Poincaré sphere, and apparatus for performing projective measurements. . . . .	43
2.9	The EPR steering task. . . . .	55
2.10	EPR steering state preparation and measurement strategies for Alice (dishonest) and Bob. . . . .	57
2.11	The entanglement swapping protocol using a Bell state measurement device . . . . .	58
3.1	Alice's optimal cheating ensembles for $n = 10$ measurement settings and heralding efficiencies $\epsilon \in 0.2, 0.5$ . . . . .	67
3.2	Loss-dependent EPR steering bounds . . . . .	69
3.3	Schematic of the experimental apparatus for demonstrating EPR steering with no detection loophole . . . . .	72
3.4	Experimental demonstration of EPR steering . . . . .	75
3.5	Conceptual representation of the EPR steering task for a dishonest Alice . . . . .	77
3.6	Experimental data for a dishonest Alice . . . . .	79

4.1	Testing nonlocality classes via nonlocal games. . . . .	84
4.2	Illustration of experimental apparatus for EPR steering with a quantum referee . . . . .	88
4.3	Reconstructed density matrices for characterising the entan- gled source for a quantum–refereed EPR steering game . . . .	90
4.4	Characterising HOM interference for measurement–device– independent EPR steering . . . . .	92
4.5	Experimental verification of measurement–device independent EPR steering: observed payoff function for Werner and sim- glet states . . . . .	94
5.1	The entanglement swapping scenario implemented in linear optics . . . . .	100
5.2	Illustration of an entanglement swapping scenario described by a bilocal model . . . . .	101
5.3	Illustration of experimental apparatus used to test bilocal in- equalities . . . . .	109
5.4	HOM dip for characterising Bob’s partial BSM device, recorded in four-fold coincidences . . . . .	113
6.1	Device–independent and semi–device–independent scenarios for entanglement certification and entangled measurement cer- tification . . . . .	120
6.2	Illustration of Alice and Bob’s ideal polarisation–encoded qubit probe states, expressed on the $XZ$ plane of the Poincaré sphere	124
6.3	Experimental schematic for semi–device–independent verifi- cation of entangled measurements and quantum unentangled measurements . . . . .	128
6.4	HOM dip recorded in four-fold coincidences for the semi– device–independent certification of entangled measurements .	130

## List of Tables

6.1	Characterisation of Alice and Bob's probe states for testing the semi-device-independent witness . . . . .	132
7.1	Size of error factors contributing to $\Delta S_n^{sys}$ – Fig. 3.4 data – without 1 km fiber . . . . .	149
7.2	Size of error factors contributing to $\Delta S_n^{sys}$ – Fig. 3.4 data – with 1 km fiber . . . . .	149
7.3	Size of systematic and statistical error factors contributing to $\Delta S_n$ – Fig. 3.4 data – without 1 km fiber . . . . .	150
7.4	Size of systematic and statistical error factors contributing to $\Delta S_n$ – Fig. 3.4 data – with 1 km fiber . . . . .	150

# Acknowledgments

## Supervisors

“Anyway, I’ve ranted enough.” – Geoff Pryde

“Yes, well, but, now hang on a minute.” – Howard Wiseman

## Friends

“Light is made of protons.” – Valentina Guevara

“Why do you guys always walk so slow?” – Morgan Weston

“Yes, my husband is homophobic. I mean claustrophobic.” – Ivonne Guevara

“Will your sister be there?” – Sacha Kocsis

“Coffee? ” – Karen Kalt

“I have this idea...” – Dylan Saunders

## Family

“I forget that some people live their lives that way.” – Louise Bennet

“You’re gross.” – Hayley Bennet

“That’s gross.” – Kaitlin Bennet

“You don’t know your own strength.” – Beverley Bennet

# Chapter 1

## Introduction

The idea that *information* could encompass a topic of rigorous scientific enquiry entered public consciousness in 1948 when mathematician Claude Shannon combined the notion of *entropy* (a measure of disorder in classical thermodynamics) with information-theoretic ideas originally developed by Harry Nyquist and Ralph Hartley working at Bell Labs [1–4], with the landmark work earning Shannon the colloquial title “the father of information theory”. Shannon’s work benefitted further by incorporating developments made during codebreaking efforts of the recently-ended World War II [5], and received strong input from Alan Turing and Rolf Landauer. The work additionally incorporated earlier ideas from John von Neumann, Alonzo Church, and David Hilbert, further supplementing the fertile new fields of information and computation sciences.

Computational technologies and artificial intelligence, derived from Shannon’s work, entered the 20th century in alignment with the performance predictions of *Moore’s law*, which states that information processing power increases exponentially with time [6]. However, nature has demonstrated its eventual incompatibility with exponential growth, as evidenced by the recent *decline* of Moore’s law for processing power arising as a result of electronic transistor technologies approaching the atomic scale [6–8]. Fortunately for computation and information technologies as a whole, the future appears auspicious in light of recent advancements in *quantum* computation and information technologies, recent fields whereby traditional computer and information sciences are fused with the science of quantum physics [9].

Interest in the integration of quantum phenomena with technological systems was further sparked by Richard Feynman’s 1982 suggestion that simu-

lations of quantum phenomena would require quantum technologies, specifically quantum computing [10]. Feynman’s ideas resulted in intense investigation, and expanded upon the pioneering work of original quantum theory conducted in 1900–1930 dedicated to distilling the principles of quantum physics from key unsolved problems in classical physics. Specific motivating factors integral to the development of the original quantum theory were the so-called “ultraviolet catastrophe” (whereby the Rayleigh-Jeans law predicted infinite radiative energy from heated bodies [11]), Heinrich Hertz’s discovery that electrodes illuminated with UV light created electric sparks more easily [12], and Rutherford’s model of the atom (predicting electrons orbiting atomic nuclei would radiate energy until they crashed into the nucleus [13]). The calamities of classical physics rested at the precipice between classical and quantum understanding, and bestowed the early 1900s with special significance in scientific history. The events that transpired provide an interesting taste of the nonintuitive flavour of quantum theory, and revisiting them presents a convenient introduction and stepping stone into quantum information concepts, which form a central focus of this thesis.

In resolving the ultraviolet catastrophe<sup>1</sup> Max Planck presented work on the derivation of Wien’s empirical law describing the radiation emitted by a black body, in 1900. Planck derived a model accurately predicting and reproducing experimental observations from radiative black bodies by describing the number of ways a given amount of energy could be distributed across a set of oscillators. As a matter of convenience, Planck proposed that the total energy of a system could be comprised of a finite number of energy units, a process known as “quantisation”. Interestingly, Planck was the first to consider energy as consisting of discrete packets - “energy elements” [15] – although he considered the concept “a purely formal assumption” [14]. It was not until 1908 that Planck, influenced by Dutch physicist Hendrik Lorentz, openly accepted quantised energy units as hinting towards an alternative fundamental theory.

Planck’s law and its derivation were accepted, but the underlying significance of abstract oscillator behaviours and discretised energies were overshadowed by the introduction of a new constant of nature ( $h = 6.62 \times 10^{-34} \text{ m}^2\text{kg/s}$ ) and the accuracy of the new theory. In 1905, when Albert Einstein released the first paper of his *Annus Mirabilis* on the photoelectric effect

---

<sup>1</sup>The problem of infinite energies was never actually referred to as the “ultraviolet catastrophe” by contemporaries of the time - it was coined as being “catastrophic” later, in 1911 by Paul Ehrenfest [11, 14].

(addressing the problem initially reported by Heinrich Hertz in 1887 [16]), Planck's insight began to gain traction, as academic perception meandered towards a new model of nature. Contemplating discrete energies similarly inspired Neils Bohr to resolve problems with Rutherford's electron cloud model of the atom, proposing that electrons orbit atomic nuclei in restricted orbits, leading to discrete energy levels [17]. These ideas formed a semi-classical model of physics and marked the first quantum revolution – now referred to as the ‘old quantum theory’. The principles introduced during the first quantum revolution sparked increased interest in the fundamentals of nature, an evolution continuing into the 1920’s when the inception of quantum mechanics marked the second quantum revolution, foreshadowing modern quantum theory.

Today there exist several interpretations of quantum theory [18–21], a testament to the complex workings of nature and the still numerous unsolved problems in physics [22–26]. One such interpretation that garners widespread acceptance is the Copenhagen interpretation of quantum mechanics, introduced between 1924 and 1927 by Neils Bohr and Werner Heisenberg. The introduction of the Copenhagen interpretation accompanied a turbulent period in the history of physics, as Bohr and Heisenberg argued in an obstinate (bordering on dogmatic) manner for the universal acceptance of their interpretation<sup>2</sup> [27]. A key criticism levelled at the Copenhagen interpretation was conflict with a principal feature of Einstein’s special relativity - that an effect and its cause in spacetime must exist within the same lightcone, so that distant events cannot have instantaneous influences across spacetime. In the Copenhagen interpretation the state (or wavefunction  $\psi$ ) of a single particle could become arbitrarily spread out in spacetime, creating a superposition of configurations (the quantum superposition). In quantum mechanics, information about a particle is gathered through measurement, necessarily disturbing the particle and sharply defining the particle’s position or momentum (depending on which ‘observable’ is measured). A feature of the Copenhagen interpretation that greatly troubled Einstein was the sharp alteration of a particle’s wavefunction (which for Einstein, represented physical reality) from a superposition of configuration states to a single configuration state (known as ‘wavefunction collapse’). This alteration appeared to happen instantaneously across all of spacetime, so violating Einstein’s ‘local causality’. Furthermore, the quantum mechanical wavefunction designated

---

<sup>2</sup>The widespread acceptance of the Copenhagen interpretation today may be attributed to the outspoken attitudes and determination adopted by Bohr and Heisenberg against the critiques of contemporaries.

no definite value to observables until the moment of measurement, making reality an emergent feature of measurement (as opposed to an objective feature of the universe), another feature that unsettled Einstein.

In 1927, de Broglie (with support from Einstein) addressed their perceived problems surrounding the Copenhagen interpretation by introducing a ‘pilot wave’ theory, whereby quantum particles were designated pre-existing features [28] (meaning that a particle’s properties exist in objective reality prior to measurement). Unfortunately, de Broglie’s theory was also found to violate local causality for instances describing two or more particles representing physical reality. By 1931, Einstein had accepted the formalism of quantum mechanics, although Einstein did not accept Bohr’s interpretation of the theory, famously quoting [29]:

I, at any rate, am convinced that *He* (God) does not throw dice.

Einstein’s dissatisfaction with the Copenhagen interpretation led to the well known 1935 paper by EPR (Einstein, Boris Podolsky and Nathan Rosen), titled “Can quantum-mechanical description of physical reality be considered complete? [30]”.

EPR’s argument of 1935 demonstrated that if quantum theory truly and accurately described nature, then it must be incomplete. Their argument was based on a special ‘entangled’ state<sup>3</sup> or wavefunction  $\psi$  permitted by quantum mechanics describing two particles that are well separated and correlated in their relative position and total momentum. The pure entangled state considered by EPR had the feature that a position measurement on one particle (called  $S_1$ ) would reveal the precise position of a second particle (called  $S_2$ ) by virtue of the correlated nature of the entangled state. Similarly, a momentum measurement on  $S_1$  would reveal the precise momentum of  $S_2$  for the same reason. Importantly, Einstein’s formulation of local causality implied that measurements upon  $S_1$  cannot instantaneously influence events that transpire at the locale of  $S_2$ . EPR then went on to argue that if a physical quantity can be predicted with certainty (that is, without measuring or disturbing the system of interest), then by local causality that physical quantity must represent some ‘element of physical reality’. That is to say, in the case of  $S_1$  and  $S_2$ , the position or momentum measurement outcome from  $S_1$  predicts with certainty the corresponding physical

---

<sup>3</sup>Such states were coined ‘entangled’ by Schrödinger [31], and these entangled states are precisely the foundation behind the utility and power of many quantum technologies being researched and developed today.

quantity of position or momentum on  $S_2$ , meaning that  $S_2$ 's position and momentum are elements of physical reality. Hence by EPR's reasoning the position *and* momentum of  $S_2$  must therefore be predefined prior to measurement on  $S_1$ . Having made the assumption of Einstein's local causality and defined the elements of physical reality, EPR then concluded the following: If Bohr's principle of complementarity holds (a principle closely related to the Copenhagen interpretation stating that particles possess complementary properties that cannot be accurately measured at the same time), then the position *and* momentum of  $S_2$  cannot be defined simultaneously prior to measurement, and in particular for the entangled state in question, quantum mechanics ascribes to *both* position and momentum an arbitrarily large uncertainty. Essentially, *for a single instance of the experiment*, the quantum mechanical wavefunction wholly failed to capture elements of reality for position and momentum, and hence EPR concluded that quantum mechanics must be incomplete [27]. Importantly, the question was not whether quantum mechanics gave a correct statistical description, but rather if the apparent lack of knowledge could not be overcome with a more complete theory.

Bohr's reply [32] to the EPR paper was received favourably at the time, however his arguments were convoluted [27]. In fact, Bohr's proponents themselves had difficulty deciphering his response [27, 33, 34], and his arguments were clouded to such an extent that when his views were reprinted in 1983, reviewers failed to notice that the pages were printed out of order [27, 35]. Schrödinger's perspectives at the time brought further attention to the issue of wavefunction collapse, introducing the famous paradox of 'Schrödinger's cat' [31] - a thought experiment that saw quantum effects propagating into the macroscopic realm, with counter-intuitive outcomes sometimes referred to as the *measurement problem* [18, 25]. Unfortunately, the arguments of Einstein and Schrödinger were further overshadowed by von Neumann's 1932 supposed proof<sup>4</sup> on the impossibility of 'hidden variables'. Hidden variable theories, like de Broglie's, assigned to particles an element of physical reality through the proposed existence of inaccessible but nevertheless manifest 'hidden' variables.

Despite von Neumann's theorem being ultimately discredited, the public perception was that hidden variable theories were an infeasible solution to

---

<sup>4</sup>Supposed, because it was later found that von Neumann had unknowingly used unfounded strong assumptions in order to prove his impossibility theorem [36].

the EPR paradox. However, in 1952 David Bohm extended de Broglie's original pilot wave theory, developing a consistent theory based on hidden variables that circumvented the measurement problem [18] but still violated local causality, however, academic opinion prevailed over Bohm's theory in favour of the still effective Copenhagen interpretation even though it violated local causality *and* produced the measurement problem. Einstein, while in favour of Bohm's developments, remained lackluster as he was aware of the local causality violations in Bohm's interpretation, all the while hoping for a radical hidden variable theory that honoured local causality and realism [27].

Einstein's preference for a local realistic theory was eventually proven to be fruitless in 1964, when John Bell proved that any realistic theory of quantum phenomena (assuming the objective existence of reality) must violate Einstein's local causality [37]. The profound work of Bell highlights a great paradox - that realism and local causality cannot co-exist in a consistent theory of the universe. In 1982, Alain Aspect *et. al.* conducted an experiment verifying the predictions of Bell's theorem [38] (using an experimentally testable version of Bell's theorem, derived by Clauser, Horne, Shimony and Holt [39]), quieting concerns raised by Schrödinger in 1936 that EPR correlations might not exist in practice [40]. The experiment indicated that quantum mechanics does indeed permit correlations between distant parties that exceed those allowed in a universe that honours both local causality and realism simultaneously. Research has since expanded on Bell's theorem, and made evident further underlying assumptions that may account, in a local realistic manner, for the results of Bell's theorem and Aspect's results<sup>5</sup>, including the possibility that free will is an illusion [44]. Regardless of personal perspective, it seems at this juncture that a) local causality may not be honoured by the workings of the universe, b) that reality may be an emergent feature of continuous measurement (to such an extent that an experimenter is justified in denying the independent objective reality of others - blatant solipsism [45,46]), or c) that free will is an illusion.

These possibilities are the focus of much study in fundamental quantum physics. Remarkably, the implications of Bell's theorem are not only philosophical. Akin to the work of Shannon and Feynman, there exist legitimate technological applications of Bell's theorem, and more broadly of entangle-

---

<sup>5</sup>One can point to certain experimental loopholes, for instance a “fair-sampling” assumption was needed due to detector inefficiencies. Alternatively, one can a) refuse correlations are mysterious [41], b) posit backward-in-time causation [42], or c) claim that boolean logic is invalid in our universe [43].

ment and quantum effects in general. These properties of nature underly the rich tapestry of possibility offered by modern quantum technologies. Promised advantages of quantum resources include increases in computing efficiency [47]; unparalleled advancements in numerical analysis, codebreaking, and data processing [48, 49]; perfectly private and unhackable communication protocols [50, 51]; enhanced simulations of quantum effects [10], imaging and sensing [52]; with further indirect applications limited only by imagination [53].

This thesis explores several such novel areas of quantum technologies. The proof-of-principle demonstrations herein serve a dual purpose: they probe the nonclassical nature of quantum systems, especially entangled quantum systems; and they serve as stepping stones for advances in quantum computing and notably (of relevance to this thesis) quantum information science – a multidisciplinary field primarily concerned with the acquisition, analysis, manipulation and distribution of information encoded in the states of quantum systems. The experiments presented in this thesis explore several areas of quantum information science, with particular focus on research in shared quantum correlations (finding application in the secure sharing of private information between remote parties), quantum network architectures (concerning the generation, characterisation, and distribution of quantum information and correlations), and quantum foundations (the study of quantum physics, nonlocality, and the fabric of reality itself).

Chapter 2 introduces a number of concepts relevant to performing experiments on shared quantum correlations, beginning with an introduction to quantum mechanical formalism. Key concepts in quantum optics are then outlined, as is the generation and manipulation of quantum states of light. These elements prelude the introduction of a framework for quantum information science. Nonclassical correlations are then introduced in the form of Bell’s theorem and EPR correlations, followed by an overview of entanglement swapping.

Chapter 3 presents experimental research towards EPR steering, a quantum effect originally coined by Schrödinger [54]. The EPR steering effect can be used to enhance the security of private information sharing between two remote parties. The structure of the EPR steering protocol requires trust in one of the two parties, meaning one agent of the pair is trusted to perform an appropriate measurement strategy, and additionally, that agent’s device and associated description of the device is known and trusted. Chapter

3 makes a novel enhancement to the EPR steering protocol by introducing loss-tolerant EPR steering protocols, allowing for the absolutely secure sharing of information (in principle) over a lossy transmission channel. From an applied perspective, the work finds use in a class of cryptographic protocols known as *asymmetric one-sided device-independent* protocols [55]. From a fundamental standpoint, the research demonstrates the EPR steering effect over lossy channels with no fair-sampling assumption [56].

Chapter 4 presents a second EPR-steering experiment. The verification of the EPR steering effect between remote parties is introduced via an EPR steering *game*, whereby an impartial *referee* mediates the EPR steering protocol. By allowing the referee of the game to employ a quantum signal, the sharing of private information between two untrusted parties may be established. The protocol achieves this by requiring that a referee trust only his own ability to prepare and send quantum states. This modification removes the referee's need for trust in remote parties, their devices, and the description of their devices. The work presented in chapter 4 finds application in improving one-sided device-independent protocols [55], with the research presented acting as a measurement-device independent EPR steering protocol, a scenario typically reserved for instances of Bell-inequality violations [57,58].

Chapter 5 details a quantum foundations experiment that explores correlations arising between particles that have never interacted, for example in entangled particle pairs generated in entanglement swapping protocols [60–65]. The experiment demonstrates the efficacy of recent theoretical work which rectifies a disconnect between the framework of Bell's theorem as applied to entanglement swapping architectures [66,67]. The work presented in chapter 5 finds potential application in benchmarking quantum networks, and has implications towards causal interpretations of the universe.

Chapter 6 presents an experiment that determines the character of a measurement without making assumptions about the physical implementation of the measurement. The experiment expands upon and tests recent theoretical work that treats measurement devices as “black boxes” and uses experimental statistics only to deduce useful information about the type of measurement performed [68]. The research presents a means of answering the question: can unknown measurements be distinguished as classical, quantum, or entangled?

Chapter 7 concludes this thesis. The main results are summarised and put into context, and future directions for research are discussed.

## Chapter 2

# Quantum Optics and Quantum Information

### 2.1 Introduction

The current chapter presents no new contributions to scientific knowledge, serving only to inform a general readership of important theoretical concepts and experimental techniques employed in conducting experimental research on shared quantum correlations as presented in this thesis. New contributions to knowledge are presented in chapters 3 to 6.

This thesis focuses on studying shared quantum correlations in the context of *optical quantum information science* - a nascent topic of research combining the fields of quantum physics, optics, and information science. The current chapter presents general introductory material on quantum optics, nonlinear optics, quantum state generation and characterisation, polarisation encoding, and nonclassical effects and correlations. Readers familiar with particular components of the current chapter may skip sections as necessary.

### 2.2 Qubits

In classical information and computer theory, the fundamental unit of information is called a *bit*, physically manifested by (for example) an engraving on a stone tablet, a spin, a charge, a hole in a punched card, a mark on paper, or some other equivalent [69]. The bit is a two level system with ‘0’ and ‘1’ logical states, where collective bits convey complex data and information is manipulated through bitwise operations and processing.

The analogous quantum bit, or *qubit* [70], is a quantum system with two *basis states* represented in Dirac bra-ket notation as  $|0\rangle$  and  $|1\rangle$ . The bra-ket notation ‘ $| \rangle$ ’ represents a vector in quantum mechanical *Hilbert space*, which is an inner product space [70]. The basis states in a Hilbert space are chosen to be *orthonormal* (orthogonal and normalised), meaning the inner products are  $\langle 0|0\rangle = \langle 1|1\rangle = 1$ , and  $\langle 0|1\rangle = \langle 1|0\rangle = 0$ , where  $|x\rangle^\dagger = \langle x|$  is the Hermitian adjoint.

In optical quantum information science, qubits may be physically represented by *photons*, as is consistently the case in this thesis. Photons are naively considered as single particles of light, or more precisely as elementary excitations of the quantised electromagnetic field (Sec 2.3). Photons are chargeless, massless, interact weakly with the environment, are bosons (any number of photons can occupy a single optical mode), and are easily manipulated. These properties make photons ideal candidates for the study of quantum information science.

Qubits possess properties unlike classical bits. Because the qubit lies in the quantum realm, the qubit  $|\psi\rangle$  can exist in a *quantum superposition* of basis states

$$|\psi\rangle = \alpha|0\rangle + \beta|1\rangle, \quad (2.1)$$

where  $\{\alpha, \beta\} \in \mathbb{C}$ , and  $|\alpha|^2 + |\beta|^2 = 1$  is called the *normalisation condition*. Quantum mechanics is a statistical theory, evaluating the probability for a qubit in the superposition state  $|\psi\rangle$  to occupy the basis state  $|0\rangle$  as

$$|\langle 0|\psi\rangle|^2 = \langle 0|\psi\rangle\langle\psi|0\rangle \quad (2.2)$$

$$= \langle 0|(\alpha|0\rangle + \beta|1\rangle)| \times (\alpha^*\langle 0| + \beta^*\langle 1|)|0\rangle \quad (2.3)$$

$$= |\alpha|^2. \quad (2.4)$$

Similarly, the probability of the qubit occupying state  $|1\rangle$  is  $|\langle 1|\psi\rangle|^2 = |\beta|^2$ . The quantum superposition allows a particle-like entity (for example, a single photon) to also exhibit wave-like propagation and interference effects, resulting in the *wave-particle duality* exhibited by quantum mechanical systems [71].

### 2.2.1 Describing Qubits

A single qubit can be expressed on the *Bloch* sphere<sup>1</sup> [70]. A *pure* qubit state  $|\psi\rangle$  extends to the surface of the sphere, finding expression geometrically as [71]

$$|\psi\rangle = \cos\frac{\theta}{2}|0\rangle + e^{i\phi}\sin\frac{\theta}{2}|1\rangle, \quad (2.5)$$

where  $\theta$  and  $\phi$  are real numbers depending on  $\alpha$  and  $\beta$ , and a global phase  $e^{i\gamma}$  is omitted because it contributes no observable effects [70]. Figure 2.1 illustrates the quantum states  $|0\rangle$ ,  $|1\rangle$ ,  $\frac{1}{\sqrt{2}}(|0\rangle \pm |1\rangle)$ , and  $|\psi\rangle$  on the Bloch sphere.

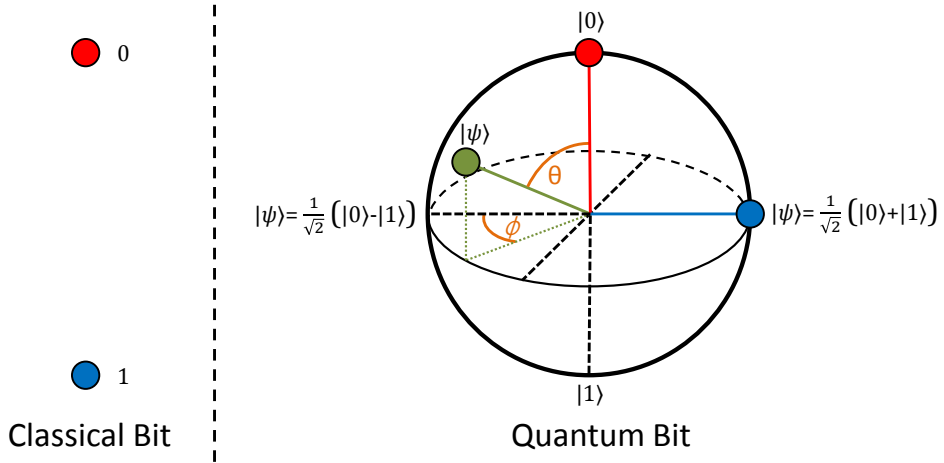


Figure 2.1: A qubit described on the Bloch Sphere. A pure state  $|\psi\rangle$  is described by a vector extending from the origin to the surface of the sphere. The angles  $\{\theta, \phi\}$  uniquely define the state vector for a pure state  $|\psi\rangle = \cos(\theta/2)|0\rangle + e^{i\phi}\sin(\theta/2)|1\rangle$ .

A more general description of a quantum state is given by the *density matrix* or *density operator* [70]. The density operator describes a probabilistic mixture of pure states (called a *mixed state*), and may describe states that lie inside the surface of the Bloch sphere<sup>2</sup>. The density operator is expressed as the statistical ensemble

$$\hat{\rho} = \sum_i p_i |\psi_i\rangle \langle \psi_i|, \quad (2.6)$$

<sup>1</sup>The Bloch sphere represents general spin-half quantum systems. The *Poincaré* sphere is used for the special case of polarisation encoded qubits, discussed in Sec. 2.5.

<sup>2</sup>Quantum states lie inside the Bloch sphere when they encounter environmental noise, accuracy limitations in state preparation or measurement apparatus, temperature dependent processes, and transmission or absorption losses.

where  $p_i$  is the probability of finding the system in the pure state  $|\psi_i\rangle$ , given a suitable measurement. The key difference between a pure superposition state and an ensemble of pure states is this: the pure superposition state is a state  $|\psi\rangle$  occupying multiple configurations simultaneously, whereas a mixed state is a statistical distribution of pure states  $|\psi_i\rangle$ , where each individual pure state is capable of occupying multiple configurations simultaneously.

Pure states like  $|\psi\rangle = \alpha|0\rangle + \beta|1\rangle$  are expressed in density operator formalism as

$$\hat{\rho} = |\psi\rangle\langle\psi| = |\alpha|^2|0\rangle\langle 0| + \alpha^*\beta|0\rangle\langle 1| + \alpha\beta^*|1\rangle\langle 0| + |\beta|^2|1\rangle\langle 1|, \quad (2.7)$$

corresponding to the density operator

$$\hat{\rho} = \begin{bmatrix} |\alpha^2| & \gamma \\ \gamma^* & |\beta^2| \end{bmatrix}. \quad (2.8)$$

where  $0 \leq \gamma \leq \alpha^*\beta$ . The diagonal terms  $|\alpha^2|$  and  $|\beta^2|$  are the qubit occupation probabilities for the  $|0\rangle$  and  $|1\rangle$  configuration states respectively. The off-diagonal elements represent *coherence* between basis states, appearing as non-zero when the qubit is in a superposition state and  $\gamma = \alpha^*\beta$  for maximum coherence. The *eigenvectors* and *eigenvalues* of a density matrix are found via the *characteristic equation*  $c(\lambda) = 0$ , where  $c(\lambda) \equiv \det|\hat{\rho} - \lambda\mathbb{I}|$  is the *characteristic function*.

To represent an applied quantum mechanical system, a density operator is derived which satisfies the following mathematical constraints:

$$\hat{\rho}^\dagger = \hat{\rho}, \quad \text{The matrix is Hermitian.} \quad (2.9)$$

$$\lambda_j \geq 0, \quad \text{The matrix has non-negative eigenvalues.} \quad (2.10)$$

$$\text{Tr}(\hat{\rho}) = 1, \quad \text{Diagonal matrix elements sum to 1 ('Trace 1').} \quad (2.11)$$

By satisfying the conditions of Eqs. 2.9, 2.10, and 2.11, a density operator can be derived to reproduce probability distributions for measurement outcomes given particular measurements performed in tests that probe quantum systems. The density operator most closely resembling a quantum state may be reconstructed by preparing identical qubit copies and performing several instances of different measurements. This process is called *quantum state tomography*, whereby measurement statistics are collected and a density operator corresponding to a quantum state consistent with the set of observed

statistics is deduced [72, 73]. Quantum state tomography is often a necessary precursor to experiment, acting as a tool for the characterisation of quantum states in the laboratory. Quantum state tomography is discussed further in Sec. 2.5.7.

### 2.2.2 Entangled Qubits

Quantum mechanics permits *entangled* qubit states. An entangled state exhibits correlation and superposition simultaneously. Some well known maximally entangled states are the *Bell states*, describing a pair of distinct qubit subsystems labelled  $A$  and  $B$  that cannot be characterised independently of one another [70]:

$$|\Psi^+\rangle = \frac{1}{\sqrt{2}}|0\rangle_A \otimes |1\rangle_B + \frac{1}{\sqrt{2}}|1\rangle_A \otimes |0\rangle_B, \quad (2.12)$$

$$|\Psi^-\rangle = \frac{1}{\sqrt{2}}|0\rangle_A \otimes |1\rangle_B - \frac{1}{\sqrt{2}}|1\rangle_A \otimes |0\rangle_B, \quad (2.13)$$

$$|\Phi^+\rangle = \frac{1}{\sqrt{2}}|0\rangle_A \otimes |0\rangle_B + \frac{1}{\sqrt{2}}|1\rangle_A \otimes |1\rangle_B, \quad (2.14)$$

$$|\Phi^-\rangle = \frac{1}{\sqrt{2}}|0\rangle_A \otimes |0\rangle_B - \frac{1}{\sqrt{2}}|1\rangle_A \otimes |1\rangle_B. \quad (2.15)$$

$$(2.16)$$

Here, the symbol "⊗" denotes the tensor product (this symbol is often omitted for brevity, as is the case for the remainder of this thesis). The Bell states belong to a class of maximally entangled states, and form a complete set of basis states (called the Bell state basis)  $\{|\Psi^\pm\rangle, |\Phi^\pm\rangle\}$ . The state  $|\Psi^-\rangle$ , called the singlet state, spans the *antisymmetric* subspace of the Bell basis (because  $|\Psi^-\rangle$  is an antisymmetric wavefunction, i.e. is antisymmetric under particle exchange), with the remaining states  $|\Psi^+\rangle$ ,  $|\Phi^-\rangle$ , and  $|\Phi^+\rangle$ , called the triplet states, spanning the *symmetric* subspace.

The Bell states are a special case of maximally entangled pure states. There also exist states that are pure and partially entangled, and states that are partially mixed and entangled. A well known class of partially mixed entangled states are so-called *Werner* states [74]. Werner states model entangled states in the presence of noise or mixture, expressed as

$$W_\mu = \mu|\Psi^-\rangle\langle\Psi^-| + \frac{1-\mu}{4}\mathbb{I} \otimes \mathbb{I}, \quad (2.17)$$

where the parameter  $\mu$  characterises the degree of noise or mixture in the entangled state. The Werner state is a weighted sum of the maximally entangled  $|\Psi^-\rangle$  Bell state with random “white” noise<sup>3</sup>, finding maximal entanglement for  $\mu = 1$  and complete mixture for  $\mu = 0$ . Alternatively, the Werner state can be expressed as a weighted sum of the singlet and triplet Bell states,

$$W_\mu = \frac{1-3\mu}{4} |\Psi^-\rangle\langle\Psi^-| + \frac{1-\mu}{4} (|\Psi^+\rangle\langle\Psi^+| + |\Phi^-\rangle\langle\Phi^-| + |\Phi^+\rangle\langle\Phi^+|). \quad (2.18)$$

The Werner state is a well studied and useful model of entangled states. The Werner state finds application in various optical quantum information protocols, and forms a key component of the experimental research presented in chapter 4.

## 2.3 Quantum Optics

Having discussed some basics of quantum mechanics, the focus now turns to optics and quantum optics, which comprise the experimental testbed for all research presented in this thesis. In this section, a quantum optical framework is introduced by supplementing Maxwell’s classical theory of vector electromagnetism with the formalism of quantum electrodynamics. The existence of what are known to be photons is revealed, and formalism for describing quantum states of light is introduced to facilitate the later discussion of how quantum states of light are experimentally generated in the laboratory.

Light is a propagating electromagnetic wave [75]. The synchronous relationship between the electric and magnetic fields is responsible for the propagating form of electromagnetic radiation, and the free electromagnetic field<sup>4</sup> is mathematically expressed using the source-free Maxwell’s equations

---

<sup>3</sup>Meaning the degree of noise is equal in all bases.

<sup>4</sup>Fields are physical quantities that take on definite values at different points in space [75].

$$\nabla \cdot \vec{\mathbf{B}} = 0, \quad (2.19)$$

$$\nabla \times \vec{\mathbf{E}} = -\frac{\partial \vec{\mathbf{B}}}{\partial t}, \quad (2.20)$$

$$\nabla \cdot \vec{\mathbf{E}} = 0, \quad (2.21)$$

$$\nabla \times \vec{\mathbf{B}} = \epsilon_0 \mu_0 \frac{\partial \vec{\mathbf{E}}}{\partial t}, \quad (2.22)$$

where  $\mu_0$  and  $\epsilon_0$  are the magnetic and electric permittivities of free space ( $\mu_0 \epsilon_0 = c^{-2}$ , with  $c$  being the speed of light in vacuum). The fields  $\vec{\mathbf{E}}(\vec{\mathbf{r}}, t)$  and  $\vec{\mathbf{B}}(\vec{\mathbf{r}}, t)$  can be related to the *vector potential*  $\vec{\mathbf{A}}(\vec{\mathbf{r}}, t)$ , justified in its existence because of the mathematical properties of the curl and divergence of vector fields [75]. Using  $\vec{\mathbf{A}}(\vec{\mathbf{r}}, t)$ , the electric and magnetic fields can be written as

$$\vec{\mathbf{B}}(\vec{\mathbf{r}}, t) = \nabla \times \vec{\mathbf{A}}(\vec{\mathbf{r}}, t) \quad \text{and} \quad \vec{\mathbf{E}}(\vec{\mathbf{r}}, t) = -\frac{\partial \vec{\mathbf{A}}(\vec{\mathbf{r}}, t)}{\partial t}, \quad (2.23)$$

with the Coulomb gauge condition  $\nabla \cdot \vec{\mathbf{A}}(\vec{\mathbf{r}}, t) = 0$ , meaning  $\vec{\mathbf{A}}(\vec{\mathbf{r}}, t)$  is a *transverse* field. The vector potential  $\vec{\mathbf{A}}(\vec{\mathbf{r}}, t)$  satisfies the wave equation

$$\nabla^2 \vec{\mathbf{A}}(\vec{\mathbf{r}}, t) = \frac{1}{c^2} \frac{\partial^2 \vec{\mathbf{A}}(\vec{\mathbf{r}}, t)}{\partial t^2}, \quad (2.24)$$

evidenced by substituting the equations for  $\vec{\mathbf{B}}(\vec{\mathbf{r}}, t)$  and  $\vec{\mathbf{E}}(\vec{\mathbf{r}}, t)$  in Eq. 2.23 into Eq. 2.22. The vector potential therefore has propagating solutions, which are arbitrarily assumed to be confined inside a cube of sides  $L$  with periodic boundary conditions. The standing waves formed inside the cube have wave vectors

$$\mathbf{k} = \frac{2\pi}{L}(n_x, n_y, n_z), \quad (2.25)$$

where  $n_x$ ,  $n_y$ , and  $n_z$  are integers  $0, \pm 1, \pm 2, \dots$ . The vector potential  $\vec{\mathbf{A}}(\vec{\mathbf{r}}, t)$  can be expressed generally as [76]

$$\vec{\mathbf{A}}(\vec{\mathbf{r}}, t) = \vec{\mathbf{A}}^{(+)}(\vec{\mathbf{r}}, t) + \vec{\mathbf{A}}^{(-)}(\vec{\mathbf{r}}, t), \quad (2.26)$$

where  $\vec{\mathbf{A}}^{(+)}(\vec{\mathbf{r}}, t)$  and  $\vec{\mathbf{A}}^{(-)}(\vec{\mathbf{r}}, t)$  each contain amplitudes that vary as  $e^{-i\omega_{\mathbf{k}}t}$  and  $e^{i\omega_{\mathbf{k}}t}$  respectively (for  $\omega_{\mathbf{k}} = c|\mathbf{k}|$ ) and  $\vec{\mathbf{A}}^{(-)} = (\vec{\mathbf{A}}^{(+)})^*$ . The individual terms of the vector potential can be discretely decomposed in a three dimensional Fourier expansion as [77]

$$\vec{\mathbf{A}}^{(+)}(\vec{\mathbf{r}}, t) = L^{-\frac{3}{2}} \sum_{\mathbf{k}, \lambda} \boldsymbol{\varepsilon}_{\mathbf{k}}^{\lambda} a_{\mathbf{k}}^{\lambda}(t) e^{i\mathbf{k} \cdot \mathbf{r}} \quad \text{and} \quad (2.27)$$

$$\vec{\mathbf{A}}^{(-)}(\vec{\mathbf{r}}, t) = L^{-\frac{3}{2}} \sum_{\mathbf{k}, \lambda} (\boldsymbol{\varepsilon}_{\mathbf{k}}^{\lambda})^* a_{\mathbf{k}}^{\lambda}(t)^* e^{-i\mathbf{k} \cdot \mathbf{r}}, \quad (2.28)$$

where the Fourier coefficients are given by  $a_{\mathbf{k}}^{\lambda}(t) = a_{\mathbf{k}}^{\lambda} \cdot e^{-i\omega_{\mathbf{k}} t}$  and  $(a_{\mathbf{k}}^{\lambda}(t))^* = (a_{\mathbf{k}}^{\lambda})^* \cdot e^{i\omega_{\mathbf{k}} t}$ , and the polarisation unit vectors  $\boldsymbol{\varepsilon}_{\mathbf{k}}^{\lambda}$  for  $\lambda = 1, 2$  are defined such that  $\boldsymbol{\varepsilon}_{\mathbf{k}}^{\lambda} \cdot \vec{\mathbf{k}} = 0$  and  $\boldsymbol{\varepsilon}_{\mathbf{k}}^{\lambda} \cdot \boldsymbol{\varepsilon}_{\mathbf{k}}^{\lambda'} = \delta^{\lambda, \lambda'}$ , signifying transversality and orthonormality. The unit vectors  $\boldsymbol{\varepsilon}_{\mathbf{k}}^1$  and  $\boldsymbol{\varepsilon}_{\mathbf{k}}^2$  therefore define a pair of orthogonal linear polarisations. The vector potential  $\vec{\mathbf{A}}(\vec{\mathbf{r}}, t)$  has propagating solutions of the form

$$\vec{\mathbf{A}}(\vec{\mathbf{r}}, t) = B^{\frac{1}{2}} \sum_{\mathbf{k}, \lambda} [\boldsymbol{\varepsilon}_{\mathbf{k}}^{\lambda} a_{\mathbf{k}}^{\lambda}(t) e^{i\mathbf{k} \cdot \mathbf{r}} + (\boldsymbol{\varepsilon}_{\mathbf{k}}^{\lambda})^* (a_{\mathbf{k}}^{\lambda}(t))^* e^{-i\mathbf{k} \cdot \mathbf{r}}], \quad (2.29)$$

where the constant  $B = 1/(\epsilon_0 L^3)$ . The corresponding electric field vector  $\vec{\mathbf{E}}(\vec{\mathbf{r}}, t)$  and magnetic field vector  $\vec{\mathbf{B}}(\vec{\mathbf{r}}, t)$  may then be found from the vector potential using Eqs. 2.23, revealing

$$\vec{\mathbf{E}}(\vec{\mathbf{r}}, t) = i\omega_{\mathbf{k}} B^{\frac{1}{2}} \sum_{\mathbf{k}, \lambda} [\boldsymbol{\varepsilon}_{\mathbf{k}}^{\lambda} a_{\mathbf{k}}^{\lambda}(t) e^{i\mathbf{k} \cdot \mathbf{r}} + (\boldsymbol{\varepsilon}_{\mathbf{k}}^{\lambda})^* (a_{\mathbf{k}}^{\lambda}(t))^* e^{-i\mathbf{k} \cdot \mathbf{r}}], \quad (2.30)$$

$$\vec{\mathbf{B}}(\vec{\mathbf{r}}, t) = iB^{\frac{1}{2}} \sum_{\mathbf{k}, \lambda} [(\mathbf{k} \times \boldsymbol{\varepsilon}_{\mathbf{k}}^{\lambda}) a_{\mathbf{k}}^{\lambda}(t) e^{i\mathbf{k} \cdot \mathbf{r}} + (\mathbf{k} \times \boldsymbol{\varepsilon}_{\mathbf{k}}^{\lambda})^* (a_{\mathbf{k}}^{\lambda}(t))^* e^{-i\mathbf{k} \cdot \mathbf{r}}]. \quad (2.31)$$

The total energy of the electromagnetic field is represented by the classical Hamiltonian

$$H = \frac{1}{2} \int_{L^3} (\epsilon_0 \vec{\mathbf{E}}^2 + \mu_0^{-1} \vec{\mathbf{B}}^2) d^3 r. \quad (2.32)$$

Performing the integration yields the expression for the total energy of the electromagnetic field over modes  $\mathbf{k}$  and  $\lambda$  as [77]

$$H = 2 \sum_{\mathbf{k}, \lambda} \omega_{\mathbf{k}}^2 |a_{\mathbf{k}}^{\lambda}(t)|^2 = 2 \sum_{\mathbf{k}, \lambda} \omega_{\mathbf{k}}^2 a_{\mathbf{k}}^{\lambda}(t) (a_{\mathbf{k}}^{\lambda}(t))^*. \quad (2.33)$$

### 2.3.1 Quantisation of the Electromagnetic Field

The electromagnetic field can now be quantised. To do so, it is convenient to express the total energy  $H$  in Hamiltonian form by introducing the pair of real canonical variables

$$q_{\mathbf{k}}^{\lambda}(t) = [a_{\mathbf{k}}^{\lambda}(t) + (a_{\mathbf{k}}^{\lambda}(t))^*] \quad \text{and} \quad p_{\mathbf{k}}^{\lambda}(t) = -i\omega_{\mathbf{k}}[a_{\mathbf{k}}^{\lambda}(t) - (a_{\mathbf{k}}^{\lambda}(t))^*], \quad (2.34)$$

representing the amplitudes of the vector potential and electric fields respectively (Eqs. 2.29 and 2.30). By rearranging the canonical variables  $q_{\mathbf{k}}^{\lambda}(t)$  and  $p_{\mathbf{k}}^{\lambda}(t)$  in terms of  $a_{\mathbf{k}}^{\lambda}(t)$  and  $(a_{\mathbf{k}}^{\lambda}(t))^*$ , the total energy of the field may then be expressed as

$$H = \frac{1}{2} \sum_{\mathbf{k}, \lambda} [(p_{\mathbf{k}}^{\lambda}(t))^2 + \omega_{\mathbf{k}}^2(q_{\mathbf{k}}^{\lambda}(t))^2]. \quad (2.35)$$

Quantisation of the electromagnetic field is achieved by choosing the canonical variables  $p_{\mathbf{k}}^{\lambda}(t)$  and  $q_{\mathbf{k}}^{\lambda}(t)$  to be mutually adjoint quantum mechanical operators. The canonical conjugate variables  $p_{\mathbf{k}}^{\lambda}(t)$  and  $q_{\mathbf{k}}^{\lambda}(t)$ , traditionally related by Poisson brackets, are therefore replaced by quantum mechanical operators  $\hat{p}_{\mathbf{k}}^{\lambda}(t)$  and  $\hat{q}_{\mathbf{k}}^{\lambda}(t)$  that are related by commutators. It is useful to define *non-Hermitian* operators, called the *annihilation* and *creation* operators

$$\hat{a}_{\mathbf{k}}^{\lambda}(t) = \frac{1}{\sqrt{2\hbar\omega_{\mathbf{k}}}}[\hat{q}_{\mathbf{k}}^{\lambda}(t) + i\hat{p}_{\mathbf{k}}^{\lambda}(t)] \quad \text{and} \quad (\hat{a}_{\mathbf{k}}^{\lambda}(t))^{\dagger} = \frac{1}{\sqrt{2\hbar\omega_{\mathbf{k}}}}[\hat{q}_{\mathbf{k}}^{\lambda}(t) - i\hat{p}_{\mathbf{k}}^{\lambda}(t)] \quad (2.36)$$

respectively. These operator equations are invertible, such that the operators  $\hat{p}_{\mathbf{k}}^{\lambda}(t)$  and  $\hat{q}_{\mathbf{k}}^{\lambda}(t)$  can be expressed in terms of  $\hat{a}_{\mathbf{k}}^{\lambda}(t)$  and  $(\hat{a}_{\mathbf{k}}^{\lambda}(t))^{\dagger}$ . The creation and annihilation operators obey the bosonic commutation relations

$$[\hat{a}_{\mathbf{k}}^{\lambda}(t), \hat{a}_{\mathbf{k}'}^{\lambda'}(t)] = [(\hat{a}_{\mathbf{k}}^{\lambda}(t))^{\dagger}, (\hat{a}_{\mathbf{k}'}^{\lambda'}(t))^{\dagger}] = 0, \quad [\hat{a}_{\mathbf{k}}^{\lambda}(t), (\hat{a}_{\mathbf{k}'}^{\lambda'}(t))^{\dagger}] = \delta_{\mathbf{k}\mathbf{k}'}\delta_{\lambda\lambda'}, \quad (2.37)$$

and relate to the complex vector potential amplitudes  $a_{\mathbf{k}}^{\lambda}(t) = a_{\mathbf{k}}^{\lambda}e^{-i\omega_{\mathbf{k}}t}$  and  $(a_{\mathbf{k}}^{\lambda}(t))^* = (a_{\mathbf{k}}^{\lambda})^*e^{i\omega_{\mathbf{k}}t}$ , sharing a similarly related time dependence:

$$\hat{a}_{\mathbf{k}}^{\lambda}(t) = \hat{a}_{\mathbf{k}}^{\lambda}(0)e^{-i\omega_{\mathbf{k}}t} \quad \text{and} \quad (\hat{a}_{\mathbf{k}}^{\lambda}(t))^{\dagger} = (\hat{a}_{\mathbf{k}}^{\lambda}(0))^{\dagger}e^{i\omega_{\mathbf{k}}t}. \quad (2.38)$$

Clearly the operator products  $\hat{a}_{\mathbf{k}}^{\lambda}(t) \cdot (\hat{a}_{\mathbf{k}}^{\lambda}(t))^{\dagger}$  and  $(\hat{a}_{\mathbf{k}}^{\lambda}(t))^{\dagger} \cdot \hat{a}_{\mathbf{k}}^{\lambda}(t)$  are time independent, and so we safely suppress the time dependence with the understanding that all operators are evaluated at the same time. Substituting the quantum mechanical operator forms of Eq. 2.34 into Eq. 2.35 and making use of the commutation relation 2.37 we find the quantum mechanical Hamiltonian for the electromagnetic field is

$$\hat{H} = \hbar \sum_{\mathbf{k}} \omega_{\mathbf{k}} [(\hat{a}_{\mathbf{k}}^{\lambda})^{\dagger} \hat{a}_{\mathbf{k}}^{\lambda} + \frac{1}{2}]. \quad (2.39)$$

The Hamiltonian operator for the electromagnetic field represents the total energy of a countably infinite number of independent modes  $\mathbf{k}, \lambda$ . The individual modes are associated to a quantity of energy  $\hbar\omega_{\mathbf{k}}$  related to the product of the annihilation and creation operators, plus a *zero-point energy*  $\frac{1}{2}\hbar\omega_{\mathbf{k}}$ . The Hamiltonian of Eq. 2.35 is also recognised as the total energy of a system of independent harmonic oscillators (one for each  $\mathbf{k}, \lambda$ ), and so the zero-point energy contribution represents the fact that a quantum mechanical oscillator cannot come to rest, even in the lowest energy state, such that each mode has a zero-point energy associated with vacuum fluctuations.

Quantum states of light can now be studied in greater detail. For ease of notation, a single linearly polarised mode  $k$  of the Hamiltonian is considered, such that we can drop the indices  $\mathbf{k}$  and  $\lambda$ .

### 2.3.2 Number States

The operator  $\hat{a}^{\dagger}\hat{a}$  is called the *number operator*, also expressed as  $\hat{n}$ . The eigenvalues of  $\hat{n}$  correspond to the number of elementary excitations  $n$ , or quanta, in a single mode:  $n = 0, 1, 2, \dots, \infty$ . The eigenstates of the number operator are the *number states*  $|n\rangle$  (also known as *Fock states*) and adhere to the eigenvalue equation

$$\hat{a}^{\dagger}\hat{a}|n\rangle = n|n\rangle. \quad (2.40)$$

Here, the elementary excitations of the electromagnetic field are called photons, and the number of photons in a single mode, each with energy  $\hbar\omega$ , is given by  $n$ . The Hamiltonian for a single mode therefore has eigenvalues  $\hbar\omega(n + \frac{1}{2})$ , representing the total energy in that mode.

The action of the annihilation and creation operators on a number state  $|n\rangle$  are

$$\hat{a}|n\rangle = \sqrt{n}|n-1\rangle \quad \text{and} \quad \hat{a}^{\dagger} = \sqrt{n+1}|n+1\rangle, \quad (2.41)$$

such that the individual application of the creation and annihilation operators adds or subtracts a single photon, respectively, from the energy eigenstate  $|n\rangle$ . The creation operator can be used to generate all possible number

states by starting with the *vacuum state*  $|0\rangle$  and successively applying the creation operator:

$$|n\rangle = \frac{(\hat{a}^\dagger)^n}{\sqrt{n!}} |0\rangle. \quad (2.42)$$

The electromagnetic field need not exist in an energy eigenstate of the Hamiltonian, and indeed it is difficult to prepare a single mode of the electromagnetic field in a number state with  $n > 0$ . Most optical fields exist as either a superposition of number states (a pure state), or as a statistical mixture of number states (a mixed state).

### 2.3.3 Coherent states

The superposition of number states, called a *coherent state*, is an important means of expressing quantum states of light throughout the wider quantum optics community. This thesis is not concerned with coherent states, however it is useful to briefly consider the properties of coherent states as a motivation for the particular methods used in generating single-photon states employed for the research presented in this thesis. A coherent state is expressed as

$$|\alpha\rangle = e^{-\frac{|\alpha|^2}{2}} \sum_n^{\infty} \frac{\alpha^n}{\sqrt{n!}} |n\rangle, \quad (2.43)$$

and represents the closest quantum mechanical approximation of classical coherent light (such as that emitted by a laser). The probability of observing  $n$  photons in a coherent state  $|\alpha\rangle$  follows the Poissonian distribution given by

$$P(n) = |\langle n|\alpha\rangle|^2 = \frac{(|\alpha|^2)^n e^{-|\alpha|^2}}{n!}, \quad (2.44)$$

where  $\langle\alpha|\hat{n}|\alpha\rangle = |\alpha|^2$  is the mean photon number, equivalent to the classical prediction [78].

One might imagine that to create single photons, the backbone of discrete-variable optical quantum information science, one could significantly attenuate a laser beam (quantum-mechanically described by a coherent state) such that only a single photon exists in the relevant optical mode at a given time. However, because the coherent state is a superposition of number states, we find that the attenuated coherent state may indeed have a well defined *mean* photon number  $|\alpha|^2 = 1$ , but the Poissonian distribution of number states ensures the probability of finding the attenuated optical mode with a single

excitation is 36.7%, with the remaining probabilities attributed to the vacuum state (36.7%), the two-photon number state (18.4%), the three photon number state (6.1%), and the four photon number state (1.5%) plus negligible higher terms. Thus, 63.3% of the time, the coherent state with an average photon number  $|\alpha|^2 = 1$  is not in a single photon state.

Therefore, another mechanism must be implemented if we are to generate single photon number states. Fortunately, approximations to quantum states of light for small photon number  $n$  are accessible, by making use of intense laser fields and *nonlinear* optical phenomena.

## 2.4 Nonlinear Optics

Nonlinear optics is a branch of electromagnetic optics concerned with the behaviour of dielectric materials placed within optical fields. A dielectric material is an insulator (meaning internal charges do not flow freely) that responds to an applied electric field. What follows is a discussion of how a nonlinear dielectric material can be used for optical frequency conversion and for the generation of quantum states of light.

An electric field applied to dielectric material induces a response in the material's *polarisation density*  $\vec{P}(\vec{r}, t)$ , a vector field representing the material's average dipole response, comprised of an aggregate of the material's individual electric dipole moments. A dielectric medium is characterised by the interplay between  $\vec{P}(\vec{r}, t)$  and  $\vec{E}(\vec{r}, t)$ , and as such there are a number of definitions related to the properties of the relationship (called the *constitutive relation*). For example, a *linear* dielectric material will experience a linear response in  $\vec{P}(\vec{r}, t)$  as a result of an applied field  $\vec{E}(\vec{r}, t)$ . A *nondispersive* dielectric will experience instantaneous changes in  $\vec{P}(\vec{r}, t)$  as a result of the applied field  $\vec{E}(\vec{r}, t)$  (in practice, all materials experience a finite response time, so nondispersiveness is at best an approximation). A *homogenous* medium demonstrates a position-independent relationship between  $\vec{P}(\vec{r}, t)$  and  $\vec{E}(\vec{r}, t)$ . Finally, a medium is *isotropic* if the relationship between  $\vec{P}(\vec{r}, t)$  and  $\vec{E}(\vec{r}, t)$  is independent of the direction of  $\vec{E}(\vec{r}, t)$ , so that  $\vec{P}(\vec{r}, t)$  is the same for all  $\vec{E}(\vec{r}, t)$ .

Light propagating through a linear, homogenous, nondispersive, isotropic dielectric material will obey Maxwell's equations

$$\nabla \cdot \vec{\mathbf{B}} = 0, \quad (2.45)$$

$$\nabla \times \vec{\mathbf{E}} = -\frac{\partial \vec{\mathbf{B}}}{\partial t}, \quad (2.46)$$

$$\nabla \cdot \vec{\mathbf{D}} = 0, \quad (2.47)$$

$$\nabla \times \vec{\mathbf{H}} = \frac{\partial \vec{\mathbf{D}}}{\partial t}, \quad (2.48)$$

where  $\vec{\mathbf{D}} = \epsilon \vec{\mathbf{E}}$  and  $\vec{\mathbf{B}} = \mu \vec{\mathbf{H}}$  are the constitutive relations for simple dielectric and magnetic materials, and  $\mu = \mu_0 \mu_r$  and  $\epsilon = \epsilon_0 \epsilon_r$  are the electric and magnetic permittivities of the medium ( $\epsilon_r$  and  $\mu_r$  are *relative permittivities*, defined below). In dielectric materials, the *electric displacement field*  $\vec{\mathbf{D}}$  is of particular importance. The displacement field accounts for the effects of charges inside a medium, and is expressed generally as

$$\vec{\mathbf{D}} = \epsilon_0 \vec{\mathbf{E}} + \vec{\mathbf{P}}. \quad (2.49)$$

In linear materials, the polarisation density is given by  $\vec{\mathbf{P}} = \epsilon_0 \chi \vec{\mathbf{E}}$  (here  $\vec{\mathbf{P}}$  depends linearly on  $\vec{\mathbf{E}}$ ), where  $\chi$  is the material's *electric susceptibility*, dependent on the material properties. Substituting this expression into Eq. 2.49 reveals the material's relative permittivity is given by  $\epsilon_r = 1 + \chi$ . For light propagation through a linear medium, the velocity is given by  $c = (\epsilon \mu)^{-\frac{1}{2}}$ , such that the velocity of light in a linear medium is reduced relative to free-space propagation by a factor of  $n = c_0/c = \sqrt{\epsilon/\epsilon_0}$  (using  $\mu = \mu_0$  for nonmagnetic materials; the only materials considered here), where  $n$  is called the *refractive index* of a material. Thus the only difference between light propagating through an ideal dielectric medium and light propagating through free space is that the propagation velocity is reduced by a factor of  $n$ .

This model is clearly idealistic, since materials are almost never characterised as perfectly and simultaneously linear, nondispersive, homogeneous, and isotropic. Taking a step towards useful realistic materials, we focus on nonlinear anisotropic materials. In a nonlinear material the relationship between  $\vec{\mathbf{P}}$  and  $\vec{\mathbf{E}}$  is modelled as a Taylor series expansion around  $\vec{\mathbf{E}} = 0$ :

$$\vec{\mathbf{P}} = \epsilon_0 (\chi \vec{\mathbf{E}} + \chi^{(2)} \vec{\mathbf{E}}^2 + \chi^{(3)} \vec{\mathbf{E}}^3 + \dots), \quad (2.50)$$

where the coefficients  $\chi^{(n)}$  are the  $n^{th}$  order electric susceptibilities, representing  $n^{th}$  order nonlinearities. For the purposes of frequency conversion and generating quantum states of light, the focus is on second-order nonlinearities, related to the  $\chi^{(2)}$  coefficient. This type of nonlinearity exists

in anisotropic media. In such materials, an inversion of the material in the presence of a field  $\vec{\mathbf{E}}(\vec{\mathbf{r}}, t)$  does not necessarily result in a reversal of  $\vec{\mathbf{P}}(\vec{\mathbf{r}}, t)$ , so the function describing  $\vec{\mathbf{P}}(\vec{\mathbf{r}}, t)$  may be an even function ( $\vec{\mathbf{P}}(-\vec{\mathbf{r}}, t) = \vec{\mathbf{P}}(\vec{\mathbf{r}}, t)$ ). In this case, the second order nonlinear coefficient  $\chi^{(2)}$  is nonzero, and is of magnitude  $\chi^{(2)} \propto 10^{-21} - 10^{-24}$  [79].

To see how a material with nonzero  $\chi^{(2)}$  coefficient affects the propagation of light, we first perform the curl operation  $\nabla \times$  on Eq. 2.46:

$$\nabla \times (\nabla \times \vec{\mathbf{E}}) = -\nabla \times \left( \frac{\partial \vec{\mathbf{B}}}{\partial t} \right). \quad (2.51)$$

Using  $\vec{\mathbf{B}} = \mu \vec{\mathbf{H}}$  and Eq. 2.48, as well as the identity  $\nabla \times (\nabla \times \vec{\mathbf{E}}) = \nabla(\nabla \cdot \vec{\mathbf{E}}) - \nabla^2 \vec{\mathbf{E}}$  (noting that  $\nabla \cdot \vec{\mathbf{E}} = 0$ ), the equation becomes

$$\nabla^2 \vec{\mathbf{E}} = \mu \frac{\partial^2 \vec{\mathbf{D}}}{\partial t^2}. \quad (2.52)$$

We consider the form of the electric displacement vector  $\vec{\mathbf{D}} = \epsilon_0 \vec{\mathbf{E}} + \vec{\mathbf{P}}$  with a nonlinear expansion of the polarisation density (Eq. 2.50):

$$\vec{\mathbf{D}} = \epsilon_0 \vec{\mathbf{E}} + \epsilon_0 (\chi \vec{\mathbf{E}} + \chi^{(2)} \vec{\mathbf{E}}^2 + \chi^{(3)} \vec{\mathbf{E}}^3 + \dots) \quad (2.53)$$

which can be rewritten as

$$\vec{\mathbf{D}} = \epsilon \vec{\mathbf{E}} + \epsilon_0 \sum_{n=2}^{\infty} \chi^{(n)} \vec{\mathbf{E}}^n, \quad (2.54)$$

where the first order term is encapsulated in the expression  $\epsilon = \epsilon_0 \epsilon_r = \epsilon_0 (1 + \chi)$ . If the sum of higher order coefficients is expressed thusly:

$$\vec{\mathbf{P}}^{(\text{NL})} = \epsilon_0 \sum_{n=2}^{\infty} \chi^{(n)} \vec{\mathbf{E}}^n, \quad (2.55)$$

then equation 2.52 becomes

$$\nabla^2 \vec{\mathbf{E}} - \frac{1}{c^2} \frac{\partial^2 \vec{\mathbf{E}}}{\partial t^2} = \mu \frac{\partial^2 \vec{\mathbf{P}}^{(\text{NL})}}{\partial t^2}. \quad (2.56)$$

This equation has the form of a driven harmonic oscillator, with the right hand side of the equation acting as a source term. The source term models the mixing of energy between optical fields, or the conversion of light from one frequency into another [79]. An important wave mixing effect relevant to the generation of quantum states of light in this thesis is the *three-wave mixing* effect, mediated by the  $\chi^{(2)}$  nonlinear coefficient.

### 2.4.1 Three-Wave Mixing Effects

Three-wave mixing effects can be used for frequency mixing and for generating quantum states of light. The effects of frequency mixing are easily observed if we consider an optical field comprised of two harmonic components at frequencies  $\omega_1$  and  $\omega_2$  incident upon a nonlinear material. The incident wave can be expressed as

$$\vec{E}(t) = \text{Re}\{\vec{E}(\omega_1)e^{i\omega_1 t} + \vec{E}(\omega_2)e^{i\omega_2 t}\} \quad (2.57)$$

$$= \vec{E}(\omega_1)e^{i\omega_1 t} + \vec{E}^*(\omega_1)e^{-i\omega_1 t} + \vec{E}(\omega_2)e^{i\omega_2 t} + \vec{E}^*(\omega_2)e^{-i\omega_2 t}, \quad (2.58)$$

where  $\vec{E}(\omega_1) = A_1 e^{-i\vec{k}_1 \vec{r}}$  and  $\vec{E}(\omega_2) = A_2 e^{-i\vec{k}_2 \vec{r}}$ . Substituting the expression for the incident field  $\vec{E}(t)$  into the expansion for the second order nonlinearity, in this case  $\vec{P}^{(NL)} = \epsilon_0 \chi^{(2)} \vec{E}(t)^2$ , we find the polarisation density described by  $\vec{P}^{(NL)}$  has five frequency components (0,  $2\omega_1$ ,  $2\omega_2$ ,  $(\omega_1 + \omega_2)$ , and  $(\omega_1 - \omega_2)$ ), each oscillating with amplitudes

$$\vec{P}^{(NL)}(0) = \epsilon_0 \chi^{(2)} [|\vec{E}(\omega_1)|^2 + |\vec{E}(\omega_2)|^2], \quad (2.59)$$

$$\vec{P}^{(NL)}(2\omega_1) = \epsilon_0 \chi^{(2)} \vec{E}(\omega_1) \vec{E}(\omega_1), \quad (2.60)$$

$$\vec{P}^{(NL)}(2\omega_2) = \epsilon_0 \chi^{(2)} \vec{E}(\omega_2) \vec{E}(\omega_2), \quad (2.61)$$

$$\vec{P}^{(NL)}(\omega_1 + \omega_2) = \epsilon_0 2 \chi^{(2)} \vec{E}(\omega_1) \vec{E}(\omega_2), \quad (2.62)$$

$$\text{and } \vec{P}^{(NL)}(\omega_1 - \omega_2) = \epsilon_0 2 \chi^{(2)} \vec{E}(\omega_1) \vec{E}^*(\omega_2). \quad (2.63)$$

The presence of an optical field in a nonlinear medium therefore results in frequency mixing at sum, difference, or second harmonic frequencies, with the term  $\vec{P}^{(NL)}(0)$  corresponding to a static field, representing a steady state dipole moment in the polarisation density, such that parallel capacitor plates placed on opposite sides of the material will register a small potential difference (several hundred  $\mu\text{V}$  for optical peak powers of several MW [79]).

For the frequency mixed waves to continually gain energy from the incident laser fields, the waves involved in the wave mixing process must oscillate in phase with each other. To ensure this condition, *phase matching* is employed. By engineering the input frequencies, phase matching condition, and material type, a specific type of interaction (i.e. sum, difference, or second harmonic generation) can be favoured.

### 2.4.2 Phase Matching

The amplitudes of the frequency mixed waves are maximised by satisfying the phase matching condition

$$\vec{k}_1 + \vec{k}_2 = \vec{k}_3, \quad (2.64)$$

where  $\vec{k}_1$  and  $\vec{k}_2$  are the wavevectors of the incident waves at frequencies  $\omega_1$  and  $\omega_2$ , and  $\vec{k}_3$  is the wavevector of the third wave at frequency  $\omega_3$ . For the cases of sum frequency generation, difference frequency generation, and second harmonic generation (a case of particular importance for the research in this thesis), the phase matching condition equates to momentum conservation, and similarly energy conservation requires

$$\omega_1 + \omega_2 = \omega_3. \quad (2.65)$$

Because all optical media are dispersive, waves with different frequencies  $\omega_1$ ,  $\omega_2$ , and  $\omega_3$  experience frequency dependent refractive indices  $n(\omega_1)$ ,  $n(\omega_2)$ , and  $n(\omega_3)$ . The frequency dependent refractive indices are modelled by the *Sellmeier equations*, relating the refractive index  $n(\omega)$  with the optical wavelength and material properties [79, 80]. The geometry of three wave mixing is often *collinear*, meaning all fields propagate parallel to one another in the same spatial mode  $\vec{k}$ . Unless otherwise specified, all interactions are considered collinear with propagation in the  $+z$  direction. For frequency dependent refractive indexes, Eqs. 2.64 and 2.65 can be expressed as scalar relationships

$$n_1(\omega_1)\omega_1 + n_2(\omega_2)\omega_2 = n_3(\omega_3)\omega_3 \quad \text{and} \quad \omega_1 + \omega_2 = \omega_3, \quad (2.66)$$

and cannot be satisfied simultaneously in general. Fortunately, phase-matching can be implemented by using *birefringence* to counter material-induced dispersion.

Birefringence is an effect arising in optically anisotropic dielectric materials that fall into two main categories: *uniaxial* materials, and *biaxial* materials. Uniaxial materials have one axis, called the *optical axis*, governing the optical anisotropy. It is useful to define a plane relative to the optical axis, called the *principal plane*, which is defined by the optical axis and the direction of beam propagation  $\vec{k}$ . In a uniaxial material, light polarised along the principal plane experiences a refractive index  $n_e$  and is called the *extraordinary ray*, or *e-ray*. Light polarised perpendicular to the principal plane

is called the *ordinary ray*, or *o-ray*, and experiences a refractive index  $n_o$ . In a negative uniaxial crystal  $n_e < n_o$ , and in a positive uniaxial crystal  $n_e > n_o$ . Biaxial materials have two optical axes and are substantially more complex. More information on biaxial crystals can be found in Refs. [79–81].

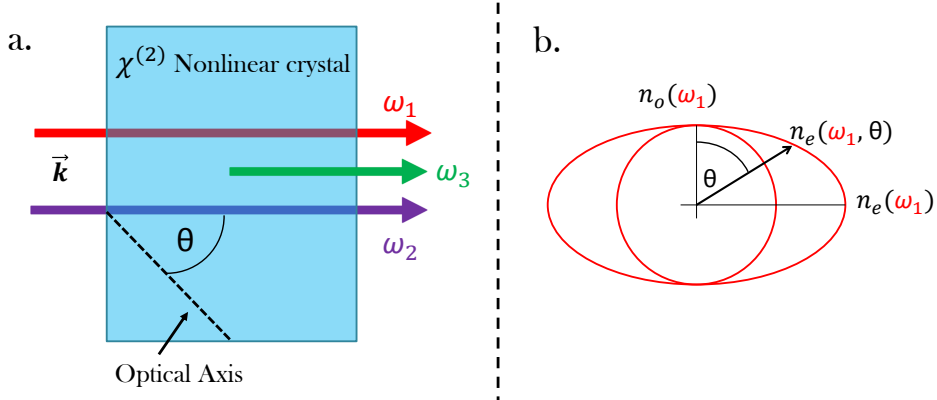


Figure 2.2: The optical axis and index ellipsoid of a uniaxial dielectric material. Incident waves  $\omega_1$ ,  $\omega_2$ , and  $\omega_3$  all experience frequency dependent refractive indices. By appropriately tuning the angle  $\theta$ , the phase velocities of some frequencies may be equalised.

The refractive index experienced by the *e-ray* in a positive uniaxial crystal takes values  $n_e(\omega) \geq n_e(\omega, \theta) \geq n_o(\omega)$ , where  $\theta$  is the angle formed between the incident light propagation axis  $\vec{k}$  and the optical axis of the material (Fig 2.2). The value of  $n_e(\omega, \theta)$  traces out an ellipse (called the *index ellipsoid*) depending on  $\theta$ , obeying the equation

$$\frac{1}{n_e^2(\theta)} = \frac{\cos^2(\theta)}{n_o^2} + \frac{\sin^2(\theta)}{n_e^2}. \quad (2.67)$$

For appropriate input frequencies and material parameters,  $\theta$  may be adjusted to satisfy the phase matching condition in Eq. 2.66, allowing the generated waves to remain in-phase with the initial driving fields (called angle-tuning). For angle-tuned phase-matching to be possible, some combination of waves must have orthogonal polarisations. In *Type-I* phase matching, the waves  $\omega_1$ ,  $\omega_2$ , and  $\omega_3$  are polarised in the order *o-o-e* or *e-e-o*. In *Type-II* phasematching, the waves  $\omega_1$ ,  $\omega_2$ , and  $\omega_3$  are polarised in the order *o-e-o* or *e-o-e*.

An effect called *spatial walk-off* also occurs in birefringent materials, occurring as a result of the direction-dependent refractive index. In cases where

spatial walk-off is present, a negative uniaxial crystal will deflect the *e*-ray away from the optic axis, whereas a positive uniaxial crystal will deflect the *e*-ray towards the optic axis [82]. This effect may be enacted to spatially separate orthogonal *e* and *o* polarisation components, or in other cases may introduce undesirable misalignment issues, therefore requiring compensation. As a result, thin nonlinear crystals are typically employed in three-wave mixing processes (with the exception of periodically poled materials, discussed below).

In this thesis, the three-wave mixing effect called *second harmonic generation* is used for frequency conversion. The three-wave mixing effect called *spontaneous parametric down conversion* is used to generate quantum states of light.

### 2.4.3 Second Harmonic Generation

Second harmonic generation (SHG), or *frequency doubling*, corresponds to the degenerate three wave mixing condition

$$\omega_1 = \omega_2 = \omega \quad \text{and} \quad \omega_3 = 2\omega. \quad (2.68)$$

Here, the *pump* field oscillates at frequency  $\omega$ , and the second harmonic field oscillates at  $2\omega$ . Typically-employed nonlinear materials that can satisfy the phase matching conditions of SHG are BBO (Beta-Barium Borate), LBO (Lithium tri-Borate), and KTP (Potassium Titanyl Phosphate). In this thesis, SHG is achieved in BBO using a femtosecond pulsed laser system (*Tsunami* model Titanium–Sapphire laser by manufacturer *Spectrapysics*) to convert pulses of light at wavelength 820nm into pulses with wavelength 410nm at a power conversion efficiency of  $\approx 30\%$ .

The intensity of the second harmonic field depends strongly on the *phase mismatch* of the phase matching process. The phase mismatch is generally described by

$$\Delta \vec{k} = \vec{k}_3 - \vec{k}_1 - \vec{k}_2. \quad (2.69)$$

SHG is typically collinear, so we consider collinear propagation along the  $z$  direction, reducing the expression for the phase mismatch to the scalar equation  $\Delta k = k_3 - k_1 - k_2$ . The intensity of the second harmonic wave labelled  $I_3$  is proportional to [79]

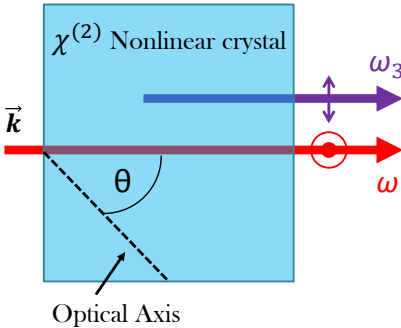


Figure 2.3: Type-I collinear second harmonic generation in a  $\chi^{(2)}$  nonlinear crystal. A pair of waves with frequencies  $\omega$  and  $\omega_3$  are angle-phase matched inside a  $\chi^{(2)}$  nonlinear crystal. In a single photon picture, two photons of frequency  $\omega$  are annihilated to create one photon at frequency  $\omega_3 = 2\omega$ .

$$I_3 \propto L^2 \text{sinc}^2 \left( \frac{\Delta k L}{2\pi} \right), \quad (2.70)$$

demonstrating the intensity of SHG is a maximum for  $\Delta k = 0$ , and reaches a minimum for  $|\Delta k| = 2\pi/L$ , where  $L$  is the crystal length. Importantly, phase matching can only be satisfied exactly for a single frequency. Because laser pulses often have large bandwidths, approximate phase matching for a broad spectrum of frequencies is important. The range of frequencies that achieve approximate phase matching is called the *phase matching bandwidth*. The phase matching bandwidth increases as crystal length decreases, so nonlinear SHG crystals are typically limited in length to 0.5mm-2mm.

The additional effect of *temporal walkoff* is an important consideration when using laser pulses for three-wave mixing effects in nonlinear crystals. Temporal walkoff occurs because a pulse with frequency  $\omega$  experiences a different *group velocity* to a pulse at  $2\omega$ , and so the propagation of two pulses with different central frequencies through a nonlinear medium will accumulate a temporal walkoff  $\tau$ . When  $\tau$  approaches the temporal pulse length, second harmonic generation will cease. This effect is not emphasised particularly in short crystals. In long crystals, group velocity matching must be enacted either through engineering the pulses (for example by introducing angular dispersion [83]) or by careful selection of materials and frequencies.

Because it is not always possible to match optical frequencies and materials such that the effects of phase mismatch are negated, an alternative means of phase matching in nonlinear crystals is *quasi-phase matching*. This pro-

cess allows access to materials with higher second order nonlinearities that cannot ordinarily satisfy phase matching requirements. In this method of phase matching, the nonlinear crystal is engineered such that the crystal periodically offsets the effects of phase mismatch. Ideally, the nonlinear coefficient  $\chi^{(2)}$  would vary harmonically in space, becoming  $\chi^{(2)}(\vec{r})$ , however, engineering a material with harmonic nonlinearities such as these is difficult. Therefore, a compromise is to engineer a nonlinear material such that the sign of the nonlinear coefficient  $\pm\chi^{(2)}$  changes with spatial period  $\Lambda = 2\pi/\Delta k$ . In this way the waves become slightly out of phase over a period  $\Lambda/2$  (corresponding to a phase shift of  $180^\circ$ ), and then return in phase over the remaining spatial period  $\Lambda/2$ . The second harmonic conversion efficiency is then partially restored. Quasi-phase matched crystals are typically fabricated commercially by applying a strong electric field to the crystal via patterned surface electrodes in a process called *periodic poling*. As a result of the applied strong electric field, the crystal orientation (and the sign of the nonlinear coefficient) are permanently reversed in the vicinity of the electrodes. Once the crystal has undergone spatial modulation of the nonlinear coefficient, the patterned surface electrodes are removed. The poling period  $\Lambda$  determines the frequencies that can be quasi-phase-matched, and adjustment of the quasi-phase matching condition can be achieved by angle-tuning or temperature-tuning the nonlinear crystal. In Chapter 3 of this thesis, a periodically poled KTP crystal (ppKTP) is used in combination with a CW laser to generate photon pairs in the nonlinear process of spontaneous parametric down conversion.

#### 2.4.4 Spontaneous Parametric Down Conversion

The generation of approximate single-photon number states is facilitated by the nonlinear optical process of spontaneous parametric down conversion (SPDC). In SPDC, a pump field at frequency  $\omega_p$  gives rise to *signal* and *idler* fields at frequencies  $\omega_s$  and  $\omega_i$ . The phase matching condition for SPDC may be collinear (quasi-phase matched) or noncollinear (angle-phase matched), satisfying

$$\omega_p = \omega_s + \omega_i \quad \text{and} \quad \Delta\vec{k} = \vec{k}_p - \vec{k}_s - \vec{k}_i. \quad (2.71)$$

The noncollinear vectorial phase matching conditions permit a spectrum of valid solutions. The pump field down converts energy into lower frequency signal and idler fields  $\omega_s = \omega_p/2 + \Omega$  and  $\omega_i = \omega_p/2 - \Omega$ . The spectrum of side-bands  $\Omega \neq 0$  are correlated in energy and momentum, as is the degenerate case  $\Omega = 0$ , which is of special significance to this thesis. The degenerate

case is specified approximately by enacting and frequency filtering, leaving only light in the degenerate SPDC mode (to within the bandwidth of the optical frequency filters employed).

The phenomenon of SPDC is a quantum effect, evidenced by treating the zero-point vacuum fluctuations of optical modes at frequencies  $\omega_s$  and  $\omega_i$  as inputs. The derivation of the quantum mechanical output field for an input field of frequency  $\omega_p$  is nontrivial, and yields [82]

$$|\psi\rangle_{SPDC} \approx |0\rangle_s|0\rangle_i + \eta|1\rangle_s|1\rangle_i + \eta^2|2\rangle_s|2\rangle_i + \dots \quad (2.72)$$

The efficiency coefficient  $\eta$  is typically small ( $\eta \sim 10^{-2}$ ), and is related to the nonlinear coefficient  $\chi^{(2)}$ , the pump power, and phase matching condition. For this reason, the higher order terms may be neglected and output state can be approximated as

$$|\psi\rangle_{SPDC} \approx |0\rangle_s|0\rangle_i + \eta|1\rangle_s|1\rangle_i. \quad (2.73)$$

Here, the vacuum term dominates so that most of the time signal and idler outputs are in the vacuum number state. The  $\eta|1\rangle_s|1\rangle_i$  term models the presence of a single-photon number state in separable signal and idler modes. The detection of a photon in the signal mode heralds the presence of a corresponding idler photon, which may be manipulated without detection (assuming zero losses). Importantly, the signal and idler photons are correlated in time, energy, spatial direction, and polarisation (depending on Type-I or Type-II phase matching). Polarisation–entanglement is employed exclusively as a resource for quantum information science throughout this thesis (Sec. 2.5). To generate polarisation–entangled photon pairs, SPDC sources are employed. Figure 2.4 illustrates some typical SPDC configurations used to generate polarisation–entangled photon pairs.

In this thesis, Type-I SPDC sources are primarily employed for generating polarisation entangled states (chapters 4, 5, and 6). In a Type-I SPDC event, a femtosecond pump beam of frequency  $\omega_p$  pumps a pair of appropriately angle-tuned nonlinear crystals placed against one another with their optic axes orthogonally oriented (called the *sandwich* configuration [84]). If the polarisation of the pump beam is aligned to fall between the optic axes of each crystal, then polarisation–entangled states are generated between photons in the signal and idler modes with frequencies  $\omega_s$  and  $\omega_i$ . In the single photon picture, a pump photon undergoes down conversion in a superposition of the first and second crystals (Fig. 2.4a), resulting in

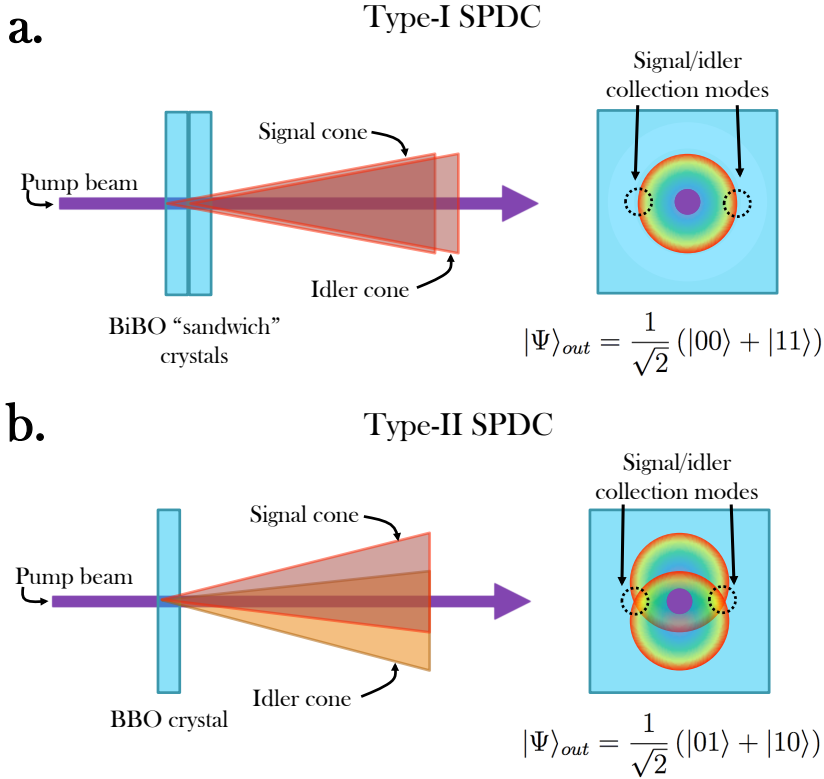


Figure 2.4: Type-I and Type-II noncollinear spontaneous parametric down conversion (SPDC) configurations. Polarisation–entangled photon pairs are generated using SPDC, with correlated or anticorrelated statistics dependent on the type of down conversion employed (Type–I down conversion is primarily employed in this thesis) **a.** A pump beam at 410nm enters pairs of sandwiched nonlinear crystals and undergoes SPDC in a superposition of the first and second crystals. The arrangement of signal and idler photons satisfy the phase matching conditions for a spectrum of correlated frequency and spatial modes. By introducing frequency filtering and spatial filtering, polarisation–entangled photon pairs (degenerate in all other degrees of freedom) may be collected. **b** A pump beam at 410nm enters a single nonlinear crystal, phase–matched for Type–II SPDC. By employing frequency filtering and spatial filtering, polarisation–entangled photon pairs (degenerate in all other degrees of freedom) are collected at the cone intersections.

the polarisation–entangled state  $|\Psi\rangle = 1/\sqrt{2}(|0\rangle_s|0\rangle_i + |1\rangle_s|1\rangle_i)$  (where  $|0\rangle$  and  $|1\rangle$  label orthogonal polarisation modes and subscripts  $s$  and  $i$  label all remaining degrees of freedom). The frequency degenerate case  $\omega_s = \omega_i$  is enacted by employing spectral filtering using bandpass filters centered

at 820nm (typically with  $\pm 3\text{nm}$  bandwidth). Spatial filtering using single-mode fibres also assists in collecting degenerate photon pairs because the spatial emission direction is correlated with frequency (although this may be more efficient for Type-II sources due to angular dispersion of the phase matching). In Fig. 2.4a, it is evident that the down conversion cones from the first and second crystals are not overlapped, introducing temporal distinguishability between photon pairs. This distinguishability degrades the quality of entanglement. To rectify this, a *pre-compensation* crystal made of quartz (12.64mm long) is placed in front of the SPDC source [84]. The quartz pre-compensation crystal is birefringent, and has its optic axis aligned such that one polarisation component of the pump beam is delayed relative to the other, hence pre-compensating for the temporal delay in SPDC modes.

Alternatively, the polarisation-entangled state  $|\Psi\rangle = 1/\sqrt{2}(|0\rangle_s|1\rangle_i + |1\rangle_s|0\rangle_i)$  may be generated in a single-crystal *crossed-cone* Type-II configuration. In this configuration, the signal and idler down conversion cones are collected at intersecting points (Fig. 2.4b). Collinear quasi-phase matched crystals may also be used to generate polarisation-entangled states, created by placing the crystal inside an optical Sagnac interferometer [85, 86] (Chapter 3). In this case, the superposition of pumping directions results in an entangled output state. Collinear down conversion sources have the advantage of high heralding efficiencies because the photons are down converted into optical modes that are tailored to maximise collection into single-mode optical fibres.

The properties of entangled states are heavily researched. Throughout this thesis, polarisation-entangled photon states are extensively studied and characterised by exploring their degree of quantum correlation, also known as *nonclassical correlation*. The last section of this chapter is devoted to the discussion of nonclassical correlations. Prior to that discussion is a section outlining the use of photons for conducting experiments in quantum optical information science.

## **2.5 Techniques for Optical Quantum Information Science**

Photons are powerful carriers of information because they are easy to manipulate, have high transmission speeds, and interact weakly with the environment. These properties make photons ideal candidates for the study

of quantum information science. In this section, the results from previous sections are combined and expanded into a framework for manipulating polarisation-encoded photons for experiments on shared quantum correlations using techniques in quantum optical information science.

### 2.5.1 Polarisation

It is convenient to talk about polarisation more practically, in terms of a reference frame that doesn't depend on crystal symmetry axes or arbitrary orthonormality conditions. In the laboratory, the *horizontal* polarisation state  $|H\rangle$  is defined as occupying a plane parallel to the surface of vibrationally-isolated tables we attach optics to. The orthogonal polarisation state is the *vertical* polarisation state  $|V\rangle$ , occupying a plane orthogonal to the table surface. Polarisation is represented on the Poincaré sphere, the optical equivalent of the Bloch sphere. The difference in naming convention between the Bloch sphere and Poincaré sphere is attributed to a difference in axis labelling; in the Bloch sphere representation, the logical  $|0\rangle$  and  $|1\rangle$  states lie on the latitudinal poles, whereas in the Poincaré sphere representation the  $|H\rangle$  and  $|V\rangle$  states are usually assumed to lie on the longitudinal meridian. Equivalence between the logical states and the polarisation states is reached by making the standard assumption  $|H\rangle \equiv |0\rangle$  and  $|V\rangle \equiv |1\rangle$ . A common set of polarisation superposition states are therefore (Figure 2.5)

$$|D\rangle = \frac{1}{\sqrt{2}}(|H\rangle + |V\rangle), \quad |A\rangle = \frac{1}{\sqrt{2}}(|H\rangle - |V\rangle), \quad (2.74)$$

$$|R\rangle = \frac{1}{\sqrt{2}}(|H\rangle + i|V\rangle), \quad \text{and} \quad |L\rangle = \frac{1}{\sqrt{2}}(|H\rangle - i|V\rangle), \quad (2.75)$$

where D, A, R, and L are the diagonal, anti-diagonal, right-hand circular, and left-hand circular polarisation states respectively. The sets of polarisation states H/V, D/A, and R/L each form pairs of orthogonal basis states, with rotations between different polarisation states performed using *wave plates* made of birefringent materials.

### 2.5.2 Wave plates

Wave plates are often manufactured from quartz, a positive uniaxial birefringent crystal. The work in this thesis employs quartz wave plates from manufacturers Thorlabs and CASIX. Wave plates are optically flat discs that have their optic axis oriented in the plane orthogonal to the direction of incident light propagation. Therefore, a normally incident beam will

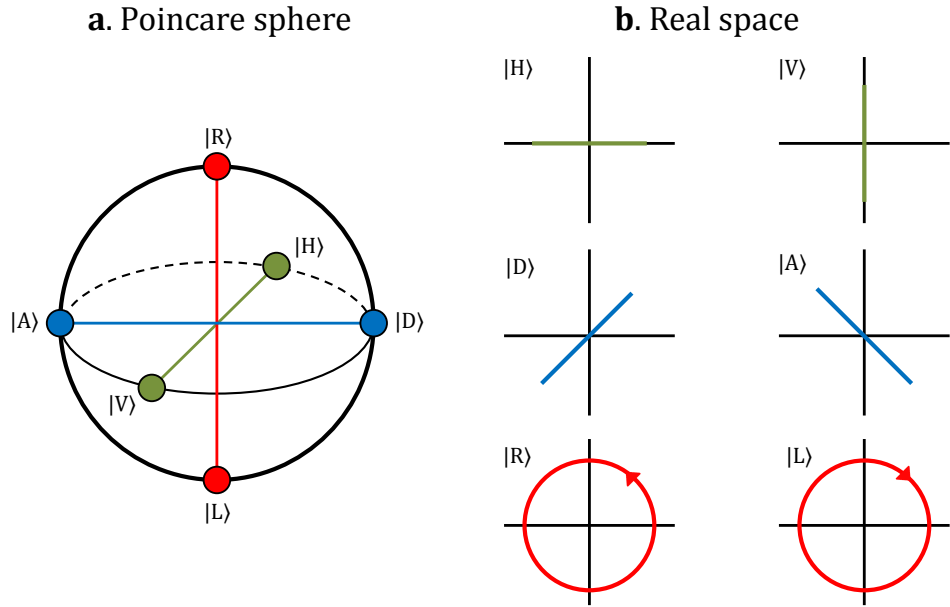


Figure 2.5: Polarisation encoded qubit states on the Poincaré sphere and in real space. **a** Single qubit polarisation states can be described on the Poincaré sphere, with well known sets of polarisation states lying on the poles and the equator. The red, green, and blue sets form pairs of orthogonal basis states. **b.** The polarisation states in real space, looking into an oncoming polarisation-encoded qubit.

experience the maximum distinction between refractive indices  $n_e$  and  $n_o$ , and experience no spatial walk-off [82]. Generally, a monochromatic plane wave traversing a wave plate of thickness  $d$  will accumulate a relative phase difference  $\Delta\phi$  between the  $e$ -ray and  $o$ -ray of [81]

$$\Delta\phi = \frac{2\pi}{\lambda_0} d(|n_o - n_e|). \quad (2.76)$$

In a negative uniaxial material the  $e$ -ray will advance (the axis defining the  $e$ -ray will be the *fast axis*), whereas the  $e$ -ray in a positive uniaxial crystal will lag (the axis defining the  $e$ -ray is the *slow axis*). There are several means of manufacturing waveplates to apply a specified phase shift. *True zero-order* wave plates are engineered to apply a phase shift  $0 < \Delta\phi < 2\pi$  directly, and are relatively thin and fragile as a result. *Multi-order* waveplates apply a phase shift  $0 < \Delta\phi < 2\pi$  plus an additional  $2\pi n$  phase shift for integer  $n$ . These wave plates are thicker and stronger at the expense of altering the optical path length difference experienced between the  $e$ -ray and  $o$ -ray. A solution is *effective zero-order* wave plates, often just referred

to as zero-order wave plates. Zero order wave plates consist of a pair of multi-order wave plates cemented together (or air-spaced) with their optic axes orthogonal. In the first wave plate the H polarisation component is aligned with the fast axis and advances, whereas in the second orthogonally oriented wave plate the V polarisation component is aligned with the fast axis and advances. The wave plate thicknesses are engineered such that the multi-order effect of the first wave plate is offset by the second wave plate, except for a remaining specified phase shift  $0 < \Delta\phi < 2\pi$ .

The experiments of later chapters exclusively employ *half-wave plates* and *quarter-wave plates*. A half-wave plate is engineered to apply a phase shift<sup>5</sup>  $\Delta\phi = \pi$ . When the polarisation vector of a normally incident beam forms an angle  $\theta$  with the optic axis, the orthogonal components of the polarisation vector experience different different refractive indices  $n_o$  and  $n_e$ , thereby rotating the output polarisation vector. The general operation of a half-wave plate is modelled by the *unitary*<sup>6</sup> matrix

$$U_H(\theta) = i \begin{bmatrix} \cos(2\theta) & \sin(2\theta) \\ \sin(2\theta) & -\cos(2\theta) \end{bmatrix}. \quad (2.77)$$

The action of a half-wave plate on a polarisation-encoded qubit can be described by the quantum mechanical operator  $\hat{U}_H(\theta)$ . For a general polarisation encoded qubit state  $\hat{\rho}$ , the resultant state  $\hat{\rho}'$  after an applied half-wave plate rotation is modelled by  $\hat{\rho}' = \hat{U}_H(\theta)\hat{\rho}\hat{U}_H^\dagger(\theta)$ .

A quarter-wave plate is engineered to apply a phase shift  $\Delta\phi = \pi/2$ . The general operation of a quarter-wave plate is modelled by the unitary matrix

$$U_Q(\theta) = \frac{1}{\sqrt{2}} \begin{bmatrix} 1 + i \cos(2\theta) & i \sin(2\theta) \\ i \sin(2\theta) & 1 - i \cos(2\theta) \end{bmatrix}, \quad (2.78)$$

and its operation on a polarisation-encoded qubit may be described by the quantum mechanical operator  $\hat{U}_Q(\theta)$ . Any point on the Poincaré sphere can be rotated to another arbitrary point by the unitary  $\hat{U}_Q(\theta_1)\hat{U}_H(\theta_2)\hat{U}_Q(\theta_3)$ . For initial or final linear polarisation states – for example, state preparation or projective measurement (described below), respectively, only  $\hat{U}_Q(\theta_1)\hat{U}_H(\theta_2)$  or  $\hat{U}_H(\theta_1)\hat{U}_Q(\theta_2)$  are necessary, with the order depending on initial or final linearity. Importantly, the real-space polarisation orientations are related

---

<sup>5</sup>The wave plates employed in this work apply their specified phase shift to within  $2\pi/250\text{rad}$ .

<sup>6</sup>A unitary matrix satisfies  $UU^\dagger = U^\dagger U = \mathbb{I}$ . Here,  $U^\dagger = [U^*]^\text{T}$ . Therefore,  $U^\dagger = U^{-1}$ .

to the Poincaré sphere polarisation orientations by a factor of 2, i.e.  $|H\rangle$  and  $|V\rangle$  polarisation states are separated by  $90^\circ$  in real-space, and by  $180^\circ$  on the Poincaré sphere. In the above matrices,  $\theta$  is a real-space angle.

### 2.5.3 Beam splitters

*Beam splitters* (BS) separate an incident beam into two distinct spatial paths. The work employed in this thesis utilises beam splitters manufactured by Melles Griot, Thorlabs, Edmund Optics, and Newport. Beam splitters employ a half-silvered interface or dielectric stack to divide the power in an input beam approximately evenly amongst the spatially separated output ports of the beam splitter. *Polarising beam splitters* (PBS) separate an incident beam into two orthogonal polarisation components, such that an appropriately oriented polarising beam splitter will leave the beam in one output port horizontally polarised, and the beam in the other output port vertically polarised (Figure 2.6). Polarising beam splitters are made of birefringent material (or dielectric stacks), and are useful for converting polarisation modes into spatial modes. Polarising beam splitters separate an incident beam into its orthogonal polarisation components by taking advantage of the fact that  $n_e$  and  $n_o$  have different critical angles for total internal reflection [81]. The PBSs employed in this work typically exhibit polarisation extinction ratios of  $\approx 1/400$ .

### 2.5.4 Hong–Ou–Mandel interference

A disadvantage encountered in linear optical quantum information science is the fact that photons don't ordinarily interact with one another. *Cross-phase modulation* offers one solution (encountered in  $\chi^{(3)}$  nonlinear materials), although the effect is typically too weak to be observed at the single photon level [79]. Fortunately, beam splitters can mediate photon-photon interactions by selecting appropriate input states and finely tuning experimental parameters to ensure nonclassical photon–photon interference. A well known type of nonclassical two-photon interference is *Hong-Ou-Mandel* (HOM) interference [87], which combines a pair of identical photons on a 50:50 beam splitter.

Nonclassical interference is used for several tasks in optical quantum information science. An important example is the revolutionary publication by Knill, Laflamme and Milburn [47], demonstrating that efficient quantum computation is possible by combining linear optical elements (like beam

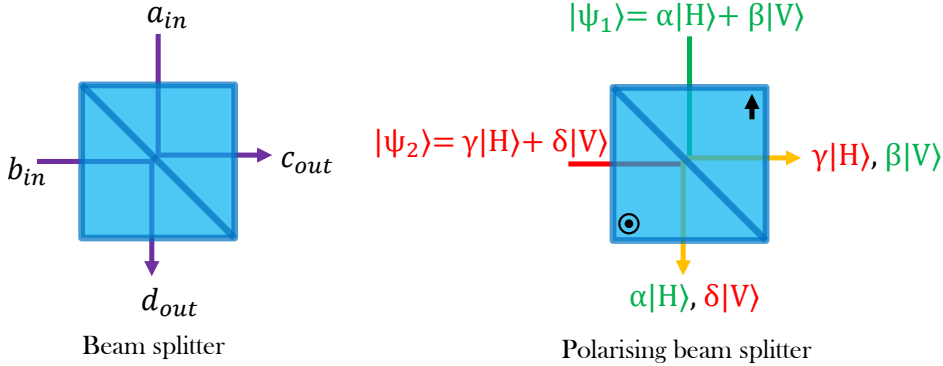


Figure 2.6: Common beam splitter types. Beam splitters (acronym BS, left) split incident light in modes  $a_{in}, b_{in}$  amongst the outputs  $c_{out}, d_{out}$ . The most common type of beam splitters are 50:50 beam splitters, which split incident light evenly amongst the output ports. Beam splitters may be constructed from half-silvered mirrors or dielectric stacks. Polarising beam splitters (acronym PBS, right) split incident light into its orthogonal polarisation components. PBSs may be constructed from birefringent materials (the black arrows on the right figure indicate optic axis alignment) or dielectric stacks.

splitters, mirrors, and wave plates), photon-photon interactions (mediated by Hong-Ou-Mandel interference), and measurement-induced nonlinearities in the form of single-photon detection. Another important process relying on nonclassical interference is entangled measurements, discussed in Sec. 2.6.5. Here, the important nonclassical interference effect called HOM interference is explored in detail.

To model the iconic HOM interference (an effect used routinely throughout this thesis), the beam splitter is modelled using quantum mechanical creation and annihilation operators (Eq. 2.41). The general creation and annihilation operators for beam splitter input modes  $a$  and  $b$  (Fig. 2.6, left) are

$$\hat{a}^\dagger = re^{i\phi_{ac}}\hat{c}^\dagger + te^{i\phi_{ad}}\hat{d}^\dagger, \quad \hat{a} = re^{-i\phi_{ac}}\hat{c} + te^{-i\phi_{ad}}\hat{d}, \quad (2.79)$$

$$\hat{b}^\dagger = re^{i\phi_{bd}}\hat{d}^\dagger + te^{i\phi_{bc}}\hat{c}^\dagger, \quad \hat{b} = re^{-i\phi_{bd}}\hat{d} + te^{-i\phi_{bc}}\hat{c}, \quad (2.80)$$

where  $r$  and  $t$  are the beam splitter reflectivities and transmittivities (quantified below) and  $\phi_{ij}$  are the phases accumulated in traversing path  $i \rightarrow j$ . The beam splitter should conserve energy and momentum, meaning the input and output photon numbers

$$\hat{a}^\dagger \hat{a} + \hat{b}^\dagger \hat{b} = \hat{c}^\dagger \hat{c} + \hat{d}^\dagger \hat{d} \quad (2.81)$$

should equate. Substituting Eqs. 2.79 and 2.80 into Eq. 2.81, the LHS equates to

$$\begin{aligned} \hat{a}^\dagger \hat{a} + \hat{b}^\dagger \hat{b} &= r^2 \hat{c}^\dagger \hat{c} + t^2 \hat{d}^\dagger \hat{d} \\ &\quad + rte^{i(\phi_{ac}-\phi_{ad})} \hat{c}^\dagger \hat{d} + rte^{i(\phi_{ad}-\phi_{ac})} \hat{d}^\dagger \hat{c} \\ &\quad + rte^{i(\phi_{bd}-\phi_{bc})} \hat{d}^\dagger \hat{c} + rte^{i(\phi_{bc}-\phi_{bd})} \hat{c}^\dagger \hat{d}. \end{aligned} \quad (2.82)$$

Therefore, the cross terms ( $\hat{d}^\dagger \hat{c}$  and  $\hat{c}^\dagger \hat{d}$ ) must cancel to conserve energy. This occurs when

$$e^{i(\phi_{ac}-\phi_{ad})} = -e^{i(\phi_{bc}-\phi_{bd})} = e^{i\phi}. \quad (2.83)$$

Using this definition,  $e^{i\phi_{ac}}$  and  $e^{i\phi_{bd}}$  can be expressed as

$$e^{i\phi_{ac}} = e^{i(\phi+\phi_{ad})} \quad \text{and} \quad e^{i\phi_{bd}} = -e^{-i(\phi-\phi_{bc})}. \quad (2.84)$$

Substituting these into the general expression for the beam splitter yields

$$\hat{a}^\dagger = e^{i\phi_{ad}} (re^{i\phi} \hat{c}^\dagger + t \hat{d}^\dagger), \quad \hat{a} = e^{-i\phi_{ad}} (re^{-i\phi} \hat{c} + t \hat{d}) \quad (2.85)$$

$$\hat{b}^\dagger = e^{i\phi_{bc}} (t \hat{c}^\dagger - re^{-i\phi} \hat{d}^\dagger), \quad \hat{b} = e^{-i\phi_{bc}} (t \hat{c} - re^{i\phi} \hat{d}). \quad (2.86)$$

Ignoring the global phase factor, these relations form the interchangeable *symmetric* and *asymmetric* beam splitter relations. In the symmetric relation,  $\phi = \pi/2$  so that the reflectivity  $r$  and transmittivity  $t$  enter symmetrically and are imaginary. The creation operators are expressed as

$$\hat{a}^\dagger = t \hat{d}^\dagger + ir \hat{c}^\dagger \quad \text{and} \quad \hat{b}^\dagger = t \hat{c}^\dagger + ir \hat{d}^\dagger. \quad (2.87)$$

In the asymmetric relation,  $\phi = 0$  so that the reflectivity  $r$  and transmittivity  $t$  enter asymmetrically and are real. In this case, the creation operators are

$$\hat{a}^\dagger = t \hat{d}^\dagger + r \hat{c}^\dagger \quad \text{and} \quad \hat{b}^\dagger = t \hat{c}^\dagger - r \hat{d}^\dagger. \quad (2.88)$$

To demonstrate HOM interference, the symmetric beam splitter relation will be used, noting that the asymmetric beam splitter relation produces the same result. The symmetric beam splitter relation intuitively models the  $\pi/2$  phase shift induced upon reflection at an interface. To demonstrate

the HOM interference effect, a pair of photons incident upon individual beam splitter ports  $a$  and  $b$  are modelled as

$$|\psi\rangle = \hat{a}^\dagger \hat{b}^\dagger |0\rangle_a |0\rangle_b. \quad (2.89)$$

Using the creation and annihilation operators defined by the symmetric beam splitter relation (Eq. 2.87), and expressing  $|0\rangle_a |0\rangle_b$  as  $|00\rangle$ ,  $|\psi\rangle$  becomes

$$\begin{aligned} |\psi\rangle &= (t\hat{d}^\dagger + ir\hat{c}^\dagger)(tc^\dagger + ird^\dagger)|00\rangle \\ &= (t^2\hat{d}^\dagger\hat{c}^\dagger + irt\hat{d}^\dagger\hat{d}^\dagger + irt\hat{c}^\dagger\hat{c}^\dagger - r^2\hat{c}^\dagger\hat{d}^\dagger)|00\rangle. \end{aligned} \quad (2.90)$$

For bosonic input particles (like photons), the bosonic commutation relation  $[\hat{c}^\dagger, \hat{d}^\dagger] = 0$  (Eq. 2.37) holds, so  $\hat{c}^\dagger$  and  $\hat{d}^\dagger$  commute. In this case,  $|\psi\rangle$  becomes

$$|\psi\rangle = \left[ (t^2 - r^2)\hat{c}^\dagger\hat{d}^\dagger + irt(\hat{d}^\dagger\hat{d}^\dagger + \hat{c}^\dagger\hat{c}^\dagger) \right] |00\rangle. \quad (2.91)$$

For a 50:50 beam splitter,  $|r| = |t| = 1/\sqrt{2}$ , yielding

$$|\psi\rangle = i\left(\frac{1}{2}\hat{d}^\dagger\hat{d}^\dagger + \frac{1}{2}\hat{c}^\dagger\hat{c}^\dagger\right)|00\rangle. \quad (2.92)$$

The creation operators  $\hat{c}^\dagger$  and  $\hat{d}^\dagger$  adhere to Eq. 2.41, each adding a single photon to output modes  $c$  and  $d$ , resulting in (ignoring the global phase factor)

$$|\psi\rangle = \frac{1}{\sqrt{2}}|02\rangle + \frac{1}{\sqrt{2}}|20\rangle. \quad (2.93)$$

This state is a nonclassical entangled state<sup>7</sup>. When the pair of input photons are degenerate in arrival time, spatial mode, frequency, and polarisation at the interface of a 50:50 beam splitter, they exit the beam splitter together in a superposition of output modes (Eq. 2.93). A measure of the nonclassical interference visibility can be recorded experimentally by monitoring the 50:50 beam splitter output ports for photon coincidences as distinguishability is introduced between the pair. In the experiments performed in this thesis, the temporal degree of freedom is used to introduce distinguishability (implemented by introducing an optical delay on one photon so the incident photons may no longer overlap at the 50:50 beam splitter). When the photons are maximally distinguishable (the photons do not overlap at

---

<sup>7</sup>If the input states are fermionic, their commutation relations are  $\{\hat{c}^\dagger, \hat{d}^\dagger\} = \hat{c}^\dagger\hat{d}^\dagger + \hat{d}^\dagger\hat{c}^\dagger = 0$ , and  $\{\hat{c}^\dagger, \hat{c}^\dagger\} = \hat{c}^\dagger\hat{c}^\dagger + \hat{c}^\dagger\hat{c}^\dagger = 0$ . This implies  $\hat{c}^\dagger\hat{c}^\dagger = 0$  and  $\hat{d}^\dagger\hat{d}^\dagger = 0$ , yielding the output state  $|\psi\rangle = |11\rangle$  for a 50:50 beam splitter.

the 50:50 beam splitter), the individual photons encounter the beam splitter independently, with photon pairs capable of registering coincidences 50 percent of the time (when both photons exit opposing beam splitter ports). However, when the photons are indistinguishable in every degree of freedom, a characteristic *HOM-dip* appears in coincidences as the photon pairs begin to exit the same beam splitter port, and therefore cannot register photon coincidences (Fig. 2.7). The optical delay is controlled using a high-precision translation stage attached to a fibre coupler sending one of the photons towards the 50:50 beam splitter. The width of the HOM-dip is related to the coherence length of the photons, set by the interference filters employed in the photon sources (used to filter out background light). The 820nm interference filters employed throughout this thesis typically have a bandpass of  $\pm 1.5\text{nm}$ , which corresponds to a coherence length for single photons at 820nm of  $\approx 300\mu\text{m}$ , equivalent to the full-width half maximum of the HOM-dip. The HOM interference effect plays a crucial role in the experiments of chapters 4, 5, and 6.

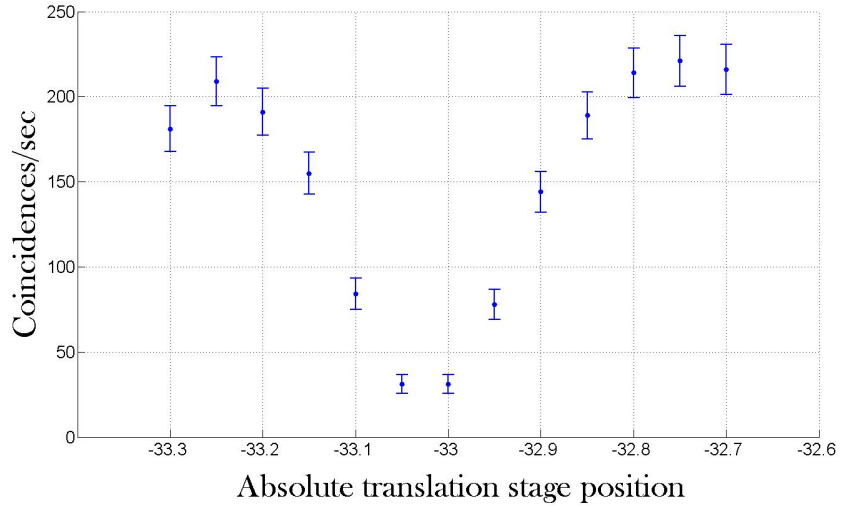


Figure 2.7: Coincidence pattern indicative of Hong-Ou-Mandel (HOM) interference, with absolute translation stage position expressed in units of mm. Degenerate photon pairs arriving at a 50:50 beam splitter exit at the same output port, resulting in a dip in beam splitter output port coincidence rates. As the optical delay of one photon relative to the other introduces distinguishability between the photon pairs, the interference disappears and the coincidence rate is restored. The full-width half maximum of the HOM dip is equivalent to the coherence length of the photon pairs.

### 2.5.5 Photon Detection

The work presented in this thesis employs *avalanche photodiode* (APD) detection to detect single photons. Coincidence detection between pairs of APDs can affirm photon–photon interaction effects like HOM interference. APDs can also be used to herald the presence of an idler photon after the detection of a signal photon. The APDs employed in this thesis were provided by two manufacturers: Perkin Elmer and Laser Components. A photodiode utilises the photo–electric effect to convert energy in the electromagnetic field into an electronic current. The APDs employed in this work utilize an active area constructed of silicon, with the devices having an overall detection efficiency (including the probability that a single photon will be absorbed and converted into an electric current) at 820nm (the wavelength of our single photons) of  $\approx 50\%$ . The active area is a silicon semiconductor with a strong reverse bias, so that the absorption of a single photon creates an electron–hole pair in the semiconductor depletion zone which accelerates in the presence of an applied external electric field [79]. In an APD, the reverse bias is such that an accelerated electron–hole pair generates additional electron–hole pairs via impact ionisation, which produces a measurable current ( $O \propto 10^{-3}$  Amps). The APDs cannot resolve photon number, although there exist various means of photon detection other than APDs with higher quantum efficiencies and/or number resolving capabilities (see Ref. [88] for a general overview).

By using APDs to affirm effects like nonclassical interference and to signify the generation of polarisation–entangled photon pairs from SPDC sources, powerful protocols in optical quantum information science may be enacted. A crucial ingredient of such protocols are *projective measurements*, performed using wave plates, PBSs, and APDs.

### 2.5.6 Projective Measurements

Projective measurements are the primary type of quantum measurement operator employed throughout this thesis. For the simple case of a single qubit, a projective measurement will map an input qubit state onto a measurement basis (typically the H/V basis) defined by the transmission and reflection ports of a polarising beam splitter. In this thesis, polarising beam splitters perform projective measurements in the H/V basis, wave plates impart the appropriate unitaries so that general measurements can be performed, and single photon APD detections register electronic signals corresponding to the eigenvalue of the measurement event.

A projective measurement is described by an observable  $\hat{M}$  on the state space of the system being observed, described by

$$\hat{M} = \sum_m m \hat{\Pi}_m. \quad (2.94)$$

where  $\hat{\Pi}_m$  is the projector onto the eigenspace of  $M$  with eigenvalue  $m$ , and  $\sum_m \hat{\Pi}_m^\dagger \hat{\Pi}_m = \mathbb{I}$  (where  $\mathbb{I}$  is the identity matrix). The probability of observing result  $m$  upon measurement  $|\psi\rangle$  is

$$p(m) = \langle \psi | \hat{\Pi}_m | \psi \rangle, \quad (2.95)$$

resulting in an output state  $|\psi'\rangle$  immediately after measurement of

$$|\psi'\rangle = \frac{\hat{\Pi}_m |\psi\rangle}{\sqrt{p(m)}}. \quad (2.96)$$

In this thesis, projective measurements in the H/V, D/A, and R/L polarisation bases are described respectively as

$$\hat{M}_z = \hat{\Pi}_H - \hat{\Pi}_V = |H\rangle\langle H| - |V\rangle\langle V|, \quad (2.97)$$

$$\hat{M}_x = \hat{\Pi}_D - \hat{\Pi}_A = |D\rangle\langle D| - |A\rangle\langle A|, \quad (2.98)$$

$$\text{and } \hat{M}_y = \hat{\Pi}_R - \hat{\Pi}_L = |R\rangle\langle R| - |L\rangle\langle L|. \quad (2.99)$$

The projective measurements  $\hat{M}_z$ ,  $\hat{M}_x$ , and  $\hat{M}_y$  are equivalent to the *Pauli spin matrices*, given by

$$\sigma_z = \begin{bmatrix} 1 & 0 \\ 0 & -1 \end{bmatrix}, \quad \sigma_x = \begin{bmatrix} 0 & 1 \\ 1 & 0 \end{bmatrix}, \quad \sigma_y = \begin{bmatrix} 0 & -i \\ i & 0 \end{bmatrix}. \quad (2.100)$$

The polarisation states  $\{H, V\}$ ,  $\{D, A\}$ , and  $\{R, L\}$  are associated with the eigenstates of the operators  $\hat{\sigma}_z$ ,  $\hat{\sigma}_x$ , and  $\hat{\sigma}_y$  respectively, with eigenvalues  $\pm 1$  in all cases. Finally, individual measurement operators for the H, V, D, A, R, and L polarisation states are expressed as

$$\hat{M}_\alpha^\pm = \frac{\mathbb{I} \pm \hat{\sigma}_\alpha}{2} \quad (2.101)$$

where again  $\mathbb{I}$  is the identity matrix and  $\alpha = \{x, y, z\}$ . The measurement operators for the individual polarisation states are determined from the sign of the ‘ $\pm$ ’ in Eq. 2.101.

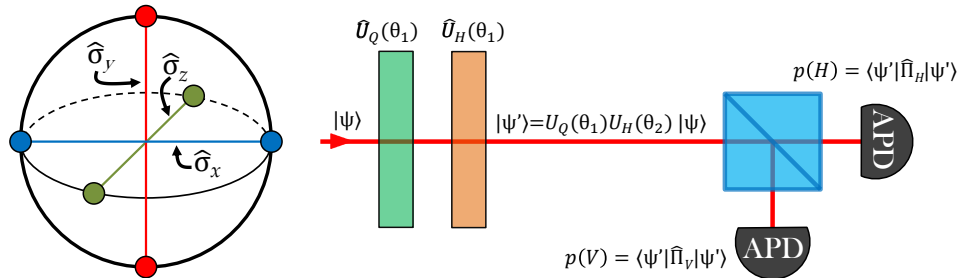


Figure 2.8: Illustration of the axes corresponding to the Pauli spin matrices on the Poincaré sphere (left), and apparatus for performing projective measurements (right). The Pauli spin matrices define a set of axes on the Poincaré sphere, with the polarisation basis states  $\{H, V\}$ ,  $\{D, A\}$ , and  $\{R, L\}$  associated with the eigenstates of the Pauli spin matrices. Projective measurements are performed using a QWP, HWP, PBS, and APDs. The APDs coupled to the PBS output ports register electronic signals corresponding to measurement eigenvalues, firing (in principle) with probabilities  $p(H)$  and  $p(V)$  given a state  $|\psi'\rangle = \hat{U}_Q(\theta_1)\hat{U}_H(\theta_2)|\psi\rangle$  incident upon the PBS.

The wave plate settings required to implement the unitaries appropriate to projective measurements in the H/V, D/A, and R/L polarisation bases are  $\hat{U}_H(\theta = 0^\circ)\hat{U}_Q(\theta = 0^\circ)$  for the HV basis,  $\hat{U}_H(\theta = 22.5^\circ)\hat{U}_Q(\theta = 45^\circ)$  for the DA basis, and  $\hat{U}_H(\theta = 0^\circ)\hat{U}_Q(\theta = 45^\circ)$  for the RL basis (Figure 2.8). To ensure repeatability, all wave plates in this work are controlled using computerised and motorised rotation stages from manufacturer Newport, having a systematic error in waveplate setting of  $\pm 0.02^\circ$  (although there are larger errors associated with locating the optic axis of a waveplate).

The Pauli spin matrices can be used to describe an arbitrary quantum state  $\hat{\rho}$  in *Bloch vector notation*. In this notation, an arbitrary quantum state  $\hat{\rho}$  is expressed as  $\hat{\rho} = (\mathbb{I} + \vec{r} \cdot \vec{\sigma})$ , where  $\vec{\sigma} = (\sigma_x, \sigma_y, \sigma_z)$ , and  $\vec{r} = (x, y, z)$  is a vector containing the  $x$ ,  $y$ , and  $z$  cartesian components of the state  $|\psi\rangle$  corresponding to  $\hat{\rho}$  on the Bloch sphere. The cartesian components of  $\vec{r}$  are given by  $x = |\vec{r}|\sin(\theta)\cos(\phi)$ ,  $y = |\vec{r}|\sin(\theta)\sin(\phi)$ , and  $z = |\vec{r}|\cos(\theta)$ . The Bloch vector notation defined here can be easily rotated onto the Poincaré sphere. Additionally, the measurement operators  $\hat{\sigma}_x$ ,  $\hat{\sigma}_y$ , and  $\hat{\sigma}_z$  form an overcomplete set of measurements for two-qubit quantum state tomography.

### 2.5.7 Quantum State Tomography

The work in following chapters employs quantum state tomography [72, 73, 82] to completely characterise the state of a quantum system. Classically, the *Stokes parameters*  $\vec{S} = \{S_0, S_1, S_2, S_3\}$  completely characterise the polarisation state of light. Because the density operator  $\hat{\rho}$  completely characterises the quantum state of light, we expect parallels between the classical Stokes parameters and the quantum mechanical projective operators when considering the quantum state of light. The quantum Stokes parameters are related to the probabilities of detecting the individual polarisation states:

$$\langle \hat{S}_1 \rangle = \langle \hat{\sigma}_z \rangle = \text{Tr}(\hat{\rho}\hat{\sigma}_z) = p(H) - p(V), \quad (2.102)$$

$$\langle \hat{S}_2 \rangle = \langle \hat{\sigma}_x \rangle = \text{Tr}(\hat{\rho}\hat{\sigma}_x) = p(D) - p(A), \quad (2.103)$$

$$\langle \hat{S}_3 \rangle = \langle \hat{\sigma}_y \rangle = \text{Tr}(\hat{\rho}\hat{\sigma}_y) = p(R) - p(L), \quad (2.104)$$

and

$$\langle \hat{S}_0 \rangle = \langle \hat{\sigma}_0 \rangle = \text{Tr}(\hat{\rho}\hat{\sigma}_0) = p(H) + p(V) = p(D) + p(A) = p(R) + p(L) = 1, \quad (2.105)$$

where  $\hat{\sigma}_0 = |H\rangle\langle H| + |V\rangle\langle V| = |D\rangle\langle D| + |A\rangle\langle A| = |R\rangle\langle R| + |L\rangle\langle L|$ , and  $\langle \hat{S}_0 \rangle = 1$  for all states. The quantum state  $\hat{\rho}$  for a single qubit is expressed in terms of the quantum Stokes parameters as

$$\hat{\rho} = \frac{1}{2} \begin{bmatrix} \langle \hat{S}_0 \rangle + \langle \hat{S}_1 \rangle & \langle \hat{S}_2 \rangle - i\langle \hat{S}_3 \rangle \\ \langle \hat{S}_2 \rangle + i\langle \hat{S}_3 \rangle & \langle \hat{S}_0 \rangle - \langle \hat{S}_1 \rangle \end{bmatrix}, \quad (2.106)$$

provided the measurements are repeated upon multiple identical copies of  $\hat{\rho}$ .

Reconstructing the density operator for two-qubit states follows a similar procedure, whereby every combination of H, V, D, A, R, and L are measured amongst the individual qubits, revealing correlations amongst the basis states. This thesis has a strong focus on the generation, manipulation and characterisation of two-qubit quantum states. Because of experimental fluctuations in collecting data, the reconstructed density operator may be *non-physical* (the reconstructed two-qubit density operator doesn't adhere to Eqs. 2.9, 2.10, and 2.11). In two-qubit quantum state tomography, non-physical density operators arising from experimental errors (typically errors resulting from Poissonian counting statistics) are eliminated by performing

a numerical maximum-likelihood search to ensure the reconstructed density operators are representative of a physical system. Unfortunately, the method for directly propagating Poissonian errors through such a numerical search is unknown. To solve this, we recognise the Poissonian error in the number of coincident events for each two-qubit measurement forms a multi-dimensional Poissonian distribution. This allows us to perform a Monte Carlo simulation, which randomly selects sets of values from the distribution of coincident data to undergo maximum-likelihood reconstruction. The characterisation employed in this thesis uses a Monte Carlo simulation to perform a maximum-likelihood search for 200 different random sets of data taken from the distribution. The result is a distribution of physical density operators, from which an average density operator is retrieved.

Reconstructing experimental density operators in this way allows the derivation of a number of useful parameters used for characterising quantum states. Specific parameters relevant to this thesis are the *purity*, *tangle*, and *fidelity* – useful monotonic metrics implemented widely throughout the quantum optics community.

The purity is a figure of merit for characterising the quality of a quantum state, particularly in the presence of mixture or noise. The purity is related to the off-diagonal coherence terms in a density matrix, and is defined as

$$P = \text{Tr}(\hat{\rho}^2) \quad (2.107)$$

where  $P = 1$  is called a *pure* state and  $P < 1$  corresponds to a mixed state. For a single qubit, the purity corresponds to the magnitude of a state vector on the Poincaré sphere. The minimum purity for a quantum state depends on its dimension  $d$ , with  $P_{\min} = 1/d$ , equating to  $P_{\min} = 1/2$  for qubits.

The tangle is a figure of merit for quantifying the degree of entanglement present in a two-qubit quantum state. The tangle is a monotonic measure ranging from  $T = 0$  (separable) to  $T = 1$  (maximally entangled), and is found from the reconstructed density operator  $\hat{\rho}$  by defining a *spin flipped* density operator  $\tilde{\hat{\rho}}$

$$\tilde{\hat{\rho}} = (\hat{\sigma}_y \otimes \hat{\sigma}_y) \hat{\rho}^* (\hat{\sigma}_y \otimes \hat{\sigma}_y), \quad (2.108)$$

where  $\hat{\rho}^*$  is the complex conjugate of  $\hat{\rho}$  and  $\hat{\sigma}_y$  is the Pauli spin operator. The tangle is then defined as

$$T = (\max\{\lambda_1 - \lambda_2 - \lambda_3 - \lambda_4, 0\})^2, \quad (2.109)$$

where  $\{\lambda_1 - \lambda_2 - \lambda_3 - \lambda_4\}$  are the eigenvalues of  $R = \sqrt{\sqrt{\hat{\rho}}\hat{\rho}\sqrt{\hat{\rho}}}$  in decreasing order.

Finally, the state fidelity measures the similarity or degree of overlap between two quantum states. Importantly, the fidelity allows a meaningful comparison between tomographically reconstructed states and ideal theoretical states. The fidelity (also a monotonic measure) between a pair density operators  $\hat{\rho}$  and  $\hat{\sigma}$  is given by

$$F(\hat{\rho}, \hat{\sigma}) = \text{Tr} \left[ \sqrt{\sqrt{\hat{\rho}}\hat{\sigma}\sqrt{\hat{\rho}}} \right]^2. \quad (2.110)$$

Quantum state tomography is largely autonomous by virtue of automated wave plates and counting electronics. As a result, reconstructing a density operator and finding associated parameters is relatively simple, facilitating characterisation processes. Throughout this thesis, quantum state tomography is used to completely characterise and optimise polarisation–entangled two-qubit states. Such entangled states are often alternatively characterised in an incomplete way by measuring their degree of nonclassical correlation.

## 2.6 Nonclassical Correlations

The term “spooky-action-at-a-distance” was famously coined by Albert Einstein in reference to the unusual properties of entangled states [89], with the phrase since becoming a colloquial expression for nonlocally correlated phenomena. In 1964, nine years after Einstein’s passing, Irish mathematician John Bell introduced *Bell’s theorem* [37], a work of profound insight that modelled the constraints applicable to a universe respecting Einstein’s favoured notions of *realism* (from objective determinism), *locality* (from relativity), and *free will* (wholly instinctive). Bell’s theorem presented the possibility for an experimentally realisable litmus test of nature’s allowed correlations, with the test itself derived by considering quantitative constraints on Bell’s theorem (called a Bell test). Recently, further work into nonlocal effects has provoked researchers to ask whether *all* entangled quantum states are nonlocal. Answering that question has revealed the existence of different *nonlocality classes*, such that an experimental quantum state may not pass Bell’s test (corresponding to the strongest class of nonlocality), but still demonstrate quantum correlations of a weaker form by passing

a different test containing one or more additional assumptions (depending on the nonlocality class).

In this section, correlations are studied by considering *local models* that formalise common intuitions about nature and its correlations into theoretical assumptions. Bell's theorem is the first of these models considered in this thesis.

### 2.6.1 Bell's theorem

Bell's theorem constrains the correlations allowed in a universe obeying the intuitive notion of local causality, asserting that the state of a physical system (for example, a particle) exists independently of measurement and is affected only by immediate spatial influences [9, 27]. A powerful feature of Bell's theorem is that it makes no assumptions about the physical manifestations of correlated systems, or about the interpretation of their workings. Bell's theorem considers two spatially separated parties – called Alice and Bob – who each control individual measurement devices. Alice and Bob can make measurements  $a$  and  $b$  respectively on a pair of separated physical systems, each mutually prepared by some reproducible process  $\epsilon$ . The joint probability of Alice and Bob obtaining measurement outcomes  $A = \pm 1$  and  $B = \pm 1$  after making measurements  $a$  and  $b$  on their respective physical systems prepared in  $\epsilon$  can be expressed as [90]

$$P(A, B|a, b, \epsilon). \quad (2.111)$$

The preparation procedure  $\epsilon$  encompasses all of the explicitly known variables relevant to the demonstration. Bell's theorem introduces a further local variable  $\lambda$  encompassing any additional variables relevant to the demonstration but that may not be explicitly known. For this reason, the variable  $\lambda$  is called a *local hidden variable* (LHV), not because the variable  $\lambda$  is unknowable or hidden in principle, but because it is not explicitly accessible in the instance of the demonstration and is therefore not included in  $\epsilon$ . The probability distribution  $P(A, B|a, b, \epsilon)$  is said to be locally causal (adheres to a locally causal model) if there exists a determinism condition (a probability distribution  $P(\lambda|\epsilon)$  over the hidden variables conditional on the preparation procedure  $\epsilon$ ) and a locality condition (independent probability distributions for Alice and Bob given by  $P(A|a, \epsilon, \lambda)$  and  $P(B|b, \epsilon, \lambda)$  respectively). The quantitative criteria for the joint probability of Alice and Bob's measurement outcomes in Bell's theorem is then [90]

$$P(A, B|a, b, \epsilon) = \sum_{\lambda} P(\lambda|\epsilon)P(A|a, \epsilon, \lambda)P(B|b, \epsilon, \lambda). \quad (2.112)$$

This expression<sup>8</sup> encapsulates locality in the sense that Alice and Bob's individual probabilistic outcomes  $A$  and  $B$  depend only on local processes; namely, the local measurement settings  $a$  or  $b$ ; and on events in the past light cones of the physical systems sent to Alice and Bob depending on known processes  $\epsilon$  and unknown processes  $\lambda$ . Bell's model also encapsulates determinism (particle properties exist objectively) in the existence of  $\lambda$ , since in the local model  $\lambda$  is knowable in principle (perhaps in a different but undeveloped theory). Any apparently random behaviour in the outcomes  $A$  and  $B$  are therefore the result of unknown but causally determined local processes at the source of the systems sent to Alice and Bob, with  $\sum_{\lambda} P(\lambda|\epsilon)$  in Eq. 2.112 accounting for the different possible manifestations of  $\lambda$  in any given preparation run  $\epsilon$ . EPR's notion of 'elements of reality' are therefore formalised in Bell's theorem, whereby the elements of reality relate to the predetermined outcomes of local measurements made by distant parties – with one example of elements of reality being those factors which determine outcomes of polarisation measurements.

### 2.6.2 Bell's Inequality

Any constraint on the quantitative criteria of Bell's local model in Eq. 2.112, that is, a constraint on  $P(A, B|a, b, \epsilon)$ , is called a *Bell inequality*. In this thesis the introductory focus is on Bell's original inequality [37] and the Clauser, Horne, Shimony, and Holt (CHSH) inequality [39]. Bell's inequality is conveniently introduced and experimentally implemented in an experimental quantum optical protocol, therefore motivating the convention followed here. It is, however, important to recall that Bell's theorem is constructed such that the framework applies to any physical system with dichotomic measurement outcomes arbitrarily called  $\pm 1$ .

To introduce Bell's original inequality, we consider a pair of polarisation-entangled photons generated in a SPDC event (Sec. 2.4.4), where one photon is sent to observer Alice and the other to Bob, with Alice and Bob mutually separated by a significant distance. Alice makes a freely determined choice of polarisation measurement on her photon, deciding between two

---

<sup>8</sup>The hidden variable  $\lambda$  may exist in a continuum, in which case the sum in Eq. 2.112 is replaced by an integral.

measurements, denoted  $a$  or  $c$ , with each measurement appropriating outcomes  $A = \pm 1$  or  $C = \pm 1$ . Here, ‘freely determined’ means Alice makes a measurement choice of her own volition, assuming in this context that Alice’s volition is entirely uninfluenced and random in the decision of choosing a measurement (called *measurement independence*). Bob similarly chooses freely between two polarisation measurements, denoted  $b$  or  $c$ , where  $c$  is the same as Alice’s (this restriction is lifted in the CHSH inequality to follow), with outcomes  $B = \pm 1$  or  $C = \pm 1$ . Bell’s theorem asserts that these measurement outcomes depend only on local processes, either known ( $\epsilon$ ) or unknown ( $\lambda$ ), where in the latter case the outcomes are determined by local hidden variables, conferring any model that satisfies the criterion in Eq. 2.112 the name ‘LHV model’, or alternatively *Bell-local* model or *locally-causal* model. When Alice and Bob each choose the same measurement alignment  $c$ , they observe the same outcome  $C$ , because of the correlated nature of the photon pairs. Bell showed that the results  $A$ ,  $B$  and  $C$  satisfy [9,37]

$$A(B - C) \equiv \pm(1 - BC), \quad (2.113)$$

since both sides of the equation equal zero if  $B = C$ , and are equal to  $\pm 2$  if  $B \neq C$ .

The identity in Eq. 2.113 can be quantitatively evaluated experimentally if Alice and Bob repeat their randomly chosen measurements over  $N$  iterations of different photon pairs, where the results are combined into an average. In this case, Eq. 2.113 can be written as

$$A_j B_j - A_j C_j \equiv \pm(1 - B_j C_j) \quad (2.114)$$

where subscript  $j$  numerates the photon pair measured between 1 and  $N$  in the test. Alice and Bob determine  $A$ ,  $B$ , and  $C$  pseudo-simultaneously by using averages  $\langle A \rangle$  and  $\langle B \rangle$ , and correlators  $\langle AB \rangle$ , to evaluate Eq. 2.113. The individual averages are given by

$$\langle A \rangle = \sum_j \frac{A_j}{N}, \quad \langle B \rangle = \sum_j \frac{B_j}{N}, \quad \text{and} \quad \langle AB \rangle = \sum_j \frac{A_j B_j}{N}, \quad (2.115)$$

where averaging over  $j$  averages over  $\lambda$  (because  $\lambda$  changes for each  $j$ ). Eq. 2.114 can then be expressed in the form of an inequality with correlators:

$$|\langle AB \rangle - \langle AC \rangle| \leq 1 - \langle BC \rangle. \quad (2.116)$$

This is Bell's inequality. For anticorrelated measurement statistics, the right hand side of Bell's inequality becomes  $1 + \langle BC \rangle$  [37].

The power of Bells's theorem lies in its falsifiability (it can be tested, or falsified, in practice). The correlators in Bell's inequality can alternatively be analysed using quantum theory. In this case, the correlators for polarisation correlated photon pairs are modelled as [9]

$$\langle \hat{\sigma}_a \otimes \hat{\sigma}_b \rangle \equiv \langle \Psi | (\hat{\sigma}_a \otimes \hat{\sigma}_b) | \Psi \rangle = \cos 2(\theta_a - \theta_b), \quad (2.117)$$

where  $\hat{\sigma}_a$  and  $\hat{\sigma}_b$  represent measurement operators aligned at angles  $\theta_a$  and  $\theta_b$  from some arbitrary common polarisation axis  $\vec{u}$ . Using this expression, Eq. 2.116 becomes

$$|\cos 2(\theta_a - \theta_b) - \cos 2(\theta_a - \theta_c)| + \cos 2(\theta_b - \theta_c) \leq 1. \quad (2.118)$$

Surpsingly, when the angles  $\theta_a$ ,  $\theta_b$ , and  $\theta_c$  defining the measurements  $\hat{\sigma}_a$ ,  $\hat{\sigma}_b$ , and  $\hat{\sigma}_c$  are each separated by  $30^\circ$ , quantum mechanics predicts that the left hand side of Eq. 2.118 will equal  $\frac{3}{2}$ ; a clear violation of Bell's theorem. Thus, we find a conflict between the assumptions of Bell's theorem and the predictions of quantum theory. To shed light on this conflict, Bell's theorem can be directly tested using Bell's inequality, since the test requires only experimental statistics taken from a suitably arranged experiment. An early version of this experiment was conducted in 1982 by Alain Aspect *et al.* [38], using a variant of Bell's inequality; the CHSH inequality<sup>9</sup> [39].

### 2.6.3 CHSH Inequality

A more general version of Bell's inequality can be derived by giving Alice and Bob individual measurement settings, where  $c$  is no longer shared between the two parties. In this instance, Alice chooses between measurements  $a$  or  $c$ , and Bob chooses between measurements  $b$  or  $d$ , where a measurement along  $d$  will reveal a measurement outcome  $D = \pm 1$ . In this case, the results  $A$ ,  $B$ ,  $C$ , and  $D$  satisfy

$$(A + C)B + (A - C)D \equiv \pm 2, \quad (2.119)$$

because either  $A + C = 0$  or  $A - C = \pm 2$ , or  $A - C = 0$  or  $A + C = \pm 2$ . For  $N$  iterations of the test, the expression for the  $j^{\text{th}}$  photon is

---

<sup>9</sup>An earlier Bell inequality violation was performed in 1972 by Freedman and Clauser [91], using photons and a generalised Bell inequality.

$$A_j B_j + B_j C_j + C_j D_j - D_j A_j \equiv \pm 2, \quad (2.120)$$

which, like Bell's inequality, can be averaged and expressed using correlators as

$$|\langle AB \rangle + \langle BC \rangle + \langle CD \rangle - \langle DA \rangle| \leq 2. \quad (2.121)$$

This is the CHSH inequality [39], valid for any physical system with dichotomic variables. If the CHSH inequality is interpreted using the framework of quantum theory (assuming photon pairs correlated in polarisation from a SPDC source), the inequality becomes

$$|\cos 2(\theta_a - \theta_b) + \cos 2(\theta_b - \theta_c) + \cos 2(\theta_c - \theta_d) - \cos 2(\theta_d - \theta_a)| \leq 2. \quad (2.122)$$

When the angles  $\theta_a$ ,  $\theta_b$ ,  $\theta_c$ , and  $\theta_d$  defining the measurements  $\hat{\sigma}_a$ ,  $\hat{\sigma}_b$ ,  $\hat{\sigma}_c$ , and  $\hat{\sigma}_d$  are each separated by  $22.5^\circ$ , quantum theory predicts that the left hand side of Eq. 2.122 equals  $2\sqrt{2}$ ; again a clear theoretical violation of Bell's inequality.

The CHSH inequality presents a convenient experimental test, primarily for Bell's theorem and additionally for the predictions of quantum theory. The test performed by Aspect *et al.* employed polarisation correlated photon pairs generated in a SPS cascade emitted from excited calcium atoms<sup>10</sup>. While the physical mechanism of photon generation in an SPS cascade is different to that of SPDC, the analysis of the CHSH inequality is exactly the same because Bell's theorem admits no particular interpretation for the physical mechanisms responsible for the observed correlations between the photon pair. In the Aspect experiment, Alice and Bob's measurement settings were periodically switched every 10ns by acousto-optical switches that directed their individual photons into analysers measuring  $\hat{\sigma}_a$  or  $\hat{\sigma}_c$  in the case of Alice and  $\hat{\sigma}_b$  or  $\hat{\sigma}_d$  in the case of Bob. The periodic switching altered Alice and Bob's measurement settings during the photon's time-of-flight, to ensure that Alice and Bob's measurements could not be causally accessible by the source. The mean lifetime of the intermediate P level of the Calcium atoms was 5ns, and Alice and Bob were separated by 12m, ensuring

<sup>10</sup>An atomic SPS cascade refers to an atom in an excited state S undergoing two consecutive electric dipole transitions from two-photon absorption ( $J = 0 \rightarrow J = 1 \rightarrow J = 0$ ). When the photons generated in the SPS cascade are emitted in opposite directions, they are polarised along the same axis. The state emitted in such a process is the  $|\Psi^+\rangle$  polarisation entangled state [9].

that light-speed influences would require a travel time of 40ns. Thus, the experimental data was collected before a light-speed signal could propagate between Alice and Bob, therefore enforcing the strict locality conditions required to justify a test of Bell’s theorem. The results of the Aspect experiment found the left hand side of Eq. 2.122 to equal  $2.697 \pm 0.015$ , a clear experimental violation of Bell’s inequality. Thus Bell’s theorem, coined as the “most profound discovery in science [92]”, is so precisely because Bell’s theorem *doesn’t agree* with experimental data.

Furthermore, the results of the 1982 experiment were found to agree with the quantum mechanical predictions (where the quantum prediction  $2\sqrt{2}$  is the *upper limit* allowed by quantum theory for bipartite systems, called the Tsirel’son bound [93]). The implication of the experimental violation of Bell’s inequality, if the result is to be accepted without reservations<sup>11</sup>, is that our intuitive notions about the universe are wrong, and that quantum theory accurately models the observed correlations. The results of Bell’s theorem and its violation are far reaching, resulting in technological applications and continuing research into the various interpretations of the inequality violation [19, 27, 94–97].

#### 2.6.4 Local Models for EPR Steering

Experimentally implementing Bell’s test for nonlocality is technologically demanding. Ensuring spatial remoteness of parties whilst maintaining high detection efficiencies to ensure unequivocal violation of Bell’s inequality presents the main difficulty (this amounts to closing experimental loopholes, explored in Chapter 3). To reduce the technological requirements in tests of nonlocality, additional theoretical assumptions can be introduced, with the additional assumptions resulting in a reduction of nonlocality class. EPR steering is one such class of nonlocality. The theoretical framework of EPR steering contains the initial assumptions of Bell’s theorem with an additional assumption – that one party’s measurement device (typically Bob’s) can be accurately described using quantum mechanical formalism, and that the operator of the device reliably controls its implementation. This additional assumption places EPR steering in a nonlocality class that is strictly weaker than Bell nonlocality [98].

---

<sup>11</sup>For example, the authors of the Aspect *et al.* experiment [38] admit that their experiment is subject to *loopholes*. These loopholes have since been individually addressed (but not collectively), and are discussed in detail in Chapter 3.

Steering as a concept was introduced by Erwin Schrödinger in 1935 [40], initially in reference to the unusual feature exhibited by distributed bipartite entangled quantum states that allowed one party (Alice) to nonlocally affect or *steer* another distant party's (Bob's) quantum state by performing a local measurement on Alice's half of the distributed entangled state. The quantum mechanical description for one measurement apparatus in EPR steering makes the theoretical framework an asymmetric one, and allows for unique protocols and applications. For example, the EPR steering effect may find applications in semi-device-independent or device-independent entanglement verification and quantum key distribution protocols [55, 99], with the asymmetry in EPR steering protocols providing a useful means of successfully overcoming noise [100] and loss [101] introduced by transmission channels and detectors in entanglement verification protocols.

Local models for EPR steering were introduced by Wiseman *et. al.* in 2007, resulting in new tests of quantum correlations [98, 102]. In tests of EPR steering, the probability distribution for Bob in Bell's joint probability distribution is supplemented with the assumption that quantum mechanical formalism accurately describes the workings of Bob's measurement apparatus. In practice, this means Bob manipulates a measurement device capable of accurately measuring an observable of a quantum mechanical input state (typically a polarisation-encoded qubit, as is the case herein). In this case, the joint probability distribution for Alice and Bob becomes [90]

$$P(A, B|a, b, \epsilon) = \sum_{\lambda} P(\lambda|\epsilon) P(A|a, \epsilon, \lambda) P_Q(B|b, \epsilon, \lambda), \quad (2.123)$$

where subscript  $Q$  in  $P_Q(B|b, \epsilon, \lambda)$  encapsulates the assumption of quantum mechanics for Bob (Bob makes quantum projective measurements  $\hat{\Pi}_b^B$  on quantum states  $\hat{\rho}(\epsilon, \lambda)$  yielding outcome  $B$  for measurement  $b$ ), and Alice's apparatus (and system) still admits a general description. Any constraint on Eq. 2.123 is called an EPR steering inequality, expressed as

$$S_n = \frac{1}{n} \sum_{k=1}^n \langle A_k \hat{\sigma}_k^B \rangle \leq C_n, \quad (2.124)$$

where  $n$  are the total number of measurement settings agreed upon by Alice and Bob,  $A_k$  is Alice's measurement outcome, and  $\hat{\sigma}_k^B$  is Bob's measurement operator for measurement setting  $k$  (chosen from the pre-determined set  $\{\hat{\sigma}_k^B\}_n$ ). The inequality  $S_n \leq C_n$  can be tested experimentally for violations, with a violation indicating nonclassical correlations that admit no local hidden variable model for Alice, and no *local hidden quantum state*

model for Bob (explored below). Here,  $S_n$  is known as the *steering parameter*, and  $C_n$  is the boundary distinguishing nonclassical correlations from classical correlations.

The means of deriving the bounds  $C_n$  are of critical importance to the EPR steering model. The bounds  $C_n$  are maximised for an unentangled single qubit, i.e. an unentangled single qubit will achieve  $S_n = C_n$  – the steering parameter  $S_n$  is saturated *but does not exceed* the bound  $C_n$ . The means of saturating the steering parameter  $S_n$  for an unentangled single qubit defines an *EPR steering protocol*. Therefore, before discussing how the bounds  $C_n$  are found, it is useful to first outline the general EPR steering protocol.

The general EPR steering protocol is introduced here in two cases; case i., where an unentangled single qubit is used to saturate the EPR steering bound  $S_n = C_n$ , and case ii., where an entangled qubit pair is used to exceed the EPR steering bound  $S_n > C_n$ , therefore violating the EPR steering inequality (Eq. 2.124) and certifying nonclassical correlations (attributed to a class of EPR-steerable states). The EPR steering protocol always proceeds in the same way, irrespective of case. The only way that Bob can practically distinguish between case i. and case ii. is if the EPR steering inequality is violated as a result of nonclassical correlations. The general EPR steering protocol proceeds as follows (Fig. 2.9):

**Step 1.** Bob receives his qubit. Bob may receive an unentangled single qubit (case i., Fig. 2.9), or he may receive one-half of a bipartite entangled state (case ii., Fig. 2.9). At this point, Bob is incapable of distinguishing the former from the latter.

**Step 2.** Bob announces to Alice his choice of measurement setting  $k$ , corresponding to an observable  $\hat{\sigma}_k^B$  drawn from the pre-determined set  $\{\hat{\sigma}_k^B\}_n$ .

**Step 3.** Bob measures his single qubit and secretly records his measurement outcome  $B_k$ .

**Step 4.** Alice announces her measurement outcome  $A_k$ . The announcement may be a genuine measurement outcome (as in case ii.), or a fabricated announcement (as in case i.).

**Step 5.** Steps 1-3 are repeated to gather measurement statistics so that Bob may calculate  $S_n$  and distinguish between case i. (no entanglement) or case ii. (entanglement).

In this scenario, Alice's device is treated as a “black box”, meaning no assumptions are made about Alice or the workings of her device.

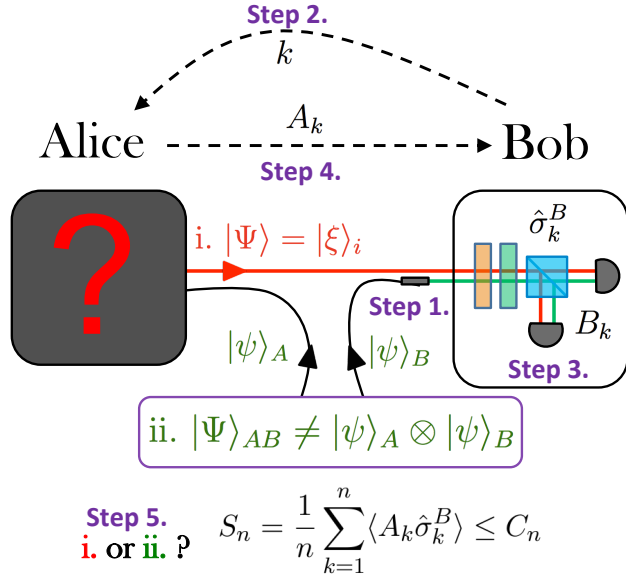


Figure 2.9: The EPR steering task. Bob employs a five-step procedure (see text for details) to determine whether he shares an EPR-steerable entangled state with Alice. Bob (clear box) performs a quantum measurement  $\hat{\sigma}_k^B$ , drawn from the pre-determined set  $\{\hat{\sigma}_k^B\}_n$  where  $n$  is the total number of measurement settings. Alice's device is considered as a “black box”, meaning no assumptions are made about its operation. Alice can, at best, achieve  $S_n = C_n$  by sending unentangled single qubits to Bob (corresponding to case i.). If Alice measures one-half of a bipartite polarisation-entangled state shared with Bob (corresponding to case ii.), then Alice can violate the EPR steering inequality ( $S_n > C_n$ ), hence demonstrating that she shares an EPR-steerable entangled state with Bob.

The derivation of the bounds  $C_n$  are now considered, recalling that the bounds  $C_n$  are saturated for an unentangled single qubit (case i.). In this case, Bob receives an unentangled single qubit, called a local hidden quantum state, from a set of possible qubit preparations  $\{|\xi\rangle_i\}_n$  made by Alice's device. Here  $i = \pm k$  indexes a state prepared in the  $\pm$  eigenstate of a measurement operator along some arbitrary axis  $\mathbf{u}_k$  on the Poincaré sphere. In this scenario, Alice can maximise correlations between her announced  $A_k$  and Bob's privately recorded  $B_k$  by exploiting her knowledge of Bob's set of pre-determined quantum mechanical measurements  $\{\hat{\sigma}_k^B\}_n$ , each performed along an axis  $\mathbf{u}_k$ , to inform her choice of preparation basis for the state  $|\xi\rangle_i$ . This case has been referred to as a ‘cheating Alice’, or ‘dishonest Alice’ sce-

nario, and corresponds to measurement outcomes for Bob that are described by a local hidden quantum state model.

The EPR steering bound  $C_n$  is found by considering Bob's set of measurement operators  $\{\hat{\sigma}_k^B\}_n$  on the Poincare sphere with the set of local hidden quantum states  $\{|\xi\rangle_i\}_n$  that Alice might send to Bob in an attempt to optimise correlations between  $A_k$  and  $B_k$  and hence maximise the steering parameter  $S_n$ . By way of example, the bound  $C_2$  for  $n = 2$  measurement settings  $\hat{\sigma}_1^B = \hat{\sigma}_z^B$  and  $\hat{\sigma}_2^B = \hat{\sigma}_x^B$  is derived from geometrical arguments here. For  $n = 2$  measurement settings, Alice might choose to prepare and send to Bob local hidden quantum states prepared in the  $\pm$  eigenstates of Bob's measurement operators  $\hat{\sigma}_1^B = \hat{\sigma}_z^B$  (H/V polarisation basis) and  $\hat{\sigma}_2^B = \hat{\sigma}_x^B$  (D/A polarisation basis), see Fig. 2.10ia. For simplicity, we first imagine that Alice prepares only local hidden quantum states  $|\xi\rangle_{\pm 1}$ , aligned along Bob's first measurement axis  $\mathbf{u}_1$  corresponding to measurement operator  $\hat{\sigma}_1^B$ . In this case, Alice will always know Bob's privately recorded measurement outcome  $B_1$ , and so it is easy for Alice to correlate her announced  $A_1$  perfectly with Bob's privately recorded outcome  $B_1$ . Alternatively, if Bob chooses to measure in the  $\hat{\sigma}_2^B = \hat{\sigma}_x^B$  basis (lying along a different axis to Alice's prepared states  $|\xi\rangle_{\pm 1}$ ), then Alice can only randomly guess Bob's privately recorded measurement outcome, yielding zero correlation on average. Thus Alice arrives at a steering parameter  $S_2 = \frac{1}{n} \sum_k \langle A_k \hat{\sigma}_k^B \rangle = \frac{1}{2}(\langle A_1 \hat{\sigma}_1^B \rangle + \langle A_2 \hat{\sigma}_2^B \rangle) = \frac{1}{2}(1 + 0) = 1/2$ .

In this example, it might be obvious to Bob that Alice's announcements are only correlated for the cases when he measures in the  $\hat{\sigma}_1^B = \hat{\sigma}_z^B$  basis, and random otherwise, and so he may conclude that Alice is trying to cheat. To avoid this problem and also achieve a greater degree of correlation, Alice can instead prepare her set of local hidden quantum states  $\{|\xi\rangle_i\}_n$  along a set of axes  $\{\mathbf{u}_k\}_n$  lying between Bob's measurement axes  $\hat{\sigma}_z^B$  and  $\hat{\sigma}_x^B$  (Figure 2.10ib). In this case, Alice's outcome  $A_k$  should be appropriate to the most likely outcome of Bob's measurement  $\hat{\sigma}_k^B$  on the local hidden quantum state  $|\xi\rangle_i$  that she has sent. In this case, the maximum correlation Alice can achieve by sending local hidden quantum states with two measurement settings is  $S_2 = \frac{1}{2}(\langle A_1 \hat{\sigma}_1^B \rangle + \langle A_2 \hat{\sigma}_2^B \rangle) = \frac{1}{2}(1/\sqrt{2} + 1/\sqrt{2}) = 1/\sqrt{2}$ . This is the greatest degree of correlation Alice can engineer without sharing entanglement; thus, for  $n = 2$ ,  $C_2 = 1/\sqrt{2}$ . This geometric approach is used to determine all bounds  $C_n$ , yielding  $C_2 = 1/\sqrt{2}$ ,  $C_3 = C_4 = 1/\sqrt{3}$ ,  $C_6 = 0.5393$ , and  $C_{10} = 0.5236$ . For an infinite number of measurement settings,  $C_\infty = 1/2$  [100].

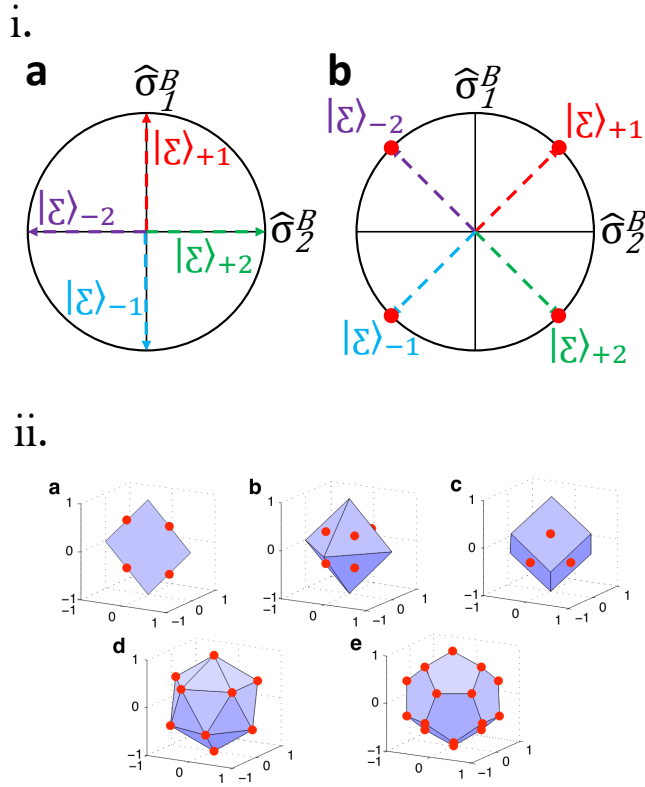


Figure 2.10: EPR steering state preparation and measurement strategies for Alice (dishonest) and Bob. In i., a dishonest Alice prepares states from a set  $\{|\xi\rangle_i\}_n$ , for  $n = 2$  measurement settings and  $i = \pm 1, \pm 2$ . Figs. i.a and i.b illustrate two different cheating strategies: Fig. i.a is an example case where Alice's preparations are aligned with Bob's measurements (see text), and Fig. i.b is an optimal case for maximising correlations between Alice's announcements  $A_k$  and Bob's recorded measurement outcomes  $B_k$  given measurements  $\hat{\sigma}_1^B$  and  $\hat{\sigma}_2^B$  performed, by Bob, upon an unentangled single qubit  $|\xi\rangle_i$  prepared by Alice. Fig. ii. illustrates Alice's optimal cheating strategies for Bob's various choices of measurement setting  $n$ , each of which define a corresponding EPR steering inequality. The red dots correspond to a dishonest Alice's set of optimal states  $\{|\xi\rangle_i\}_n$  given Bob's measurement settings  $\{\hat{\sigma}_k^B\}_n$ , with antipodal pairs of vertices in Figs. ii.a-e defining Bob's set of measurement axes  $\{\mathbf{u}_k\}_n$ . Note equivalence between Fig. i.b and ii.a). The shapes in Figs. ii.a-e are the platonic solids, corresponding to  $n = 2, 3, 4, 6$ , and  $10$  evenly spaced measurement settings.

In the case where Alice and Bob do genuinely share a bipartite entangled

state (for example, a maximally entangled Bell state  $|\Psi^-\rangle_{AB}$ ), as in case ii., then Alice can steer Bob's half of the entangled state  $|\psi\rangle_B$  into an eigenstate of his announced measurement  $\hat{\sigma}_k^B$  by measuring her half of the entangled state  $|\psi\rangle_A$  in that same basis, i.e. perform the measurement  $\hat{\sigma}_k$  on her half of the entangled state. In this ideal case, the measurement outcome  $A_k$  announced by Alice will be perfectly correlated with Bob's privately recorded measurement outcome  $B_k$  in each run of the protocol, and so Bob will in-principle observe  $S_2 = 1$ . This violates the  $n = 2$  steering inequality and so demonstrates nonclassical correlations belonging to a class of EPR steerable states that cannot be described by a local hidden variable model for Alice and a local hidden quantum state model for Bob.

### 2.6.5 Entanglement Swapping

Even more remarkable in the story of entanglement was the discovery of *entanglement swapping* [60, 62–64]. Entanglement swapping in quantum optical systems employs a *Bell state measurement* device (BSM, Fig. 2.11) to generate entanglement between particles with no common history<sup>12</sup>, with these particles then capable of demonstrating Bell nonlocal correlations.

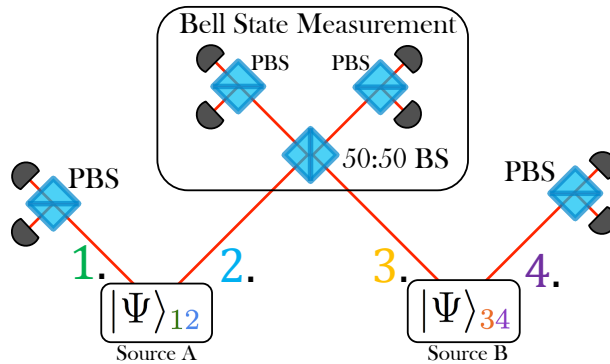


Figure 2.11: The entanglement swapping protocol using a Bell state measurement (BSM) device. Source A and B each emit entangled particles in the states  $|\Psi\rangle_{12} \neq |\psi\rangle_1 \otimes |\psi\rangle_2$  and  $|\Psi\rangle_{34} \neq |\psi\rangle_3 \otimes |\psi\rangle_4$  respectively. By combining qubits in modes 2 and 3 on a 50:50 beam splitter comprising the BSM device, initial entanglement existing between modes 1,2 and 3,4 is transferred to modes 1 and 4.

The BSM device plays a significant role in quantum information protocols,

<sup>12</sup>Entanglement swapping may result in nonclassical correlations between particles that never co-existed in time [65].

and forms the key ingredient in quantum teleportation protocols [103]. The BSM device illustrated in Fig. 2.11 combines a pair of separable polarisation encoded qubits at the interface of a 50:50 beam splitter (one qubit in each input mode). Ideally, the 50:50 beam splitter performs a joint measurement on the incident qubits, and projects the initially separable quantum states onto the entangled Bell state basis  $\{|\Psi^\pm\rangle, |\Phi^\pm\rangle\}$ , making the BSM device an *entangled measurement* device<sup>13</sup> (see chapter 6). Importantly, the BSM device will only perform an entangled measurement if the two incident states undergo nonclassical interference at the 50:50 beam splitter (Sec. 2.5.4). In principle, detector firing patterns at the outputs of the BSM device subsequently determine which of the four Bell states the incident qubits have been probabilistically projected onto. Unfortunately, using only linear optical elements (mirrors, beam splitters, wave plates, and single photon detection), an *ideal* BSM device that perfectly resolves all four Bell states cannot be realised [105]. However, a *partial* BSM device can be designed from linear optical components, and is capable of accurately resolving the individual Bell states  $|\Psi^-\rangle$  and  $|\Psi^+\rangle$ , with the two remaining Bell states  $|\Phi^-\rangle$  and  $|\Phi^+\rangle$  being combined into a single indistinguishable outcome [60]. The experimentally realisable partial BSM forms a key component of research in Chapters 4, 5, and 6.

A BSM device can be made to enact entanglement swapping if the qubit states incident upon the 50:50 beam splitter are each subsystems  $|\psi\rangle_2$  and  $|\psi\rangle_3$  of distinct bipartite polarisation–entangled states  $|\Psi\rangle_{12} \neq |\psi\rangle_1 \otimes |\psi\rangle_2$  and  $|\Psi\rangle_{34} \neq |\psi\rangle_3 \otimes |\psi\rangle_4$ . For an initial joint state  $|\Psi^-\rangle_{12} \otimes |\Psi^-\rangle_{34}$ , the interaction with the BSM device can be modelled as

$$|\Psi^-\rangle_{12} \otimes |\Psi^-\rangle_{34} = \frac{1}{2} (|\Psi^-\rangle_{14} |\Psi^-\rangle_{23} + |\Psi^+\rangle_{14} |\Psi^+\rangle_{23} + |\Phi^-\rangle_{14} |\Phi^-\rangle_{23} + |\Phi^+\rangle_{14} |\Phi^+\rangle_{23}). \quad (2.125)$$

Studying this expression, it becomes evident that once the BSM device projects the initially separable states in modes 2 and 3 onto one of the Bell states, entanglement occurs between the qubits in modes 1 and 4, transfer-

<sup>13</sup>Sometimes the terminology ‘entangling measurements’ is used. However, an entangling measurement is one that projects a state held by distant observers onto an entangled state. An example is the  $\sigma_x$  measurement on one third of a tripartite entangled GHZ state [104]. The  $\sigma_x$  measurement on one particle will project the remaining pair of particles onto a bipartite entangled state. In this instance, the  $\sigma_x$  measurement is not entangled, but it is entangling.

ring initial entanglement between modes 1 and 2, and separately modes 3 and 4, to modes 1 and 4.

## **2.7 Summary**

This chapter has presented introductory concepts in optical quantum information science, and additionally covered some important physical processes related to the generation and manipulation of quantum optical systems. The material presented will assist in understanding the experimental work presented in later chapters. Additional background information will be presented in the remaining chapters and appendices as necessary.

## Chapter 3

# Loss-Tolerant Einstein-Podolsky-Rosen Steering

### Statement of work

Chapter 3 contributes experimental and theoretical research towards Einstein-Podolsky-Rosen (EPR) steering. The work presented is based on theoretical investigations undertaken by H. M. Wiseman, S. J. Jones, A. C. Doherty, M. D. Reid, E. G. Cavalcanti, C. Branciard, and D. A. Evans [90, 98, 100–102].

The research contributed in this chapter theoretically explores and experimentally demonstrates the transmission-loss-tolerant features of an EPR steering experiment, finding potential application in quantum key distribution (QKD) protocols. The loss-tolerant EPR steering experiment was undertaken by Dylan Saunders and myself. I constructed the experiment and optimised the photon source. Dylan and I collected and analysed the experimental data together. Dylan contributed significantly to the non-trivial systematic error analysis (Appendix 2). The work resulted in a *Physical Review X* publication to which all authors contributed [101].

### 3.1 Introduction

The strongest tests of quantum correlations are based on Bell’s theorem (Sec. 2.6), which certifies quantum correlations as being Bell nonlocal. Weaker classes of nonlocality are introduced by supplementing Bell’s theorem with

additional theoretical assumptions. EPR steering is one such weaker class of nonlocality, containing the assumptions of Bell’s theorem with one additional assumption – that quantum mechanical formalism faithfully describes the workings of one party’s measurement device (Sec. 2.6.4).

Many experimental tests of Bell’s theorem and EPR steering are technologically demanding. To mitigate technological demands in tests of quantum correlations, it is common practice to make additional assumptions pertaining to the action of experimental devices; assumptions that lie *outside* of the theoretical framework applicable to a nonlocality class. Because additional assumptions of this sort relate only to experimental devices, they do not affect the class of nonlocality tested. Devices acting in conflict with such assumptions are said to exploit an *experimental loophole*. To eliminate or identify such potentialities, we require *loophole-free* experimental tests of quantum correlations.

The key experimental assumptions often made in tests of Bell’s theorem, EPR steering, and other tests of quantum correlations are the following:

**Fair sampling assumption:** Non-unit-efficiency photon detection devices record events that constitute a fair sample of all possible detection events. The detection loophole is opened if it is possible that detectors record a subset of events that are not representative of the entire set. The detection loophole is traditionally closed by employing high-efficiency detectors, or overcoming channel/transmission losses [56].

**No-signalling assumption:** Experimental devices cannot signal information to each other. The signalling loophole is opened if it is possible that apparatuses share light-speed influences between one another. The signalling loophole is closed by enforcing space-like separation [106].

**Measurement-independence assumption:** Experimental measurement devices behave as-per design, and their workings are not influenced by deterministic sources of measurement choice. The freedom-of-choice loophole is opened if devices could, in principle, condition their behaviour on a pre-determined measurement choice. The freedom-of-choice loophole is closed by enforcing genuinely random measurement setting choices [107].

The first experiment to close the signalling and freedom-of-choice loopholes

in a photonic Bell test was T. Scheidl *et al.* [108]. The first experiment to close the detection loophole in a variation of a Bell test was the experiment by B. G. Christensen *et al.* [109]. The first experiments to close loopholes in tests of EPR steering were conducted in a suite of experiments by A. J. Bennet *et al* (detection loophole, presented in this chapter) [101], D. H. Smith *et al.* (detection loophole) [110], and B. Wittman *et al.* (signalling, freedom-of-choice, and detection loopholes) [111]. For a conclusive summary of these experiments and the associated loopholes, see Ref. [112].

Closing loopholes in tests of quantum correlations are important for technological applications exploiting nonlocal effects, for instance in entanglement-based QKD protocols [51, 70]. In such QKD protocols, open loopholes can be exploited, resulting in compromised security and the reduction of private key distribution efficacy [113–116]. Therefore, the unambiguous closure of experimental loopholes will signify an important milestone as the advent of the quantum computer approaches.

The work in this chapter focusses on closing the detection loophole in an EPR steering experiment. The detection loophole is opened in photonic experiments when demonstrations encounter significant sources of photon loss. Typically, the major source of photon loss in photonic tests of quantum correlations are due to detector inefficiencies (for instance, typically-employed Silicon avalanche photodiodes used for single-photon detection have efficiencies  $\approx 50\%$  at 820nm). Therefore, a clear means of overcoming photon losses of this kind are to employ high efficiency single-photon detectors, several of which have efficiencies approaching unity (see Ref. [88]). Unfortunately, photon losses based on transmission channel inefficiencies cannot be overcome by employing high-efficiency single-photon detection, since transmission losses can only be averted by improving the transmission channel characteristics. In photonic experiments, transmission channels tend to be optical fibre or free space channels. Theoretical studies have demonstrated that quantum communication via earth-bound fibre and free-space transmission channels based on current technologies are restricted to  $\approx 100\text{km}$  in length [117]. Therefore, as a way forward, photonic quantum information protocols capable of overcoming transmission losses find critical importance towards long-distance loophole free tests of quantum correlations and corresponding applied technologies.

In this chapter, one such transmission-loss-tolerant protocol for EPR steering is introduced in a photonic setting. The loss-tolerant protocol is in-

troduced by first showing how loss negatively affects the traditional EPR steering protocol performed by Alice and Bob, introduced in Sec. 2.6.4. The effects of loss are explained using the “dishonest Alice” model of EPR steering, demonstrating how a dishonest Alice can use unentangled single qubits to exploit the fair-sampling assumption and seemingly show nonclassical correlations (attributed to EPR steerable states) even when nonclassical resources are not shared between Alice and Bob. Second, ammendments are made to the traditional EPR steering protocol so that a dishonest Alice can no longer exploit the fair-sampling assumption in this way, hence resulting in a loss-tolerant EPR steering protocol. Specifically, the loss-tolerance in the EPR steering protocol is acheived by allowing Bob to carefully monitor and account for Alice’s *heralding efficiency*, denoted  $\epsilon$ , in the EPR steering protocol (Alice’s heralding efficiency is the proportion of times Alice claims to have measured a photon, coincident with Bob receiving and measuring a qubit). The results presented herein conclusively demonstrate the efficacy of loss-tolerant EPR steering protocols, and may find potential application in long-distance QKD protocols and in fundamental tests of nature [57, 58].

### 3.2 A Loss-Tolerant EPR Steering Protocol

The loss-tolerant EPR steering protocol is developed by considering the effects of photon loss on the traditional EPR steering protocol (Sec. 2.6.4), performed by exploring, in detail, the case of a “dishonest Alice” EPR steering scenario, denoted by case i. in Fig. 2.9. In the dishonest Alice scenario, Alice sends Bob unentangled single-qubit states from the set  $\{|\xi\rangle_i\}_n$  where  $i = \pm k$  indexes the  $\pm$  eigenstate of Bob’s measurement operator  $\hat{\sigma}_k^B$ , and  $n$  are the number of measurement settings, pre-agreed upon by Alice and Bob. A careful analysis of this scenario reveals that a dishonest Alice can violate the traditional EPR steering inequalities presented in Sec. 2.6.4 with unentangled single-qubit states if she claims to regularly lose photons. The optimal time for Alice to make such an annoucement in the example case of the  $n = 2$  EPR steering protocol is when her preparation basis for an unentangled single-qubit state  $|\xi\rangle_i$  does not coincide with Bob’s measurement axis  $\mathbf{u}_k$ . In this scenario, Alice will generate perfect correlation with Bob and convey an average heralding efficiency  $\epsilon = 1/n = 0.5$ .

Bob achieves security against such loss-based cheating strategies by making two modifications to the traditional EPR steering protocol of Sec. 2.6.4. First, Bob calculates Alice’s heralding efficiency  $\epsilon$  from the protocol data. Second, Bob computes new,  $\epsilon$ -dependent EPR steering bounds  $C_n(\epsilon)$  which

the steering parameter  $S_n$  must exceed in order to demonstrate EPR steering. The derivation of the loss-tolerant bounds  $C_n(\epsilon)$  is described in detail below, and involves determining Alice’s optimal “cheating strategy” for a given heralding efficiency  $\epsilon$ . Of course if Alice “cheats” like this she will not actually fool Bob, as she will not violate the loss-tolerant EPR steering inequalities derived. The key result of this chapter is that if Bob closes the detection loophole by accounting for Alice’s heralding efficiency, then the effect of EPR steering can be verified experimentally even in the presence of heavy transmission losses.

### 3.2.1 Loss-Tolerant EPR-Steering Inequality

In any test of EPR steering, Bob trusts his own apparatus, meaning he trusts his own device to record a fair sample of all possible detection events and can discard without consequence those experimental runs where he fails to detect a photon. However, Bob cannot trust any claims Alice makes about apparent propagation losses or the efficiency of her detectors. Therefore, he does not trust Alice’s claims about how often she sees a photon, conditional on his detecting one. Bob instead knows only Alice’s heralding efficiency  $\epsilon$ : the probability that she heralds receiving a photon by declaring a prediction  $A_k$  for it. This is a quantity determined by Bob wholly from the experimental statistics.

Bob’s measurements are described using quantum observables; in this case Pauli matrices  $\hat{\sigma}_k^B$  for  $k \in \{1, \dots, n\}$ . No assumptions are introduced about Alice, and thus her declared results are represented by a random variable  $A_k \in \{-1, 0, 1\}$ , with  $A_k = 0$  corresponding to a null result: Alice “loses” her photon (defined as zero for mathematical convenience). Loss-tolerant EPR steering bounds  $C_n(\epsilon)$  are derived such that when the experimental statistics, post-selected on Alice’s conclusive results, violate the inequality

$$\mathcal{S}_n \equiv \frac{1}{n} \sum_{k=1}^n \langle A_k \hat{\sigma}_k^B \rangle \leq C_n(\epsilon), \quad (3.1)$$

EPR steering is demonstrated with no detection loophole (i.e. without relying on a fair-sampling assumption for Alice).

To discuss the derivation of the loss-tolerant bounds  $C_n(\epsilon)$ , it is useful to first consider the derivation of the traditional bounds  $C_n$ , which correspond to an idealised scenario where Alice never loses, or claims to lose, a photon (i.e.  $\epsilon = 1$ ). In such a scenario, Alice declares a non-null result for all emitted pairs

of systems. This condition equates the traditional EPR steering protocol with the loss-tolerant one ( $C_n = C_n(\epsilon = 1)$  in Eq. 3.1). The EPR steering bounds in this case are given by [100]

$$C_n = \max_{\{A_k\}} \left\{ \lambda_{\max} \left( \frac{1}{n} \sum_k A_k \hat{\sigma}_k^B \right) \right\}, \quad (3.2)$$

where  $\lambda_{\max}(\hat{O})$  is the maximum eigenvalue of  $\hat{O}$ . The eigenvectors associated with the  $\lambda_{\max}$  for every set  $\{A_k\}_n$  that attains the maximum define the set of optimal states  $\{|\xi\rangle_i\}_n$  which Alice can send to Bob in order to attain the bound<sup>1</sup>  $C_n$ . The set of states  $\{|\xi\rangle_i\}_n$  are known as Alice's *optimal* "cheating ensemble" (although a dishonest Alice cannot actually cheat Bob). For two qubits, the maximum value of  $S_n$  that can be achieved is unity, and this requires a maximally entangled state, while  $C_n < 1$  for  $n > 1$  as long as Bob's settings correspond to different observables.

To derive the loss-dependent bounds  $C_n(\epsilon)$ , scenarios where Alice's heralding efficiency is non-unity are considered in detail. Alice's optimal cheating strategies are considered first as *deterministic strategies*, in which Alice's declaration of  $A_k = +1, -1$ , or 0 (null) is conditioned upon the unentangled single-qubit state  $|\xi\rangle_i$  she prepares and the setting  $k$  Bob specifies. For each state  $|\xi\rangle_i$  sent to Bob, Alice declares a  $|\xi\rangle_i$ -dependent outcome  $A_k = \pm 1$  only when Bob's measurement setting announcement  $k$  resides within a particular subset containing  $m$  elements of the total measurement settings  $n$ , and declares a null result  $A_k = 0$  for the remaining  $n - m$  measurement settings. This gives Alice an apparent heralding efficiency  $\epsilon = m/n$ . For a given  $m$ , the set of states which allow Alice to maximize her correlation defines a "cheating ensemble". When Alice chooses to send unentangled single-qubit states from a single cheating ensemble, she is employing a deterministic cheating strategy. In such a strategy, the optimal bound on  $S_n$  that Alice can attain by sending unentangled single-qubit states was calculated by theory collaborators Howard Wiseman and David Evans, and is given by

$$S_n(m) = \max_{\{A_k\}_m} \left\{ \lambda_{\max} \left( \frac{1}{m} \sum_k A_k \hat{\sigma}_k^B \right) \right\}, \quad (3.3)$$

where the maximisation is over sets  $\{A_k\}_m$  where exactly  $m$  of the  $A_k$  take values  $\pm 1$ , while the rest are 0. Performing the maximization reveals the optimal cheating ensemble, as each set  $\{A_k\}_m$  for which the maximum  $\lambda_{\max}$

---

<sup>1</sup>Deriving the bounds  $C_n$  in this way equates with the geometric derivation discussed in Sec. 2.6.4.

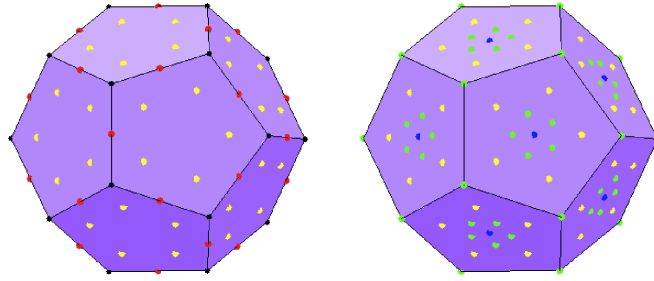


Figure 3.1: Alice’s optimal cheating ensembles for  $n = 10$  measurement settings and heralding efficiencies  $\epsilon \in [0.2, 0.5]$ . This figure shows, on the Poincare sphere, the directions of the states in Alice’s optimal “cheating ensembles” that set the bound  $C_n(\epsilon)$  for EPR steering when  $\epsilon \in [0.2, 0.3]$  (on the left) and when  $\epsilon \in [0.3, 0.5]$  (on the right), for the exemplary case of  $n = 10$ . The black dots (only visible on the left) define Bob’s measurement axes: the vertices of the dodecahedron. For the deterministic strategy where Alice gives non-null results for only two of Bob’s settings ( $m = 2$ ), the red dots (on the left) define the optimal states Alice should send, and likewise for  $m = 3$  (yellow; both),  $m = 4$  (green; right) and  $m = 5$  (blue; right). For any heralding efficiency  $0.2 < \epsilon < 0.3$  (left) Alice’s optimal strategy is nondeterministic: a mixture of the  $\epsilon = 0.2$  strategy (red) and the  $\epsilon = 0.3$  strategy (yellow). For any  $0.3 < \epsilon < 0.5$  (right) a dishonest Alice should use a mixture of the  $\epsilon = 0.3$  (yellow) and  $\epsilon = 0.5$  (blue) strategies. [Figure courtesy of David Evans].

in Eq. (3.3) is attained defines a state: the eigenstate corresponding to that  $\lambda_{\max}$ . In general there are several such sets  $\{A_k\}_m$  which attain the maximum in Eq. (3.3), and  $p(m)$  is used to denote their number, which is thus also the number of states in the optimal cheating ensemble for a given  $m$ . Examples of such cheating ensembles  $\{|\xi\rangle_i^{(m)}\}_{p(m)}$  are shown in Fig. 3.1, for  $n = 10$  and  $m \in \{2, 3, 4, 5\}$  (figure courtesy of David Evans). For an in-depth analysis of the cheating ensembles, see Ref. [118].

Alice may also employ more general, *nondeterministic* cheating strategies, where the condition that her announcements  $A_k = \pm 1$  are non-zero for exactly  $m$  out of  $n$  measurement settings is lifted. Importantly, the optimal deterministic strategies just considered are not necessarily the optimal strategies for Alice even for an apparent efficiency such that  $\epsilon n$  is an integer  $m$ , and do not apply if  $\epsilon n$  is not an integer. For an arbitrary heralding

efficiency  $\epsilon$ , Alice's most general cheating strategy is considered to be a probabilistic mixture of optimal deterministic strategies of different  $m$ , with weights  $w_m$ . Because the EPR steering inequalities are linear, the bound yielded by a nondeterministic cheating strategy for an arbitrary heralding efficiency  $\epsilon$  is [101]

$$C_n(\epsilon) = \max_{\{w_m\}} \left[ \sum_{m=1}^n w_m S_n(m) \right], \quad (3.4)$$

with the constraints  $0 \leq w_m \leq 1$ ,  $\sum_{m=1}^n w_m = 1$ , and  $\sum_{m=1}^n (m/n) w_m = \epsilon$ . The maximum is achieved with at most two nonzero  $w_m$ s (by linearity), so the bound  $C_n(\epsilon)$  can be evaluated numerically for any finite set of measurement settings  $k$ . Bob's privately recorded set of statistics  $\{B_k\}_n$  resulting from Alice sending unentangled single-qubit states in such a nondeterministic strategy will appear completely random (mixed), and so the only way Bob can distinguish between case i. (unentangled single-qubit cheating strategy) and case ii. (shared entanglement) in Fig. 2.9 is to determine Alice's heralding efficiency and evaluate the loss-tolerant EPR steering inequality Eq. 3.1. If Bob finds  $S_n > C_n(\epsilon)$  using the new loss tolerant EPR steering bound for his post selected statistics, then he can be certain that he shares an EPR-steerable entangled state with Alice, with no detection loophole.

The theoretical values for  $C_n(\epsilon)$  are shown in Fig. 3.2. As expected,  $C_n(\epsilon)$  monotonically decreases with  $\epsilon$ ; the values on the  $\epsilon = 1$  vertical axis correspond to the traditional EPR steering protocol bounds  $C_n$ , and the  $C_n(\epsilon) = 1$  horizontal axis corresponds to heralding efficiencies  $\epsilon = 1/n$  marking the point that a dishonest Alice can achieve  $S_n = 1$  in the traditional EPR steering protocol. The key point is that, for any arrangement of  $n$  different measurement settings, it is possible for Alice to demonstrate EPR steering ( $S_n > C_n(\epsilon)$ ) using a maximally entangled state if and only if  $\epsilon > 1/n$  (lying in the upper right plot region, Fig. 3.2). This is because  $S_n$  can reach its maximum value of 1 with maximally entangled states, while the only way for Alice to obtain  $S_n = 1$  by preparing and sending unentangled single-qubit states would be to prepare a state aligned perfectly with one of Bob's measurement settings, and giving a null result for the other  $n - 1$  settings (restricting her to, at best, the upper left plot regions, Fig. 3.2).

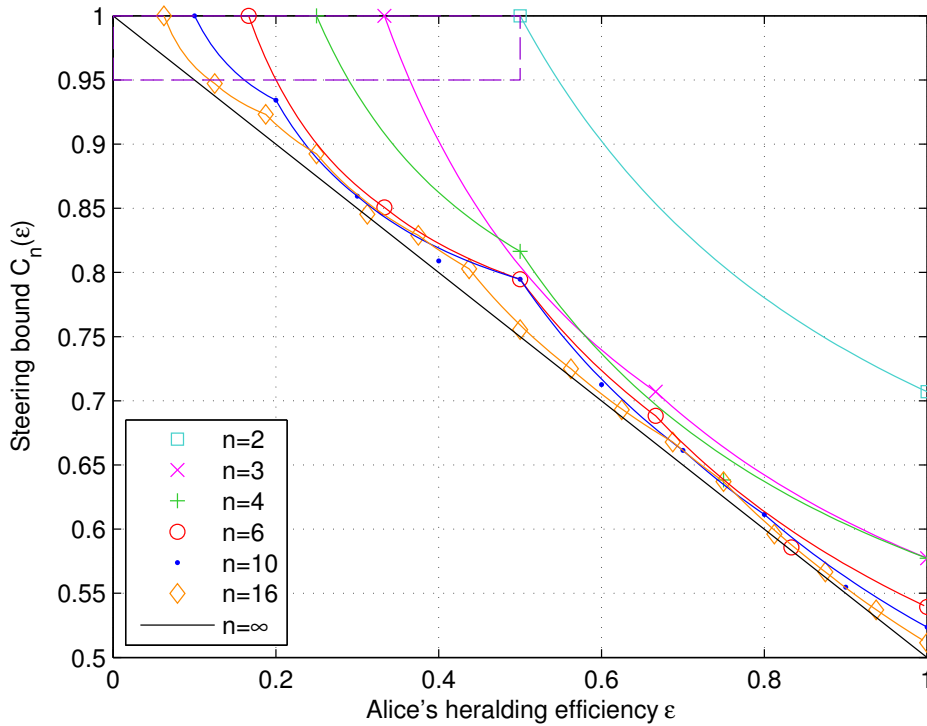


Figure 3.2: Loss-dependent EPR steering bounds. The solid curves are the theoretical bounds  $C_n(\epsilon)$  on  $S_n$  for demonstrating EPR steering with no detection loophole, for  $n = 2, 3, 4, 6, 10, 16$ , and  $\infty$ . The same-coloured symbols (some of which do not lie on the curves) correspond to the steering parameter  $S_n$  theoretically obtainable by a cheating Alice using a deterministic strategy. The dashed purple box (upper left) is the target region used for data collection (see Fig. 3.4, Results and Analysis).

For an infinite number of measurements ( $n = \infty$ ) uniformly distributed on the Bloch sphere,  $C_\infty(\epsilon) = 1 - \frac{1}{2}\epsilon$  (black line, Fig. 3.2). That is, there is a gap between the maximum quantum correlation,  $S_\infty = 1$ , and the EPR-steering bound  $C_\infty(\epsilon)$  for any  $\epsilon > 0$  (Ref. [101]). Thus, it becomes possible to demonstrate steering with *arbitrarily high* losses, as long as Alice and Bob share a sufficiently high-fidelity entangled state (in this case, the singlet state is selected) and employ a sufficiently elaborate many-setting measurement scheme. This is the scenario employed for the experimental demonstration to follow.

### 3.3 Demonstration of Loss-Tolerant EPR Steering

The goal of the experimental demonstration was to successfully certify the sharing of EPR-steerable states using the new loss-tolerant EPR steering inequalities for  $n = 3, 4, 6, 10$ , and  $16$  measurement settings using a source of polarisation-entangled photon pairs. In terms of the EPR steering protocol outlined above, this equates to a scenario where Alice is honest (Alice and Bob genuinely share entanglement, case ii. in Fig. 2.9), and Alice therefore attempts to steer Bob's half of the entangled state so that he may observe violations of the loss-tolerant EPR steering inequalities. For this to occur, Alice required heralding efficiencies  $\epsilon > 1/n$ , targeting the upper-right region of Fig. 3.2. For the measurement settings tested here, this corresponded to a maximum heralding efficiency  $\epsilon > 0.33$  (corresponding to the case of  $n = 3$  measurement settings). Typical “bulk nonlinear crystal” polarisation-entangled photon pair sources utilising spontaneous parametric down conversion (SPDC) normally achieve maximum heralding efficiencies  $\approx 15\%$  (such as those outlined in Sec. 2.4.4). Therefore, for this experiment, an improved source of polarisation-entangled photon pairs was required. To that end, a 10mm-long periodically-poled KTP (PPKTP) crystal was used as the source of photon pairs. To generate entanglement between the pairs, the PPKTP crystal was placed inside a Sagnac interferometer, based on Refs. [85, 86]. Such SPDC sources are known to have improved heralding efficiencies primarily because the collinear down-conversion modes emitted by the PPKTP crystal are approximately Gaussian, which have good overlap with single-mode fibres placed at the interferometer outputs (see Fig. 3.3). In addition to the efficient photon source, a 1km long optical fibre was also employed in one arm of the experiment, to act as a source of loss for demonstrating the EPR steering effect in the presence of heavy transmission losses for  $n = 10$  and  $n = 16$  measurement settings. A separate source of unentangled single-qubit states was also required to demonstrate

a dishonest Alice scenario, showing her inability to cheat using unentangled single-qubit states against the new loss-tolerant bounds  $C_n(\epsilon)$ .

### 3.3.1 Photon Source

The polarisation-entangled photon source based on the Sagnac interferometer was pumped by a *Toptica iBeam 405* laser (with a diode of nominally 410nm centre wavelength installed), operated with an external diffraction grating (Thorlabs GR25-1204) in the Littrow configuration [79]. The diffraction grating was installed to stabilise the spectral output of the laser, and afforded a small margin of wavelength tunability ( $\pm 1\text{nm}$ ) around the centre wavelength, to assist in reaching the phase-matching condition of our SPDC crystal. The power in the output mode of the laser/grating assembly was 3mW. The laser/grating output was fiber coupled into single mode fibre and used to pump a 10mm-long PPKTP crystal bidirectionally. The PPKTP crystal was sourced from manufacturer Raicol and embedded in the centre of the Sagnac interferometer, giving rise to polarisation-entangled photon pairs at 820 nm via SPDC. The Sagnac interferometer was constructed from a bare minimum of optics, to ensure high heralding efficiencies, which were particularly important for the  $n = 3$  test, requiring  $\epsilon > 0.33$ . The stepwise procedure employed for constructing the Sagnac interferometer is presented in Appendix 1. A schematic of the Sagnac source constructed for the experiment is depicted in Fig. 3.3.

The optimal phase-matching temperature of the PPKTP crystal was found to be  $\approx 12^\circ\text{C}$ . A 10mmx10mm Peltier thermoelectric cooler was attached to a brass crystal mount to ensure the crystal reached the phase-matching temperature, with the Peltier thermoelectric cooler controlled by a Thorlabs temperature control unit (Thorlabs TEC200C). The phase-matching temperature was equivalent to the dew point of the laboratory, so condensation had to be managed by installing a plastic hose directed towards the crystal designed to drift a steady stream of dry Nitrogen gas over and around the crystal, displacing the surrounding water-vapor-carrying air and preventing condensation.

The polarisation-entangled Sagnac source achieved a high heralding efficiency primarily because the collinear quasi-phase-matched PPKTP crystal provided SPDC modes that were approximately Gaussian, allowing efficient coupling into single-mode fiber. At one output (Alice's side), a high-transmission long pass filter (Semrock EdgeBasic,  $> 93\%$  transmission effi-

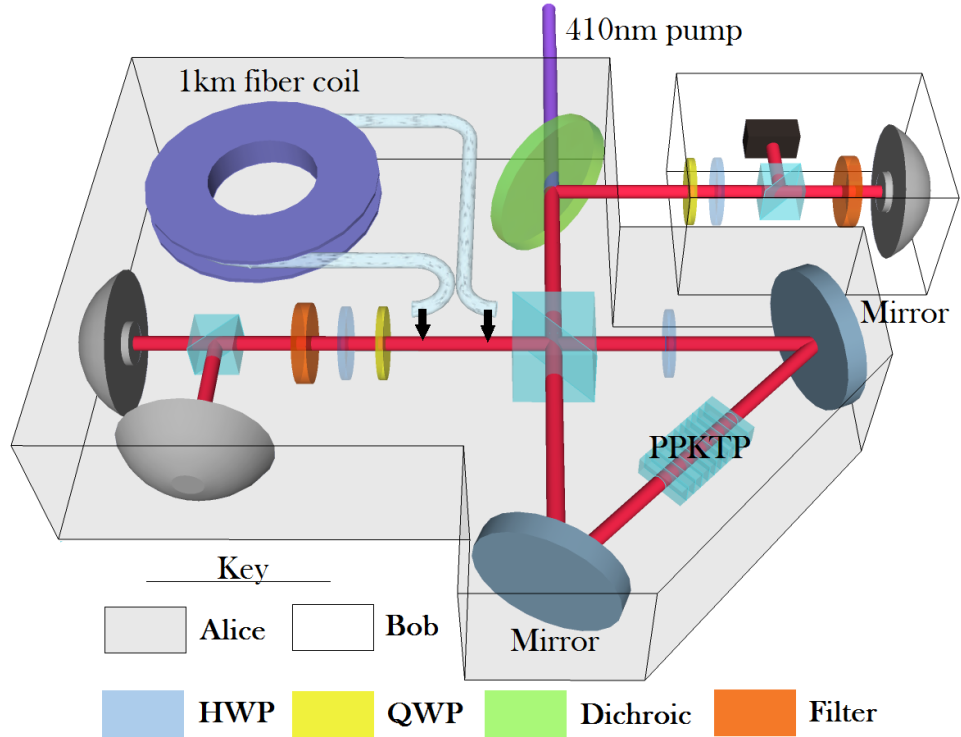


Figure 3.3: Schematic of the experimental apparatus for demonstrating EPR steering with no detection loophole. Bob’s apparatus is contained within the white box, while everything else, including the source, is assumed by Bob to be Alice’s (grey box). A 410nm 3mw CW laser pumps a 10mm long periodically-poled KTP (PPKTP) crystal creating the polarisation-entangled singlet state at 820nm. Measurement settings depend on the orientation of half- and quarter-wave plates (HWP/QWP), mounted in motorised rotation stages, relative to the axes of polarising beam splitters (PBSs, blue cubes). After filtering (Bob: 2nm interference filter, Alice: long pass filter), photons are coupled to single-mode fibers leading to single-photon counting modules and counting electronics. To test the robustness of the loss-tolerant EPR steering protocol, a 1km fiber coil is inserted between Alice’s detection apparatus and the source for the case of  $n = 10$  and  $n = 16$  measurement settings. Because Bob trusts his own apparatus, it is sufficient for him to use only one detector (grey hemisphere), corresponding to one (varied at random) of the two eigenstates of his observable  $\hat{\sigma}_k^B$ .

ciency at 820nm) was installed to maximize her heralding efficiency. At the other output (Bob’s side), a bandpass interference filter (Thorlabs FB820, 820nm centre wavelength, 2nm FWHM) was installed to select frequency-degenerate photon pairs and reject background light. A dichroic mirror (from manufacturer Lastek) separated the down conversion mode from the pump mode in Bob’s output arm. Alice and Bob used quarter and half-wave plates mounted in automated rotation stages (Newport PR50CC) to implement appropriate single-qubit unitary operations, and used PBS cubes (10mmx10mm, Thorlabs PBS102) to perform projective measurements. The central beam splitter in the Sagnac interferometer was a custom PBS cube, anti-reflection coated for wavelengths 410nm and 820nm (also exhibiting extinction ratios  $\approx 1:600$  for both wavelengths), sourced from manufacturer Bernhard Halle Nachfl. GmbH., Germany. The dual-wavelength half-wave plate (acting as a half-wave plate for wavelengths 410nm and 820nm) inside the Sagnac interferometer was a custom item sourced from manufacturer CASIX. Alice and Bob’s outputs were coupled into anti-reflection coated single-mode fibers and connected to Perkin Elmer single photon counting modules (SPCM-AQR-14-FC, quantum efficiency  $\approx 50\%$  at 820nm) and counting electronics. Using an electronic coincidence window of  $\sim 3$  ns, a coincidence count rate of approximately 6000 counts per second was achieved. The measured contribution in the coincidence rate from double-pair SPDC emission events was very small, approximately 0.1 per second. The entangled state emitted by the Sagnac source was tomographically reconstructed to reveal a  $0.992 \pm 0.002$  fidelity with the ideal singlet state [72, 73] (Sec. 2.5.7). From our experimental data we also recorded a maximum heralding efficiency of  $\epsilon = 0.354 \pm 0.001$  (taken from the  $n = 3$  experimental data, see Results and Analysis, below).

For the single photon source used in the separate experimental implementation of Alice’s optimal cheating strategy, Alice’s unentangled single-qubit states were prepared by collecting idler photons from one arm of a polarisation-unentangled angle-phase-matched Type-I SPDC source, with the signal photons acting as a heralding signal. This SPDC source was constructed by experimental collaborator Dylan Saunders, and was pumped by a 60mW 410nm CW laser from Toptica Photonics. Alice’s idler photons were collected into optical fibre and prepared as unentangled single-qubit states using a PBS, QWP and HWP. To implement the cheating strategy, Alice’s qubits were sent to Bob who performed projective measurements using a QWP, HWP, and PBS.

### 3.3.2 Results and Analysis

EPR steering with no detection loophole was experimentally demonstrated using entangled states generated by the Sagnac interferometer. A high quality maximally entangled state was required to observe a high steering parameter  $S_n$ . This was ensured experimentally by generating a state from the entangled Sagnac source having a fidelity of  $0.992 \pm 0.002$  with the ideal singlet state. The  $n = 3, 4, 6, 10$  and  $16$  measurement schemes were implemented using the entangled Sagnac source, and experiments yielded values  $S_n \approx 0.99$  in each case (see Fig. 3.4). This resulted in an absolute ( $n = \infty$ ) lower bound on Alice's required heralding efficiency of  $\epsilon \approx 0.02$ . The source and detector configuration achieved a maximum heralding efficiency of  $\epsilon = 0.354 \pm 0.001$  (as calculated from Bob's statistics in the  $n = 3$  EPR-steering protocol), far above the minimum requirement of  $0.02$ , enabling a demonstration of EPR-steering for  $n = 3$  measurement settings and greater (Fig. 3.4), with no detection loophole.

To test the robustness of the loss-tolerant EPR steering protocol, a 1 km long single-mode fiber at 820 nm (Thorlabs SM800-5.6-125) was introduced between Alice's output of the Sagnac interferometer and her measurement apparatus (see Fig. 3.3). In addition to loss, transmission through the single-mode optical fiber caused polarisation mode dispersion [119] and small polarisation rotations due to imperfectly compensated birefringence<sup>2</sup>, which slightly reduced Bob's observed steering parameter  $S_n$ . The installed fibre introduced an additional 4.3dB of loss, which permitted us to test only the  $n = 10$  and  $n = 16$  loss-tolerant EPR steering inequalities successfully. The tests revealed  $\epsilon = 0.132 \pm 0.001$  for  $n = 10$  measurement settings and  $\epsilon = 0.130 \pm 0.001$  for  $n = 16$  measurement settings. The experimental demonstration with the 1km optical fibre revealed  $S_{10} = 0.985 \pm 0.006$  and  $S_{16} = 0.981 \pm 0.006$  (Fig. 3.4), 2.6 and 5.3 standard deviations above  $C_{10}(\epsilon)$  and  $C_{16}(\epsilon)$  respectively. Based on the intrinsic fiber losses, it was estimated that the EPR-steering task could still be accomplished—with the detection loophole closed, with  $n = 16$  measurement settings and with all other experimental parameters the same – through  $\approx 2$ km of single-mode optical fibre<sup>3</sup>. Thus an honest Alice can convince Bob that they share EPR

---

<sup>2</sup>Polarisation rotations due to fibre birefringence were corrected using fibre-polarisation controllers, however unavoidable temperature fluctuations meant slight drifts in the birefringent properties of the fibre were uncompensated. The fibre-polarisation controllers were adjusted before each data run to minimise such effects.

<sup>3</sup>We couldn't test the loss-tolerance using 2kms of fibre because the fibre wasn't available in the lab at the time.

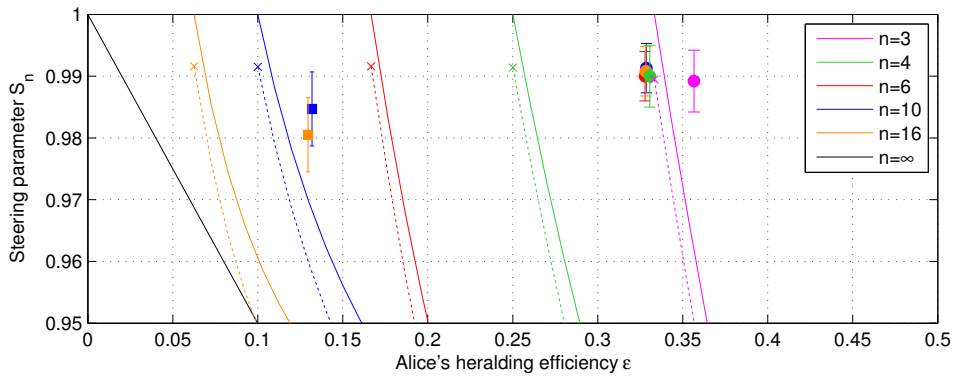


Figure 3.4: Experimental demonstration of EPR steering. A zoomed-in section of Fig. 3.2 (dashed purple box) with experimental data included. The data points show the experimental values for the steering parameter  $S_n$  obtained for  $n = 3, 4, 6, 10$  and  $16$  measurement settings. The  $\bullet$  points represent data straight from the entangled source, prior to the fibre being installed. The  $\blacksquare$  points (for  $n = 10$  and  $16$  only) represent data collected after the single mode fibre was installed, demonstrating loss-tolerant EPR steering with a transmission distance of 1 km. The error bars (one standard deviation) take into account systematic measurement errors and Poissonian photon counting noise (Appendix 2). The  $\times$  points are experimental cheating data (shown in detail in Fig. 3.6), from which we derive our dishonest Alice's closest approach to the theoretical prediction using a cheating strategy (dashed curves).

steerable entangled states with no detection loophole, even in the presence of very significant photon losses.

To ensure the recorded data was unequivocally in violation of the loss-tolerant EPR steering inequalities, the statistical and systematic uncertainties encountered in the protocol were well characterised. The statistical uncertainties resulted from Poissonian photon counting statistics, and the systematic errors resulted from slight experimental differences between Bob’s ideal measurements and his actual measurement settings. Bob’s inability to perform arbitrarily accurate rotations on the Bloch sphere (enacting his measurement choice  $\hat{\sigma}_k^B$ ) were due to: a. imperfect alignment of the optic axis of his wave plates (QWP and HWP) implementing unitaries relative to the projection axis ( $\hat{\sigma}_z$ ) of his PBS; b. the repeatability error in the motorised stages controlling Bob’s unitaries (having an angular setting error of  $\pm 0.02^\circ$ ); and c. wave plate imperfections – wave plate polarisation retardances had a  $\pm \pi/250$  manufacturing tolerance. An in-depth error analysis performed by theory collaborators Cyril Branciard and David Evans, with input from experimental collaborator Dylan Saunders, determined the effects of the encountered statistical and systematic experimental errors (presented in Appendix 2), providing accurate error estimates (shown in Fig. 3.4) towards the loss-tolerant protocol.

The loss-tolerant EPR steering protocol was also tested for the case of a dishonest Alice, where Alice and Bob did not share entanglement (replicating case i., Fig. 2.9). For this demonstration, Alice’s optimal “cheating ensembles”, were tested for correspondence between  $C_n(\epsilon)$  and the maximal correlation  $S_n^{\text{cheat}}$  attainable by a dishonest Alice. The experimental apparatus for demonstrating Alice’s optimal cheating strategy involved using Alice’s unentangled single-qubit state preparation device, which prepared and sent states from Alice’s optimal cheating ensembles to Bob’s single-qubit measurement device, which was identical to that used in the case of the genuine EPR steering experiment. For clarity, it is worth stating that this experimental setup was completely separate from the Sagnac interferometer, and was performed on a separate optical table. Figure 3.5 presents a conceptual illustration of the cheating experiment.

The state preparation stage of the cheating experiment allowed Alice to prepare and send any pure state to Bob. The measurement stage represented Bob’s ability to freely draw measurements from the set  $\{\hat{\sigma}_k^B\}_n$ , with  $n = 3, 4, 6, 10$ , and  $16$ , as in the case of genuine EPR-steering. Additionally,

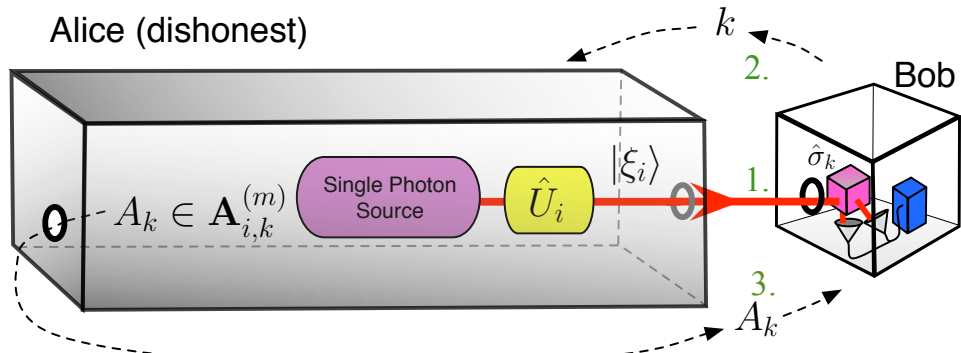


Figure 3.5: Conceptual representation of the EPR steering task for a dishonest Alice, equivalent to case i. in Fig. 2.9. In each round of the protocol, **1.** Bob receives a photonic qubit, **2.** announces a measurement setting,  $k$ , **3.** measures his qubit and records his outcome, and **4.** receives a ‘‘measurement’’ result from Alice. These steps are repeated to gather experimental statistics so that Bob may evaluate the steering parameter  $S_n$ . Bob must assume that Alice controls the source, her line, and her detectors (all enclosed in the grey boxes). In the case of a dishonest Alice, Alice’s optimal ‘‘cheating’’ strategy involves sending a single qubit prepared in a pure state  $|\xi\rangle_i$  (using a single photon with a polarisation state prepared by the corresponding unitary  $\hat{U}_i$ ), chosen from an optimal set. She announces a ‘‘measurement result’’  $A_k$ , or a null result (announces nothing) based on her preparation and Bob’s announced measurement direction. Note that the bounds for demonstrating EPR steering, with no detection loophole, are set precisely to ensure that Alice cannot *actually* cheat – a dishonest Alice will fail to surpass the upper bound of any loss-tolerant EPR steering inequality.

Bob was allowed to implement the  $n = 2$  measurement settings case, which corresponded to a pair of maximally complementary measurement settings. Alice prepared one of the  $p(m)$  states in the optimal deterministic cheating ensemble  $\{|\xi_i^{(m)}\rangle\}_{p(m)}$ , each of which is (theoretically) equally good at enabling Alice to predict Bob's outcome, given that she is obliged to give a non-null result only for  $m$  of Bob's  $n$  settings. As explained above, for a given  $\epsilon$ , Alice's optimal strategy is usually a mixture of two different cheating ensembles ( $m'$  and  $m''$  say), with weights  $w_{m'}$  and  $w_{m''} = 1 - w_{m'}$ . In a noiseless case, Bob's observed  $S_n^{\text{cheat}}$  is therefore predicted to be

$$S_n^{\text{cheat}} = \frac{1}{n} \sum_{k=1}^n \sum_{m=m',m''} w_m \frac{1}{p(m)} \sum_{p(m)} \mathbf{A}_i^{(m)} \langle \xi_i^{(m)} | \hat{\sigma}_k^B | \xi_i^{(m)} \rangle \quad (3.5)$$

$$= C_n(\epsilon). \quad (3.6)$$

Here  $\mathbf{A}_i^{(m)} \in \{+1, 0, -1\}$  (stored as a look-up table, in which a null result is treated as 0) is the optimal announcement for Alice given that she has sent state  $|\xi_i^{(m)}\rangle$  and Bob has announced that he is measuring along an axis on the Poincaré sphere  $\mathbf{u}_k$  corresponding to measurement operator  $\hat{\sigma}_k^B$ .

This technique experimentally demonstrated that Alice could indeed come close to saturating (but not exceeding) the bounds  $C_n(\epsilon)$  (Figs 3.4 and 3.6). The small discrepancies between the measured  $S_n^{\text{cheat}}$  and the theoretical bound  $C_n(\epsilon)$  arose from slightly imperfect state preparation and measurement settings.

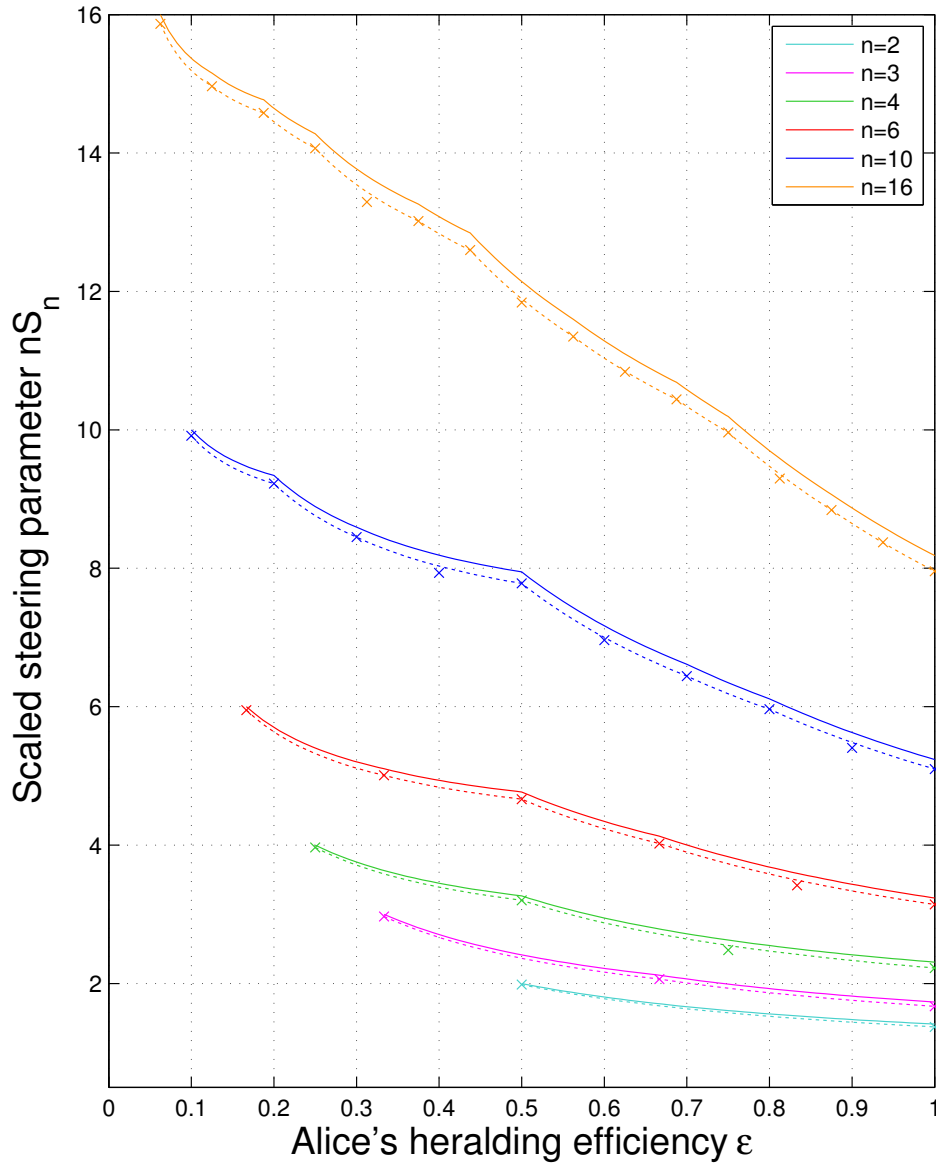


Figure 3.6: Experimental data for a dishonest Alice. The solid curves are the bounds  $C_n(\epsilon)$  on  $S_n$ , for measurement settings  $n = 2, 3, 4, 6, 10$  and  $16$ . The vertical axis shows a scaled version of the steering parameter,  $nS_n$ , purely for clarity when comparing the different bounds. The same-coloured  $\times$ 's correspond to the experimentally observed steering parameter  $S_n^{\text{cheat}}$  obtained by a cheating Alice using a deterministic strategy. The dashed lines, derived from the data points, show the maximum  $S_n^{\text{cheat}}$  a dishonest Alice could achieve by combining two different deterministic strategies to simulate a heralding efficiency  $\epsilon$ . Error bars (resulting from Poissonian counting statistics) are smaller than marker dimensions.

### 3.4 Discussion

This chapter experimentally demonstrates the closure of the detection loop-hole in a photonic quantum correlation experiment using loss-tolerant EPR steering protocols. The loss-tolerant EPR steering protocols presented in this chapter are applicable to arbitrarily-high photon loss, differentiating the protocol presented here [101] from similar works [110, 111]. As an example, the loss-tolerant protocol was used to demonstrate the sharing of EPR steerable states over a 1 km optical fiber, with a heralding efficiency for Alice of  $-8.9\text{dB}$  (13%). A potential improvement to the experiment could be made by increasing the number of shared measurement settings  $n$ , and increasing Alice’s channel and detection efficiency, so that the EPR steering effect could be demonstrated over substantially longer distances. Such changes could be implemented by performing the experiment with downconverted photons at 1550nm, where transmission losses and detector efficiencies are known to be improved.

The transmission of entanglement over long, lossy optical channels is important for real-world applications. For instance, EPR steering finds a natural application in one-sided DI-QKD protocols [55]. In such scenarios, line losses are acceptable to a certain degree if the entangled source lies close to Alice, since Bob can post-select on his (trusted) detection events. However, in instances where Alice is far from the entangled source (or perhaps if she were a mobile field agent and the entangled source were at a base station), then line losses to Alice would be strongly detrimental to standard entanglement certification protocols, making loss-tolerant protocols such as the one introduced here highly favourable. Importantly, in such applied demonstrations, Bob must choose his measurement setting  $\hat{\sigma}_k^B$  independently from one shot to the next (closing the freedom-of-choice loophole). In the proof-in-principle demonstration explored in this chapter, this level of rigour was not imposed. The experiment could therefore be further improved by using quantum random number generators to choose Bob’s measurement settings. In addition, since the experimenters (myself and Dylan Saunders) controlled Alice’s implementation of honest or dishonest strategies (each performed using separate experimental apparatuses), there was no need to force the usual time ordering of events outlined in the EPR steering protocol (Sec. 2.6.4). However, in a field deployment, the protocol demands a strict time ordering of events which could be enforced using an optical delay line for Alice. From a fundamental standpoint, further improvements to the experiment could be offered by adjusting experimental parameters to close the signaling loophole.

Such applied demonstrations closing all experimental loopholes are readily accessible with current technologies [111], and mark an important milestone towards the verification of quantum correlations.

The ability to verify quantum correlations whilst keeping the detection loophole closed in the presence of large losses allows for future demonstrations of long-range transmission of photonic entanglement in a number of scenarios, for instance over long optical fibers, across great free-space expanses [120], or to a satellite [121]. Additionally, loss-tolerant protocols such as the one introduced in this chapter could be used to certify quantum correlations over lossy channels in distributed entanglement protocols, for instance in quantum teleportation [103] or remote quantum computation protocols [122]. Such possibilities allow for tests of Einstein’s “spooky action” over unprecedented distances, and likely find application in perfectly secure cryptographic protocols.

## Chapter 4

# Quantum Refereed EPR Steering

### Statement of work

This chapter presents research towards a measurement–device independent EPR steering protocol. The work presented is based on theoretical investigations undertaken by E. G. Cavalcanti, M. J. W. Hall, H. M. Wiseman, F. Buscemi, N. Brunner, and N. Linden [123–125].

The experiment explores the EPR steering phenomenon in the context of a quantum–refereed ‘game’, whereby a referee–controlled quantum signal lifts the requirement for trust in any party or measurement device involved in the EPR steering protocol. The quantum–refereed EPR steering experiment was undertaken by Sacha Kocsis and myself. I constructed the experiment with input from Dylan Saunders. Sacha and I modified and optimised the experiment, and collected the experimental data. Sacha primarily analysed the experimental data with input from me. The work resulted in a *Nature Communications* publication which all authors contributed to [99].

### 4.1 Introduction

All local models embody, at the very least, the assumptions of local causality. Recently, a link was drawn between the theoretical framework of local models and principles in *Bayesian game theory* [125]. Bayesian game theory concerns decision making between game participants via *payoffs*, where the complete knowledge of the private information held by one participant

remains unknown to the others, and vice versa. The players of a Bayesian game may share some common information obtained from an impartial *referee*, and the players may update their perceived information about one another as the game progresses via *Bayes' rule* [70].

Interestingly, the fact that individual players hold private information that remains unknown to other players coincides precisely with the notion of locality in physics [125]. Secondly, the common advice proffered by the referee does not allow a player to obtain information about the private information of other players; this coincides with the concept of no-signalling in physics [125]. Importantly, players having access to nonlocal resources can outperform players having access to the most general classical resources. It has been shown that a Bayesian game can be reformulated as a Bell test scenario [125], and more generally that ‘semiquantum games’ – meaning games that employ a one-way quantum channel from the referee to the players – may be formulated to test any class of nonlocality [123, 124].

In this chapter, we explore and experimentally demonstrate how a semiquantum game can be theoretically constructed from EPR steering inequalities. We call the game a ‘quantum–refereed EPR steering game’, and we experimentally demonstrate how the game can certify entanglement in a measurement–device independent quantum information sharing protocol (Fig. 4.1). The quantum–refereed EPR steering game introduced in this chapter does not implement Bayesian updating like the original semiquantum games described above, but as a key innovation does similarly employ a quantum referee in control of a one–way quantum channel. The quantum referee in our EPR steering game sends a classical signal to one player, and a quantum signal to the other, thereby transferring the usual assumption of quantum mechanics in an EPR steering protocol from party to referee. This removes the referee’s need to trust remote parties – meaning no assumptions are made about remote parties, their measurement apparatus, or the description of their measurement apparatus (this is *measurement–device independence*). Until now, only an existence proof for such games was known. For the case of entanglement witnesses, a recent measurement–device independent protocol and demonstration has addressed a similar question [126, 127], although EPR steering, Bell nonlocality, and the characterisation of the quantum signals were not considered. The work presented here theoretically and experimentally realises complete measurement–device independence in an EPR steering protocol for the first time.

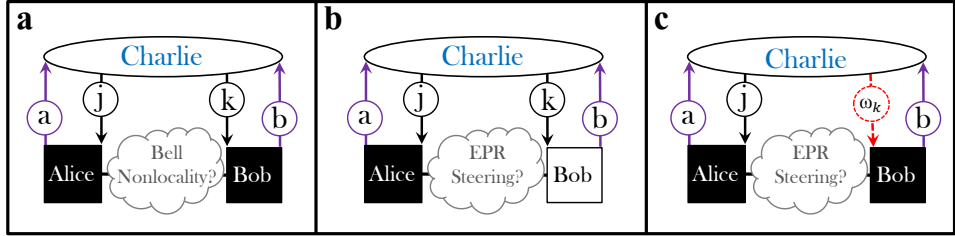


Figure 4.1: Testing nonlocality classes via nonlocal games. **(a)** In ‘nonlocal games’ a referee (Charlie) can verify that Alice and Bob share a Bell-nonlocal resource, by sending classical input signals  $j$  and  $k$ , receiving output signals  $a$  and  $b$ , and checking whether the corresponding correlations violate a Bell inequality. No trust in Alice and Bob or their devices is necessary, as indicated by the black boxes. **(b)** The referee may similarly use an ‘EPR steering game’ to verify the presence of an EPR steering resource, by checking whether the correlations violate a suitable EPR steering inequality. However, all known EPR steering games require the referee to fully trust one of the observers and their devices, as indicated by the transparent box. **(c)** Using the measurement–device–independent protocols of this chapter, the referee can now unconditionally verify EPR steering, by using ‘quantum–refereed EPR steering games’ that replace the need for trust with *quantum* input signals, labelled  $\omega_k$  (defined below).

## 4.2 Formulating the Quantum Refereed EPR Steering game

In alignment with adversarial-type protocols, it can be helpful to introduce a third party into the EPR-steering protocol, called Charlie, who acts as a ‘referee’ for the EPR steering protocol [98]. In the case of the standard EPR steering protocol (Sec. 2.6.4), Charlie is introduced as a referee who must trust Bob, Bob’s apparatus, and Bob’s description of his apparatus (assumed to be a quantum mechanical description), but Charlie makes no claims about Alice. Charlie must also trust that Bob shares no prearranged measurement strategy with Alice. It is then the task of Alice and Bob to convince Charlie that they share a bipartite entangled state (although in the case of Charlie trusting Bob, Charlie and Bob may be collapsed into one, which is why only Alice and Bob are considered initially in Sec. 2.6.4). For additional rigour in the EPR steering protocol, it is useful to consider whether the requirement that Charlie trusts Bob can also be lifted, making Charlie a truly impartial referee. Here, is it shown that Charlie may implement a quantum–refereed EPR steering game, whereby the requirement

for trust in Bob (in all its forms) is indeed lifted. Charlie then need only trust his own ability to prepare and send quantum signals – in our case, polarisation-encoded qubit states – to Bob.

The quantum-refereed EPR steering game is played as follows (Fig. 4.1c). Charlie randomly chooses a pair of numbers  $k = (j, s)$ , where  $j \in \{1, 2, 3\}$  and  $s = \pm 1$ . Charlie sends to Alice a classical signal  $j$ , and sends to Bob a polarisation-encoded qubit  $\omega_k^C$  in the  $s$  eigenstate of the Pauli spin observable  $\hat{\sigma}_j^C$ , where  $j = 1, 2, 3$  label the  $x$ ,  $y$ , and  $z$  Pauli spin matrices (Section 2.5.6), expressed as  $\omega_k^C = \frac{1}{2}(\mathbb{I} + s\hat{\sigma}_j^C)$ . Alice is in possession of an arbitrary measurement device that takes the classical signal  $j$  as an input and outputs  $a = \pm 1$ . Bob possesses an arbitrary measurement device that takes a quantum signal  $\omega_k^C$  as an input, returning  $b = 0$  or  $1$  as an output. Alice and Bob may plan a joint measurement strategy beforehand, although they are restricted from communication during the game (ideally by enforcing space-like separation to close the signalling loophole).

To construct a verifier of EPR steering in our quantum refereed game, we adapt a method recently used by Branciard *et al.* for constructing entanglement verification games [126]. Our quantum-refereed EPR steering game uses a modified  $n = 3$  EPR steering inequality to generate a payoff function [99] (Appendix 3):

$$P(r) = 2 \sum_{j,s} \left[ s \langle ab \rangle_{j,s} - \frac{r}{\sqrt{3}} \langle b \rangle_{j,s} \right], \quad (4.1)$$

which for payoff function values  $P(r) > 0$  will convince Charlie that Alice and Bob share an  $n = 3$  EPR steerable state without making any demands upon their measurement devices or strategies. Here  $r$  is an experimental parameter describing how well Charlie’s states  $\omega_k^C$  can be prepared, with  $r = 1$  being perfect preparation (this parameter discussed in detail below, and in Appendix 3). In particular, the addition of the correlator  $\langle b \rangle_{j,s}$  ensures that the payoff function is positive only when Alice and Bob share an entangled quantum state that is EPR steerable for  $n = 3$  measurement settings.

If Alice and Bob genuinely wish to convince Charlie that they can win the game, then they must exploit a nonlocal resource<sup>1</sup>. A well-known class of nonlocal quantum states appropriate to this task are Werner states (Sec

---

<sup>1</sup>This condition is necessary but not sufficient. As demonstrated here, positivity in the payoff function will only be achieved for a subset of entangled states.

2.2.2). Werner states are expressed generally as

$$W_\mu = \mu |\Psi^-\rangle\langle\Psi^-| - \frac{1-\mu}{4} \mathbb{I} \otimes \mathbb{I}, \quad (4.2)$$

$$= \frac{1+3\mu}{4} |\Psi^-\rangle\langle\Psi^-| + \frac{1-\mu}{4} (\mathbb{I} \otimes \mathbb{I} - |\Psi^-\rangle\langle\Psi^-|), \quad (4.3)$$

$$= \frac{1+3\mu}{4} |\Psi^-\rangle\langle\Psi^-| + \frac{1-\mu}{4} (|\Psi^+\rangle\langle\Psi^+| + |\Phi^-\rangle\langle\Phi^-| + |\Phi^+\rangle\langle\Phi^+|), \quad (4.4)$$

where  $\mathbb{I}$  is the identity matrix. Eq. 4.3 demonstrates how a Werner state can be expressed as a weighted sum of the maximally entangled singlet state coupled with symmetric ‘white’ noise from the identity matrix, with Eq. 4.4 forming an equivalent representation (key to our experimental demonstration, detailed below). Werner states are a well studied class of entangled states, and are known to be entangled for  $\mu > 1/3$  [74]. Additionally, it is known that Werner states cannot violate *any* Bell-type inequality with a parameter  $\mu < 0.6595$  [128], and no explicit Bell-type inequalities are known for the range  $\mu = 0.6595$  to  $\mu = 0.7056$ . A Werner state will violate an explicit Bell-type inequality for  $\mu \geq 0.7056$ , called the Vértesi bound [129], and will violate the CHSH inequality for  $\mu > 1/\sqrt{2} \approx 0.7071$  [39]. Werner states will violate the  $n = 3$  EPR steering inequality  $S_3 \leq C_3$  for  $\mu > 1/\sqrt{3} \approx 0.5774$  [102]. Thus, there is an interesting range between  $\mu = 0.5774$  and  $\mu = 0.7056$  where there exist  $n = 3$  EPR steerable states, and no explicit Bell-type inequalities. In this investigation, we employ our semiquantum game based on an  $n = 3$  EPR steering inequality to demonstrate a successful measurement-device-independent EPR steering game with a Werner state having  $\mu = 0.698$ , i.e. a value in the range  $0.5774 < \mu < 0.7056$ , below both the Vértesi and CHSH bounds.

In addition to sharing an EPR-steerable state, Alice and Bob will only win the game if Bob genuinely performs a joint measurement between his half of the entangled state  $\hat{\rho}_B$  shared with Alice and the qubit state  $\omega_k^C$  sent to him by Charlie. An appropriate joint measurement for our protocol is  $\{|\Psi^-\rangle\langle\Psi^-|, \mathbb{I} - |\Psi^-\rangle\langle\Psi^-|\}$ , conveniently implemented in linear optics using a partial Bell state measurement (BSM) device (Section 2.6.5). Using the partial BSM, Bob performs a joint measurement on his initially separable input state  $\hat{\rho}_B \otimes \omega_k^C$ , returning eigenvalue  $b = 1$  for successful projections onto the singlet subspace  $|\Psi^-\rangle\langle\Psi^-|$ , otherwise returning eigenvalue  $b = 0$  for projections onto the remaining triplet subspace<sup>2</sup>  $\mathbb{I} - |\Psi^-\rangle\langle\Psi^-|$ . If Alice

---

<sup>2</sup>In the original semiquantum game proposed in [124], Bob performed a full Bell state

and Bob share a Werner state in our quantum–refereed EPR steering game, the theoretical value for the payoff function is predicted to be

$$P_\mu(r) = 3\mu - \sqrt{3}r, \quad (4.5)$$

demonstrating that for a Werner state with  $\mu > r/\sqrt{3}$ , Alice and Bob can win the quantum–refereed EPR steering game [99]. Although the quantum–refereed EPR steering game introduced here is tailored for  $n = 3$  EPR steerable Werner states, similar games can be constructed for every state that is EPR steerable [98], allowing for diverse possibilities in measurement–device–independent EPR steering protocols.

### 4.3 Experiment

To implement our quantum–refereed EPR steering game, a source of well calibrated single photon states was required for Charlie to send quantum referee signals to Bob. A source of entangled photon pairs was also required for Alice and Bob to share, and Alice required a single qubit measurement station, with Bob requiring a partial BSM device. A schematic of the experimental apparatus for EPR steering with a quantum referee is depicted in Figure 4.2.

The primary laser system was a *Tsunami* model Titanium Sapphire laser supplied by manufacturer *Spectra-physics*. The laser was a pulsed system operating at 820nm centre wavelength with an 80MHz pulse repetition rate and pulse lengths  $\approx 100$ fs, corresponding to a full width half maximum bandwidth of  $\approx 5.5$ nm. The power in the output beam was  $\approx 1.6$ W at 820nm, and was focussed into a BBO crystal (pump beam diameter  $\approx 60\mu\text{m}$ ) for collinear SHG conversion from 820nm to 410nm at a conversion efficiency of  $\approx 30\%$ . The BBO crystal was 2mm thick and sourced from *Newlight Photonics*. The 820nm beam was separated from the 410nm SHG beam using a pair of dispersion–compensating prisms and four dichroic mirrors, each with  $\approx 98\%$  filtering efficacy in separating 820nm from 410nm. These preliminary systems are not displayed in figure 4.2.

For the quantum refereed EPR steering protocol, the 410nm beam was used to pump a pair of separate type–I down conversion sources each constructed

---

measurement on his combined state. In [126], it was theoretically shown that a simple projection onto a maximally entangled state was enough in their protocol. This is the strategy we employ here: the eigenvalue  $b = 1$  corresponds to projecting Bob’s combined state onto the singlet state, which is the easiest measurement to implement experimentally.

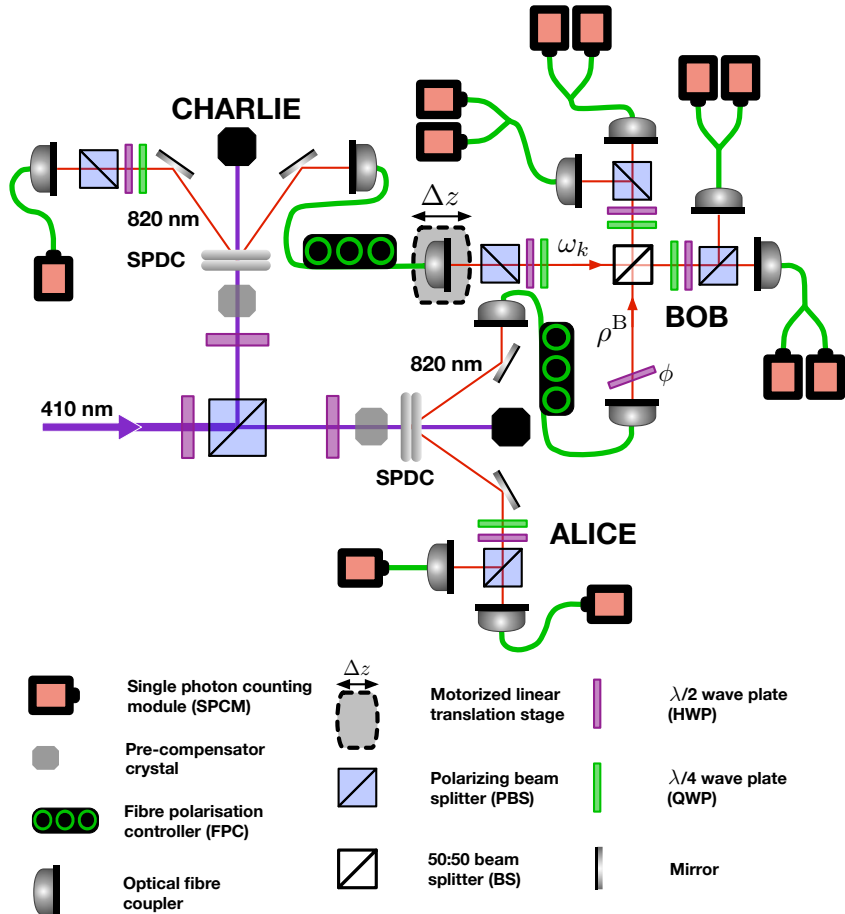


Figure 4.2: Illustration of experimental apparatus for EPR steering with a quantum referee. A pair of separate spontaneous parametric down conversion (SPDC) sources create Alice’s, Bob’s and Charlie’s photons. One photon from Charlie’s source acts as a heralding signal, with the remaining photon prepared in the quantum state  $\omega_k$  and sent via optical fibre to the input of Bob’s partial BSM device, accompanied by a corresponding classical signal  $j \in \{1, 2, 3\}$  sent to Alice. Using a 50:50 beam splitter, Bob combines Charlie’s photon (prepared in state  $\omega_k$ ) with his own photon  $\rho^B$  (comprising half of the entangled state  $\rho^{AB}$  shared with Alice), and projects onto the singlet subspace  $|\Psi_{BC}^-\rangle\langle\Psi_{BC}^-|$ . Alice receives Charlie’s announcement  $j$  accompanied by the other half of the shared entangled state  $\rho^{AB}$ , and measures  $\sigma_j$ . To execute the entanglement verification, Charlie receives Alice’s and Bob’s output signals  $a \in \{\pm 1\}$  and  $b \in \{0, 1\}$ , and computes a payoff function  $P$ , where  $P > 0$  witnesses EPR steering in a measurement-device-independent setting.

of a pair of BiBO crystals in the sandwich configuration [84]. The beam was directed towards each source via a polarising beam splitter. The sources each included a 12.64mm long piece of quartz to pre-compensate for temporal walk-off inside the BiBO crystals [84]. For the experimental demonstration of our quantum-refereed EPR steering game, only one source needed to generate entanglement (the source shared between Alice and Bob), meaning that pre-compensation was necessary for only this single source. However, because the apparatus was used as the framework for several experiments (Chapters 4, 5, and 6), the pre-compensation remained in both sources with no ill effects.

### 4.3.1 Photon Sources

The entangled source shared by Alice and Bob nominally generated the maximally polarisation-entangled state  $|\Psi^+\rangle = 1/\sqrt{2}(|HH\rangle + e^{i\phi}|VV\rangle)$  for a diagonally polarised pump beam, and could be made to generate any of the four Bell states by applying an appropriate unitary operation to Bob's qubit using a fibre polarisation controller and tilted quarter wave plate (tilted about the  $y$  cartesian axis for photon propagation along the  $z$  axis). The quality of the preliminary entangled state shared between Alice and Bob was characterised by making measurements to perform quantum state tomography [72, 73] (Section 2.5.7), with the experimental statistics recorded in coincidences between Alice's and Bob's detectors. The average tangle, fidelity (with the density matrix  $\hat{\sigma}$  of an appropriate Bell state), and purity for all four Bell state preparations was  $T(\hat{\rho}) = 0.909 \pm 0.012$ ,  $F(\hat{\rho}, \hat{\sigma}) = 0.976 \pm 0.003$ , and  $P(\hat{\rho}) = 0.955 \pm 0.005$  (Figure 4.3). The quantum-refereed EPR steering game was initially played for the case where Alice and Bob shared a high quality singlet state (results below), however, our primary goal was to play the quantum-refereed EPR steering game while Alice and Bob shared a Werner state having parameter  $\mu$  in the range  $0.5774 < \mu < 0.7056$ . Thus, symmetric noise had to be added to the entangled state shared between Alice and Bob in order to generate the desired Werner state. Our procedure for introducing this noise made use of the fact that symmetric white noise can be modelled by combining the singlet state in appropriate proportions with the triplet states (Eq. 4.4, discussed below).

The remaining SPDC source was operated by Charlie in an unentangled configuration, enacted by adjusting the pump polarisation to generate separable SPDC pairs from one of the sandwiched crystals. Charlie's quantum signal  $\omega_k^C$  was prepared in the  $s$  eigenstate of the Pauli operator  $\hat{\sigma}_j$  using

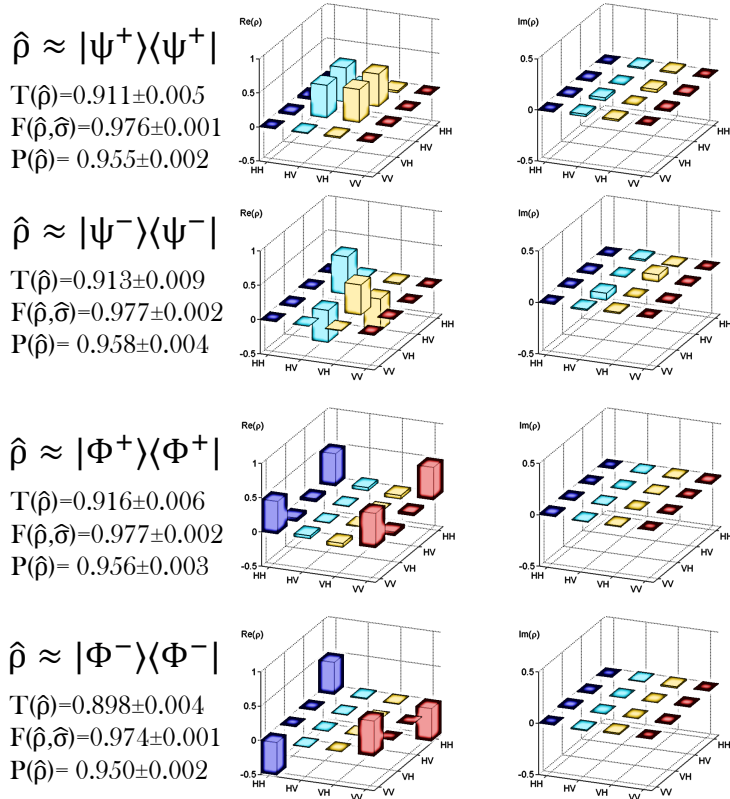


Figure 4.3: Reconstructed density matrices for characterising the entangled source shared between Alice and Bob. The coloured images show the real (left) and imaginary (right) components of the tomographically reconstructed density matrices  $\hat{\rho}$  for the four maximally-entangled Bell states shared between Alice and Bob. The experimentally determined tangle  $T(\hat{\rho})$ , fidelity with the ideal theoretical bell states  $F(\hat{\rho}, \hat{\sigma})$ , and purity  $P(\hat{\rho})$  are given for each state.

half- and quarter-wave plates and a PBS, and sent to Bob’s partial BSM device via optical fibre. Charlie’s remaining photon from the unentangled SPDC source acted as a heralding signal. Charlie’s ability to prepare the six  $s$  eigenstates  $\omega_k^C$  of the Pauli operators was tomographically characterised by monitoring appropriate coincidences between Charlie’s heralding signal and Bob’s detectors, with the half- and quarter-wave plates and PBSs in Bob’s apparatus used to enact the appropriate measurements. The average state preparation fidelity between Charlie’s experimental states  $\omega_k^{C(e)}$  and his ideal referee states  $\omega_k^{C(i)}$  was measured from the tomographic data to be  $F(\omega_k^{C(e)}, \omega_k^{C(i)}) = 0.987 \pm 0.006$ . The experimental parameter  $r \geq 1$  in the payoff function (Eq. 4.1) is a different measure of how well Charlie

can prepare the states  $\omega_k^C$ . The parameter  $r$  was determined by generating Bloch vectors  $\vec{n}^{(k)}$  from Charlie's experimentally characterised states  $\omega_k^{C(e)}$ . The experimentally determined Bloch vectors  $\vec{n}^{(k)}$  were run through a maximisation procedure (comparing the Bloch vectors for Charlie's experimental states  $\omega_k^{C(e)}$  with the Bloch vectors of Charlie's ideal states  $\omega_k^{C(i)}$ ), by theory collaborator Michael Hall, to determine  $r$  (The derivation of  $r$  is nontrivial, and can be found in Ref. [99], and in Appendix 3). This characterisation resulted in  $r \geq 1 = 1.081 \pm 0.009$ , where  $r = 1$  indicates perfect preparation.

### 4.3.2 Partial Bell State Measurement Device

Bob's joint measurement was performed by a linear optical partial BSM device [60] (Section 2.6.5). The partial BSM accurately resolves the Bell states  $|\Psi^-\rangle$  and  $|\Psi^+\rangle$ , with the two remaining Bell states  $|\Phi^-\rangle$  and  $|\Phi^+\rangle$  being combined into a single indistinguishable measurement outcome. Detecting the states  $|\Phi^\pm\rangle$  also required number resolving detection because the signal corresponding to  $|\Phi^\pm\rangle$  consists of two identically polarised photons in the same output mode. We employed 50:50 fibre beam splitters at the outputs of Bob's measurement apparatus to correctly resolve the identically polarised photon pairs corresponding to the  $|\Phi^\pm\rangle$  states 50% of the time, a fact accounted for in data processing.

Bob's joint measurement combined Charlie's state  $\omega_k^C$  with Bob's own qubit state  $\hat{\rho}^B$  on a 50:50 beam splitter, resulting in nonclassical interference (Section 2.5.4). The nonclassical interference was characterised prior to the collection of data for the payoff function by measuring a HOM dip (Sec. 2.5.4) in four-fold coincidences between Alice, Bob, and Charlie's detectors: a signal photon detection event at Alice's detector heralded the presence of an idler photon arriving at Bob's 50:50 beam splitter; similarly another signal photon detection event at Charlie's detector heralded the presence of another idler photon arriving at Bob's 50:50 beam splitter. Bob's  $z$ -translation stage adjusted the relative time of arrival between Bob's separate qubit states, with coincidence electronics recording a HOM dip in four-fold coincidences between Alice and Charlie's single photon detectors (acting as heralding signals), and various pairwise combinations of Bob's single photon detectors. The HOM interference quality was characterised by fitting a Gaussian function to the data set (Figure 4.4). Movement of the  $z$ -translation stage caused slight decoupling of the photon spatial modes with Bob's couplers, resulting in a slight decrease in coincidence count rates as the stage was scanned in the  $z$ -direction. An average coincidence rate outside the inter-

ference window (dotted black line in Fig. 4.4) was introduced to account for this offset, resulting in a calculated HOM interference visibility of  $\approx 89\%$  (courtesy of Sacha Kocsis [130]).

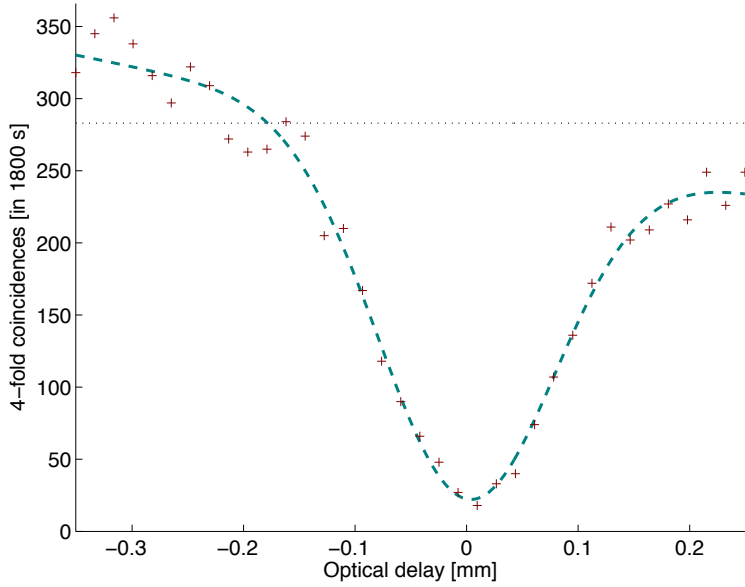


Figure 4.4: Characterising HOM interference for measurement-device-independent EPR steering. The data points were recorded in four-fold coincidences between Alice, Bob, and Charlie’s detectors (collected for 1800s each). The dip appears in four-fold coincidences as one of the degrees of freedom between the initially identical photon pairs is varied as they combine at Bob’s 50:50 beam splitter. In this case, a  $z$ -translation stage on one of Bob’s input couplers adjusts the relative arrival time between photon pairs. Figure courtesy of Sacha Kocsis [130].

### 4.3.3 Results and Analysis

By playing our quantum-refereed EPR steering game, Alice and Bob can convince Charlie that they share an  $n = 3$  EPR steerable state in a measurement-device-independent setting. Data for the semiquantum game was collected for the experiment by recording four-fold coincidences between Alice, Bob, and Charlie’s detectors for each of Charlie’s six quantum referee state preparations  $\omega_k^C$  with Alice always measuring in the  $j$  basis. As a preliminary test, the payoff function was experimentally determined for the case where Alice and Bob shared a state close to the ideal maximally entangled singlet state.

This high-quality experimental singlet state shared by Alice and Bob was tomographically characterised to have  $\approx 98\%$  fidelity with an ideal singlet state (Fig. 4.3). In this case, the experimental payoff function for the singlet state yielded  $P(r) = 1.09 \pm 0.03$  (Figure 4.5). This value approaches the theoretical value of  $P(r) = 3 - \sqrt{3}r \approx 1.13$  for  $\mu = 1$ , and demonstrates EPR steering of a Bell state in a measurement-device independent setting for  $n = 3$  measurement settings.

To demonstrate measurement-device-independent EPR steering with a Werner state having parameter  $\mu$  in the range  $0.5774 < \mu < 0.7056$ , we made use of the fact that a Werner state can be expressed as a weighted mixture of all four maximally entangled Bell states (Eq. 4.4). We therefore collected payoff function data in four stages, where in each stage Alice and Bob shared one of the states  $\{|\Psi^\pm\rangle, |\Phi^\pm\rangle\}$ . In each stage of the data collection, data for the payoff function was collected in small runs, called iterations, which allowed us to add singlet and triplet data together in different proportions when evaluating the payoff function for positivity (below). For Alice and Bob sharing the singlet state, payoff function data was recorded in four-fold coincidences for  $\approx 30$  hours. For Alice and Bob sharing each of the triplet states, payoff function data was recorded in four-fold coincidences for  $\approx 3$  hours each.

Once the payoff function data had been collected, the payoff function was evaluated for the case where Alice and Bob shared a Werner state having  $\mu$  in the range  $0.5774 < \mu < 0.7056$ . This was performed in two stages: first, the payoff function was evaluated for positivity using the recorded payoff function data. Second, the Werner state associated with the positivity was calculated based on the payoff function data proportions used in achieving positivity. The first step, evaluating the payoff function, was performed by incrementally adding four-fold triplet data iterations to the four-fold singlet data iterations and evaluating the payoff function in each case. Positivity was achieved to within error;  $P(r) = 0.050 \pm 0.040$  (the quoted error being the result of propagating Poissonian counting statistics), by combining 12 iterations of triplet data (4,445 four-fold coincidences) with 23 iterations of singlet data (17,789 four-fold coincidences); Fig. 4.5.

The second step, calculating the Werner state associated with this experimental payoff function value, was then performed. This was done by combining the tomographically reconstructed density matrices for the four possible Bell states shared between Alice and Bob (Figure 4.3) in proportions equal

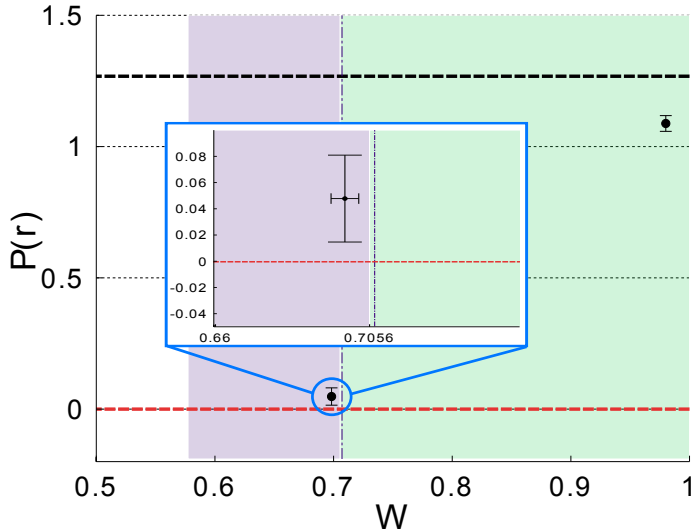


Figure 4.5: Experimental verification of measurement-device independent EPR steering: observed payoff function for Werner and singlet states. The figure shows the measured values of the payoff function  $P(r)$  for  $r = 1.081 \pm 0.009$ , for the cases of (i, blue box) a Werner state with  $W = 0.698 \pm 0.005$ , and (ii, upper right corner) a state with fidelity  $F \approx 0.98$  to the ideal singlet Bell state. The upper dashed horizontal line indicates the maximum possible payoff,  $3 - \sqrt{3}$ , while the lower dashed horizontal line at  $P(r) = 0$  denotes the cutoff value for demonstrating steering. The purple shaded region indicates the range of  $W$  corresponding to steerable Werner states that do not violate any known Bell inequality, and the dot-dashed vertical line corresponds to the minimum value of  $W$  required to violate the standard CHSH Bell inequality. As is most clearly seen in the inset figure, the data point for  $W = 0.698 \pm 0.005$  lies to the left of the values required to violate known Bell inequalities, with  $P(r) > 0$ . Hence EPR steering is verified in a measurement-device-independent setting.

to the relative amount of payoff function data used to calculate the payoff function, to generate an experimentally reconstructed density matrix

$$\hat{\rho}_e = \frac{1+3\mu_e}{4} |\Psi^-\rangle\langle\Psi^-|_e + \frac{1-\mu_e}{4} (|\Psi^+\rangle\langle\Psi^+|_e + |\Phi^-\rangle\langle\Phi^-|_e + |\Phi^+\rangle\langle\Phi^+|_e) . \quad (4.6)$$

Based on the data proportions, a composite density matrix  $\hat{\rho}_e$  was generated, having  $\approx 80\%$  contribution from the singlet state, corresponding to a Werner state with  $\mu_e \approx 0.73$ . This value of  $\mu$  was then used as an initial search

point for a maximum-likelihood Monte Carlo optimisation script (written by Sacha Kocsis). In each iteration of the script, the composite density matrix had Poissonian noise added to generate slightly different experimental states  $\{|\Psi^\pm\rangle_e, |\Phi^\pm\rangle_e\}$ . At the same time, the experimental parameter  $\mu_e$  was varied as the total counts in the singlet and triplet contributions were varied within Poissonian uncertainty. In each iteration, an ideal Werner state of the form

$$W_\mu = \frac{1+3\mu}{4}|\Psi^-\rangle\langle\Psi^-| + \frac{1-\mu}{4}(|\Psi^+\rangle\langle\Psi^+| + |\Phi^-\rangle\langle\Phi^-| + |\Phi^+\rangle\langle\Phi^+|) \quad (4.7)$$

was fitted to the experimental Werner state  $\hat{\rho}_e$ , by varying the parameter  $\mu$  in 4.7 to maximise the fidelity between the ideal and experimental Werner state:

$$F(\hat{\rho}_e, W_\mu) = \text{Tr} \left( \sqrt{W_\mu^{1/2} \hat{\rho}_e W_\mu^{1/2}} \right)^2. \quad (4.8)$$

After each iteration, the fitted Werner parameter  $\mu$  and the fidelity  $F(\hat{\rho}_e, W_\mu)$  were recorded. At the end of the 200 iterations, the average fitted Werner parameter and fidelity were calculated, as were their standard deviations. The optimisation revealed that our experimental Werner state  $\hat{\rho}_e$  with parameter  $\mu_e = 0.698 \pm 0.004$  had an average maximum fidelity of 97.6% with an ideal Werner state  $W_\mu$  having parameter  $\mu = 0.698$ .

The theoretical prediction for the payoff function  $P(r)$  with parameter  $r \approx 1.08$  and a Werner state having parameter  $\mu_e \approx 0.698$  is  $P(r) \approx 0.222$ . This value was much larger than the experimentally determined value  $P(r) = 0.050 \pm 0.040$ . This discrepancy was attributed to imperfections in the optimised experimental Werner state  $\hat{\rho}_e$ , where the experimental density matrix is given by

$$\hat{\rho}_e = \begin{pmatrix} 0.0736 & 0.0036 + 0.0012i & -0.0123 + 0.0048i & -0.0089 + 0.0011i \\ 0.0036 - 0.0012i & 0.4495 & -0.3094 + 0.1281i & -0.0048 - 0.0029i \\ -0.0123 - 0.0048i & -0.3094 - 0.1281i & 0.3975 & 0.0086 + 0.0027i \\ -0.0089 - 0.0011i & -0.0048 + 0.0029i & 0.0086 - 0.0027i & 0.0793 \end{pmatrix}. \quad (4.9)$$

Comparing the experimental density matrix  $\hat{\rho}_e$  with the ideal density matrix for a Werner state  $W_\mu$  having  $\mu = 0.698$ :

$$\hat{\rho}_e = \begin{pmatrix} 0.0754 & 0 & 0 & 0 \\ 0 & 0.4246 & -0.3491 & 0 \\ 0 & -0.3491 & 0.4246 & 0 \\ 0 & 0 & 0 & 0.0754 \end{pmatrix}, \quad (4.10)$$

it is evident that the experimental state had imperfections, including an undesired population imbalance and an undesired phase shift between HV and VH logical states. Modelling of the imperfect HOM visibility coupled with the effects of the imperfect experimental Werner state (conducted by my supervisor Geoff Pryde and theory collaborator Michael Hall) accounted for the imperfection to within experimental error, predicting a theoretical payoff function of  $P(r) = 0.067$ .

## 4.4 Discussion

This chapter experimentally demonstrates the first violation of an  $n = 3$  EPR steering inequality via a quantum–refereed EPR steering game when neither party can be trusted. Traditionally, the referee Charlie requires trust in Bob, Bob’s apparatus, and the description of Bob’s apparatus, in order to witness EPR steering. By using a quantum referee, the requirement for trust in Bob is lifted, as is the possibility for false entanglement certification via pre–arranged measurement strategies between Alice and Bob.

The experimental demonstration yielded a payoff function value  $P(r) = 0.050 \pm 0.040$  for  $r = 1.081 \pm 0.009$ ; just positive within error. The payoff function could be more strongly positive for better calibration of the quantum referee’s (Charlie’s) state by making  $r$  closer to unity and reducing uncertainty in  $r$ . The discrepancy between the observed  $P(r) = 0.050 \pm 0.040$  and the theoretical prediction  $P(r) \approx 0.222$  was first assumed to be from imperfect HOM visibility in Bob’s BSM. However, modelling by my supervisor Geoff Pryde and theory collaborator Michael Hall demonstrated that the imperfect HOM visibility could not fully explain the discrepancy. By investigating the experimentally reconstructed density matrix  $\hat{\rho}_e$ , it was determined that the undesired phase shift between the H/V and V/H logical basis had a stronger contribution towards reducing the observed  $P(r)$  than the effects of imperfect HOM visibility. To observe stronger positivity, the state population imbalances (likely resulting from count rate asymmetries when collecting data for the states  $\{|\Psi^\pm\rangle, |\Phi^\pm\rangle\}$  shared between Alice and Bob) could be more closely monitored and controlled. By introducing these ammendments, it is expected that the quantum–refereed EPR steering game

could be played for stronger positivity in the payoff function, and additionally for a case where Alice and Bob share a Werner state having  $\mu$  in the range  $0.5774 < \mu < 0.6595$  – a region where it is known for sure that Werner states cannot violate a Bell inequality.

EPR steering may be applicable to one-sided device-independent quantum key distribution protocols [55], an asymmetric variant of device-independent protocols. Fully device-independent protocols via Bell inequality violations demand strict requirements on overall detection efficiencies [109, 131], whereas EPR steering protocols have fewer technological limitations [101, 110, 111] at the expense of requiring trust in parties and measurement devices. By introducing a quantum referee, an EPR steering inequality can be tested in the form of a quantum-refereed EPR steering game, which removes the need for trust in parties and measurement devices. The quantum-refereed EPR steering game introduced in this chapter could be performed for space-like separated parties, random preparations/measurements and high detection efficiencies to close all experimental loopholes, with such a demonstration benefiting the development of measurement-device-independent quantum key distribution protocols. Theoretical investigations are indeed exploring the connection between EPR steering and quantum-refereed measurement-device-independent quantum key distribution protocols. The work presented in this chapter is therefore an important addition to the array of techniques for securing the distribution of quantum information in different scenarios.

## Chapter 5

# Locality and Bi-locality

### Statement of work

This chapter presents experimental research for the verification of nonlocal correlations between particles with no common history. The experimental demonstration tests nonlinear Bell-like inequalities (introduced as ‘bilocal inequalities’) between particles generated in an entanglement swapping protocol. The theoretical investigations that formed a background for this work were undertaken by C. Branciard, D. Rosset, N. Gisin, and S. Pironio [66,67].

The experiment was conducted by Dylan Saunders and myself. I constructed the experiment with Dylan Saunders. Dylan and I optimised the experiment and collected the experimental data. Dylan primarily analysed the experimental data with secondary input from myself and our supervisor Geoff Pryde. A manuscript detailing the experimental findings is in preparation.

### 5.1 Introduction

Advanced quantum information protocols will utilise quantum teleportation, quantum repeater, and quantum network architectures that make use of particles originating from independent sources, potentially in different parts of the world. Spatially displaced protocols such as these rely on the unambiguous generation of nonclassical correlations amongst particles with no common history. Nonclassical correlations between particles with no common history are often certified via constraints on local models that assume particles *do share* a common history (for example, in Bell tests – Sec. 2.6). It is therefore instructive to consider what may happen to the constraints

on local models if a different assumption is made, for instance, one that is in alignment with the physical distinctness of particle sources used in such protocols.

In linear optics, nonclassical correlations between particles with no common history are most simply generated in entanglement swapping scenarios (Sec. 2.6.5, Refs. [60–64]). A characteristic feature of entanglement swapping is the presence of two physically distinct particle sources, where each source emits a pair of (in principle) maximally polarisation–entangled photons. In an entanglement swapping scenario, one party (called Bob) receives one half of an entangled state from each source and performs a joint Bell state measurement (BSM, Sec. 2.6.5) on his two photons (Fig. 5.1). The remaining photons, one from each source, are sent to projective measurement stages controlled by Alice and Charlie whom can perform measurements to verify the nonclassical correlations generated between their particles. Importantly, the particles received by Alice and Charlie need share no common history in the presence of such strong correlations – a paradoxical feature of the entanglement swapping scenario.

A well-known test for certifying the presence of strong nonclassical correlations is the Bell test, derived from Bell’s theorem. The Bell test can be successfully performed between entangled particles generated in entanglement swapping scenarios. However, the theoretical framework of Bell’s theorem employs only a single local hidden variable  $\lambda$ , assumed to influence the sole particle source. This is clearly inconsistent with the case of entanglement swapping; there are *two* independent particle sources. Because the pair of particle sources used in entanglement swapping are physically distinct and can therefore be assumed independent, it seems natural that this independence might carry over to a local model. Recent theoretical investigations by Branciard *et al.* [66, 67] explored this possibility by introducing a new theoretical framework whereby a *pair* of independent local hidden variables (LHVs)  $\lambda_1$  and  $\lambda_2$  influence independent sources of correlated particles, eliciting the description ‘bilocal model’ (Fig. 5.2). The crucial assumption of the bilocal model is the independence of LHVs  $\lambda_1$  and  $\lambda_2$ , reflecting the fact that separate parts of the world can be considered independently of one another. If such an assumption were false, then powerful implications would follow, as mentioned by John Bell [106, 132], who stated: “This way of arranging quantum mechanical correlations would be even more mind-boggling than one in which causal chains go faster than light. Apparently separate parts of the world would be deeply and conspiratorially entangled.”

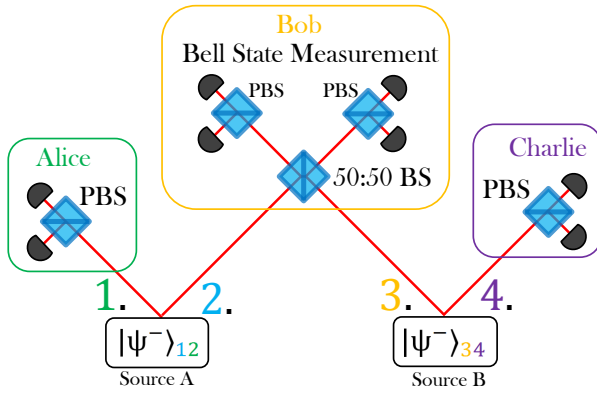


Figure 5.1: The entanglement swapping scenario implemented in linear optics. Spontaneous parametric downconversion sources A and B emit (in principle) maximally polarisation–entangled photon pairs in the states  $|\Psi^-\rangle_{12}$  and  $|\Psi^-\rangle_{34}$ . Bob enacts entanglement swapping using his Bell state measurement (BSM) device by projecting photons in modes 2 and 3 onto one of the four maximally entangled Bell states (for an ideal BSM). Correlations measured by Alice and Bob between photons in modes 1 and 4 can be strongly nonclassical, conditioned upon Bob’s successful Bell state detections. The strong correlations observed between Alice and Charlie’s measurement outcomes signifies the swapping of entanglement from initial mode pairs 1,2 and 3,4 to modes 1 and 4, correlating particles with no common history.

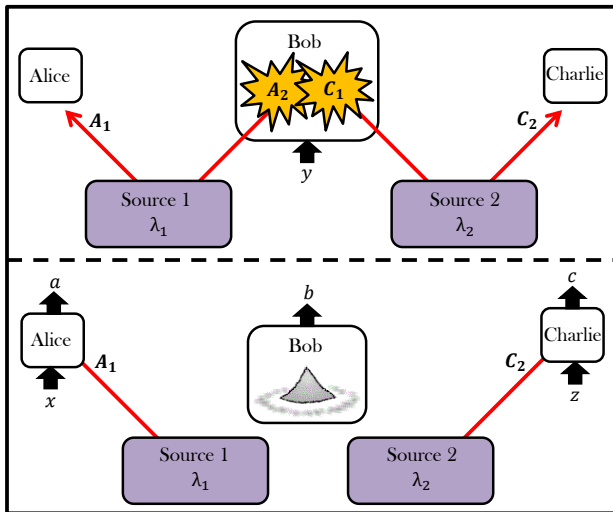


Figure 5.2: Illustration of an entanglement swapping scenario described by a bilocal model. Sources 1 and 2 are each assigned independent local hidden variables  $\lambda_1$  and  $\lambda_2$ , mirroring the physical independence of sources 1 and 2. In the top panel, Bob receives one particle from each source, labelled  $A_2$  and  $C_1$ , and performs a joint measurement  $y$  upon them. In the bottom panel, Bob receives a measurement outcome  $b$  (where the measurement has destroyed the initial particle pair), and Alice and Charlie perform respective measurements  $x$  and  $z$  on the remaining particles  $A_1$  and  $C_2$ . Repeating the complete task a number of times reveals a probability distribution  $P(a, b, c|x, y, z)$ .

Bell's quote implies that the assumption of source independence used in the bilocal model is a natural and intuitive one.

This chapter introduces the bilocal framework derived by Branciard *et al.*, and details experimental tests of constraints on bilocal models (called bilocal inequalities). The experimental investigations utilise a photonic entanglement swapping scenario to test bilocal inequalities using entangled photon pairs, finding inequality violations in agreement with quantum mechanical predictions. In the experimental demonstration, the assumption of source independence is strengthened by erasing coherences between the pump beams of each source. The new bilocal models allow for tests of nonclassicality (or *quantumness*) for entangled state visibilities as low as  $v = 0.50$ , below the  $v \approx 0.71$  required for tests of Bell's inequality. Here, the entangled state visibility  $v$  equates directly with the parameter  $\mu$  of a Werner state, Eq. 2.17.

## 5.2 The Bilocal model

The bilocal model is derived by first considering the local model associated with Bell's theorem, followed by the introduction of modifications appropriate to the entanglement swapping architecture. The complete construction of the bilocal models and associated constraints is lengthy and can be found in Refs. [66, 67], with a concise overview presented here.

In Bell's local realistic model, pairs of particles from a common source are expected to exhibit correlations in accordance with the probability distribution [66, 106]

$$P(a, b|x, y) = \int d\lambda \rho(\lambda) P(a|x, \lambda) P(b|y, \lambda), \quad (5.1)$$

where  $a$  and  $b$  are measurement outcomes for Alice and Bob given measurement inputs  $x$  and  $y$ , and  $\lambda$  is a local hidden variable obeying  $\int_{\lambda} d\lambda \rho(\lambda) = 1$ . Section 2.6 demonstrates why the discovery of quantum correlations in violation of the above probability distribution is a surprising feature of nature. More surprising still are the existence of nonclassical correlations arising between particles with no common history, as is the case in an entanglement swapping scenario. An entanglement swapping scenario involves three parties: Alice, Bob, and Charlie, who each have measurement devices with settings  $x, y$ , and  $z$  yielding measurement outcomes  $a, b$ , and  $c$  respectively. In the entanglement swapping scenario, Bob's measurement is performed by a joint BSM device. Under the assumptions of Bell's theorem, the parties observe a tripartite probability distribution

$$P(a, b, c|x, y, z) = \int d\lambda \rho(\lambda) P(a|x, \lambda) P(b|y, \lambda) P(c|z, \lambda) \quad (5.2)$$

where the variable  $\lambda$  with distribution  $\rho(\lambda)$  describes the joint state of the three systems according to the local model. In the entanglement swapping scenario, however, there are two sources, labelled here as  $S_1$  and  $S_2$ . Therefore, a pair of LHV's can be introduced, with one assigned to each source (Fig. 5.2). As such, it is convenient to express 5.2 using a pair of LHV's, labelled  $\lambda_1$  and  $\lambda_2$ . For now, the LHV's may be considered equivalent ( $\lambda_1 = \lambda_2 = \lambda$  [67]), so that the probability distribution Eq. 5.2 can be re-expressed as

$$P(a, b, c|x, y, z) = \int d\lambda_1 d\lambda_2 \rho(\lambda_1, \lambda_2) P(a|x, \lambda_1) P(b|y, \lambda_1, \lambda_2) P(c|z, \lambda_2), \quad (5.3)$$

where now Alice's local distribution  $P(a|x, \lambda_1)$  depends on  $\lambda_1$ , Charlie's local distribution  $P(c|z, \lambda_2)$  depends on  $\lambda_2$ , and Bob's local distribution  $P(b|y, \lambda_1, \lambda_2)$  depends on  $\lambda_1$  and  $\lambda_2$ .

A crucial assumption can now be made to distinguish Eq. 5.2 from 5.3: namely, that the sources  $S_1$  and  $S_2$  are *independent and uncorrelated*, a property that carries over to the LHV $s \lambda_1$  and  $\lambda_2$ . In this case, the joint distribution  $\rho(\lambda_1, \lambda_2)$  should factorise:

$$\rho(\lambda_1, \lambda_2) = \rho(\lambda_1) \rho(\lambda_2). \quad (5.4)$$

This allows for cases where  $\lambda_1 \neq \lambda_2$ . Local models satifying this so-called *independence assumption* are called bilocal models.

### 5.3 Bilocal Inequalites

By considering constraints of a bilocal model for a particular correlation function, bilocal inequalities are derived, and it is these inequalities that are tested experimentally in this chapter. Branciard *et al.* derived bilocal inequalities from the bilocal model in a tripartite framework. To do so, it was noted that the bilocal distribution in Eq. 5.3 can be taken to be deterministic without loss of generality [133], so that a hidden variable  $\lambda$  conveys a deterministic measurement outcome  $a$  given measurement  $x$ , and similarly for the pairs  $b, y$  and  $c, z$ . Branciard *et al.* express the deterministic strategy for Alice as  $\tilde{\alpha} = \alpha_1, \dots, \alpha_n$ , representing a vector of deterministic outcomes  $\alpha_x \in \{0, 1\}$  for each of Alice's  $n$  set of inputs  $x$ . Similar strategies  $\tilde{\beta}$  and  $\tilde{\gamma}$  are defined for Bob and Charlie respectively, allowing the tripartite probability distribution Eq. 5.2 to be rewritten as a convex sum over deterministic strategies

$$P(a, b, c|x, y, z) = \sum_{\tilde{\alpha}, \tilde{\beta}, \tilde{\gamma}} q_{\tilde{\alpha}, \tilde{\beta}, \tilde{\gamma}} P_{\tilde{\alpha}}(a|x) P_{\tilde{\beta}}(b|y) P_{\tilde{\gamma}}(c|z), \quad (5.5)$$

where  $q_{\tilde{\alpha}, \tilde{\beta}, \tilde{\gamma}} = \int_{\Lambda_{\tilde{\alpha}, \tilde{\beta}, \tilde{\gamma}}^{12}} d\lambda_1 d\lambda_2 \rho(\lambda_1, \lambda_2) \geq 0$  and  $\sum_{\tilde{\alpha}, \tilde{\beta}, \tilde{\gamma}} q_{\tilde{\alpha}, \tilde{\beta}, \tilde{\gamma}} = 1$ . Here,  $\Lambda_{\tilde{\alpha}, \tilde{\beta}, \tilde{\gamma}}^{12}$  is the set of pairs  $\lambda_1, \lambda_2$  specifying the strategies  $\tilde{\alpha}$ ,  $\tilde{\beta}$ , and  $\tilde{\gamma}$  (interpreted as the portion of LHV space compatible with these particular outcomes). The weights  $q_{\tilde{\alpha}, \tilde{\beta}, \tilde{\gamma}}$  can be understood as the probabilities assigned by the source to the deterministic strategies  $\tilde{\alpha}$ ,  $\tilde{\beta}$ , and  $\tilde{\gamma}$ , and must sum to one (hence the normalisation condition). The source independence assumption is introduced by expressing the joint convex distribution  $q_{\tilde{\alpha}, \tilde{\beta}, \tilde{\gamma}}$  as products of  $q_{\tilde{\alpha}}$  and  $q_{\tilde{\gamma}}$ , using

$$q_{\tilde{\alpha},\tilde{\gamma}} = \sum_{\tilde{\beta}} q_{\tilde{\alpha},\tilde{\beta},\tilde{\gamma}}, \quad (5.6)$$

$$q_{\tilde{\alpha}} = \sum_{\tilde{\gamma}} q_{\tilde{\alpha},\tilde{\gamma}}, \quad (5.7)$$

$$\text{and } q_{\tilde{\gamma}} = \sum_{\tilde{\alpha}} q_{\tilde{\alpha},\tilde{\gamma}}, \quad (5.8)$$

to give

$$q_{\tilde{\alpha},\tilde{\gamma}} = q_{\tilde{\alpha}} q_{\tilde{\gamma}} \quad \forall \tilde{\alpha}, \tilde{\gamma}. \quad (5.9)$$

This is equivalent to the independence assumption in Eq. 5.4. Expressing the bilocal model in this compact way allowed a set of correlators, related to the weights  $q_{\tilde{\alpha},\tilde{\beta},\tilde{\gamma}}$ , to be defined and allowed for a numerical optimisation over all deterministic strategies, resulting in bilocal inequalities satisfying the independence assumption. The correlator notation used by Branciard *et al.* is not covered here, with only their main results to follow.

Importantly, the correlators introduced by Branciard *et al.* can be experimentally determined, and in particular depend on the type of joint measurement Bob implements. The two types of joint measurements for Bob considered in this chapter are an ideal BSM and a partial BSM (Sec. 2.6.5). Because the bilocal inequalities are derived from the correlators (shown in the next section), different inequalities result depending on the type of measurement Bob implements. What follows is the introduction of two bilocal inequalities: the first inequality introduced is for the case when Bob implements an (in principle) ideal BSM, and the second is for the case when Bob implements a partial BSM.

### 5.3.1 Bilocal Inequality for Ideal Bell–State Measurement

An ideal BSM device is a one–input, four–output measurement device (expressed as “14” for simplicity), having one measurement input  $y$  (“perform BSM”) and four measurement outputs  $b$  corresponding to projections onto the  $|\Psi^-\rangle$ ,  $|\Psi^+\rangle$ ,  $|\Phi^-\rangle$ , and  $|\Phi^+\rangle$  Bell states (Sec. 2.6.5). Unfortunately, an ideal BSM device cannot be realised in practice using linear optics [105]. However, an ideal BSM device can be experimentally *simulated* using linear optics by treating it as a four–input, one–output measurement device. The simulation is performed by first noting that a linear optics partial BSM device can be used to make a projective measurement

$\{|\Psi^-\rangle\langle\Psi^-|, \mathbb{I} - |\Psi^-\rangle\langle\Psi^-|\}$ . Second, it is noted that performing a local unitary on one of the input qubits allows the device to perform the following projections:  $\{|\Psi^+\rangle\langle\Psi^+|, \mathbb{I} - |\Psi^+\rangle\langle\Psi^+|\}$  for unitary  $\hat{\sigma}_z$ ,  $\{|\Phi^-\rangle\langle\Phi^-|, \mathbb{I} - |\Phi^-\rangle\langle\Phi^-|\}$  for unitary  $\hat{\sigma}_x$ , and  $\{|\Phi^+\rangle\langle\Phi^+|, \mathbb{I} - |\Phi^+\rangle\langle\Phi^+|\}$  for unitary  $\hat{\sigma}_x\hat{\sigma}_z$ . Therefore, by performing appropriate unitaries on the input qubits and using the partial BSM device to perform each of the four projective measurements, experimental statistics from each case can be aggregated into a single data set that simulates the behaviour of an ideal  $14$  BSM device. In this way, a bilocal inequality for a  $14$  measurement device can be experimentally tested. The experimental details of how the ideal BSM was simulated are covered in Sec. 5.4.3.

To derive the  $14$ -bilocal inequality, Alice is allowed a pair of measurements  $x \in \{0, 1\}$  with outputs  $a \in \{0, 1\}$ , Charlie is similarly given a pair of measurements  $z \in \{0, 1\}$  with outputs  $c \in \{0, 1\}$ , and Bob is allowed to perform an ideal joint BSM with single input  $y$  and output  $b = b^0b^1$  with  $b^0, b^1 \in \{0, 1\}$ . Bob's two-bit outcome  $00, 01, 10$ , and  $11$  corresponds, respectively, to projections onto the states  $|\Psi^+\rangle, |\Psi^-\rangle, |\Phi^+\rangle$ , and  $|\Phi^-\rangle$ .

Bilocal inequalities of the form

$$\sqrt{|I^{14}|} + \sqrt{|J^{14}|} \leq 1, \quad (5.10)$$

are introduced by Branciard *et al.*, where  $I^{14}$  and  $J^{14}$  are linear combinations of the probability distribution  $P(a, b, c|x, y, z)$  (Eq. 5.10, and evaluated below), and the  $14$  superscript references the one-input, four-output measurement nominally performed by Bob. To bound the bilocal inequalities presented herein, Branciard *et al.* studied the mathematical constraints on Eq. 5.5 using arguments from set theory and the conditions imposed by Eqs. 5.8 and 5.9. The proof is lengthy, and can be found in Ref. [67]. Importantly, the  $14$ -bilocal inequality can be violated for quantum states generated in entanglement swapping having an entangled state visibility  $v > 0.5$ ; a visibility bound that is more relaxed than the bound for a traditional Bell test, requiring entangled state visibilities  $v > 0.707$ .

Because this chapter is concerned with the experimental violation of bilocal inequalities, the scheme yielding a maximum quantum violation is of interest. The maximum quantum violation of the  $14$ -bilocal inequality occurs when Alice and Charlie implement the same measurements, these being  $\hat{A}_0 = \hat{C}_0 = \frac{1}{\sqrt{2}}(\hat{\sigma}_z + \hat{\sigma}_x)$  and  $\hat{A}_1 = \hat{C}_1 = \frac{1}{\sqrt{2}}(\hat{\sigma}_z - \hat{\sigma}_x)$ . The probability distri-

bution for Alice's and Charlie's measurements, with Bob implementing his ideal BSM is predicted by quantum mechanics to be

$$P_Q^{14}(a, b^0 b^1, c|x, z) = \frac{1}{16} \left[ 1 + (-1)^{a+c} \frac{(-1)^{b^0} + (-1)^{x+z+b^1}}{2} \right], \quad (5.11)$$

where  $y$  has been omitted because Bob nominally has only one measurement input setting, and the values  $a, b^0, b^1, c, x$ , and  $z$  take the values of Alice, Bob, and Charlie's input/output binaries. The 14–bilocal inequality parameters  $I^{14}$  and  $J^{14}$  are related to the probability distribution  $P_Q^{14}(a, b^0 b^1, c|x, z)$  by the correlators

$$\langle A_x B^j C_z \rangle_{P_Q^{14}} = \sum_{a, b^0 b^1, c} (-1)^{a+b^j+c} P_Q^{14}(a, b^0 b^1, c|x, z), \quad (5.12)$$

$$I^{14} = \frac{1}{4} \sum_{x, z} \langle A_x B^0 C_z \rangle_{P_Q^{14}}, \quad (5.13)$$

$$J^{14} = \frac{1}{4} \sum_{x, z} (-1)^{x+z} \langle A_x B^1 C_z \rangle_{P_Q^{14}}, \quad (5.14)$$

where the  $j$  in  $B^j$  denotes whether  $b^0$  or  $b^1$  are used in the right hand side of Eq. 5.12 ( $b^0$  for  $j = 0$ , and  $b^1$  for  $j = 1$ ). The quantum prediction therefore yields  $I^{14} = J^{14} = 1/2$  for the specified arrangement of measurements, yielding  $\sqrt{|I^{14}|} + \sqrt{|J^{14}|} \approx 1.41$ , in direct violation of the 14–bilocal inequality (Eq. 5.10). The correlators  $\langle A_x B^j C_z \rangle_{P_Q^{14}}$  can be experimentally determined from the observed probability distributions  $P(a, b, c|x, y, z)$ . A photonic experiment executing Alice and Charlie's measurements and simulating Bob's ideal BSM device can therefore expect to observe an experimental violation of the 14–bilocality inequality.

### 5.3.2 Bilocal Inequality for Partial BSM

A bilocal inequality is also introduced for the case where Bob implements a partial BSM upon his pair of photons. The partial BSM device accurately resolves the Bell states  $|\Psi^-\rangle$  and  $|\Psi^+\rangle$ , with the two remaining Bell states  $|\Phi^\pm\rangle$  being combined into a single indistinguishable measurement outcome. Therefore, the partial BSM is a one–input, three–output device (“13” for short), and can be implemented in linear optics [60]. To derive a 13–bilocal inequality, Alice once again has a pair of measurements  $x \in \{0, 1\}$  with outputs  $a \in \{0, 1\}$ , as does Charlie:  $z \in \{0, 1\}$  with outputs  $c \in \{0, 1\}$ .

Bob implements a partial BSM having a single input setting  $y$ , with outputs  $b = 00, 01$ , and  $\{10 \text{ or } 11\}$  corresponding to projections onto the states  $|\Psi^+\rangle, |\Psi^-\rangle$ , and  $|\Phi^\pm\rangle$  respectively.

The bilocal inequality for Bob's partial BSM is [67]

$$\sqrt{|I^{13}|} + \sqrt{|J^{13}|} \leq 1, \quad (5.15)$$

where again  $I^{13}$  and  $J^{13}$  are linear combinations of the probability distribution  $P(a, b, c|x, y, z)$ . The maximum quantum violation of the  $13$ -bilocal inequality occurs when Alice and Charlie's measurements are  $\hat{A}_0 = \hat{C}_0 = \frac{1}{\sqrt{3}}(\sqrt{2}\hat{\sigma}_z + \hat{\sigma}_x)$  and  $\hat{A}_1 = \hat{C}_1 = \frac{1}{\sqrt{3}}(\sqrt{2}\hat{\sigma}_z - \hat{\sigma}_x)$ . These measurements are rotated towards the  $\hat{\sigma}_z$  axis, where the correlation contribution from states  $|\Psi^+\rangle$  and  $|\Psi^-\rangle$  are larger. In this case, Alice and Charlie's measurements are optimal for the  $13$ -bilocal inequality but not complementary. For Alice, Bob, and Charlie's measurements, the quantum prediction for the probability distribution is

$$P_Q^{13}(a, 0b^1, c|x, z) = \frac{1}{16} \left[ 1 + (-1)^{a+c} \frac{2 + (-1)^{x+z+b^1}}{3} \right], \quad (5.16)$$

$$\text{and } P_Q^{13}(a, \{10 \text{ or } 11\}, c|x, z) = \frac{1}{8} \left[ 1 - \frac{2}{3}(-1)^{a+c} \right]. \quad (5.17)$$

The  $13$ -bilocal inequality parameters  $I^{13}$  and  $J^{13}$  are related to the probability distributions  $P_Q^{13}(a, 0b^1, c|x, z)$  and  $P_Q^{13}(a, \{10 \text{ or } 11\}, c|x, z)$  by correlators

$$\begin{aligned} \langle A_x B^0 C_z \rangle_{P_Q^{13}} &= \sum_{a,c} (-1)^{a+c} [P^{13}(a, 00, c|x, z) \\ &\quad + P^{13}(a, 01, c|x, z) - P^{13}(a, \{10 \text{ or } 11\}, c|x, z)] \end{aligned} \quad (5.18)$$

and

$$\begin{aligned} \langle A_x B^1 C_z \rangle_{P_Q^{13}, b^0=0} &= \sum_{a,c} (-1)^{a+c} [P^{13}(a, 00, c|x, z) \\ &\quad - P^{13}(a, 01, c|x, z)], \end{aligned} \quad (5.19)$$

where here the label  $j$  is simply a label;  $b^j$  does not appear on the right-hand side. The correlators then define the inequality parameters

$$I^{13} = \frac{1}{4} \sum_{x,z} \langle A_x B^0 C_z \rangle_{P_Q^{13}}, \quad (5.20)$$

$$\text{and } J^{13} = \frac{1}{4} \sum_{x,z} (-1)^{x+z} \langle A_x B^1 C_z \rangle_{P_Q^{13}, b^0=0}. \quad (5.21)$$

The quantum prediction for parameters  $I^{13}$  and  $J^{13}$  given Alice, Bob, and Charlie's measurements is  $I^{13} = 2/3$  and  $J^{13} 1/6$ , yielding  $\sqrt{|I^{13}|} + \sqrt{|J^{13}|} \approx 1.22$ , in direct violation of the 13-bilocal inequality (Eq. 5.15). The correlators  $\langle A_x B^0 C_z \rangle_{P_Q^{13}}$  and  $\langle A_x B^1 C_z \rangle_{P_Q^{13}, b^0=0}$  can be experimentally determined from the observed probability distributions  $P(a, b, c|x, y, z)$ . The 13-bilocal inequality can be violated for entangled states generated in entanglement swapping having visibilities  $v > 0.666$ ; again a less stringent requirement when compared to the standard Bell test.

## 5.4 Experiment

The bilocal inequalities derived by Branciard *et al.* as outlined above were tested using pairs of entangled photons arising from an entanglement swapping scenario. To generate the photons, a pair of separate polarisation-entangled photon pair sources was required, labelled source 1 ( $S_1$ ) and source 2 ( $S_2$ ). Qubit measurement stages were also required for the roles of Alice and Charlie, and a joint BSM stage was required for the role of Bob. The source-independence assumption (Eq. 5.4) was also implemented experimentally. A schematic of the experimental apparatus used to test the bilocal inequalities is depicted in Fig. 5.3.

The primary laser system was a *Tsunami* model Titanium:Sapphire laser supplied by manufacturer *Spectra-physics*. The laser was a pulsed system operating at 820nm centre wavelength with an 80MHz pulse repetition rate and pulse lengths  $\approx 100\text{fs}$ , corresponding to a full width half maximum bandwidth of  $\approx 5.5\text{nm}$ . The power in the output beam was  $\approx 1.6\text{W}$  at 820nm, and was focussed into a BBO crystal (pump beam diameter  $\approx 60\mu\text{m}$ ) for collinear SHG conversion from 820nm to 410nm at a conversion efficiency of  $\approx 30\%$ . The BBO crystal was 2mm thick and sourced from *Newlight Photonics*. The 820nm beam was separated from the 410nm SHG beam using a pair of dispersion-compensating prisms and four dichroic mirrors, each with  $\approx 98\%$  filtering efficacy in separating 820nm from 410nm. These preliminary systems are not displayed in figure 4.2.

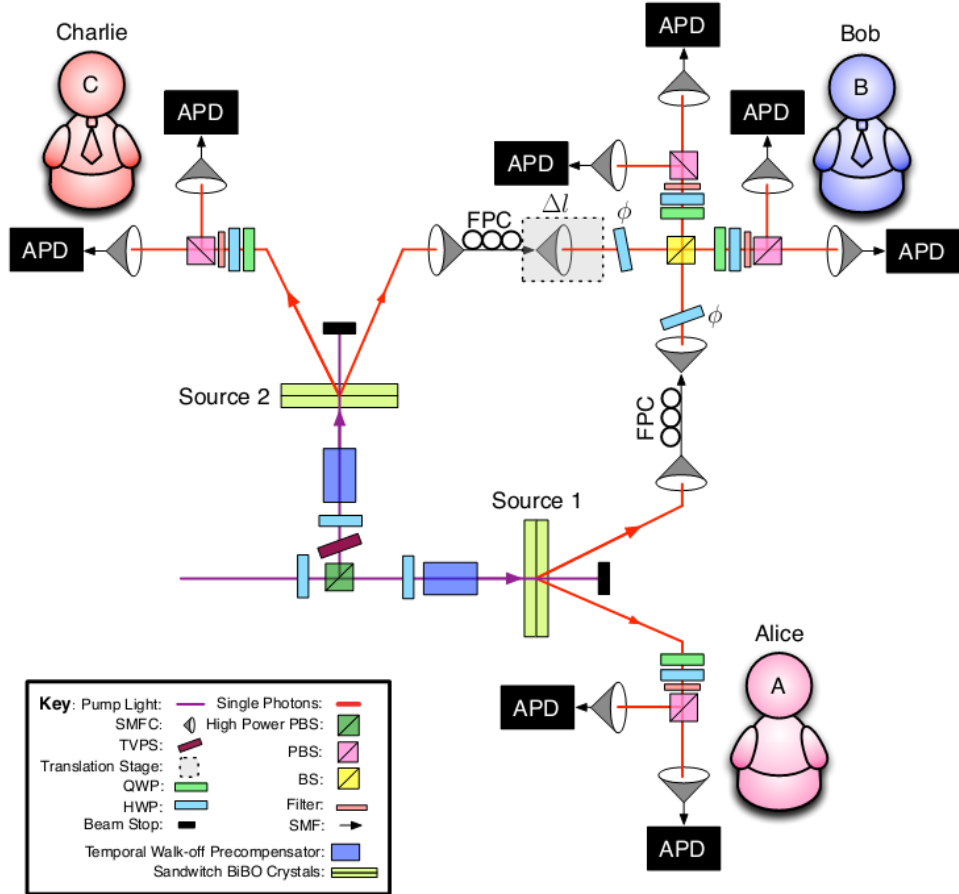


Figure 5.3: Illustration of experimental apparatus used to test bilocal inequalities. Independent sources 1 and 2 are pumped by a mode-locked 410nm 80-MHz frequency doubled Ti–Sapph. oscillator. Coherence in the pump beam between the two sources is erased using a time varying phase shifter (TVPS) set using a quantum random number generator (see Sec. 5.4.2). Alice and Charlie implement their measurements using polarisation projection optics: a quarter-wave plate (QWP), half-wave plate (HWP) and polarising beam splitter (PBS). Bob implements his BSM using a 50:50 beam-slitter (BS) and polarisation projective optics. Four-fold coincidences – one detection for Alice and Charlie each, and two for Bob – between the avalanche photodiodes (APDs) signify successful entanglement swapping from which all combinations of  $P(a, b, c|x, y, z)$  are calculated. [Figure courtesy of Dylan Saunders].

#### 5.4.1 Photon Sources

To test the bilocal inequalities, the 410nm beam was used to pump a pair of separate type-I down conversion sources each constructed of a pair of BiBO

crystals in the sandwich configuration [84] (Sec. 2.4.4). The beam was directed towards each source via a polarising beam splitter which split the input pump beam evenly amongst the two sources, resulting in  $\approx 200\text{mW}$  pump power per source. The sources each included a 12.64mm long piece of quartz to pre-compensate for temporal walk-off inside the BiBO crystals [84].

Sources 1 and 2 natively generated states close to the maximally polarisation–entangled state  $|\Phi^\phi\rangle = 1/\sqrt{2}(|HH\rangle + e^{i\phi}|VV\rangle)$  for diagonally polarised pump beams. However, unitary operations allowed for rotations onto any of the four maximally entangled Bell states. These unitaries were performed by a fibre polarisation controller mounted to the optical fibre directing each qubit to Bob’s BSM device, combined with a tilted quarter wave plate (tilted about an axis perpendicular to beam propagation). Unitaries were applied to generate the states  $|\Psi^-\rangle$  in sources 1 and 2, with the states characterised using quantum state tomography [72] (Sec. 2.5.7). Experimental statistics for the tomography were recorded in photon–pair coincidences between Alice and Bob’s detectors in the case of tomography for source 1, and Charlie and Bob’s detectors in the case of tomography for source 2. The reconstructed density matrices  $\hat{\rho}_1$  and  $\hat{\rho}_2$  corresponding to source 1 and source 2 respectively were found to have fidelities  $F(\hat{\rho}_1, \hat{\sigma}) = 0.95 \pm 0.01$  and  $F(\hat{\rho}_2, \hat{\sigma}) = 0.96 \pm 0.01$ , with the ideal Bell state  $|\Psi^-\rangle$  corresponding to density matrix  $\hat{\sigma}$  (i.e.  $\hat{\sigma} = |\Psi^-\rangle\langle\Psi^-|$ ).

### 5.4.2 Strengthening Source Independence

The entangled states  $\hat{\rho}_1$  and  $\hat{\rho}_2$  generated by sources 1 and 2 were considered to be independent from one another because the states were generated in random and uncorrelated SPDC events seeded by quantum mechanical vacuum fluctuations in separate modes from separate crystals. However, because the bilocal inequalities are derived upon the assumption of source independence, extra measures were implemented to further strengthen the assertion of source independence. To that end, a time variable phase shifter (TVPS) was inserted into the pump beam of source 2 to erase relative coherence between the pump beams of source 1 and 2. The TVPS was an anti-reflection coated glass plate (BK7 glass, 6.53mm thick, CVI Melles Griot Part No. W2-PW1-1525-UV-255-532-0) on an angular rotation stage connected to a remote quantum random number generator (sourced online, from the Australian National University, Ref. [134]) that imparted a random phase between 0 and  $2\pi$  on Bob’s pump beam every 502ms. Over the course

of the experiment, the phase shifter erased any entanglement that might have conceivably existed between the two pump modes and which might be thought to be converted into entanglement between the downconverters.

The TVPS was characterised by constructing a Michelson–Morely interferometer (separate from the main experiment), where the TVPS was placed into one arm of the interferometer. The TVPS was set to a large initial test angle of  $30^\circ$  from normal such that slight rotations about an axis perpendicular to the beam propagation axis caused minimal translation of the pump beam. The interference fringes at the output of the Michelson–Morely interferometer were used to calibrate the TVPS. It was found from the interference fringes that a rotation of the TVPS from  $30^\circ$  to  $30.032^\circ$  from normal resulted in a phase shift of  $\approx 2\pi$ . Because the minimum resolution of the rotation stage controlling the TVPS rotation was  $0.005^\circ$  (Newport model URS100CC), there were 64 angular subdivisions between 0 and  $2\pi$  accessible to the rotation stage. Once the TVPS was calibrated using the Michelson–Morely interferometer, the TVPS and rotation stage assembly was placed in the pump beam of source 2 at an angle of  $30^\circ$  from normal, mirroring the calibration. The rotation stage was connected to a QRNG that randomly selected subdivisions in the range  $[0, 63]$ , which determined a corresponding angular setting between 0 and  $2\pi$  from a lookup table, changing every 0.502ms. The TVPS therefore erased any relative phase information between the pump beams of source 1 and source 2 on average, experimentally strengthening the validity of the source independence assumption.

### 5.4.3 Bell State Measurement Device

To test the  $13$  and  $14$  bilocal inequalities Bob required both a partial and simulated–ideal BSM device constructed from linear optical elements [60] (Sec. 2.6.5). The native implementation of Bob’s measurement device was the partial BSM, meaning the  $13$  bilocal inequality could be tested directly with Bob’s device, having measurement elements  $\{\hat{M}_b\}$ :

$$\hat{M}_{00} = |\Psi^+\rangle\langle\Psi^+|, \quad (5.22)$$

$$\hat{M}_{01} = |\Psi^-\rangle\langle\Psi^-|, \quad (5.23)$$

$$\text{and } \hat{M}_{\{10 \text{ or } 11\}} = \mathbb{I} - \hat{M}_{00} - \hat{M}_{01}, \quad (5.24)$$

where  $\mathbb{I}$  is the identity matrix. Importantly, detection of the states  $|\Phi^\pm\rangle$  required photon–number resolution because the signal corresponding to  $|\Phi^\pm\rangle$  consisted of two identically polarised photons in the same output mode.

However, because photon–number resolving detectors were not available, pseudo–number resolution was implemented using 50:50 fibre beam splitters at the outputs of Bob’s measurement apparatus, so that the  $|\Phi^\pm\rangle$  coincidence signals were correctly resolved 50% of the time (a fact accounted for in data processing).

The efficacy of Bob’s BSM device was characterised by recording a Hong–Ou–Mandel (HOM) dip between photon pairs degenerate in all degrees of freedom and optimising the HOM interference visibility (Sec. 2.5.4). The HOM dip was recorded by preparing unentangled photon pairs from sources 1 and 2 and combining one photon from each pair on Bob’s 50:50 beam splitter. For the HOM experiment, the remaining photons from each source were used as heralding signals; one at Charlie’s measurement station, and the other at Alice’s. A HOM dip was measured in four–fold coincidences between Alice, Bob, and Charlie’s detectors ( $\approx 200$  per hour) as the arrival time of the photons was adjusted using a translation stage on one of Bob’s input fibre couplers. The HOM visibility was optimised to  $0.90 \pm 0.04$  (Fig. 5.4).

To test the  $14$  bilocal inequality Bob required a simulated ideal BSM device. The ideal BSM was simulated by performing the local unitaries  $\mathbb{I}$ ,  $\hat{\sigma}_z$ ,  $\hat{\sigma}_x$ , or  $\hat{\sigma}_x\hat{\sigma}_z$  on one of the qubits incident to Bob’s partial BSM device. Coincidence patterns appropriate to the measurement  $\{|\sigma\rangle\langle\sigma|, \mathbb{I} - |\sigma\rangle\langle\sigma|\}$  were monitored for each respective unitary, where  $\sigma$  corresponds to  $\Psi^-$ ,  $\Psi^+$ ,  $\Phi^-$ , or  $\Phi^+$ , depending on the local unitary applied. The resultant  $|\sigma\rangle\langle\sigma|$  projections for each of the four cases were then aggregated into a single data set to simulate the statistics expected from an ideal  $14$  BSM device. To better intuit how this process could simulate an ideal Bell state measurement device, consider the expression for an initial joint state  $|\Psi^-\rangle_{12} \otimes |\Psi^-\rangle_{34}$  prior to interaction with an ideal BSM device (where 1, 2, 3, and 4 label spatial modes: 1 and 4 are the modes to Alice and Charlie, respectively, and 2 and 3 are the modes to Bob’s joint BSM device; see Fig. 5.1), expressed as

$$|\Psi^-\rangle_{12} \otimes |\Psi^-\rangle_{34} = \frac{1}{2}(|\Psi^-\rangle_{14}|\Psi^-\rangle_{23} + |\Psi^+\rangle_{14}|\Psi^+\rangle_{23} + |\Phi^-\rangle_{14}|\Phi^-\rangle_{23} + |\Phi^+\rangle_{14}|\Phi^+\rangle_{23}). \quad (5.25)$$

For an ideal BSM device, projection of modes 2 and 3 onto one of the Bell states projects the remaining photons in modes 1 and 4 onto an equivalent Bell state. Equation 5.25 can equivalently be expressed as [61]

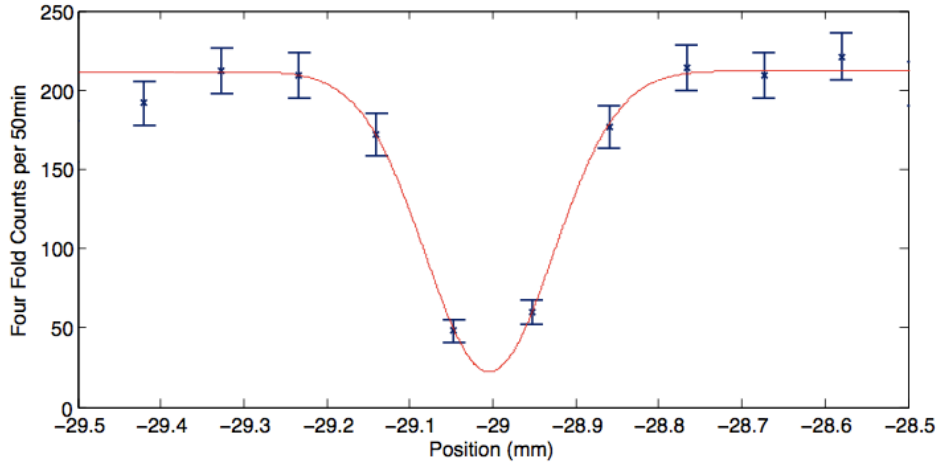


Figure 5.4: HOM dip for characterising Bob’s partial BSM device, recorded in four-fold coincidences. The dip appears in four-cold coincidences as one of the degrees of freedom between the initially identical photon pairs is varied. In this case, the relative difference in arrival time between photon pairs is adjusted by increasing the path length of one photon relative to the other, performed using a  $z$ -translation stage on one of Bob’s input couplers to his 50:50 beam splitter. A Gaussian fit to the data revealed a HOM visibility  $0.90 \pm 0.04$ . [Figure courtesy of Dylan Saunders].

$$\begin{aligned} |\Psi^-\rangle_{12} \otimes |\Psi^-\rangle_{34} = & \frac{1}{2} (|\Psi^-\rangle_{14} (\mathbb{I} \otimes \mathbb{I}) |\Psi^-\rangle_{23} + |\Psi^+\rangle_{14} (\hat{\sigma}_z \otimes \mathbb{I}) |\Psi^-\rangle_{23} \\ & + |\Phi^-\rangle_{14} (\hat{\sigma}_x \otimes \mathbb{I}) |\Psi^-\rangle_{23} + |\Phi^+\rangle_{14} ((\hat{\sigma}_x \hat{\sigma}_z) \otimes \mathbb{I}) |\Psi^-\rangle_{23}, \end{aligned} \quad (5.26)$$

where  $\mathbb{I}$  is the identity and  $\hat{\sigma}_x$  and  $\hat{\sigma}_z$  are the Pauli spin operators. Equivalence between Eqs. 5.25 and Eq. 5.26 suggests that BSM mode projections onto the states  $|\Psi^-\rangle_{23}$ ,  $|\Psi^+\rangle_{23}$ ,  $|\Phi^-\rangle_{23}$ , and  $|\Phi^+\rangle_{23}$  can be performed by performing the following local unitaries on mode 2 (and the identity on mode 3):

$$|\Psi^-\rangle_{23} = (\mathbb{I} \otimes \mathbb{I}) |\Psi^-\rangle_{23}, \quad (5.27)$$

$$|\Psi^+\rangle_{23} = (\hat{\sigma}_z \otimes \mathbb{I}) |\Psi^-\rangle_{23}, \quad (5.28)$$

$$|\Phi^-\rangle_{23} = (\hat{\sigma}_x \otimes \mathbb{I}) |\Psi^-\rangle_{23}, \quad (5.29)$$

$$|\Phi^+\rangle_{23} = ((\hat{\sigma}_x \hat{\sigma}_z) \otimes \mathbb{I}) |\Psi^-\rangle_{23}. \quad (5.30)$$

Thus, by performing unitary operations on one of Bob’s received qubits (the one in mode 2), each of the four BSM projections  $\{|\sigma\rangle\langle\sigma|, \mathbb{I} - |\sigma\rangle\langle\sigma|\}$

for  $\sigma$  corresponding to  $\Psi^-$ ,  $\Psi^+$ ,  $\Phi^-$ , and  $\Phi^+$  could be performed. This was the case in the experiment, and the unitaries were applied using a fibre-polarisation-controller and tilted quarter-wave plate affecting Bob's qubit received from source 1.

#### 5.4.4 Results and Analysis

Before testing the bilocal inequalities, the entangled state generated between Alice and Charlie (after Bob performed his entanglement swapping stage) was characterised. This was done by performing a test of the CHSH inequality (Sec. 2.6) on the final state shared between Alice and Charlie after entanglement swapping, finding  $S_{CHSH} = 2.41 \pm 0.05$ ; a clear violation of the CHSH inequality. Additionally, an estimate of the visibility of the final entangled state could be made by combining the HOM visibility  $v_{HOM}$  with the entangled state visibilities from source 1 and source 2, which were measured to be  $v_1 = 0.94 \pm 0.01$  and  $v_2 = 0.96 \pm 0.01$ . Combining these with the HOM interference visibility  $v_{HOM} = 0.90 \pm 0.04$ , the visibility of the final entangled state  $v_f$  after entanglement swapping was expected to be  $v_f = v_1 v_2 v_{HOM} \approx 0.80$ , above the requirements of  $v_f > 0.66$  and  $v_f > 0.50$  required for violations of the *13* and *14* bilocal inequalities respectively.

Having established the existence of nonclassical correlations between particles sharing no common history, data for the *14* and *13* inequalities was then collected. Evaluating the nonlinear bilocal inequalities  $\sqrt{|I^{14}|} + \sqrt{|J^{14}|} \leq 1$  and  $\sqrt{|I^{13}|} + \sqrt{|J^{13}|} \leq 1$  required collecting data for 48 and 64 combinations of  $a, b, c, x$  and  $z$  respectively.

Data collection for the *14*-bilocal inequality was performed in four stages corresponding to the four inputs to Bob's BSM. Each individual stage consisted of a pre-data collection characterisation stage, followed by 24 hours of data collection. The characterisation stage occurred in three steps: first, a single-qubit unitary was applied to source 1 to generate the input for Bob's simulated ideal BSM. Second, quantum state tomography was performed on sources 1 and 2 to ensure high state fidelities. Finally, a HOM scan was performed to ensure the proper operation of Bob's BSM device. After completing the pre-data collection analysis, data was collected for 24 hours as Alice and Charlie rotated through their measurements. This procedure was repeated for each of the four local unitaries required to change Bob's BSM projection for simulating Bob's ideal BSM device, with the final four data sets aggregated to evaluate the inequality parameters  $I^{14}$  and  $J^{14}$ . The

results of the data collection and analysis yielded

$$I^{14} = 0.432 \pm 0.001, \quad (5.31)$$

$$J^{14} = 0.356 \pm 0.001, \quad (5.32)$$

where the error in each term was calculated by propagating Poissonian counting statistics through the analysis. The observed parameters were in the vicinity of (but less than) the expected values  $I^{14} = J^{14} = 0.5$ , with the experimental discrepancy being the result of imperfect state preparation in sources 1 and 2, imperfect HOM visibility, and small undesired phase drift accumulated over the course of data collection. The evaluation of the  $14$  bilocal inequality yielded  $\sqrt{|I^{14}|} + \sqrt{|J^{14}|} = 1.25 \pm 0.04$ , a direct violation of the bilocal inequality for a simulated ideal BSM device.

Data collection for the  $13$  bilocal inequality was performed in a single data run. Prior to data collection, sources 1 and 2 were optimised to have high fidelities with the  $|\Psi^-\rangle$  Bell states, and Bob's partial BSM was optimised by performing a HOM scan. Data was collected for 24 hours as Alice and Charlie rotated through their measurements. The inequality parameters  $I^{13}$  and  $J^{13}$  were evaluated from the experimental data, finding

$$I^{13} = 0.634 \pm 0.001, \quad (5.33)$$

$$J^{13} = 0.125 \pm 0.001, \quad (5.34)$$

where the error in each term was calculated by propagating Poissonian counting statistics through the analysis. The observed parameters were close to the expected values  $I^{13} = 0.666$  and  $J^{13} = 0.166$ . The evaluation of the  $13$  bilocal inequality yielded  $\sqrt{|I^{13}|} + \sqrt{|J^{13}|} = 1.15 \pm 0.02$ , a direct violation of the bilocal inequality for a partial BSM device.

## 5.5 Discussion

The experimental violations of the  $13$  and  $14$  bilocal inequalities demonstrate the efficacy of bilocal models and fill a pre-existing disconnect between the theoretical framework of Bell's theorem and the architecture of

entanglement swapping scenarios. Interestingly, the generation of entanglement between particles sharing no common history suggests the possibility of a form of entanglement that is stronger than entanglement generated between particles sharing a common history. Indeed, Branciard *et al.* have demonstrated that the bilocal models belong to a stronger class than those of Bell’s theorem, resulting in lower requirements for the demonstration of quantumness in entanglement swapping experiments [66]. The framework introduced in this chapter can be extended to scenarios with multiple measurement inputs and outputs, multiple parties, quantum states of higher dimensions and different kinds of measurements [66]. Another possible extension is the application of the theoretical framework to quantum network scenarios, with multiple independent sources, allowing for the (non-trivial) derivation of  $n$ -local models. The assessment of such scenarios and the evaluation of associated visibility thresholds remains an open problem.

The experimental discrepancy of the  $I^{14}$  and  $J^{14}$  parameters with the quantum theoretical predictions is thought to be due to time-dependent variations in experimental parameters when collecting data for simulating the ideal  $14$  BSM. Because the data was collected in four separate 24 hour sets, fluctuations of the sources and other experimental components between and during data runs resulted in slightly different overall count rates for each set, likely skewing the data in a direction away from optimality. This hypothesis could be tested by improving source stability and count rates, so that data could be taken over shorter intervals. An additional improvement to the experiment presented in this chapter could be offered by accurately recording and reducing the visibility of the final entangled state to be  $v_f < 0.707$ , so that the bilocal inequalities can be tested for a state that cannot violate the CHSH inequality. Additionally, an entangled state having  $0.50 < v_f < 0.66$  could test the region where only a  $14$ -bilocal inequality can confirm quantum correlations. Such tests would demonstrate the efficacy of bilocal inequalities over inequalities based on Bell’s theorem for tests of quantumness in entanglement swapping scenarios. Branciard *et al.* have also alluded to the possibility for bilocal models capable of demonstrating quantumness for entangled states having visibilities as low as  $v_f = 0.25$ , leaving a gap in the visibility threshold  $0.25 < v_f < 0.50$  worth investigation.

Because the experiment presented in this chapter does not close any experimental loopholes (the detection loophole, the no-signalling loophole, and the freedom-of-choice loophole), future experimental work could demonstrate loophole free bilocal inequality violations. Such demonstrations could

even employ separate laser systems, further strengthening the assumption of source independence.

The noise tolerance of the bilocal inequalities (making use of data collected over the course of the experiment) is currently under investigation, as is the possibility for using bilocal inequalities as certification protocols for the presence of a quantum teleportation channel. Finally, an in-depth study of the implications of the independent sources assumption may lead to a better understanding of nonlocality, especially in the applied case of quantum networks. One example is the question of how powerful quantum networks can be when compared to classical resources for executing information processing tasks.

## Chapter 6

# Verifying Entangled Measurements

### Statement of work

This chapter presents the experimental verification of entangled measurements, and of quantum unentangled measurements, via witnesses. The verification uses only experimental statistics gathered from an in-principle arbitrary measurement, and uses in-principle uncharacterised quantum states of restricted Hilbert space dimension as probe states, making the verification scenario a semi-device-independent one. The work presented is based on theoretical investigations undertaken by T. Vértesi, M. Navascués, and N. Brunner [68].

The entangled measurement experiment was undertaken primarily by myself. I constructed the experiment with assistance from Dylan Saunders. I optimised the experiment and collected the experimental data. I analysed the experimental data with contributions from Geoff Pryde. The work resulted in a *Physical Review Letters* publication, which all authors participated in writing [135].

### 6.1 Introduction

Quantum mechanics permits entangled measurements, described by an operator for which at least one of the measurement eigenstates corresponds to an entangled state. Entangled measurements have been studied much less than entangled states; however, such measurements play a fundamental role

in many manifestations of quantum information science, including quantum teleportation [103], quantum repeaters [136], quantum computation [70], dense coding [137], and parameter estimation [138] protocols, making the characteristics of entangled measurements an active area of research. A well known example of such a measurement is the partial Bell state measurement (BSM, Sec. 2.6.5, Refs. [60, 61]), whereby two of the three measurement elements correspond to the  $|\Psi^-\rangle$  and  $|\Psi^+\rangle$  entangled Bell states, with the third measurement element being a subspace corresponding to a variety of entangled and unentangled states.

In typical experimental demonstrations of optical quantum information science, the efficacy of measurements (entangled or otherwise) can be well characterised by *quantum detector tomography* [139] or *quantum process tomography* [140, 141] procedures (in the latter case, measurements are treated as a process to be characterised). Such tomographic procedures are an effective means of completely characterising measurements for proof-in-principle demonstrations, but notably require a well calibrated and stable source of quantum states that span the state-space of the measurement. Such necessities may not be optimal in applied scenarios of quantum technologies. Citing the well-known existence of witnesses for characterising the nonclassical nature of entangled quantum states (for example Bell's inequality, Sec. 2.6), one may ask whether there may similarly exist a means of characterising measurement processes (particularly entangled measurement processes) using witnesses. Such a question garners additional weight in light of *semi-device-independent* and *device-independent witnesses* for entangled states, which can certify the nonclassical nature of quantum states without making assumptions about the physical systems, agents operating physical systems, or descriptions of physical systems [59, 126, 127]. This chapter explores and introduces two such semi-device-independent witness for certifying the nature of a measurement device using measurement statistics only.

Recent work (both theoretical and experimental) has considered entangled measurement certification in a device-independent setting [142, 143]. Unfortunately, these approaches turn out to be experimentally limited because they are not robust to noise and/or involve experimentally unfeasible measurements. This chapter experimentally demonstrates entangled measurement verification under the assumption that a pair of quantum probe states are of restricted Hilbert space dimension, making the protocol a semi-device-independent verifier of entangled measurements [68] (Fig. 6.1iii.). The semi-device-independent witnesses introduced here offer a powerful

tool for the characterisation of measurement devices, and should find use in applied and fundamental quantum tests requiring the certification of entangled measurements.

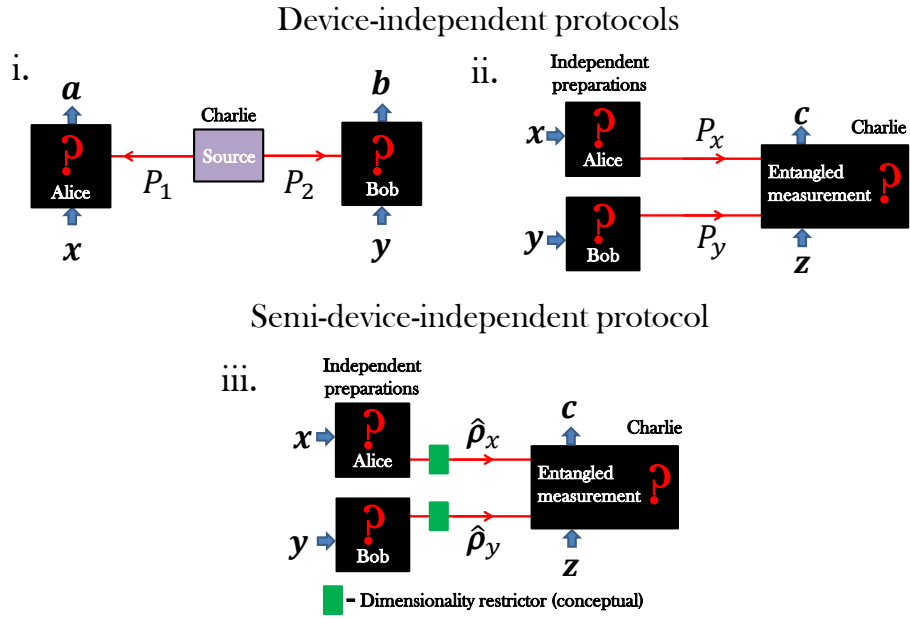


Figure 6.1: Device-independent and semi-device-independent scenarios for entanglement certification and entangled measurement certification. Part i. illustrates an uncharacterised source emitting particles  $P_1$  and  $P_2$  which are collected and measured by uncharacterised measurement devices controlled by Alice and Bob. Bell nonlocality can be certified from the statistics of  $a, b, x$ , and  $y$ . Part ii. illustrates a device-independent entangled measurement verification scenario, akin to a reversal of the Bell test. Uncharacterised preparation devices controlled by Alice and Bob prepare and send particles  $P_x$  and  $P_y$  to Charlie's measurement device. In-principle, the nature of Charlie's measurement is verified from the statistics of  $x, y, z$ , and  $c$ . Part iii. illustrates the semi-device-independent entangled measurement verification scenario introduced in this thesis. Uncharacterised preparation devices controlled by Alice and Bob prepare and send quantum states  $\hat{\rho}_x$  and  $\hat{\rho}_y$  of restricted Hilbert space dimension into Charlie's uncharacterised measurement device. The nature of Charlie's measurement device can be certified using the statistics of  $x, y, z$ , and  $c$ .

The initial derivation of semi-device-independent witnesses for measurements was undertaken by Vértesi and Navascués [68]. The authors demon-

strated the existence of a measurement heirarchy, governed by the inclusion relation (related by the superset symbol “ $\supset$ ”): General measurements  $\supset$  Unentangled measurements  $\supset$  Local operation classical communication (LOCC) measurements  $\supset$  Classical measurements. General measurements are defined to have no restrictions beyond the minimum required by quantum mechanics, and include entangled quantum measurements; i.e. those described by an operator where at least one measurement eigenstate corresponds to an entangled state. Unentangled measurements are defined to include quantum measurements where each of the eigenstates of a measurement operator correspond to separable quantum states for all inputs and outputs. LOCC measurements are defined to include local measurements strategies where the measurements may possibly depend on the outcomes of prior measurements. Finally, classical measurements are defined to take classical states (eg. bits) as inputs, and yield classical states as outputs.

The pair of witnesses introduced in this chapter are designed to witness a) entangled measurements (belonging to the class of general measurements), and b) unentangled measurements. The witnesses employed depend on the class of measurement one wishes to witness, akin to the case of witnesses for entangled states, whereby (for instance) a Bell test can only certify an entangled state as belonging to a class of Bell nonlocal states. Therefore, an entangled measurement witness certifies whether a measurement belongs to a class of general measurements, and an unentangled measurement witness certifies whether a measurement belongs to a class of unentangled (quantum) measurements. The witnesses are developed by first considering a scenario involving three parties: Alice, Bob, and Charlie. Charlie possesses an in-principle uncharacterised measurement device<sup>1</sup> (Fig. 6.1iii). Alice and Bob each possess in-principle independent uncharacterised qubit state preparation devices of restricted Hilbert space dimension. Notably, no claims are made about the underlying operation of Alice, Bob, and Charlie’s devices, outside of the restricted Hilbert space dimension assumption, making the scenario semi-device-independent.

The protocol for evaluating the nature of Charlie’s measurement proceeds as follows: Alice and Bob choose one of  $n$  preparations  $x = 0, \dots, n - 1$  and  $y = 0, \dots, n - 1$  corresponding to independent qubit probe state preparations  $\hat{\rho}_x^A$  and  $\hat{\rho}_y^B$  respectively, and send them into Charlie’s uncharacterised

---

<sup>1</sup>Meaning Charlie’s measurement device may, in-principle, belong to any measurement class. However, for the experimental demonstration, Charlie’s measurement was chosen to belong to the class appropriate to the witness being tested.

measurement device. Upon receiving the qubit states, Charlie chooses a measurement setting  $z$  and records a measurement outcome  $c$  from the device. If the elements of Charlie's measurement operator are denoted  $\{M_{c|z}\}$ , then over many runs the parties develop a probability distribution

$$p_{c|x,y,z} = \text{Tr}(\hat{\rho}_x^A \otimes \hat{\rho}_y^B \cdot M_{c|z}) \quad (6.1)$$

that corresponds to the experimental data. The goal of this work is to verify, using appropriate witnesses, whether Charlie's uncharacterised measurement device belongs to a particular class of measurements based solely on the recorded probability distribution.

## 6.2 Witness for Entangled Measurements

The first measurement verification scenario introduced is one for witnessing Charlie's measurement as entangled. The class of general measurements contains all entangled measurements, and here a witness for entangled measurements is introduced based on the partial BSM device, which performs an entangled measurement and can be conveniently implemented experimentally. To construct a witness for such a scenario, Charlie's in-principle uncharacterised measurement device is allowed a single fixed input setting  $z$  with three possible outcomes  $c = 1, 2, 3$  (a ternary measurement), and Alice and Bob are each allowed  $n = 3$  qubit state preparations ( $x = 0, 1, 2$  and  $y = 0, 1, 2$ ). A linear witness for entangled measurements may then be constructed [135]:

$$w = \sum_{c=1,2} \sum_{x,y=0}^2 W_{c|x,y} p_{c|x,y}, \quad (6.2)$$

where  $z$  is omitted due to the fixed nature of Charlie's ternary measurement. The  $c = 3$  measurement outcome is required for normalisation, but plays no role in the witness. The coefficient matrices  $W_{c|x,y}$  are given by

$$W_{1|x,y} = \begin{pmatrix} 1 & -1 & -1 \\ -1 & 1 & -1 \\ -1 & -1 & 1 \end{pmatrix}, \quad W_{2|x,y} = \begin{pmatrix} 1 & -1 & -1 \\ -1 & -1 & 1 \\ -1 & 1 & -1 \end{pmatrix}, \quad (6.3)$$

determining whether a given probability is added or subtracted from the sum. Theory collaborator Tamas Vértesi determined the maximal bounds of the witness for classical and unentangled measurement strategies. By noting the witness linearity, the maximal value for a classical measurement strategy was obtained from a deterministic measurement strategy. There

were a finite number of such strategies, with an exhaustive evaluation finding the maximal value  $w \leq w_{class} = 1$  [68, 135]. For unentangled measurement strategies, the maximal value of the witness was evaluated as  $w \leq w_{unent} = 1$  using the seesaw iteration numerical method [144] (with the large number of iterations providing strong evidence for optimality [135]). These findings therefore act as a witness for entangled measurements: any  $w > 1$  cannot be obtained using quantum unentangled measurements<sup>2</sup>.

In the experimental demonstration to follow, statistics yielding  $w > 1$  will witness an entangled measurement. In the experimental demonstration, the role of Charlie's in-principle uncharacterised general measurement device is fulfilled by the partial BSM device (Sec. 2.6.5). The partial BSM device is easily implemented in linear optics and is regularly used as an entangled measurement device, having measurement elements  $\{M_c\}$  given by

$$M_1 = |\Psi^-\rangle\langle\Psi^-|, \quad (6.4)$$

$$M_2 = |\Psi^+\rangle\langle\Psi^+|, \quad (6.5)$$

$$\text{and } M_3 = \mathbb{I} - M_1 - M_2. \quad (6.6)$$

The partial BSM perfectly resolves the  $|\Psi^-\rangle$  and  $|\Psi^+\rangle$  eigenstates corresponding to  $M_1$  and  $M_2$ , and combines the remaining pair of eigenstates  $|\Phi^\pm\rangle$  into a third measurement outcome  $M_3$ .

To ensure a maximal experimental violation of the witness for entangled measurements, Alice and Bob's probe states must be evenly spaced – this means Alice and Bob's polarisation-encoded qubits are chosen to be uniformly distributed on the  $XZ$  plane of the Poincaré sphere (Fig. 6.2). Charlie therefore receives the following polarisation-encoded qubit states  $|r_x^A\rangle$  from Alice:

$$|r_0^A\rangle = |H\rangle, \quad |r_1^A\rangle = \frac{1}{2}|H\rangle + \frac{\sqrt{3}}{2}|V\rangle, \quad \text{and} \quad |r_2^A\rangle = \frac{1}{2}|H\rangle - \frac{\sqrt{3}}{2}|V\rangle, \quad (6.7)$$

and similarly receives the following polarisation-encoded qubit states  $|r_y^B\rangle$  from Bob:

$$|r_0^B\rangle = |V\rangle, \quad |r_1^B\rangle = \frac{1}{2}|V\rangle + \frac{\sqrt{3}}{2}|H\rangle, \quad \text{and} \quad |r_2^B\rangle = \frac{1}{2}|V\rangle - \frac{\sqrt{3}}{2}|H\rangle. \quad (6.8)$$

---

<sup>2</sup>From the measurement inclusion relation outlined above we find  $w_{general} \geq w_{ent} \geq w_{unent} \geq w_{LOCC} \geq w_{class}$ .

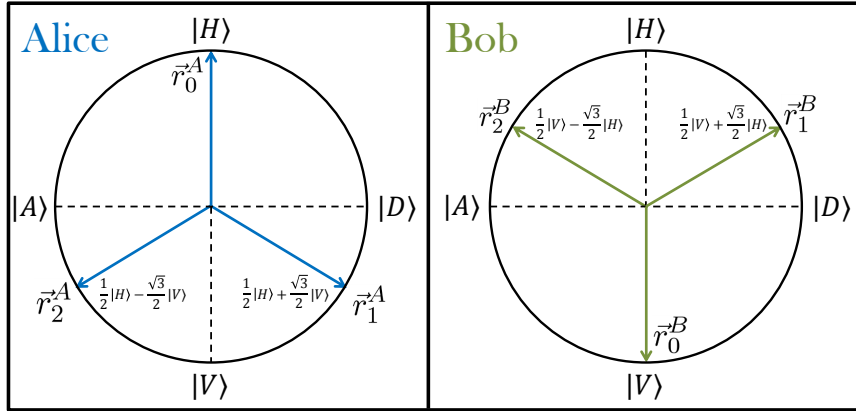


Figure 6.2: Illustration of Alice and Bob's ideal polarisation-encoded qubit probe states, expressed on the  $XZ$  plane of the Poincaré sphere. The states  $|A\rangle$  and  $|D\rangle$  correspond to the antidiagonal and diagonal polarisation states respectively (Sec. 2.5.1). The uniformly distributed states allow for a maximal violation of the witness for entangled measurements. The states may be uncharacterised in principle (in the sense that the validity of the witness does not depend on knowing the states); although such a situation would be unlikely to lead to a witness violation, much less a maximal one.

The qubit states  $\hat{\rho}_x^A$  and  $\hat{\rho}_y^B$  for Alice and Bob find expression in density matrix formalism as  $\hat{\rho}_x^A = |r_x^A\rangle\langle r_x^A|$  and  $\hat{\rho}_y^B = |r_y^B\rangle\langle r_y^B|$ , these being:

$$\hat{\rho}_0^A = \begin{pmatrix} 1 & 0 \\ 0 & 0 \end{pmatrix}, \quad \hat{\rho}_0^B = \begin{pmatrix} 0 & 0 \\ 0 & 1 \end{pmatrix}, \quad (6.9)$$

$$\hat{\rho}_1^A = \begin{pmatrix} \frac{1}{4} & \frac{\sqrt{3}}{4} \\ \frac{\sqrt{3}}{4} & \frac{3}{4} \end{pmatrix}, \quad \hat{\rho}_1^B = \begin{pmatrix} \frac{3}{4} & \frac{\sqrt{3}}{4} \\ \frac{\sqrt{3}}{4} & \frac{1}{4} \end{pmatrix}, \quad (6.10)$$

$$\hat{\rho}_2^A = \begin{pmatrix} \frac{1}{4} & -\frac{\sqrt{3}}{4} \\ -\frac{\sqrt{3}}{4} & \frac{3}{4} \end{pmatrix}, \quad \text{and} \quad \hat{\rho}_2^B = \begin{pmatrix} \frac{3}{4} & -\frac{\sqrt{3}}{4} \\ -\frac{\sqrt{3}}{4} & \frac{1}{4} \end{pmatrix}. \quad (6.11)$$

Using Charlie's measurement elements  $\{M_c\}$  and Alice and Bob's probe state arrangements  $\hat{\rho}_x^A$  and  $\hat{\rho}_y^B$ , the theoretical table of probabilities  $p_{c|x,y} = \text{Tr}(\rho_x^A \otimes \rho_y^B \cdot M_c)$  can be evaluated to determine the maximal theoretical value of the witness  $w_{th}$  expected given such an arrangement. The example case of  $x, y = 0$  and  $c = 1$  yields

$$\begin{aligned}
p_{1|0,0} &= \text{Tr}(\rho_0^A \otimes \rho_0^B \cdot M_1) \\
&= \text{Tr} \left( \begin{pmatrix} 1 & 0 \\ 0 & 0 \end{pmatrix} \otimes \begin{pmatrix} 0 & 0 \\ 0 & 1 \end{pmatrix} \cdot \begin{pmatrix} 0 & 0 & 0 & 0 \\ 0 & \frac{1}{2} & \frac{1}{2} & 0 \\ 0 & \frac{1}{2} & \frac{1}{2} & 0 \\ 0 & 0 & 0 & 0 \end{pmatrix} \right) \\
&= \text{Tr} \left( \begin{pmatrix} 0 & 0 & 0 & 0 \\ 0 & 1 & 0 & 0 \\ 0 & 0 & 0 & 0 \\ 0 & 0 & 0 & 0 \end{pmatrix} \cdot \begin{pmatrix} 0 & 0 & 0 & 0 \\ 0 & \frac{1}{2} & \frac{1}{2} & 0 \\ 0 & \frac{1}{2} & \frac{1}{2} & 0 \\ 0 & 0 & 0 & 0 \end{pmatrix} \right) \\
&= 1/2.
\end{aligned} \tag{6.12}$$

Following this example, the complete theoretical probability distribution  $p_{c|x,y}$  for the different combinations of  $x, y = 0, 1, 2$ , and  $c = 1, 2$  can be constructed (omitting  $c = 3$  because it is not used in the witness, and can be derived or found from normalisation), giving

$$p_{1|x,y} = \left( \begin{array}{c|ccc} x, y & 0 & 1 & 2 \\ \hline 0 & 1/2 & 1/8 & 1/8 \\ 1 & 1/8 & 1/2 & 1/8 \\ 2 & 1/8 & 1/8 & 1/2 \end{array} \right), \tag{6.13}$$

$$p_{2|x,y} = \left( \begin{array}{c|ccc} x, y & 0 & 1 & 2 \\ \hline 0 & 1/2 & 1/8 & 1/8 \\ 1 & 1/8 & 1/8 & 1/2 \\ 2 & 1/8 & 1/2 & 1/8 \end{array} \right). \tag{6.14}$$

Coupling the probability distributions  $p_{c|x,y}$  with the witness coefficient matrices  $W_{c|x,y}$  (Eq. 6.3), the maximum theoretical value of the witness is found to be

$$\begin{aligned}
w_{th} &= \sum_{c=1,2} \sum_{x,y=0}^2 W_{c|x,y} p_{c|x,y}, \\
&= 1/2 - 1/8 - 1/8 - 1/8 + 1/2 - 1/8 - 1/8 - 1/8 + 1/2 \\
&\quad + 1/2 - 1/8 - 1/8 - 1/8 - 1/8 + 1/2 - 1/8 + 1/2 - 1/8, \\
&= 3/2.
\end{aligned} \tag{6.15}$$

The value  $w_{th} = 3/2$  exceeds the bound  $w = 1$ , and therefore the presented configuration of measurement device and probe state preparations can cer-

tify an entangled measurement. This is the arrangement employed in the experimental demonstration (Sec. 6.3).

### 6.2.1 Witness for Quantum Unentangled Measurements

A witness for quantum unentangled measurements can also be constructed. The witness for unentangled measurements certifies an in-principle uncharacterised measurement as belonging to a class of unentangled measurements, distinguishing it from the higher class of general measurements, and the lower class of LOCC and classical measurements. Standard projective polarisation measurements belong to the class of unentangled measurements, and are chosen as the basis for the unentangled measurement witness tested experimentally in this chapter. In this case, a maximal demonstration is again offered if Alice and Bob prepare the same evenly spaced arrangement of qubit probe states (Fig. 6.2). For the case of standard projective measurements, Charlie is allowed to choose between a pair of dichotomic measurements  $z = 0, 1$ , each with outcome  $c = 1, 2$ . In this case, the measurement setting  $z = 0$  corresponds to a projective measurement in the  $Z$  basis (H/V polarisation basis), and measurement setting  $z = 1$  corresponds to a projective measurement in the  $X$  basis (D/A polarisation basis). This measurement device is experimentally implemented with the same optical components as the partial BSM device, where the condition for nonclassical interference between the incident qubit states at the 50:50 beam splitter is removed<sup>3</sup>. In this case, Charlie's measurement device performs a standard projective measurement, with measurement elements  $\{M_{c|z}\}$  for outcome  $c = 1$  being

$$M_{1|z=0} = |0\rangle\langle 0| \otimes |0\rangle\langle 0|, \quad (6.16)$$

$$M_{1|z=1} = |+\rangle\langle +| \otimes |+\rangle\langle +| + |- \rangle\langle -| \otimes |- \rangle\langle -|, \quad (6.17)$$

where  $|\pm\rangle = (|0\rangle \pm |1\rangle)/\sqrt{2}$ . A witness  $v$  for quantum unentangled measurements can then be constructed [135]:

$$v = \sum_{z=0,1} \sum_{x,y=0}^2 V_{c=1|x,y,z} p_{c=1|x,y,z}. \quad (6.18)$$

For simplicity, the notation  $c = 1$  is suppressed (the  $c = 2$  statistics are required for normalisation but play no role in the witness), writing instead

---

<sup>3</sup>This is done experimentally by adjusting the relative arrival time of the photon pairs incident upon the 50:50 beam splitter so that the photons do not arrive coincidentally.

$V_{x,y,z}$  and  $p_{x,y,z}$ . The maximal value of the witness for classical deterministic strategies was evaluated by theory collaborator Tamas Vértesi as  $v_{class} \leq 2$  [68], which is the witness for detecting quantum unentangled measurements. The coefficient matrices  $V_{x,y,z}$  are given by

$$V_{x,y,z=0} = \begin{pmatrix} 2 & 0 & 0 \\ 0 & 2 & -2 \\ 0 & -2 & -2 \end{pmatrix}, \quad V_{x,y,z=1} = \begin{pmatrix} 0 & 0 & 0 \\ 0 & 1 & -1 \\ 0 & -1 & 1 \end{pmatrix}, \quad (6.19)$$

and the theoretical probability distributions are

$$p_{x,y,z=0} = \left( \begin{array}{c|ccc} x, y & 0 & 1 & 2 \\ \hline 0 & 1 & 1/4 & 1/4 \\ 1 & 1/4 & 1/16 & 1/16 \\ 2 & 1/4 & 1/16 & 1/16 \end{array} \right), \quad (6.20)$$

$$p_{x,y,z=1} = \left( \begin{array}{c|ccc} x, y & 0 & 1 & 2 \\ \hline 0 & 1/2 & 1/2 & 1/2 \\ 1 & 1/2 & 7/8 & 1/8 \\ 2 & 1/2 & 1/8 & 7/8 \end{array} \right). \quad (6.21)$$

For the arrangement of qubit probe states (Fig. 6.2) and measurements presented, the maximum theoretical value of the witness for unentangled measurements is  $v_{th} = 3$ , clearly outperforming classical measurements ( $v_{class} \leq 2$ ). The witness for unentangled measurements was tested experimentally using this configuration of probe states and measurements.

### 6.3 Experiment

To experimentally test the semi-device-independent witnesses for entangled and quantum unentangled measurements, independent quantum state preparation devices were required to prepare Alice and Bob's qubit probe states, and a partial BSM device was required to act as Charlie's measurement device. A schematic of the experimental apparatus used for the demonstration is shown in figure 6.3.

The primary laser system employed in the experiment was a *Tsunami* model Titanium Sapphire laser supplied by manufacturer *Spectra-physics*. The laser was a pulsed system operating at 820nm centre wavelength with an 80MHz pulse repetition rate and pulse lengths  $\approx 100\text{fs}$ , corresponding to a full width half maximum bandwidth of  $\approx 5.5\text{nm}$ . The power in the output

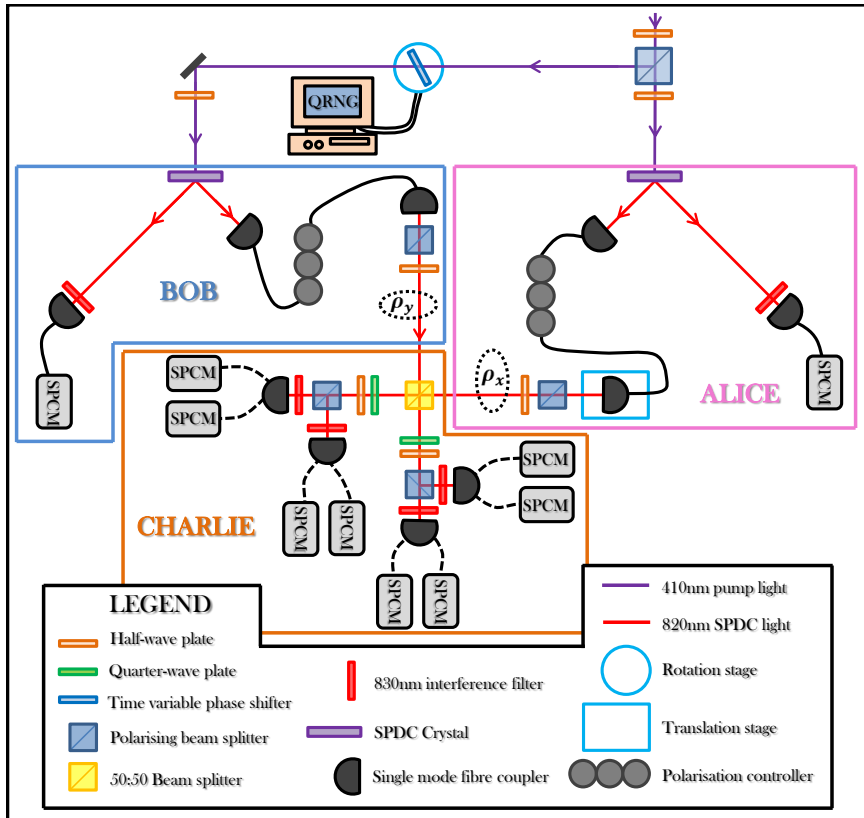


Figure 6.3: Experimental schematic for semi-device-independent verification of entangled measurements and quantum unentangled measurements. A pair of separate spontaneous parametric down-conversion (SPDC) sources creates Alice and Bobs photon pairs. One photon from each pair of Alice and Bobs sources acts as a heralding signal, detected by single-photon counting modules (SPCM). The remaining photons are sent via optical fiber (solid lines) to the inputs of Charlies partial BSM device. The type of measurement that Charlie enacts is changed with the translation stage. Dashed lines represent outputs from a 50:50 fiber beam splitter. The time variable phase shifter is a glass plate on a rotation stage connected to an online quantum random number generator [134], its purpose being to erase coherence between the pump beam shared by Alice and Bob, enforcing source independence and separability.

beam was  $\approx 1.6\text{W}$  at 820nm, and was focussed into a BBO crystal with a pump beam diameter  $\approx 60\mu\text{m}$  for collinear SHG, converting the 820nm pump to 410nm with a conversion efficiency of  $\approx 30\%$ . The BBO crystal was 2mm thick and sourced from *Newlight Photonics*. The 820nm pump beam was separated from the 410nm SHG beam using a pair of dispersion-

compensating prisms and four dichroic mirrors, each with  $\approx 98\%$  filtering efficacy in separating 820nm from 410nm. These preliminary systems are not displayed in figure 6.3.

### 6.3.1 Photon Sources

For the experimental demonstration, the 410nm SHG beam was used to pump a pair of separate type-I down conversion sources each constructed of a pair of BiBO crystals in the sandwich configuration [84]. The 410nm pump beam was directed towards each source, one for Alice and one for Bob, via a polarising beam splitter. Because the experiment didn't require polarisation-entangled photon pairs, each source ran in a non-polarisation-entangled configuration, ensured by pumping only one of the two sandwiched crystals in each source. The pump beam for each source was therefore horizontally polarised, which generated a pair of separable signal and idler photons in the state  $|\psi\rangle = |V\rangle_s \otimes |V\rangle_i$ . For both Alice and Bob, the signal photon  $|V\rangle_s$  was used to herald the presence of the idler photon  $|V\rangle_i$ . Alice and Bob's heralded idler photons were collected into optical fibres and directed towards Charlie's partial BSM device. Before arriving at Charlie's measurement device, Alice and Bob's idler photons were encoded in polarisation to act as the independent qubit probe states  $\hat{\rho}_x^A$  and  $\hat{\rho}_y^B$ . The encoding was performed using a PBS and half-wave plate. The joint state  $\hat{\rho}^{AB} = \hat{\rho}_x^A \otimes \hat{\rho}_y^B$  was assumed separable by virtue of the independent sources. To further strengthen the assumption of source independence, a time-varying-phase-shifter (TVPS) was placed in the pump beam of one source. The TVPS was attached to a rotation stage (rotating on an axis perpendicular to the pump beam) controlled by a quantum random number generator [134]. The function of the TVPS was to apply a random relative phase shift  $0 < \Delta\phi < 2\pi$  between the beams pumping each source every 502ms, further removing any possible coherence between the pump beams (see Chapter 5, Sec, 5.4.2).

### 6.3.2 Partial Bell State Measurement Device

Charlie's partial BSM was constructed from linear optical elements [60] (Sec. 2.6.5). The partial BSM device was characterised by measuring and optimising the nonclassical two-photon interference visibility, deduced from recording a Hong-Ou-Mandel (HOM) dip in four-fold coincidences. A Gaussian fit to the data resulted in a visibility  $\approx 90\%$  (Fig. 6.4). The slight asymmetry in count rates outside of the HOM dip was due to spatial decoupling

of an input-optical fibre resulting from slight off-axis translation of the  $z$ -translation stage.

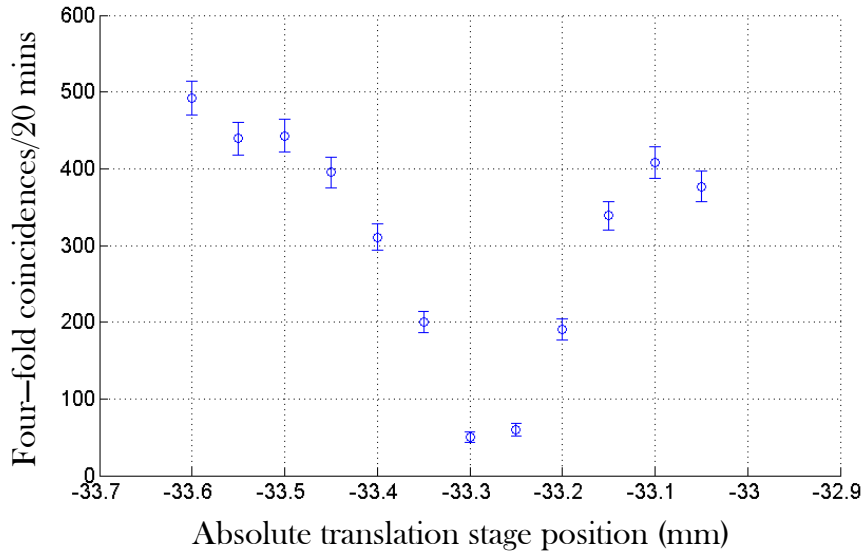


Figure 6.4: HOM dip recorded in four-fold coincidences for the semi-device-independent certification of entangled measurements. The dip appears in four-fold coincidences as one of the degrees of freedom between the initially identical photon pairs is varied. In this case, the relative difference in arrival time between photon pairs is adjusted by increasing the path length of one photon relative to the other, performed using a  $z$ -translation stage on one of Charlie's input couplers to his 50:50 beam splitter. A Gaussian fit to the data yielded a HOM visibility of  $\approx 90\%$ . The slight asymmetry in count rates outside of the HOM dip was due to spatial decoupling of an input-optical fibre resulting from slight off-axis translation of the  $z$ -translation stage.

In order to test the semi-device-independent witness for entangled measurements, it was noted that Charlie's partial BSM natively performed an entangled measurement, having measurement elements  $\{M_c\}$  corresponding to detection of the states  $|\Psi^+\rangle$ ,  $|\Psi^-\rangle$ , and  $|\Phi^\pm\rangle$  (Eqs. 6.4, 6.5, and 6.6). Experimentally, the device resolved the states  $|\Psi^+\rangle$  and  $|\Psi^-\rangle$  in coincidences between orthogonally polarised photon pairs. The states  $|\Phi^\pm\rangle$ , however, corresponded to degenerate-in-polarisation photon pairs leaving the 50:50 beam splitter in the same spatial mode. Detection of the  $|\Phi^\pm\rangle$  states therefore required photon-number resolution. Because Charlie's partial BSM

was constructed with single-photon counting modules, detection of the  $|\Phi^\pm\rangle$  states was performed using pseudo-number resolution. Psuedo-number resolution was achieved by replacing Charlie's standard output fibres with 50:50 fibre beam splitters. Photon pairs arriving at the 50:50 fibre beam splitters corresponding to the states  $|\Phi^\pm\rangle$  were therefore resolved in coincidences 50% of the time, corresponding to those times when the individual photons exited different beam splitter ports. A characterisation of Charlie's four 50:50 fibre beam splitters was performed to ensure the missed  $|\Phi^\pm\rangle$  detections were correctly accounted for. For an ideal 50:50 fibre beam splitter, a pair of photons will exit different output modes half of the time, so that a 2x multiplication of coincidence count rates accounts for the remainder of the  $|\Phi^\pm\rangle$  detections. In practice, splitting ratios different from 50:50 result in multiplication factors different from 2x when accounting for the remainder of the  $|\Phi^\pm\rangle$  detections. The actual multiplication factors were determined by first measuring the splitting ratios of each beam splitter using an 820nm laser diode. From these measured splitting ratios, the total probability for pairs of photons to exit different beam splitter output ports was calculated. From these probabilities, multiplication factors of 2.02, 2.04, 2.26, and 2.26 were determined which accounted for the missed  $|\Phi^\pm\rangle$  detections. This characterisation also aided in the interpretation of the experimental results.

To test the semi-device-independent witness for unentangled quantum measurements, Charlie's partial BSM device had to be modified to perform standard projective measurements, having measurement elements  $\{M_{c|z}\}$  given in Eqs. 6.16 and 6.17. This was achieved by eliminating the condition for nonclassical two-photon interference at the 50:50 beam splitter, performed by introducing distinguishability between incident photon pairs in the temporal degree of freedom. A translation stage on Alice's input coupler to Charlie's measurement device achieved this task. The random photon splitting effects of the 50:50 beam splitter and the four 50:50 fibre beam splitters were accounted for by recognising and appropriately grouping the detector firing patterns signalling detection of each measurement eigenstate.

### 6.3.3 Results and Analysis

Before testing the semi-device-independent witnesses, the qubit probe states  $\hat{\rho}_x^A$  and  $\hat{\rho}_y^B$  underwent a preliminary characterision to ensure accurate probe state preparations. The results of the characterisation also aided in understanding the final experimental results.

The preliminary characterisation measured the expectation values of the projective measurement operators  $\hat{\Pi}_H$  and  $\hat{\Pi}_V$  and compared the outcomes with theoretical predictions for each probe state preparation. To conduct the preliminary characterisation, the qubit probe states for Alice and Bob were prepared using a PBS and half-wave plate and sent into Charlie’s measurement device. Charlie’s measurement device was the partial BSM, so the qubit probe states undergoing characterisation first encountered the 50:50 beam splitter before reaching the necessary projective measurement elements. This was simply accounted for by treating Charlie’s 50:50 beam splitter as introduced loss, allowing the effects of the beam splitter to be ignored. Coincidences recorded between Alice and Bob’s heralding detectors and Charlie’s detectors after projective measurement in the H/V basis allowed the qubit probe states  $\hat{\rho}_x^A$  and  $\hat{\rho}_y^B$  to be characterised in this preliminary way. Table 6.1 presents the probe state characterisation results.

Probe state prep.	$\langle \hat{\Pi}_H^{Theory} \rangle$	$\langle \hat{\Pi}_V^{Theory} \rangle$	$\langle \hat{\Pi}_H^{Exp} \rangle$	$\langle \hat{\Pi}_V^{Exp} \rangle$
$ r_0^A\rangle =  H\rangle$	1	0	0.993	0.007
$ r_1^A\rangle = \frac{1}{2} H\rangle + \frac{\sqrt{3}}{2} V\rangle$	0.25	0.75	0.256	0.744
$ r_2^A\rangle = \frac{1}{2} H\rangle - \frac{\sqrt{3}}{2} V\rangle$	0.25	0.75	0.251	0.749
$ r_0^B\rangle =  V\rangle$	0	1	0.009	0.991
$ r_1^B\rangle = \frac{1}{2} V\rangle + \frac{\sqrt{3}}{2} H\rangle$	0.75	0.25	0.750	0.250
$ r_2^B\rangle = \frac{1}{2} V\rangle - \frac{\sqrt{3}}{2} H\rangle$	0.75	0.25	0.743	0.257

Table 6.1: Characterisation of Alice and Bob’s probe states for testing the semi-device-independent witness. Good agreement between experiment and theory was indicative of satisfactory state preparation. Uncertainties in experimental quantities are  $\pm 0.001$ .

The results of the preliminary characterisation found strong agreement with theory. The strong agreement led to the conclusion that Alice and Bob’s probe state preparation stages appeared to be preparing the appropriate qubit probe states required for a maximum violation of the semi-device-independent witnesses, however, because coherences were not measured (in the D/A and R/L polarisation bases), a conclusive statement of the fidelity between the experimental preparations and the ideal probe states could not be made.

After the preliminary characterisation, experimental statistics were gathered for the semi-device-independent verification of an entangled measurement performed by Charlie's partial BSM device. The experimental statistics  $p_{c|x,y}$  were collected for 24 hours in four-fold coincidences ( $\approx 300$  four-folds per hour) between Alice, Bob, and Charlie's detectors for all nine combinations  $x$  and  $y$  of Alice and Bob's qubit probe state preparations, finding

$$p_{1|x,y} = \left( \begin{array}{c|ccc} x,y & 0 & 1 & 2 \\ \hline 0 & 0.481 & 0.103 & 0.143 \\ 1 & 0.125 & 0.494 & 0.141 \\ 2 & 0.100 & 0.144 & 0.447 \end{array} \right), \quad (6.22)$$

$$\text{and } p_{2|x,y} = \left( \begin{array}{c|ccc} x,y & 0 & 1 & 2 \\ \hline 0 & 0.502 & 0.149 & 0.120 \\ 1 & 0.099 & 0.130 & 0.452 \\ 2 & 0.112 & 0.458 & 0.148 \end{array} \right), \quad (6.23)$$

where the experimental quantities have an associated statistical error resulting from Poissonian counting statistics ranging from  $\pm 0.01$  to  $\pm 0.025$ . The experimental statistics are to be compared with Eqs. 6.13 and 6.14, with divergence from theoretical predictions being the result of imperfect state preparation and measurement, and imperfections in optical elements (see Discussion). The semi-device-independent witness for an entangled measurement was then evaluated (Eq. 6.15), finding

$$w_{exp} = \sum_{c=1,2} \sum_{x,y=0}^2 W_{c|x,y} p_{c|x,y}, \quad (6.24)$$

$$= 1.32 \pm 0.07. \quad (6.25)$$

A witness parameter  $1 < w_{exp} < 1.5$  implies an entangled measurement, hence violating the bound for purely classical measurements  $w_{unent} = 1$  by more than 4 standard deviations. The theoretical prediction for the witness value given Alice and Bob's probe state arrangements and Charlie's measurement was  $w_{th} = 1.5$ , meaning the experimental observation was not maximal. Possible reasons for this discrepancy are outlined in the discussion.

Experimental statistics were also collected for the semi-device-independent certification of quantum unentangled measurements, performed by removing

nonclassical interference from Charlie’s partial BSM device. In that case, the device could be made to perform unentangled projective measurements in the H/V and D/A basis for settings  $z = 0$  and  $z = 1$  respectively. The experimental statistics  $p_{c|x,y,z}$  were again collected for all nine combinations  $x$  and  $y$  of Alice and Bob’s qubit probe state preparations, finding

$$p_{1|x,y,z=0} = \left( \begin{array}{c|ccc} x, y & 0 & 1 & 2 \\ \hline 0 & 0.994 & 0.255 & 0.232 \\ 1 & 0.241 & 0.059 & 0.065 \\ 2 & 0.262 & 0.092 & 0.065 \end{array} \right), \quad (6.26)$$

$$\text{and } p_{1|x,y,z=1} = \left( \begin{array}{c|ccc} x, y & 0 & 1 & 2 \\ \hline 0 & 0.484 & 0.384 & 0.588 \\ 1 & 0.593 & 0.827 & 0.201 \\ 2 & 0.403 & 0.120 & 0.820 \end{array} \right), \quad (6.27)$$

where all experimental quantities have an associated statistical error resulting from Poissonian counting statistics ranging from  $\pm 0.01$  to  $\pm 0.025$ . The experimental statistics are to be compared with Eqs. 6.20 and 6.21, again with divergence from theoretical predictions being the result of imperfect state preparation and measurement, and imperfections in optical elements (see Discussion). The semi-device-independent witness for an unentangled measurement was then evaluated (Eq. 6.18), finding

$$v_{exp} = \sum_{z=0,1} \sum_{x,y=0}^2 V_{c=1|x,y,z} p_{c=1|x,y,z} = 2.75 \pm 0.06. \quad (6.28)$$

$$(6.29)$$

A witness parameter  $2 < v_{exp} < 3$  implies nonclassical measurement, hence violating the bound for purely classical measurements  $v_{class} = 2$  by more than 12 standard deviations.

The experimental results for the semi-device-independent certification of entangled and quantum unentangled measurements successfully certify the nature of Charlie’s measurement in each case. Importantly, the data processing for the experiment was subjected to standard assumptions for an estimation scenario. First, it was assumed that the same statistics would result if the observers were free to choose their own ordering of preparations and measurements. Next, independent trials were assumed; that is, in each

run of the experiment, the statistics were described by Eq. 6.1. Finally, the fair sampling assumption was employed.

## 6.4 Discussion

The experimental evaluation of the witnesses for entangled and quantum unentangled measurements successfully confirmed the nature of Charlie’s measurement in each case. Interestingly, Alice and Bob’s qubit probe state arrangements  $\hat{\rho}_x^A$  and  $\hat{\rho}_y^B$  were expected to yield maximal violations of the witnesses  $w$  and  $v$ . However, the experimental observations  $w_{exp} = 1.32 \pm 0.07$  and  $v_{exp} = 2.75 \pm 0.06$  did not approach the maximal theoretical values  $w_{th} = 1.5$  and  $v_{th} = 3$ . It was concluded that the most likely cause of the discrepancies in the case of entangled measurements was due to imperfect HOM visibility, having  $\approx 90\%$  in this experiment. The expected reduction in maximum witness parameter  $w_{th}$  given an imperfect HOM visibility of  $\approx 90\%$  was calculated using a Mathematica script, which simulated the effects of spatial mode mismatch at Charlie’s 50:50 beam splitter (a common cause of imperfect HOM visibility). Based on the simulation results, the maximum witness parameter was expected to be  $w_{th} = 1.37$ , finding agreement with the experimental data to within experimental error. Importantly, the HOM interference visibility plays no role in witness violations for unentangled measurements, since the photons were made to be distinguishable in this scenario. As such, a reduced witness violation in the unentangled case may be attributed to small polarisation-dependent reflection/transmission coefficients at the BSM 50:50 beam splitter. Manufacturing high-quality beam splitter devices is an ongoing problem, and as such, the discrepancy between experiment and theory in the unentangled case would be well explained by small undesired polarisation-dependent transmission/reflection characteristics. Additionally, the discrepancy between experiment and theory could have also been attributed to imperfect state preparation. Although the analysis of the expectation values  $\langle \hat{\Pi}_H \rangle$  and  $\langle \hat{\Pi}_V \rangle$  for each of Alice and Bob’s state preparations were in alignment with theoretical predictions, an analysis of the state coherences was not performed, with poor coherences possibly accounting for the experimental results. Another possible cause of the discrepancy could have been attributed to imperfections in the 50:50 fibre beam splitters used to resolve and detect photon pairs in the same spatial mode corresponding to the  $|\Psi^\pm\rangle$  states. However, an accurate analysis of the fibre-beam splitter transmission characteristics accounted for imperfections of this kind.

Improvements to the experiment could be offered by accurately characterising the probe states to determine whether imperfect coherences in the probe states affect the experimentally observed witness values. Additionally, the experiment could be modified so that some or all of the standard assumptions of an estimation scenario need not be made, for instance by enforcing randomly sequenced state preparations/measurements and employing high efficiency single-photon and/or number-resolving detectors.

The semi-device-independent certification strategies presented in this chapter are viable to be extended to arbitrary dimensional systems with multiple parties and additional measurement outcomes, and can in-principle be used to certify an unknown process as entangled (for example, a controlled-NOT gate can be configured to implement an entangled measurement [145]). The theoretical techniques employed in this chapter can be used to devise witnesses for any kind of entangled measurement, hence providing a simple and efficient certification for entangled measurements and unentangled measurements, with the semi-device-independent approach requiring less calibration than more complex characterisation procedures (like quantum process tomography or quantum detector tomography [139, 140]). The distribution of entanglement in a quantum network through entanglement swapping, and many other applied and fundamental quantum tests, require the certification and characterisation of entangled measurements. As the tests presented in this chapter are based only on measurement statistics, they provide a very practical and powerful tool for the estimation of quantum systems and should find application in many quantum information protocols.

# Chapter 7

# Conclusion

Significant breakthroughs in scientific and technological understanding have, throughout history, originated from the exploration of unsolved problems in science. The beginning of the 20th century saw the transition from classical to quantum physics, ushering in a new era of challenges and unsolved problems. A well-known mystery emanating directly from that era is the notion of entanglement. Entangled particles exhibit quantum correlations in direct violation of our intuitive understanding of nature, and continue to affirm the integrity of quantum physics as a theoretical framework for describing nature. Furthermore, quantum correlations find application as a resource in powerful new technologies, with contemporary proof-in-principle demonstrations finding widespread attention in government, industrial, and commercial settings.

This thesis explored quantum correlations between entangled photon pairs generated in linear optical systems. The entangled photon pairs were tested against models of nature adhering to intuitive principles, called local models, finding violations in instances where quantum predictions held true. Chapter 2 introduced the experimental framework of linear optics, and introduced traditional local models for correlations, namely Bell's local model and the EPR steering framework.

Chapter 3 introduced an arbitrarily-loss-tolerant EPR steering protocol, and experimentally demonstrated EPR steering with no detection loophole over 1km of optical fibre. The loss-tolerant protocol certifies quantum correlations attributed to EPR-steerable states in the presence of significant photon loss, which is typically encountered in photon transmission channels and detectors. As modern quantum information protocols continue to

rely on the verification of shared quantum correlations over larger distances, loss-tolerant protocols become important for fundamental tests, and for the secure sharing of private information over long distances. The demonstration impacts studies of fundamental physics, and finds application in one-sided quantum key distribution (QKD) protocols, a powerful technology for the secure sharing of information. As QKD protocols continue to find success over distances approaching communication feasibility [146], and EPR steering protocols are extended to multiple parties and degrees of freedom [147], it is likely that the loss tolerant protocols introduced in Chapter 3 will benefit the growing academic interest in quantum correlations and its applications.

The security of one-sided QKD protocols is guaranteed only for successful violations of EPR steering inequalities which necessarily requires trust in one protocol participant. Chapter 4 introduced a new theoretical framework for removing a referee's need to trust remote parties when certifying quantum correlations via EPR steering inequalities. The work drew inspiration from recently elucidated semiquantum games, with the protocol introduced in chapter 4 employing a so-called 'quantum referee'. The quantum-refereed EPR steering game removed the referee's need for trust in remote parties by endowing the quantum referee with a one way quantum channel. The quantum referee then only needed to trust his own ability to accurately prepare and send quantum signals, transferring the trust from remote party to referee. The protocol forms a measurement-device-independent certifier of EPR-steerable quantum correlations – a framework which has normally only been accessible through Bell inequality violations, with such frameworks garnering considerable interest from both foundational and applied standpoints. The introduction of the quantum-refereed EPR steering game may find application in one-sided device independent QKD protocols, with a particularly powerful element being the inability for parties to co-conspire against the quantum referee. Such co-conspiratorial strategies might involve the execution of pre-arranged measurement strategies, which can be countered by randomly changing the quantum referee's state preparation basis between runs. Such utility extends the range of scenarios to which one-sided device independent QKD could be applied. Improvements to the protocol and its applications could also be offered by introducing long, lossy transmission channels, and potentially applying the outcomes of research into loss-tolerant EPR steering towards loss-tolerant measurement-device-independent EPR steering games.

The certification of quantum correlations via local models is an active field

of research and an important tool for understanding nature. Chapter 5 presented an experimental test of new local models applicable to entanglement swapping scenarios, called ‘bilocal models’. The theoretical investigations were motivated by a disconnect between Bell’s local model and the experimental architecture employed in entanglement swapping protocols. In particular, Bell’s local model assumes a single particle source, whereas entanglement swapping protocols employ two particle sources. The bilocal models introduced in chapter 5 allow for simpler tests of quantum correlations in entanglement swapping scenarios, and may be extended to multiple particle sources and quantum network architectures. Such extensions could find widespread use in the characterisation of concatenated entanglement swapping stages in quantum networks, and may offer increased utility in the presence of noise. The certification of nonbilocal correlations may also find use in certifying the existence of quantum teleportation channels, and may find applications in multi-partite device-independent frameworks, akin to the fate of Bell’s inequalities in the case of standard device-independence. Bilocal models may also benefit from loophole-free demonstrations, particularly due to the perplexing nature of quantum correlations arising between particles with no common history. Recent proposals to close the freedom-of-choice loophole in tests of Bell’s theorem using distant cosmic quasars [107] may be carried over to the testing of bilocal models, whereby large numbers of quasars could be used from across the universe to inform the measurement settings employed by multiple different parties. Such an ambitious experiment would be interesting from the standpoint of fundamental physics.

The final chapter explored the certification of entangled measurements. An entangled measurement is one which entangles initially separable input states after measurement, with entangled measurements finding a wide array of applications in contemporary optical quantum information protocols. Traditionally, measurement characterisation requires access to well calibrated particle sources applicable to the measurement. Chapter 6 introduced a means of certifying unknown measurement devices as entangled using only experimental statistics derived from preparing and measuring quantum probe states of restricted Hilbert space dimension. Importantly, the newly introduced certification protocol is semi-device-independent, requiring no information about the workings of the state preparation devices (other than the restricted dimensionality assumption) or the measurement device. The certification strategy can be extended to arbitrary dimensional systems with multiple parties and measurement devices, and presents a powerful tool for the estimation of quantum systems with application in many

quantum information protocols. The semi-device-independent nature of the certification lends itself to the characterisation of untrusted measurement devices, and may potentially be used for uncovering the function of unknown quantum networks on a device-by-device basis.

By introducing and experimentally testing local models, and introducing and experimentally testing strategies for certifying the nonclassical nature of measurements, this thesis has provided direct contributions towards the understanding of quantum correlations and quantum measurements, their mysterious and powerful role in nature, and their indispensable role in developing new technologies.

# Appendix

## Appendix 1: Constructing and aligning a Sagnac interferometer

This Appendix details the procedure for constructing and aligning the Sagnac interferometer employed in chapter 3. The procedure is borrowed and adapted from Devin Smith, courtesy of his Masters thesis, Ref. [148].

Step 1. Align pump beam to a pair of level pinholes, so that the pump beam is propagating perpendicular to the table surface.

Step 2. Place a polarising element into the pump beam, for instance, a Glan Taylor polarising prism or a polarising beam splitter (PBS). Place a half-wave plate (HWP) into the pump beam after the polarising element. Calibrate if necessary and check alignment to pinholes. The GT serves to ‘clean’ the polarisation pump mode, and the HWP prepares the polarisation into the Sagnac interferometer.

Step 3. If focussing optics are required, place optics into pump beam (on translation stage if space permits) and check pinhole alignment.

Step 4. Place dichroic mirror into pump beam. The dichroic mirror is necessary to separate downconverted light from the co-propagating pump beam.

Step 5. Insert dual-wavelength anti-reflection coated PBS into pump beam. Align PBS to maximise polarisation extinction ratio.

Step 6. Place interferometer mirrors. The angle of incidence to the mirror should form an angle  $\approx 22.5^\circ$ .

Step 7. The interferometer can be prealigned by observing the point of

beam impact on the mirror surfaces. That is, by ensuring that the counter-propagating beams impact each mirror at the same point, i.e. the horizontally polarised beam impacts mirrors 1 and 2 at the same place as the vertically polarised beam, the interferometer can be prealigned. Room lights may need to be off to observe the slight glow from the mirror impact points.

Step 8. At this point, all the pump light should exit from one output of the Sagnac interferometer. The beam in this output port can be used to finely tune the interferometer alignment. Fine-tuning of the alignment is performed by placing a polarising element into the output beam, set to measure polarisation in the D/A or R/L basis. Interference fringes should occur. Fine-tuning of the interferometer alignment is performed by observing the interference fringes as the interferometer mirrors are adjusted. When the interference fringes appear very large and widely spaced (ideally only a single dark or light spot should appear), the interferometer is aligned.

Step 9. Check that the counter-propagating beams still impact the mirrors at the same point.

Step 10. Insert the dual-wavelength HWP into one arm of the interferometer. For now, set the HWP to its optic axis, so the pump beam remains unaffected.

Step 11. Place the output coupler for collecting the signal photon. Using an alignment laser directed out of the output coupler (with a centre wavelength equivalent to the desired down conversion wavelength), ensure that the optics for the coupler place the focal point in the centre of the interferometer, where the nonlinear crystal will be. Make adjustments to the collection waist and coupler position as necessary.

Step 12. As a prealignment step, couple the output coupler to the pump beam. Because the wavelengths and focussing conditions of the pump beam and output coupler fibre are mismatched, the coupling may not be optimal.

Step 13. Place the output coupler for collecting the idler photon. Using an alignment laser (again with a centre wavelength equivalent to the desired down conversion wavelength), couple the idler coupler to the signal coupler.

Step 14. Insert interference/background rejection filters. Insert one filter at a time, back-reflect the filter, and realign the signal and idler couplers to

one another after each filter is placed.

Step 15. Insert the nonlinear crystal into the centre of the Sagnac interferometer. Adjust the crystal to maximise signal–idler coupler transmission (using the same alignment laser as steps 11 and 13).

Step 16. Make minor adjustments to realign the signal and idler couplers to one another (if necessary).

Step 17. Insert polarisation analysers into each output to aid in fine tuning when detecting single photons.

Step 18. Locate the maximum single photon coincident count rates when measuring H/V (signal/idler) and V/H (corresponding to clockwise and anti-clockwise pumping respectively) without adjusting the output coupler angle degree of freedom. Adjust the couplers to ensure equality between count rates when measuring H/V and V/H.

Step 19. Use the polarisation analysers to observe the coincidence count rates while measuring one of the entangled bases (D/A or R/L). Check the visibility in this basis. Ensure the count rates in this basis are approximately equal to the count rates in the H/V basis.

Step 20. Optimise the count rates in the entangled basis by beamwalking. The zoom of the idler coupler can be adjusted if necessary.

Step 21. Monitor entanglement visibility and source efficiency. Repeating steps 18–20 may assist in increasing these parameters. If the source is performing poorly, realign the interferometer fringes (step 8). Further details can be found in Devin Smith’s Masters thesis.

## Appendix 2: Experimental Error Calculation for Loss–Tolerant EPR steering

The following Appendix is an in-depth account of the error analysis performed for the loss–tolerant EPR steering experiment (Chapter 3). The majority of the analysis was performed by theory collaborators Cyril Branciard and David Evans, with input from experimental collaborator Dylan Saunders.

In order to be sure that we have demonstrated EPR-steering, we need to know that the uncertainty in our measured  $S_n$  is not so large as to make it possible that the true value would be less than the EPR-steering bound  $C_n(\epsilon)$ . By “true value” we mean the value that would be obtained if all of the assumptions that went into deriving the bound  $C_n(\epsilon)$  were satisfied, namely that Bob’s measurements are perfect, and that the experiment yields the true quantum averages (which would require an infinite sample size). That is, we need to take into account (1) imperfection of Bob’s measurements that could lead to an over-estimation of  $S_n$  (systematic error), and (2) statistical errors in  $S_n$ . These are determined in Parts 1 and 2 below, respectively. Note that we do not have to worry about systematic errors in Alice’s measurement settings, since we make no assumptions about them in order to derive the EPR-steering bound.

### **Experimental Error Calculation, Part 1: Systematic Error**

$$\Delta S_n^{sys}$$

In an ideal experiment, Bob’s measurement corresponds to projecting his state onto one out of two orthogonal pure states, represented by opposite vectors  $\mathbf{u}_k$  and  $-\mathbf{u}_k$  on the Bloch sphere. Bob’s actual measurement will be nonideal in two ways. First, because the manufactured PBS has only a finite extinction ratio, the “projection operators” for Bob’s measurements will actually comprise a projector mixed with a very small ( $\approx 0.01$ ) amount of the identity operator. This can only ever decrease the correlation with Alice’s results, so if Bob takes this effect into account, it can only be to Alice’s benefit, by making it easier for her to convince him that she is steering his state. Therefore, to subject our demonstration of steering to the highest level of rigour, we can ignore this imperfection. The second sort of imperfection is that the true states onto which Bob projects, corresponding to vectors  $\tilde{\mathbf{u}}_k$  and  $-\tilde{\mathbf{u}}'_k$  on the Bloch sphere, differ slightly from  $\mathbf{u}_k$  and  $-\mathbf{u}_k$  respectively. Note also that in our experiment Bob used only one detector, for reasons of space efficiency; thus he needs to implement two different projections for each choice of setting  $k$ , and hence  $\tilde{\mathbf{u}}'_k$  is not necessarily equal to  $\tilde{\mathbf{u}}_k$ . These errors arise from Bob’s inability to perform rotations on the Bloch sphere to arbitrary accuracy, for the following reasons: a. due to imperfect alignment of the optic axis of his wave plates (QWP and HWP) with projection axis ( $\hat{\sigma}_z$ ) of the PBS, b. the repeatability error in the motorised stages (setting the angles of both wave plates), and c. due to wave plate imperfections – their polarisation retardance is quoted only to within  $\pm\pi/250$ . The magni-

tudes of all of these errors is systematically determined, and a Monte Carlo simulation including all of the aforementioned factors allows us to determine the maximum infidelity of Bob's actual measurements ( $\tilde{\mathbf{u}}_k$ ) with his ideal measurements ( $\mathbf{u}_k$ ). Unlike the error due to a finite PBS extinction ratio, Bob's measurement misalignment can, in principle, make it easier for Alice to fake steering his state. Therefore it is essential to bound the error in our measured  $S_n$  due to this sort of error.

Because Bob only uses a single detector, we define the outcome  $B_k = +1$  as being Bob getting a photon and “discovering” that he was projecting in the direction  $\tilde{\mathbf{u}}_k$ , and  $B_k = -1$  likewise but projecting in the direction  $-\tilde{\mathbf{u}}'_k$ . Provided (as is the case) that Bob chooses to project in the directions  $\tilde{\mathbf{u}}_k$  and  $-\tilde{\mathbf{u}}'_k$  with equal probability, if there were no misalignment errors then the rate of occurrence of the event “ $B_k = +1$  or  $B_k = -1$ ” would be independent of Alice's results. But in the nonideal situation we cannot make that assumption. Therefore the observed probabilities  $\tilde{P}(A_k, B_k)$  for the four possible coincidences (i.e. postselected on both Alice and Bob detecting a photon) are defined as

$$\tilde{P}(A_k, B_k = +1) = R_{\tilde{\mathbf{u}}_k}(A_k, B_k = +1)/\mathcal{R}_k, \quad (7.1)$$

$$\tilde{P}(A_k, B_k = -1) = R_{\tilde{\mathbf{u}}'_k}(A_k, B_k = -1)/\mathcal{R}_k, \quad (7.2)$$

$$\text{with } \mathcal{R}_k = \sum_{A_k=\pm 1} [R_{\tilde{\mathbf{u}}_k}(A_k, B_k = +1) + R_{\tilde{\mathbf{u}}'_k}(A_k, B_k = -1)]. \quad (7.3)$$

where  $R$  stands for the rate of the corresponding events occurring.

Let us represent the state Bob receives, conditioned on Alice's output  $A_k = \pm 1$ , by a vector  $\mathbf{v}_{A_k}^B$  in the Bloch sphere, with  $|\mathbf{v}_{A_k}^B| \leq 1$ ; note that these states do not depend on Bob's setup,  $\tilde{\mathbf{u}}_k$  or  $\tilde{\mathbf{u}}'_k$ . The rates  $R_{\tilde{\mathbf{u}}_k^{(\prime)}}(A_k, B_k)$  are then given by

$$R_{\tilde{\mathbf{u}}_k^{(\prime)}}(A_k, B_k) = R_{\tilde{\mathbf{u}}_k^{(\prime)}}(A_k) P_{\tilde{\mathbf{u}}_k^{(\prime)}}(B_k | A_k) \quad (7.4)$$

$$\propto P_{\tilde{\mathbf{u}}_k^{(\prime)}}(A_k) \frac{1 + (-1)^{B_k} \tilde{\mathbf{u}}_k^{(\prime)} \cdot \mathbf{v}_{A_k}^B}{2}. \quad (7.5)$$

Note that Alice's marginal probabilities,  $P_{\tilde{\mathbf{u}}_k^{(\prime)}}(A_k)$ , normalized so that they sum to one for  $A_k = \pm 1$ , do not depend on Bob's measurement setup:  $P_{\tilde{\mathbf{u}}_k}(A_k) = P_{\tilde{\mathbf{u}}'_k}(A_k) \equiv P(A_k)$ ; otherwise Bob could signal instantaneously

to Alice. Note also that these may be slightly different from Alice's experimentally observed marginals  $\tilde{P}(A_k)$  calculated from the full postselected distribution  $\tilde{P}(A_k, B_k)$ .

From equation (7.2) and equation (7.5), one can calculate the experimentally observed correlations  $\tilde{E}_k = \langle A_k \tilde{\sigma}_k^B \rangle$  (corresponding to the actual measurement “ $\tilde{\sigma}_k^B$ ”, rather than the ideal one,  $\hat{\sigma}_k^B$ ) to be

$$\tilde{E}_k \equiv \sum_{A_k, B_k} A_k B_k \tilde{P}(A_k, B_k) \quad (7.6)$$

$$\begin{aligned} &= \left[ P(A_k = +1) \frac{1 + \tilde{\mathbf{u}}_k \cdot \mathbf{v}_{A_k=+1}^B}{2} - P(A_k = -1) \frac{1 + \tilde{\mathbf{u}}_k \cdot \mathbf{v}_{A_k=-1}^B}{2} \right. \\ &\quad \left. - P(A_k = +1) \frac{1 - \tilde{\mathbf{u}}_k \cdot \mathbf{v}_{A_k=+1}^B}{2} + P(A_k = -1) \frac{1 - \tilde{\mathbf{u}}_k \cdot \mathbf{v}_{A_k=-1}^B}{2} \right] / \mathcal{N}_k. \end{aligned} \quad (7.7)$$

Here  $\mathcal{N}_k$  is defined so that the four terms above (without the minus signs) sum to one. Defining

$$\bar{\mathbf{u}}_k \equiv (\tilde{\mathbf{u}}_k + \tilde{\mathbf{u}}'_k) / 2, \quad (7.8)$$

$$\bar{\mathbf{v}}_k \equiv P(A_k = +1) \mathbf{v}_{A_k=+1}^B - P(A_k = -1) \mathbf{v}_{A_k=-1}^B, \quad (7.8)$$

$$\delta \mathbf{u}_k \equiv (\tilde{\mathbf{u}}_k - \tilde{\mathbf{u}}'_k) / 2,$$

$$\delta \mathbf{v}_k \equiv P(A_k = +1) \mathbf{v}_{A_k=+1}^B + P(A_k = -1) \mathbf{v}_{A_k=-1}^B, \quad (7.9)$$

we can rewrite  $\tilde{E}_k$  more simply as

$$\tilde{E}_k = \bar{\mathbf{u}}_k \cdot \bar{\mathbf{v}}_k / \mathcal{N}_k \quad \text{with} \quad \mathcal{N}_k = 1 + \delta \mathbf{u}_k \cdot \delta \mathbf{v}_k, \quad (7.10)$$

while the “true value”  $E_k$  of the correlation  $\langle A_k \hat{\sigma}_k^B \rangle$  (corresponding now to the ideal measurement settings  $\pm \mathbf{u}_k$ ) is simply  $E_k = \mathbf{u}_k \cdot \bar{\mathbf{v}}_k$ .

In order to quantify the deviation of  $\tilde{E}_k$  from its “true value”  $E_k$ , we characterize the misalignment of the vectors  $\tilde{\mathbf{u}}_k^{(\prime)}$  by their scalar product with  $\mathbf{u}_k$ , the ideal setting:  $\tilde{\mathbf{u}}_k^{(\prime)} \cdot \mathbf{u}_k \equiv \chi_k^{(\prime)}$ . Further, we assume that we can bound the misalignment by  $\chi_k^{(\prime)} \geq X_k > 0$ , for some  $X_k$  less than, but close to, unity. One can then immediately prove the following, which will be useful later:

$$\begin{aligned} |\bar{\mathbf{u}}_k|^2 + |\delta\bar{\mathbf{u}}_k|^2 &= 1 \\ X_k^2 \leq |\bar{\mathbf{u}}_k|^2 &\leq 1 \\ \text{and } 0 \leq |\delta\bar{\mathbf{u}}_k|^2 &\leq 1 - X_k^2. \end{aligned} \quad (7.11)$$

Let us start by bounding the normalisation coefficient  $\mathcal{N}_k$ . For that, first note that  $|\bar{\mathbf{v}}_k|, |\delta\mathbf{v}_k| \leq 1$ , and

$$\begin{aligned} |\bar{\mathbf{v}}_k|^2 + |\delta\mathbf{v}_k|^2 &= 2 P(A_k = +1)^2 |\mathbf{v}_{A_k=+1}^B|^2 \\ &\quad + 2 P(A_k = -1)^2 |\mathbf{v}_{A_k=-1}^B|^2, \\ &\leq 2 P(A_k = +1)^2 + 2 P(A_k = -1)^2 = 1 + (\delta P_k^A)^2, \end{aligned} \quad (7.12)$$

where  $\delta P_k^A \equiv P(A_k = +1) - P(A_k = -1)$ . Defining in a similar way  $\delta\tilde{P}_k^A \equiv \tilde{P}(A_k = +1) - \tilde{P}(A_k = -1)$ , we find, using equation (7.7),  $\mathcal{N}_k \delta\tilde{P}_k^A = \delta P_k^A + \delta\mathbf{u}_k \cdot \bar{\mathbf{v}}_k$ . Besides, from equation (7.10) we have  $|\bar{\mathbf{u}}_k| |\bar{\mathbf{v}}_k| \geq \mathcal{N}_k \tilde{E}_k$ . Hence, following on equation (7.12),

$$\begin{aligned} |\delta\mathbf{v}_k|^2 &\leq 1 + (\mathcal{N}_k \delta\tilde{P}_k^A - \delta\mathbf{u}_k \cdot \bar{\mathbf{v}}_k)^2 - |\bar{\mathbf{v}}_k|^2 \\ &\leq 1 + \mathcal{N}_k^2 (\delta\tilde{P}_k^A)^2 + 2 \mathcal{N}_k |\delta\tilde{P}_k^A| |\delta\mathbf{u}_k| |\bar{\mathbf{v}}_k| - |\bar{\mathbf{u}}_k|^2 |\bar{\mathbf{v}}_k|^2 \end{aligned} \quad (7.13)$$

$$\leq 1 + 2 \mathcal{N}_k |\delta\tilde{P}_k^A| \sqrt{1 - X_k^2} - \mathcal{N}_k^2 [\tilde{E}_k^2 - (\delta\tilde{P}_k^A)^2]. \quad (7.14)$$

Now, for typical experimental values, the previous expression decreases with  $\mathcal{N}_k$ . From equations (7.10) and (7.11), we have  $\mathcal{N}_k \geq 1 - |\delta\mathbf{u}_k| |\delta\mathbf{v}_k| \geq 1 - \sqrt{1 - X_k^2} |\delta\mathbf{v}_k|$ , so that we get

$$\begin{aligned} |\delta\mathbf{v}_k|^2 &\leq 1 + 2 \left(1 - \sqrt{1 - X_k^2} |\delta\mathbf{v}_k|\right) |\delta\tilde{P}_k^A| \sqrt{1 - X_k^2} \\ &\quad - \left(1 - \sqrt{1 - X_k^2} |\delta\mathbf{v}_k|\right)^2 [\tilde{E}_k^2 - (\delta\tilde{P}_k^A)^2] \end{aligned} \quad (7.15)$$

$$\leq 1 - \tilde{E}_k^2 + (\delta\tilde{P}_k^A)^2 + 2 |\delta\tilde{P}_k^A| \sqrt{1 - X_k^2} + 2 \sqrt{1 - X_k^2} \tilde{E}_k^2 |\delta\mathbf{v}_k|, \quad (7.16)$$

where the negative terms we discarded are negligible for our experimental parameters, so do essentially not affect the tightness of the above bound. By resolving the quadratic equation in  $|\delta\mathbf{v}_k|$  above, we further obtain

$$|\delta \mathbf{v}_k| \leq \sqrt{1 - X_k^2} \tilde{E}_k^2 \quad (7.17)$$

$$+ \sqrt{(1 - X_k^2) \tilde{E}_k^4 + 1 - \tilde{E}_k^2 + (\delta \tilde{P}_k^A)^2 + 2 |\delta \tilde{P}_k^A| \sqrt{1 - X_k^2}}, \quad (7.18)$$

which involves only terms obtainable from experimental data. Substituting back into equation (7.10) we obtain  $|\mathcal{N}_k - 1| \leq \delta \mathcal{N}_k$ , where

$$\begin{aligned} \delta \mathcal{N}_k &\equiv (1 - X_k^2) \tilde{E}_k^2 \\ &+ \sqrt{1 - X_k^2} \sqrt{(1 - X_k^2) \tilde{E}_k^4 + 1 - \tilde{E}_k^2 + (\delta \tilde{P}_k^A)^2 + 2 |\delta \tilde{P}_k^A| \sqrt{1 - X_k^2}}. \end{aligned} \quad (7.19)$$

Let us now decompose the vectors  $\mathbf{u}_k$  and  $\bar{\mathbf{v}}_k$  onto  $\bar{\mathbf{u}}_k$ :

$$\mathbf{u}_k = \frac{\chi_k + \chi'_k}{2|\bar{\mathbf{u}}_k|} \frac{\bar{\mathbf{u}}_k}{|\bar{\mathbf{u}}_k|} + \sqrt{1 - \frac{(\chi_k + \chi'_k)^2}{4|\bar{\mathbf{u}}_k|^2}} \bar{\mathbf{u}}_k^{\perp,u}, \quad (7.20)$$

$$\bar{\mathbf{v}}_k = \frac{\mathcal{N}_k \tilde{E}_k}{|\bar{\mathbf{u}}_k|} \frac{\bar{\mathbf{u}}_k}{|\bar{\mathbf{u}}_k|} + \sqrt{|\bar{\mathbf{v}}_k|^2 - \frac{\mathcal{N}_k^2 \tilde{E}_k^2}{|\bar{\mathbf{u}}_k|^2}} \bar{\mathbf{u}}_k^{\perp,v} \quad (7.21)$$

where  $\bar{\mathbf{u}}_k^{\perp,u}$  and  $\bar{\mathbf{u}}_k^{\perp,v}$  are two unit vectors on the Bloch sphere, both orthogonal to  $\bar{\mathbf{u}}_k$ . One then gets

$$\begin{aligned} \Delta E_k &\equiv |E_k - \tilde{E}_k| = |\mathbf{u}_k \cdot \bar{\mathbf{v}}_k - \tilde{E}_k| \\ &= \left| \frac{\chi_k + \chi'_k}{2|\bar{\mathbf{u}}_k|} \frac{\mathcal{N}_k \tilde{E}_k}{|\bar{\mathbf{u}}_k|} - \tilde{E}_k + \sqrt{1 - \frac{(\chi_k + \chi'_k)^2}{4|\bar{\mathbf{u}}_k|^2}} \sqrt{|\bar{\mathbf{v}}_k|^2 - \frac{\mathcal{N}_k^2 \tilde{E}_k^2}{|\bar{\mathbf{u}}_k|^2}} \bar{\mathbf{u}}_k^{\perp,u} \cdot \bar{\mathbf{u}}_k^{\perp,v} \right| \\ &\leq \left| \frac{\chi_k + \chi'_k}{2} \frac{\mathcal{N}_k}{|\bar{\mathbf{u}}_k|^2} - 1 \right| |\tilde{E}_k| + \sqrt{1 - X_k^2} \sqrt{1 - \mathcal{N}_k^2 \tilde{E}_k^2}. \end{aligned} \quad (7.22)$$

To bound this further, one can show that  $X_k \leq (\chi_k + \chi'_k)/2|\bar{\mathbf{u}}_k|^2 \leq 1/X_k$ . Using the bound on  $\mathcal{N}_k$  derived above, we finally obtain

$$\Delta E_k \leq (1 - X_k + \delta \mathcal{N}_k) |\tilde{E}_k| / X_k + \sqrt{1 - X_k} \sqrt{1 - (1 - \delta \mathcal{N}_k)^2 \tilde{E}_k^2}, \quad (7.23)$$

where all of these quantities are experimentally defined. Because systematic errors may not be independent, we add them linearly to obtain the total systematic error in  $S_n$  to be at most

Table 7.1: Size of error factors contributing to  $\Delta S_n^{sys}$  – Fig. 3.4 data – without 1 km fiber

$n$	$\Delta S_n^{sys}$	$\frac{1}{n} \sum (1 - X_k + \delta \mathcal{N}_k)  \tilde{E}_k  / X_k$	$\frac{1}{n} \sum \sqrt{1 - X_k} \sqrt{1 - (1 - \delta \mathcal{N}_k)^2 \tilde{E}_k^2}$
$n = 3$	0.0049	0.00290	0.00195
$n = 4$	0.0052	0.00311	0.00206
$n = 6$	0.0045	0.00272	0.00182
$n = 10$	0.0045	0.00270	0.00180
$n = 16$	0.0046	0.00277	0.00185

Table 7.2: Size of error factors contributing to  $\Delta S_n^{sys}$  – Fig. 3.4 data – with 1 km fiber

$n$	$\Delta S_n^{sys}$	$\frac{1}{n} \sum (1 - X_k + \delta \mathcal{N}_k)  \tilde{E}_k  / X_k$	$\frac{1}{n} \sum \sqrt{1 - X_k} \sqrt{1 - (1 - \delta \mathcal{N}_k)^2 \tilde{E}_k^2}$
$n = 10$	0.0057	0.00339	0.00232
$n = 16$	0.0063	0.00370	0.00256

$$\Delta S_n^{sys} = \frac{1}{n} \sum_k \left[ (1 - X_k + \delta \mathcal{N}_k) |\tilde{E}_k| / X_k + \sqrt{1 - X_k} \sqrt{1 - (1 - \delta \mathcal{N}_k)^2 \tilde{E}_k^2} \right]. \quad (7.24)$$

The size of the different components of this systematic error can be seen in Tables 7.1 and 7.2. The indicative sizes of the basic experimental parameters used to calculate the systematic error (they vary only slightly with  $n$  and  $k$ ) are:  $\tilde{E}_k \approx 0.99$ ,  $1 - X_k \approx 2 \times 10^{-4}$ , and  $|\delta \hat{P}_k^A| \approx 0.02$ , implying  $\delta \mathcal{N}_k \approx 0.002$ .

### Experimental Error Calculation, Part 2: Statistical Error $\Delta S_n^{stat}$

The statistical error component  $\Delta S_n^{stat}$  in the total error  $\Delta S_n$  is a result of having a finite ensemble size. The error in the total number of Alice–Bob coincident events  $N_c$  is  $\pm \sqrt{N_c}$ , as governed by Poissonian statistics. The error  $\Delta S_n^{stat}$  is determined by simply propagating the error in the counting errors through to the calculation of the joint probabilities  $\langle A_k \hat{\sigma}_k^B \rangle$ . This propagation provides the value  $\Delta \langle A_k \hat{\sigma}_k^B \rangle$ , and each of these terms contribute in quadrature to  $\Delta S_n^{stat}$ .

Table 7.3: Size of systematic and statistical error factors contributing to  $\Delta S_n$  – Fig. 3.4 data – without 1 km fiber

$n$	$S_n$	$\Delta S_n$	$\Delta S_n^{sys}$	$\Delta S_n^{stat}$
$n = 3$	0.989	0.0053	0.0048	0.0022
$n = 4$	0.990	0.0059	0.0052	0.0029
$n = 6$	0.990	0.0051	0.0045	0.0023
$n = 10$	0.991	0.0049	0.0045	0.0019
$n = 16$	0.991	0.0048	0.0046	0.0015

Table 7.4: Size of systematic and statistical error factors contributing to  $\Delta S_n$  – Fig. 3.4 data – with 1 km fiber

$n$	$S_n$	$\Delta S_n$	$\Delta S_n^{sys}$	$\Delta S_n^{stat}$
$n = 10$	0.9847	0.0063	0.0057	0.0028
$n = 16$	0.9805	0.0067	0.0063	0.0023

### Experimental Error Calculation, Part 3: Total Error

Combining the statistical error with the systematic error derived before, we calculate the error in the experimental value of  $S_n$  as

$$\Delta S_n = \sqrt{(\Delta S_n^{sys})^2 + (\Delta S_n^{stat})^2}.$$

The magnitude of both the systematic ( $\Delta S_n^{sys}$ ) and statistical ( $\Delta S_n^{stat}$ ) errors in the data presented in Fig. 3.4 is shown in Tables 7.3 and 7.4.

### Appendix 3: Constructing quantum-refereed steering games [99]

The following Appendix is an in-depth account of the derivation of the payoff function for the quantum refereed EPR steering protocol (chapter 4). The derivation was performed by theory collaborator Michael Hall.

A quantum state  $\rho^{AB}$  on some Hilbert space  $H_A \otimes H_B$ , shared between two parties Alice and Bob, is defined to be nonsteerable by Alice if and only if there is a local hidden state (LHS) model  $\{\rho_\lambda^B; p(\lambda)\}$  for Bob [102], i.e., if and only if the joint probability of measurement outcomes  $a$  and  $b$ , for

arbitrary measurements  $\mathcal{A}$  and  $\mathcal{B}$  made by Alice and Bob, can be written in the form  $p(a, b) = \sum_{\lambda} p(\lambda)p(a|\lambda)p(b|\lambda)$ , with  $p(b|\lambda)$  restricted to have the quantum form  $\text{Tr}_B[\rho_{\lambda}^B \mathcal{B}_b]$ . Here  $\{\mathcal{B}_b\}$  is the positive-operator-valued measure (POVM) corresponding to  $\mathcal{B}$ . Such local hidden state models, and hence nonsteerable states, satisfy various EPR steering inequalities [102], of the form

$$\sum_j \langle a_j B_j \rangle_{\{\rho_{\lambda}^B\}; p(\lambda)} \leq 0, \quad (7.25)$$

where the  $a_j$  denote classical random variables generated by Alice, and the  $B_j$  denote quantum observables on Bob's system. States nonsteerable by Bob are similarly defined in terms of LHS models for Alice, however, we may focus on EPR steering by Alice without any loss of generality. It is known that for any EPR-steerable state shared by Alice and Bob, there is a corresponding steering inequality of the above form [98]. To construct a quantum-refereed steering game (QRS game) from any such steering inequality, we adapt a method recently used by Branciard *et al.* for constructing games for verifying entanglement *per se* [126].

In particular, for a given EPR steering inequality (7.25), we define a corresponding QRS game  $G$  (see Fig. 1c) in which on each run the referee, Charlie, sends Alice a classical label  $j$  and Bob a state  $\omega_k^C$  defined on a Hilbert space  $H^C$  isomorphic to some subspace of  $H^B$ . These states must be such that the equivalent states  $\omega_k^B$  on  $H^B$  form a linear basis for the observables  $B_j$ , i.e.,  $B_j = \sum_k g_{jk} \omega_k^B$  for some set of coefficients  $g_{jk}$ . Alice and Bob are not allowed to communicate during the game, but can have a prearranged strategy and perform arbitrary local operations. Alice returns a value  $a = a_j$ , and Bob returns a value  $b = 0$  or  $1$  corresponding to some POVM  $\mathcal{B} \equiv \{\mathcal{B}_0, \mathcal{B}_1\}$  on  $H_B \otimes H_C$ . The corresponding payoff function is defined by  $P_G := \sum_{j,k} g_{jk} \langle ab \rangle_{j,k}$ , where  $\langle \cdot \rangle_{j,k}$  denotes the average over runs with a given  $j$  and  $k$ . Alice and Bob win the game if  $P_G > 0$ . The QRS game in the main text is equivalent to taking  $j = 0, 1, 2, 3$ ,  $k \equiv (j, s)$ ,  $a_j = \pm 1$  for  $j = 1, 2, 3$ ,  $a_0 = -r/\sqrt{3}$ ,  $\omega_k^C = (1 + s\sigma_j^C)/2$ , and  $g_{jk} = s$  ( $= 1$ ) for  $j \neq 0$  ( $j = 0$ ). The factor of 2 in the payoff function Eq. (4.1) for this game is chosen to make  $P(r)$  equal to the lefthand side of the steering inequality  $\sum_{j=1}^3 \langle a_j \sigma_j \rangle - r\sqrt{3} < 0$  [98]. This steering inequality can be violated for Werner states only if  $W > r/\sqrt{3}$  [98], and hence this condition is also necessary for Alice and Bob to be able to win the QRS game in the main text. For perfect state generation by the referee, i.e.,  $r = 1$  (see below), this reduces to  $W > 1/\sqrt{3}$ . Note that this corresponds to the condition for

a Werner state to allow EPR-steering, with measurements limited to three Pauli directions, in the non-quantum-refereed scenario [100, 102].

We now show Alice and Bob can win game  $G$  only if Alice and Bob share a state that is EPR steerable by Alice. Restricting Alice and Bob to no communication during the game prevents them from generating a steerable state from a nonsteerable one [123], and hence we must show that if they share any nonsteerable state on any Hilbert space  $H_A \otimes H_B$  then  $P_G \leq 0$ . Now, for such a state there is some LHS model  $\{\rho_\lambda^B; p(\lambda)\}$  (see above), and thus

$$\begin{aligned} P_G &= \sum_{j,k} g_{jk} \langle ab \rangle_{j,k} = \sum_{j,k,\lambda} g_{jk} p(\lambda) \langle a_j \rangle_\lambda \text{Tr}_{BC}[(\rho_\lambda^B \otimes \omega_k^C) \mathcal{B}_1] \\ &= \sum_{j,k,\lambda} g_{jk} N q(\lambda) \langle a_j \rangle_\lambda \text{Tr}_C[\tau_\lambda^C \omega_k^C] = N \langle a_j B_j^C \rangle_{\{\tau_\lambda^C; q(\lambda)\}}, \end{aligned}$$

where the normalisation factor  $N$ , probability distribution  $q(\lambda)$ , and density operator  $\tau_\lambda^C$  are implicitly defined via  $N q(\lambda) \tau_\lambda^C = \text{Tr}_B[(\rho_\lambda^B \otimes \mathbb{1}^C) \mathcal{B}_1]$ ;  $B_j^C := \sum_k g_{jk} \omega_k^C$  on  $H_C$  is isomorphic to  $B_j$  on  $H_B$ , and the average is with respect to the LHS model  $\{\tau_\lambda^C(\lambda); q(\lambda)\}$ . Noting the average corresponds to the left hand side of steering inequality (7.25) for this LHS model, one has  $P_G \leq 0$  as required. Conversely, analogously to the entanglement verification games of Branciard *et al.* [126], it may be shown that Alice and Bob can in principle win the game if they share a state that violates EPR steering inequality Eq. 7.25, where Bob measures the projection  $\mathcal{B}_1$  onto an appropriate Bell state on  $H_B \otimes H_C$  [see, e.g., Eq. (4.5)].

In practice, the referee cannot ensure perfect generation of the states  $\omega_k^C$ . However, by performing tomography on these states, the referee can adjust the coefficients  $g_{jk}$  appropriately, to take this into account. We describe one method of doing so below, for the experiment carried out in this paper, which can be easily generalised to other QRS games. We observe that it does not matter if the generated states are acted on nontrivially by some completely positive channel,  $\phi$ , before reaching Bob, as this is equivalent to simply replacing Bob's measurement  $\mathcal{B}$  on  $H_B \otimes H_C$  by  $(I_B \otimes \phi^*)(\mathcal{B})$ , where  $\phi^*$  denotes the dual channel and  $I_B$  is the identity map on  $H_B$ .

In particular, for the QRS game corresponding to Eq. (4.1), suppose that the referee actually generates the states  $\tilde{\omega}_k^C = \frac{1}{2}(1 + \mathbf{n}^{(j,s)}) \cdot \sigma^C$ . The payoff function (4.1) then evaluates to  $P(r) = N \sum_\lambda q(\lambda) \text{Tr}[\tau_\lambda^C T_\lambda(r)]$  for a shared

nonsteerable state, with  $N$ ,  $q(\lambda)$  and  $\tau_\lambda^C$  defined as above and

$$\begin{aligned} T_\lambda(r) &:= 2 \sum_j \left[ \langle a_j \rangle_\lambda (\tilde{\omega}_{j,+}^C - \tilde{\omega}_{j,-}^C) - \frac{r}{\sqrt{3}} (\tilde{\omega}_{j,+}^C + \tilde{\omega}_{j,-}^C) \right] \\ &= \left\langle \sum_j \left[ a_j \left( \mathbf{n}^{(j,+)} - \mathbf{n}^{(j,-)} \right) \right. \right. \\ &\quad \left. \left. - \frac{r}{\sqrt{3}} \left( \mathbf{n}^{(j,+)} + \mathbf{n}^{(j,-)} \right) \right] \cdot \sigma^C \right\rangle_\lambda - 2r\sqrt{3} \\ &\leq \max_{\{a_j=\pm 1\}} \left| \sum_j \left[ a_j \left( \mathbf{n}^{(j,+)} - \mathbf{n}^{(j,-)} \right) \right. \right. \\ &\quad \left. \left. - \frac{r}{\sqrt{3}} \left( \mathbf{n}^{(j,+)} + \mathbf{n}^{(j,-)} \right) \right] \right| - 2r\sqrt{3} \\ &= \max_{\{a_j=\pm 1\}} |\mathbf{A}(\mathbf{a}) - r\mathbf{B}| - 2r\sqrt{3}, \end{aligned}$$

where the inequality follows using  $a_j = \pm 1$  and  $\mathbf{v} \cdot \sigma \leq |\mathbf{v}|$ , and we define  $\mathbf{a} := (a_1, a_2, a_3)$ ,  $\mathbf{A}(\mathbf{a}) := \sum_j a_j (\mathbf{n}^{(j,+)} - \mathbf{n}^{(j,-)})$ , and  $\mathbf{B} := \sum_j (\mathbf{n}^{(j,+)} + \mathbf{n}^{(j,-)}) / \sqrt{3}$ .

It is straightforward to show that the right hand side of the inequality is no more than zero for  $r \geq r_*$ , with

$$r_* := \max_{\{a_j=\pm 1\}} \frac{[(\mathbf{A}(\mathbf{a}) \cdot \mathbf{B})^2 + \mathbf{A}(\mathbf{a}) \cdot \mathbf{A}(\mathbf{a})(3 - \mathbf{B} \cdot \mathbf{B})]^{1/2} - \mathbf{A}(\mathbf{a}) \cdot \mathbf{B}}{3 - \mathbf{B} \cdot \mathbf{B}}. \quad (7.26)$$

Hence, for  $r \geq r_*$ , the operator  $T_\lambda(r)$  is nonpositive, and hence  $P(r) \leq 0$  for any nonsteerable state. It is straightforward to check that  $r_* = 1$  for perfect state generation,  $\tilde{\omega}_k^C = \omega_k^C = \frac{1}{2}(1 + s\sigma_j^C)$ . Determining  $r_*$  experimentally involves tomographically characterising Charlie's state preparations  $\{j, s\}$  to find the Bloch vectors  $\mathbf{n}^{(j,s)}$ . We experimentally found  $r_* = 1.081 \pm 0.009$ .

## Bibliography

- [1] C. E. Shannon. A Mathematical Theory of Communication. *The Bell System Technical Journal*, 27:379423, 623656, 1948.
- [2] H. Nyquist. Certain Factors Affecting Telegraph Speed. *Bell System Technical Journal*, 324, 1924.
- [3] H. Nyquist. Certain Topics in Telegraph Transmission Theory. *A.I.E.E. Trans.*, 47:617, 1928.
- [4] R. V. L. Hartley. Transmission of Information. *Bell System Technical Journal*, 535, 1928.
- [5] S. Singh. *The Code Book*. Anchor Books, First edition, 1999.
- [6] G. Moore. Cramming more components onto integrated circuits. *Electronics Magazine*, 38(8):4, 1965.
- [7] M. Dubash. Moore's Law is dead, says Gordon Moore. *Techworld*, Wednesday 13th April 2005.
- [8] R. Beausoleil. Centre for Quantum Computation and Communication Technologies conference. Sunshine Coast, Queensland, Australia. April 2014.
- [9] A. Peres. Quantum Theory: Concepts and Methods. *Kluwer Academic Publishers*, 1995.
- [10] R. P. Feynman. Simulating Physics with Computers. *International Journal of Theoretical Physics*, 21(6):467488, 1982.
- [11] E. Ehrenfest. Welche Ziele der Lichtquantenhypothese spielen in der Theorie der Wrmestrahlung eine wesentliche Rolle? *Annalen der Physik*, 36:91-118, 1911.
- [12] H. Hertz. On the influence of ultraviolet light on electrical discharge. *Annalen der Physik*, 267(8):983-1000, 1887.

- [13] E. Rutherford. The scattering of  $\alpha$  and  $\beta$  particles by matter and the structure of the atom. *Philosophical Magazine*, 6(21):669-688, 1911.
- [14] H. Kragh. Max Planck: the reluctant revolutionary. *Physics World*, Saturday 1st December 2000.
- [15] M. Planck. On the law of distribution of energy in the normal system. *Annalen der Physik*, 4:553, 1901.
- [16] A. Einstein. On a Heuristic Point of View about the Creation and Conversion of Light. *Annalen der Physik*, 17(6):132-148, 1905.
- [17] N. Bohr. On the constitution of atoms and molecules. *Philosophical Magazine*, 26:476, 1913.
- [18] D. Bohm. A suggested interpretation of the quantum theory in terms of 'hidden' variables (parts I and II). *Physical Review*, 85:553-563, 1935.
- [19] H. Everett. Relative state formulation of quantum mechanics. *Reviews of Modern Physics*, 29:454-462, 1957.
- [20] C. Rovelli. Relational quantum mechanics. *International Journal of Theoretical Physics*, 35:1637-1678, 1996.
- [21] N. D. Mermin. QBism puts the scientist back into science. *Nature comment*. 26 March 2014.
- [22] E. Wigner and H. Margenau. Symmetries and Reflections, Scientific Essays. *Am. J. Phys.* 35:1169, 1967.
- [23] V. Trimble Existence and nature of dark matter in the universe. *Annual Review of Astronomy and Astrophysics*, 25:425472, 1987.
- [24] A. G. Riess *et al.* Observational Evidence from Supernovae for an Accelerating Universe and a Cosmological Constant. *The Astronomical Journal*. 116(3):10091038, 1998.
- [25] M. Schlosshauer. Decoherence, the measurement problem, and interpretations of quantum mechanics. *Rev. Mod. Phys.* 76:1267, 2005.
- [26] R. Penrose. Gravitational Collapse and Space-Time Singularities. *Phys. Rev. Lett.* 14(3):57, 1965.
- [27] H. M. Wiseman. From Einstein's theorem to Bell's theorem: A history of quantum nonlocality. *Contemporary Physics*, 47:79-88, 2006.

- [28] L. de Broglie. Non-linear wave mechanics: A Causal Interpretation. *Elsevier, Amsterdam*, 1960.
- [29] A. Einstein. Letter to Max Born, 4 December 1926. The Born-Einstein Letters. *Walker and Company*, New York, 1971.
- [30] A. Einstein, B. Podolsky, and N. Rosen. Can quantum-mechanical description of physical reality be considered complete? *Phys. Rev. Lett.* 47:777, 1935.
- [31] E. Schrödinger. The present situation in quantum mechanics. *Naturwissenschaften*, 23:823-881, 1935.
- [32] N. Bohr. Can Quantum-Mechanical Description of Physical Reality be Considered Complete? *Physical Review*, 48:696-702, 1935.
- [33] M. Beller. Quantum Dialogue: The Making of a Quantum Revolution. Chicago. *University of Chicago Press*, 1999.
- [34] D. Wick. The Infamous Boundary: Seven Decades of Controversy in Quantum Physics. *Birkhauser, Boston*, 1995.
- [35] J. A. Wheeler and W. H. Zurek. Quantum Theory and Measurement. *Princeton, New Jersey*, 1983.
- [36] J. von Neumann. Mathematical Foundations of Quantum Mechanics. *Springer, Berlin*, 1932.
- [37] Bell, J. S. On the Einstein-Podolsky-Rosen paradox. *Physics (Long Island City, N.Y.)* 1, 195, 1964.
- [38] A. Aspect, J. Dalibard, and G. Roger. Experimental Test of Bell's Inequalities Using Time- Varying Analyzers. *Phys. Rev. Lett.* 49:1804 1982.
- [39] J. F. Clauser, M. A. Horne, A. Shimony, and R. A. Holt. Proposed Experiment to Test Local Hidden-Variable Theories. *Phys. Rev. Lett.* 23(15):880-884, 1969.
- [40] E. Schrödinger. Probability relations between separated systems. *Proc. Cam. Phil. Soc.* 32:446-452, 1936.
- [41] B. C. van Fraasen. The charybdis of realism: Epistemological implications of Bell's inequality. *Synthese*, 52:25-38, 1982.

- [42] H. Price. Time's Arrow and Archimedes' point. Oxford. *Oxford University Press*, 1996.
- [43] J. Bub. The Interpretation of Quantum Mechanics. *Reidel, Dordrecht*, 1974.
- [44] H. P. Stapp. S-matrix representation of quantum theory. *Phys. Rev. D*, 3:1303-1320, 1971.
- [45] M. Bell, K. Gottfried, and M. Veltman. *John S. Bell on the Foundations of Quantum Mechanics*. World Scientific, Singapore, 2001.
- [46] K. Popper. *Quantum Theory and the Schism in Physics*. Routledge, London, 1985.
- [47] E. Knill, R. Laflamme, and G. J. Milburn. A scheme for efficient quantum computation with linear optics. *Nature*, 409:46-52, 2001.
- [48] P. W. Shor. Polynomial-time algorithms for prime factorisation and discrete logarithms on a quantum computer. *SIAM J. Comput.*, 26:1484-1509, 1997.
- [49] L. K. Grover. Quantum mechanics helps in searching for a needle in a haystack. *Phys. Rev. Lett.*, 79:325-328, 1997.
- [50] C. H. Bennett and G. Brassard. Quantum Cryptography: Public key distribution and coin tossing. *Proceedings of the IEEE International Conference on Computers, Systems, and Signal Processing, Bangalore, India*, page 175, 1984.
- [51] A. K. Ekert. Quantum cryptography based on Bell's theorem. *Phys. Rev. Lett.*, 67:661-663, 1991.
- [52] G. B. Lemos, V. Borish, G. D. Cole, S. Ramelow, R. Lapkiewicz, and A. Zeilinger. Quantum imaging with undetected photons. *Nature*, 512:409-412, 2014.
- [53] N. Myhrvold. Moore's law corollary: Pixel Power. *New York Times*, Wednesday 7th June 2006.
- [54] E. Schrödinger. Discussion of probability relations between separated systems. *Proc. Cam. Phil. Soc.* 31:553-563, 1935.
- [55] C. Branciard, E. G. Cavalcanti, S. P. Walborn, V. Scarani, and H. M. Wiseman. One-sided device-independent quantum key distribution:

- Security, feasibility, and the connection with steering. *Phys. Rev. A.* 85:010301, 2012.
- [56] P. M. Pearle. Hidden-variable example based upon data rejection. *Phys. Rev. D.* 2:14181425, 1970.
- [57] A. Acín, N. Brunner, N. Gisin, S. Massar, S. Pironio, and V. Scarani. Device-Independent Security of Quantum Cryptography against Collective Attacks. *Phys. Rev. Lett.* 98:230501, 2007.
- [58] A. Acín, N. Gisin, and L. Masanes. From Bells Theorem to Secure Quantum Key Distribution. *Phys. Rev. Lett.* 97:120405, 2006.
- [59] Y.-C. Liang, T. Vertesi, and N. Brunner. Semi-device-independent bounds on entanglement. *Phys. Rev. A.* 83:022108, 2011.
- [60] H. Weinfurter. Experimental Bell-State Analysis. *Europhys. Lett.* 25:559, 1994.
- [61] S. L. Braunstein and A. Mann. Measurement of the Bell operator and quantum teleportation *Phys. Rev. A.* 51:R1727, 1995.
- [62] J. W. Pan, D. Bouwmeester, H. Weinfurter, and Anton Zeilinger. Experimental Entanglement Swapping: Entangling Photons That Never Interacted. *Phys. Rev. Lett.* 80(18):3891, 1998.
- [63] B. Yurke and D. Stoler. Bells-inequality experiments using independent-particle sources. *Phys. Rev. A.* 46:2229, 1992.
- [64] M. Zukowski, A. Zeilinger, M. A. Horne, and A. K. Ekert. Event-ready-detectors Bell experiment via entanglement swapping. *Phys. Rev. Lett.* 71:42874290, 1993.
- [65] E. Megidish, A. Halevy, T. Shacham, T. Dvir, L. Dovrat, and H. S. Eisenberg. Entanglement Swapping between Photons that have Never Coexisted. *Phys. Rev. Lett.* 110:210403, 2013.
- [66] C. Branciard, D. Rosset, N. Gisin, and S. Pironio. Bilocal versus non-bilocal correlations in entanglement-swapping experiments. *Phys. Rev. A*, 85:032119, 2012.
- [67] C. Branciard, N. Gisin, and S. Pironio. Characterizing the nonlocal correlations created via entanglement swapping. *Phys. Rev. Lett.* 104:170401, 2010.

- [68] T. Vértesi and M. Navascués. Certifying entangled measurements in known Hilbert spaces. *Phys. Rev. A.* 83:062112, 2011.
- [69] R. Landauer. The physical nature of information. *Phys. Rev. A.* 217:188-193, 1996.
- [70] M. A. Nielsen and I. L. Chuang. Quantum Computation and Quantum Information. Cambridge. *Cambridge University Press*, 2000.
- [71] R. Blümel. Foundations of Quantum Mechanics: From Photons to Quantum Computers. *Jones and Bartlett Publishers*, 2010.
- [72] D. F. V. James, P. G. Kwiat, W. J. Munro, and A. G. White. Measurement of qubits. *Phys. Rev. A.* 64:052312, 2001.
- [73] A. G. White, A. Gilchrist, G. J. Pryde, J. L. OBrien, M. J. Bremner, and N. K. Langford. Measuring two-qubit gates. *Journal of the Optical Society of America B.* 24:172, 2007.
- [74] R. F. Werner. Quantum states with Einstein-Podolsky-Rosen correlations admitting a hidden-variable model. *Phys. Rev. A.* 40(8):42774281, 1989.
- [75] R. P. Feynman, R. B. Leighton and M. Sands. The Feynman Lectures on Physics: Volume II. *Addison-Wesley publishing Company, Inc.* Chapter 12, 1964.
- [76] D. F. Walls and G. J. Milburn. Quantum Optics. *Springer-Verlag Berlin Heidelberg*, 1994.
- [77] L. Mandel and E. Wolf. Optical Coherence and Quantum Optics. *Cambridge University Press*, 1995.
- [78] H. A. Bachor and T. C. Ralph. A Guide to Experiments in Quantum Optics. *Wiley-VCH Verlag GmbH & Co. KGaA, Weinheim*, 2004.
- [79] B. E. A. Saleh and M. C. Teich. Fundamentals of Photonics. *John Wiley and Sons*, New York, 2007.
- [80] V. G. Dmitriev, G. G. Gurzadyan, and N. Nikogosyan. Handbook of Nonlinear Optical Crystals. Vol. 64 *Springer Series in Optical Sciences*. *Springer, Berlin*. 2nd Edition, 1997.
- [81] E Hecht. Optics. *Addison Wesley Publishing Company, Reading, Massachusetts*. 2nd Edition, 1987.

- 
- [82] N. K. Langford. Encoding, manipulating and measuring quantum information in optics. *PhD Thesis*. 2007.
  - [83] J. P. Torres, M. Hendrych, and A. Valencia. Angular dispersion: an enabling tool in nonlinear and quantum optics. *Advances in Optics and Photonics*. 2(3):319-369, 2010.
  - [84] P. G. Kwiat, E. Waks, A. G. White, I. Appelbaum, and P. H. Eberhard. Ultrabright source of polarization-entangled photons. *Phys. Rev. A*, 60(2):773776, 1999.
  - [85] T. Kim, M. Fiorentino, F. N. C. Wong. Phase-stable source of polarization-entangled photons using a polarization Sagnac interferometer. *Phys. Rev. A*. **73**:012316, 2006.
  - [86] A. Fedrizzi, T. Herbst, A. Poppe, T. Jennewein, A. Zeilinger. A wavelength-tunable fiber-coupled source of narrowband entangled photons. *Opt. Expr.* 15:15377-15386, 2008.
  - [87] C. K. Hong, Z. Y. Ou, and L. Mandel. Measurement of subpicosecond time intervals between two photons by interference. *Phys. Rev. Lett.* 59:20442046, 1987.
  - [88] M. D. Eisaman, J. Fan, A. Migdall, and S. V. Polyakov. Invited Review Article: Single-photon sources and detectors. *Rev. Sci. Instrum.* 82:071101, 2011.
  - [89] M. Born. The Born-Einstein Letters, with comments by M. Born. *Walker*, New York, 1971.
  - [90] E. G. Cavalcanti, S. J. Jones, H. M. Wiseman, and M. D. Reid. Experimental criteria for steering and the EPR paradox. *Phys. Rev. A*. 80:032112, 2009.
  - [91] S. J. Freedman and J. F. Clauser. Experimental test of local hidden variable theories. *Phys. Rev. Lett.* (14)28:938, 1972.
  - [92] H. P. Stapp. Bell's Theorem and World Process. *Nuovo Cimento*. 29B:270-276, 1975.
  - [93] B. S. Cirel'son. Quantum generalizations of Bell's inequality. *Lett. Math. Phys.* 4:93, 1980.
  - [94] A. Peres and W. H. Zurek. Is quantum theory universally valid? *Am. J. Phys.* 50:807, 1982.

- [95] C. M. Caves, C. A. Fuchs, and R. Schack. Quantum probabilities as Bayesian probabilities. *Phys. Rev. A.* 65:022305, 2002.
- [96] C. A. Fuchs and R. Schack. Quantum-Bayesian coherence. *Rev. Mod. Phys.* 85:1693, 2013.
- [97] M. J. W. Hall. Relaxed Bell inequalities and Kochen-Specker theorems. *Phys. Rev. A.* 84:022102, 2011.
- [98] S. J. Jones, H. M. Wiseman, and A. C. Doherty. Entanglement, Einstein-Podolsky-Rosen correlations, Bell nonlocality, and steering. *Phys. Rev. A.* 76:052116, 2007.
- [99] S. Kocsis, M. J. W. Hall, A. J. Bennet, D. J. Saunders, and G. J. Pryde. Experimental measurement-device-independent verification of quantum steering. *Nat. Comms.* 6:5886, 2015.
- [100] D. J. Saunders, S. J. Jones, H. M. Wiseman, and G. J. Pryde. Experimental EPR-steering using Bell-local states. *Nat. Phys.* 76:845-849, 2010.
- [101] A. J. Bennet *et. al.* Arbitrarily loss-tolerant Einstein-Podolsky-Rosen-steering allowing a demonstration over 1 km of optical fibre with no detection loophole. *Phys. Rev. X.* 2:031003, 2012.
- [102] H. M. Wiseman, S. J. Jones, and A. C. Doherty. Steering, entanglement, nonlocality, and the Einstein-Podolsky-Rosen paradox. *Phys. Rev. Lett.* 98:140402, 2007.
- [103] C. H. Bennett, G. Brassard, C. Crépeau, R. Jozsa, A. Peres, and W. K. Wootters. Teleporting an unknown quantum state via dual classical and Einstein-Podolsky-Rosen channels. *Phys. Rev. Lett.* 70:1895, 1993.
- [104] D. M. Greenberger, M. A. Horne, A. Zeilinger. *Bell's Theorem, Quantum Theory, and Conceptions of the Universe*. Kluwer, 1989.
- [105] J. Calsamiglia and N. Ltkenhaus. Maximum efficiency of a linear-optical Bell-state analyzer. *Applied Physics B: Lasers and Optics.* 72:6771, 2001.
- [106] J. S. Bell. Speakable and Unspeakable in Quantum Mechanics. Cambridge, *Cambridge University Press*, 1987.
- [107] J. Gallicchio, A. S. Friedman, and D. I. Kaiser. Testing Bells inequality with cosmic photons: closing the setting-independence loophole. *Phys. Rev. Lett.* 112:110405, 2014.

- 
- [108] T. Scheidl *et. al.* Violation of local realism with freedom of choice. *Proc. Natl Acad. Sci. USA.* 107:1970819713, 2010.
  - [109] B. G. Christensen *et. al.* Detection-loophole-free test of quantum non-locality, and applications. *Phys. Rev. Lett.* 111:130406, 2013.
  - [110] D. H. Smith *et. al.* Conclusive quantum steering with superconducting transition-edge sensors. *Nat. Comms.* 3:625, 2012.
  - [111] B. Wittmann *et. al.* Loophole-free EinsteinPodolskyRosen experiment via quantum steering. *New J. Phys.* 14:053030, 2012.
  - [112] P. Shadbolt *et. al.* Testing the foundations of quantum mechanics with photons. *Nat. Phys.* 10:278-286, 2014.
  - [113] D. Gottesman, H. K. Lo, N. Lütkenhaus, and J. Preskill. Security of quantum key distribution with imperfect devices. *Quantum Inf. Comput.* 4:325, 2004.
  - [114] I. Gerhardt, Q. Liu, A. Lamas-Linares, J. Skaar, C. Kurtsiefer, and V. Makarov. Full-field implementation of a perfect eavesdropper on a quantum cryptography system. *Nat. Comms.* 2:349, 2011.
  - [115] N. J. Beaudry, T. Moroder, and N. Lütkenhaus. Squashing Models for Optical Measurements in Quantum Communication. *Phys. Rev. Lett.* 101:093601, 2008.
  - [116] T. Tsurumaru and K. Tamaki. Security proof for quantum–key–distribution systems with threshold detectors. *Phys. Rev. A.* 78:032302, 2008.
  - [117] E. Waks, A. Zeevi, and Y. Yamamoto. Security of quantum key distribution with entangled photons against individual attacks. *Phys. Rev. A.* 65:052310, 2002.
  - [118] D. A. Evans, E. G. Cavalcanti, H. M. Wiseman. Loss-Tolerant Tests Of Einstein-Podolsky-Rosen-Steering. *Phys. Rev. A.* 88:022106, 2013.
  - [119] J. P. Gordon, H. Kogelnik. PMD fundamentals: Polarization mode dispersion in optical fibers. *P. Proc. Natl. Acad. Sci. U.S.A.* 97:4541, 2000.
  - [120] R. Ursin *et. al.* Entanglement-based quantum communication over 144 km. *Nat. Phys.* 3:481, 2007.

- [121] M. Aspelmeyer, T. Jennewein, M. Pfennigbauer, W.R. Leeb, and A. Zeilinger. Long-distance quantum communication with entangled photons using satellites. *IEEE J. Sel. Top. Quantum. Electr.* 9:1541, 2003.
- [122] S. Barz, E. Kashefi, A. Broadbent, J. F. Fitzsimons, A. Zeilinger, and P. Walther. Demonstration of Blind Quantum Computing. *Science*. 335:303, 2012.
- [123] E. G. Cavalcanti, M. J. W. Hall, and H. M. Wiseman. Entanglement verification and steering when Alice and Bob cannot be trusted. *Phys. Rev. A*. 87:032306, 2013.
- [124] F. Buscemi. All Entangled Quantum States Are Nonlocal. *Phys. Rev. Lett.* 108:200401, 2012.
- [125] N. Brunner and N. Linden. Connection between Bell nonlocality and Bayesian game theory. *Nat Comms.* 4:2057, 2013.
- [126] C. Branciard, D. Rosset, Y.-C. Liang, and N. Gisin. Measurement-device-independent entanglement witness for all entangled quantum states. *Phys. Rev. Lett.* 110:060405, 2013.
- [127] P. Xu, X. Yuan, L. K. Chen, H. Lu, X. C. Yao, X. Ma, Y. A. Chen, and J. W. Pan. Implementation of a measurement-device-independent entanglement witness. *Phys. Rev. Lett.* 112:140506, 2014.
- [128] A. Acn, N. Gisin, and B. Toner. Rothendiecks contant and local models for noisy entangled quantum states. *Phys. Rev. A*. 73:062105, 2006.
- [129] Vértesi, T. More efficient Bell inequalities for Werner states. *Phys. Rev. A*. 78:032112, 2008.
- [130] S. Kocsis. Controlling Non-Classical States of Light: Experimental Techniques in Quantum Information Science. *PhD Thesis*. January 2014.
- [131] M. Giustina *et al.* Bell violation using entangled photons without the fair-sampling assumption. *Nature*. 497:227230, 2013.
- [132] J. S. Bell. Bertlmann's socks and the nature of reality. *Journal de Physique*. 42:C2 41-61, 1981.
- [133] A. Fine. Hidden variables, joint probability, and the bell inequalities. *Phys. Rev. Lett.* 48:291295, 1982.

- 
- [134] <http://qrng.anu.edu.au>; T. Symul, S. M. Assad, P. K. Lam, *Appl. Phys. Lett.* **98**, 231103 (2011).
  - [135] A. Bennet, T. Vértesi, D. J. Saunders, G. J. Pryde and N. Brunner. Experimental semi-device-independent certification of entangled measurements. *Phys. Rev. Lett.* 113:080405, 2014.
  - [136] N. Sangouard, C. Simon, H. de Riedmatten, and N. Gisin. Quantum repeaters based on atomic ensembles and linear optics. *Rev. Mod. Phys.* 83:33, 2011.
  - [137] C.H. Bennett and S. J. Wiesner. Communication via one- and two-particle operators on Einstein-Podolsky-Rosen states. *Phys. Rev. Lett.* 69:2881, 1992.
  - [138] S. Massar and S. Popescu. Optimal Extraction of Information from Finite Quantum Ensembles. *Phys. Rev. Lett.* 74:1259, 1995.
  - [139] J. S. Lundeen *et. al.* Tomography of quantum detectors. *Nature Physics.* 5:27-30, 2009.
  - [140] A. Luis and L. L. Sánchez-Soto. Complete Characterization of Arbitrary Quantum Measurement Processes. *Phys. Rev. Lett.* 83:3573, 1999.
  - [141] P. P. Rohde, G. J. Pryde, J. L. O'Brien, and T. C. Ralph. Quantum-gate characterization in an extended Hilbert space. *Phys. Rev. A.* 72:032306, 2005.
  - [142] R. Rabelo, M. Ho, D. Cavalcanti, N. Brunner, and V. Scarani. Device-Independent Certification of Entangled Measurements. *Phys. Rev. Lett.* 107:050502, 2011.
  - [143] J. D. Bancal, M. Navascus, V. Scarani, T. Vrtesi, and T. H. Yang. Opening the black box: physical characterization from nonlocal correlations. *arXiv:1307.7053*, 2014.
  - [144] K. F. Pál and T. Vértesi. Maximal violation of a bipartite three-setting, two-outcome Bell inequality using infinite-dimensional quantum systems. *Phys. Rev. A*, 82:022116, 2010.
  - [145] N. K. Langford, T. Weinhold, R. Prevedel, K. Resch, A. Gilchrist, J. OBrien, G. Pryde, and A. White. Demonstration of a Simple Entangling Optical Gate and Its Use in Bell-State Analysis. *Phys. Rev. Lett.* 95:210504, 2005.

- [146] Y. L. Tang, H. L. Yin, S. J. Chen, Y. Liu., W. J. Zhang, X. Jiang, L. Zhang, J. Wang, L. X. You, J. Y. Guan, D. X. Yang, Z. Wang, H. Liang, Z. Zhang, N. Zhou, X. Ma, T. Y. Chen, Q. Zhang, and J. W. Pan. Measurement-Device-Independent Quantum Key Distribution over 200 km. *Phys. Rev. Lett.* 113:190501, 2014.
- [147] C. Li, K. Chen, Y. N. Chen, Q. Zhang, Y. A. Chen, and J. W. Pan. Genuine High-Order Einstein-Podolsky-Rosen Steering. *arXiv.* 1501.01452, 2015.
- [148] D. H. Smith. An Ultrafast Source of Polarisation Entangled Photon Pairs based on a Sagnac Interferometer. *Masters Thesis*, 2009.